



The  
University  
Of  
Sheffield.

**Realising the Potential of the High Speed Sintering Process  
for Industrial Implementation**

By:

**Farhana Norazman**

A thesis submitted in partial fulfilment of the requirements for the degree of  
Doctor of Philosophy

The University of Sheffield  
Faculty of Engineering  
Department of Mechanical Engineering

June 2018

# Abstract

Additive manufacturing (AM) can produce three-dimensional parts from a wide range of materials like polymers, metals, and ceramics. High speed sintering (HSS) process is a developing polymer powder bed fusion process that has a high potential to be commercialised for high volume productions. The drawbacks of the HSS process are the low part quality and process repeatability. This is caused by a lack of understanding of the relationship between process parameters.

In this thesis, cost analysis was performed to measure the commercial viability of the HSS process. A systematic study of the HSS process chain was performed to reveal areas that can affect the process output. An experimental investigation on the effect of two key build parameters (lamp and ink) and a post-processing technique (PUSH process) on the dimensional accuracy and tensile strength of parts was conducted. A novel non-destructive characterisation technique using reflectance spectroscopy was introduced to monitor process repeatability and reproducibility. A novel analytical model was developed to quantify the energy density of a part and predict its future performance.

The cost analysis for potential commercial HSS machines showed that the cost per part was half the laser-sintering equivalent. An elastomeric material, ALM TPE210-S was successfully processed using HSS. The PUSH process enhanced the mechanical properties of parts by 50 – 225 % at the expense of size reduction (~5 %). The lamp irradiance and ink volume had significant effect on parts made from EOS PA2200 material.

The results showed a positive correlation between reflectance and tensile strength, which suggested the suitability of visible spectroscopy as a quality assessment tool. The constructed energy density model (HSS<sub>ED</sub> model) was validated using input data collected from the characterisations of material/equipment/part. A positive correlation was found between energy density and part properties.

The research had developed an increased understanding of the HSS process and helped it move forward towards its commercialisation.

# Table of Contents

<b>Abstract.....</b>	<b>i</b>
<b>Table of Contents .....</b>	<b>ii</b>
<b>Acknowledgements .....</b>	<b>vii</b>
<b>Nomenclatures.....</b>	<b>viii</b>
<b>List of Symbols.....</b>	<b>ix</b>
<b>List of Figures.....</b>	<b>x</b>
<b>List of Tables .....</b>	<b>xiv</b>
<b>Dissemination .....</b>	<b>xvi</b>
<b>Chapter 1 Introduction &amp; Literature Review .....</b>	<b>1</b>
1.1 Introduction.....	1
1.1.1 Research Context.....	1
1.1.2 Research Novelty .....	3
1.1.3 Aims and Objectives .....	4
1.1.4 Thesis Structure.....	5
1.2 Polymers & Polymer Sintering .....	6
1.2.1 Introduction to Polymers.....	6
1.2.2 Polyamides .....	7
1.2.3 Polymer Processing.....	10
1.2.4 Polymer Sintering.....	10
1.3 Additive Manufacturing.....	13
1.3.1 Introduction to Additive Manufacturing .....	13
1.3.2 Classification of Additive Manufacturing Technologies .....	14
1.3.3 Powder Bed Fusion Processes.....	15
1.4 High Speed Sintering .....	17
1.4.1 Introduction to High Speed Sintering.....	17
1.4.2 High Speed Sintering Build Process and Key Parameters .....	18
1.4.3 High Speed Sintering Materials .....	20
1.4.4 High Speed Sintering Applications .....	22
1.4.5 Inkjet Printing in High Speed Sintering .....	23

1.4.6	PUSh process.....	26
1.5	Heat Transfer and Energy Models in Additive Manufacturing .....	27
1.5.1	Heat Transfer in Additive Manufacturing.....	27
1.5.2	Existing Energy Models in Additive Manufacturing .....	28
1.6	Summary .....	30
1.7	References.....	31
<b>Chapter 2</b>	<b>Experimental Work .....</b>	<b>37</b>
2.1	Introduction.....	37
2.2	Powder Characterisation .....	37
2.2.1	Physical Properties of Feed Powder.....	37
2.2.2	Differential Scanning Calorimetry.....	38
2.2.3	Scanning Electron Microscope.....	40
2.3	Experiments to Evaluate the Dimensional Accuracy of High Speed Sintered TPE Parts .....	41
2.3.1	Design of Samples.....	42
2.3.2	Manufacture of TPE Samples by HSS .....	44
2.3.3	Test Methods .....	47
2.4	Experiments to Investigate the Influence of HSS Parameters on the Properties of PA12 Parts .....	54
2.4.1	Design of Experiments .....	55
2.4.2	Manufacture of PA12 Samples by HSS .....	57
2.4.3	Test Methods .....	59
2.5	Experiments to Construct the HSS Energy Density Model.....	63
2.5.1	Theory of Molecular Spectroscopy .....	64
2.5.2	Spectral Irradiance of Infrared Lamp.....	66
2.5.3	Spectral Absorption of Ink .....	67
2.5.4	Spectral Absorption of Powder .....	68
2.6	Summary .....	69
2.7	References.....	69
<b>Chapter 3</b>	<b>Characterisation of High Speed Sintering Equipment and Materials.....</b>	<b>71</b>



3.1	Introduction.....	71
3.2	Thermal Characteristics .....	71
3.2.1	HSS Processing Window .....	71
3.2.2	DSC Curves.....	72
3.3	Powder Morphology .....	74
3.4	Spectral Analysis .....	75
3.4.1	Spectral Irradiance of the Infrared Lamp .....	76
3.4.2	Spectral Absorption of Carbon Black .....	77
3.4.3	Spectral Absorption of Powder .....	79
3.5	Summary .....	80
3.6	References.....	81
<b>Chapter 4 High Speed Sintering of Elastomer - Influence of Process Chain on the Dimensional Accuracy of Parts.....</b>		<b>82</b>
4.1	Introduction.....	82
4.2	Processing of TPE by High Speed Sintering .....	82
4.2.1	HSS Build Parameters.....	82
4.2.2	Experimental Observations .....	84
4.3	Physical and Mechanical Properties of High Speed Sintered TPE.....	85
4.3.1	Part Dimensions .....	85
4.3.2	Mass .....	87
4.3.3	Surface Roughness .....	88
4.3.4	Hardness .....	90
4.3.5	Tensile Properties.....	91
4.3.6	Tear Properties .....	92
4.4	Effect of PUSH Process on the Physical and Mechanical Properties of High Speed Sintered TPE .....	93
4.4.1	Part Dimensions .....	94
4.4.2	Mass .....	96
4.4.3	Surface Roughness .....	96
4.4.4	Hardness .....	99
4.4.5	Tensile Properties.....	99

4.4.6	Tear Properties .....	102
4.5	Cost Estimation for HSS High Volume Production .....	103
4.6	Influence of HSS Process Chain on the Dimensional Accuracy and Strength of HSS Parts .....	111
4.7	Summary .....	113
4.8	References.....	114
<b>Chapter 5 High Speed Sintering of Nylon 12 – The Effect of Key Processing Parameters on Part Quality and Repeatability.....</b>		<b>116</b>
5.1	Introduction.....	116
5.2	Processing of PA12 by High Speed Sintering .....	116
5.3	Physical and Mechanical Properties of High Speed Sintered PA12.....	117
5.3.1	Part Dimensions .....	118
5.3.2	Apparent Density.....	120
5.3.3	Powder Removal .....	120
5.3.4	Tensile Properties .....	122
5.4	Analysis of Variance.....	124
5.4.1	Ultimate Tensile Strength.....	124
5.4.2	Dimensional Accuracy .....	125
5.5	Robustness, Repeatability and Reproducibility .....	127
5.5.1	Process Robustness .....	127
5.5.2	Process Repeatability .....	129
5.5.3	Process Reproducibility.....	129
5.6	Reflectance Spectroscopy as a Quality Assessment Method.....	130
5.6.1	Overview .....	130
5.6.2	Hypotheses .....	130
5.6.3	Materials and Methods .....	131
5.6.4	Results & Discussion .....	133
5.7	Summary .....	136
5.8	References.....	137

<b>Chapter 6</b>	<b>High Speed Sintering Energy Density – The Construction and Validation of an Analytical Model.....</b>	<b>138</b>
6.1	Introduction.....	138
6.2	Construction of HSS Energy Density Model.....	138
6.2.1	Consideration of Input Variables .....	139
6.2.2	Assumptions and Boundary Conditions.....	141
6.2.3	The High Speed Sintering Energy Density Equation.....	142
6.3	Determination of Input Data .....	144
6.3.1	Effective Spectral Irradiance.....	144
6.3.2	Properties of Carbon Black .....	147
6.3.3	Other Input Data.....	149
6.4	Validation of HSS Energy Density Model.....	151
6.4.1	Energy Needed to Melt Powder .....	151
6.4.2	Determination of HSS Energy Density for PA12 Experiment.....	153
6.4.3	Correlation between HSS Energy Density and Ultimate Tensile Strength .....	154
6.4.4	Correlation between Energy Gradient and Dimensional Accuracy ...	155
6.5	Summary .....	157
6.6	References.....	157
<b>Chapter 7</b>	<b>Conclusions and Recommendations for Future Work.....</b>	<b>158</b>
7.1	Conclusions.....	158
7.2	Recommendations for Future Work.....	160
	<b>Appendices.....</b>	<b>161</b>

# Acknowledgements

Firstly, I would like to acknowledge my supervisors Professor Neil Hopkinson and Dr Patrick Smith for all the support and knowledge they have given me in the last few years. To Neil, thank you for sharing your wisdom and for being a constant source of inspiration. To Patrick, I am forever grateful for the unfaltering motivation and constructive feedback that you have provided during the writing of this thesis.

I would also like to acknowledge my co-supervisors Dr Candice Majewski and Dr Adam Ellis for their most sincere support and mentorship, especially when it comes to my personal development.

For the fantastic opportunity that they have given me, I would like to thank Philips Research for sponsoring our collaborative project. My special thanks goes to Dave Beaumont and Joyce van Zanten; it has been an absolute pleasure working with you.

My gratitude extends to the members of the Advanced Additive Manufacturing (AdAM) group. Special thanks to Kurt Bonser for sharing his technical expertise and Wendy Birtwistle for all her help. Thank you to my colleagues Yas Khalil, Luke Fox, Ryan Brown, Antonino Bianco, and the rest of Garden Street for the knowledge they have shared with me.

I would like to thank my family and friends for their loves, well wishes, and prayers throughout this journey. Lastly, I would like to express my sincerest gratitude to my wonderful husband James for his endless love, support, and understanding.

# Nomenclatures

2D	Two-dimensional	RAM	Radiation Absorbing Material
3D	Three-dimensional	RM	Rapid Manufacturing
ALM	Advanced Laser Materials	RMS	Root Mean Square
AM	Additive Manufacturing	RP	Rapid Prototyping
ANOVA	Analysis of Variance	RT	Rapid Tooling
BMP	Bitmap Image File	RTV	Room-Temperature-Vulcanising
CAD	Computer-aided design	SD	Standard Deviation
CNC	Computer Numerical Control	SE	Standard Error
DOD	Drop-On-Demand	SEM	Scanning Electron Microscope
DOE	Design of Experiments	SLC	Cross-sectional layer file
DFMA	Design For Manufacture and Assembly	STL	StereoLithography
DSC	Differential Scanning Calorimetry	STSA	Statistical Thickness Surface Area
EAV	Energy Absorption Value	TPE	Thermoplastic Elastomer
ED	Energy Density	TPU	Thermoplastic Polyurethane
EMR	Energy-melt ratio	TRL	Technology Readiness Level
EOS	Electro Optical Systems	Vis	Visible
FGM	Functionally Graded Material		
GS	Greyscale		
HSS	High Speed Sintering		
HSS <sub>ED</sub>	High Speed Sintering Energy Density		
IM	Injection Moulding		
IR	Infrared		
LS	Laser Sintering		
NIR	Near Infrared		
OEM	Original Equipment Manufacturer		
PA12	Nylon 12		
PBF	Powder Bed Fusion		
PTFE	Polytetrafluoroethylene		
PUSh	Polishing at the University of Sheffield		

# List of Symbols

A	Absorbance, or Area	$\rho$	Density
a	Absorptivity	€	Euro
b	Path length	£	Pound Sterling
c	Concentration	%R	Reflectance
$C_p$	Specific heat capacity	$\sigma$	Stefan-Boltzmann constant, or Stress
CB	Carbon black	$\epsilon$	Strain
d, r	Diameter or distance	$\gamma$	Surface tension
E	Young's modulus, or Energy	$\mu, \eta$	Viscosity
$E_i$	Irradiance	$\lambda$	Wavelength
$E_\lambda$	Spectral irradiance		
$E_b$	Blackbody emissive power		
EaB	Elongation at break		
F	Force		
$h_f$	Enthalpy heat of fusion		
l	Length		
Oh	Ohnesorge number		
P	Power		
Q	Thermal energy		
Re	Reynolds number		
$R_a$	Arithmetical mean roughness		
$R_z$	Ten-point mean roughness		
t	Time		
T	Temperature		
$T_m$	Melting temperature		
$T_g$	Glass transition temperature		
$T_c$	Crystallisation temperature		
UTS	Ultimate tensile strength		
v	Speed		
V	Volume		
w	Width		
We	Weber number		

# List of Figures

<b>Figure 1-1</b> The HSS process chain, showing how polymer powder is transformed into the final part..	2
<b>Figure 1-2</b> Chain structures of thermoplastics (left) and thermosets (right) .....	6
<b>Figure 1-3</b> Amorphous and crystalline structures .....	7
<b>Figure 1-4</b> Synthesis of a polyamide.....	8
<b>Figure 1-5</b> Chemical structure of nylon 12 .....	8
<b>Figure 1-6</b> Frenkel’s model of viscous sintering.....	11
<b>Figure 1-7</b> Prediction of sinter neck radius ( $x/r$ ) against sintering time for PA12 powder (Haworth et al., 2013) .....	12
<b>Figure 1-8</b> ASTM categorisation of AM processes .....	14
<b>Figure 1-9</b> Schematic of a powder bed fusion process (Loughborough University, 2017) .....	15
<b>Figure 1-10</b> Schematic of the high speed sintering process .....	17
<b>Figure 1-11</b> The IR lamp emits a bright red glow when it irradiates the build bed during preheat and sintering passes .....	18
<b>Figure 1-12</b> Effect of build parameters on the tensile properties of TPE210-S .....	21
<b>Figure 1-13</b> Examples of high speed sintering parts; a pipe fitting, a belt buckle, and the midsole of a running shoe.....	22
<b>Figure 1-14</b> Piezoelectric drop-on-demand technology .....	23
<b>Figure 1-15</b> Oh range of printable fluid (Derby, 2010).....	24
<b>Figure 1-16</b> Ink droplet impact on powder .....	25
<b>Figure 1-17</b> 8-bit greyscale .....	25
<b>Figure 1-18</b> The PUSH process effect on test specimen. Before (top) and after (bottom) .....	26
<b>Figure 1-19</b> Schematic of heat transfer in laser sintering (Roberts et al., 2009).....	28
<b>Figure 2-1</b> Sample and reference holders in a double-furnace DSC (PerkinElmer, 2013) .....	38
<b>Figure 2-2</b> Schematic of SEM (The University of Iowa, 2018).....	40
<b>Figure 2-3</b> Flowchart of the experimental procedures to investigate the dimensional accuracy of HSS TPE parts.....	41
<b>Figure 2-4</b> Two-dimensional plan view of TPE samples on the HSS build bed.....	43
<b>Figure 2-5</b> Surface roughness profile and parameters (Ark Novin, 2015).....	48
<b>Figure 2-6</b> The top and bottom surfaces of an HSS part.....	49
<b>Figure 2-7</b> Durometer used to measure Shore A hardness of TPE specimens, and locations of measurement points .....	49
<b>Figure 2-8</b> Optical microscopy equipment.....	50

<b>Figure 2-9</b> Deformation stages during tensile testing a) elastic deformation, b) necking, and c) fracture .....	50
<b>Figure 2-10</b> The stress-strain curves for brittle (A), plastic (B), and elastic (C) polymers.....	51
<b>Figure 2-11</b> Example of a stress-strain curve showing the Young's modulus, ultimate tensile strength, and elongation at break .....	52
<b>Figure 2-12</b> a) Arrows showing the direction of applied force on specimen 5, and b) position of initial cuts and arrows showing the direction of applied force on specimen 6.....	53
<b>Figure 2-13</b> Flowchart of the experimental procedures to investigate the influence of HSS parameters on PA12 parts.....	54
<b>Figure 2-14</b> Identifiers on tensile test specimens .....	56
<b>Figure 2-15</b> Two-dimensional plan view of PA12 samples on the HSS build bed.....	57
<b>Figure 2-16</b> a) Powder removal part in powder cake before bead blasting and b) part after bead blasting .....	59
<b>Figure 2-17</b> Rectangular slots incorporated into the powder removal part.....	61
<b>Figure 2-18</b> Example of a reflectance measurement result.....	62
<b>Figure 2-19</b> Flowchart of the experimental procedures to construct the HSS energy density model ..	63
<b>Figure 2-20</b> Electromagnetic spectrum .....	64
<b>Figure 2-21</b> Spectral blackbody emissive power .....	65
<b>Figure 2-22</b> a) Experimental setup and b) schematic plan view, showing how the lamp output is fed into the light detectors.....	66
<b>Figure 3-1</b> A typical DSC curve for a polymeric material.....	71
<b>Figure 3-2</b> ALM TPE210-S DSC curve.....	73
<b>Figure 3-3</b> EOS PA2200 DSC curve.....	73
<b>Figure 3-4</b> Micrographs of ALM TPE210-S powder at a) low magnification and b) high magnification .....	74
<b>Figure 3-5</b> Micrographs of PA2200 powder at a) low magnification and b) high magnification.....	75
<b>Figure 3-6</b> Irradiance spectra of the gold and coated IR lamps.....	76
<b>Figure 3-7</b> Original absorption spectrum of carbon black powder (Han et al., 2011) .....	78
<b>Figure 3-8</b> Absorption spectrum of carbon black powder.....	79
<b>Figure 3-9</b> Absorption spectrum of PA2200 powder .....	80
<b>Figure 4-1</b> Part a) has high strength and high surface roughness, while part b) has medium strength and medium surface roughness.....	83
<b>Figure 4-2</b> Printed TPE specimens 1 – 6.....	84
<b>Figure 4-3</b> Dimensional accuracy of high speed sintered TPE specimens along x-, y-, and z-directions ( $\pm 1$ SE).....	85



<b>Figure 4-4</b> Relative deviation of TPE specimens in percentage ( $\pm 1$ SE).....	86
<b>Figure 4-5</b> The ends of a TPE part were lifted and created shadows, indicating part warpage .....	87
<b>Figure 4-6</b> Average mass of high speed sintered TPE specimens ( $\pm 1$ SE) .....	88
<b>Figure 4-7</b> Average surface roughness of high speed sintered TPE specimens on bottom and top surfaces ( $\pm 1$ SE).....	88
<b>Figure 4-8</b> Mean surface roughness of high speed sintered TPE specimens on bottom and top surfaces ( $\pm 1$ SE).....	89
<b>Figure 4-9</b> Loose white powder evident on a) TPE specimen 4, compared to b) PA12 specimen 1 ...	90
<b>Figure 4-10</b> Stress-strain curves of untreated TPE specimens.....	91
<b>Figure 4-11</b> a) Crack initiation and b) crack propagation curves of untreated TPE specimens.....	92
<b>Figure 4-12</b> Damaged PUSH test specimen 1 (bottom) compared to the original specimen (top).....	93
<b>Figure 4-13</b> Effect of PUSH on the physical dimensions of TPE specimens ( $\pm 1$ SE).....	94
<b>Figure 4-14</b> The cross-sectional view of a PUSH specimen 2 (left) and an untreated specimen 2 (right) .....	95
<b>Figure 4-15</b> Effect of PUSH on the mass of TPE specimens ( $\pm 1$ SE) .....	96
<b>Figure 4-16</b> Effect of PUSH on the $R_a$ of TPE specimens ( $\pm 1$ SE) .....	97
<b>Figure 4-17</b> Effect of PUSH on the $R_z$ of TPE specimens ( $\pm 1$ SE) .....	97
<b>Figure 4-18</b> Optical microscope images of untreated (a & c) and PUSH (b & d) specimens.....	98
<b>Figure 4-19</b> Effect of PUSH on the tensile properties of TPE specimens using a) ISO method and b) ASTM method .....	99
<b>Figure 4-20</b> Effect of PUSH on the UTS, E and EaB of TPE specimens ( $\pm 1$ SE).....	100
<b>Figure 4-21</b> Cross-sectional view of a fractured PUSH specimen.....	101
<b>Figure 4-22</b> Effect of PUSH on crack initiation in TPE specimens ( $\pm 1$ SE) .....	102
<b>Figure 4-23</b> Effect of PUSH on crack propagation in TPE specimens ( $\pm 1$ SE).....	102
<b>Figure 4-24</b> The lever part used in the cost analysis and 600 parts nested on a LS EOS P110 build platform.....	104
<b>Figure 4-25</b> Ink volume calculation .....	107
<b>Figure 4-26</b> Comparison of cost per part between HSS and LS .....	110
<b>Figure 4-27</b> Fishbone diagram showing the factors that contribute to HSS part properties .....	111
<b>Figure 5-1</b> PA12 specimens 1 (6 replicates), 2 (3 replicates), and 3 (1 replicate) .....	117
<b>Figure 5-2</b> Dimensional accuracy of high speed sintered PA12 specimens along x-, y-, and z-directions ( $\pm 1$ SE).....	118
<b>Figure 5-3</b> Mean density of high speed sintered PA12 ( $\pm 1$ SE).....	120
<b>Figure 5-4</b> Mean powder removal of high speed sintered PA12 ( $\pm 1$ SE) .....	121
<b>Figure 5-5</b> The printed area of a powder removal part covers 60% of the build bed area.....	121

<b>Figure 5-6</b> Tensile properties of high speed sintered PA12 ( $\pm 1$ SE).....	122
<b>Figure 5-7</b> Side view of the tensile parts in the build chamber, configured in a matrix of 3 x 2.....	127
<b>Figure 5-8</b> UTS of PA12 parts against position in the build chamber .....	128
<b>Figure 5-9</b> Batch-to-batch variation of UTS of PA12 parts .....	129
<b>Figure 5-10</b> Data processing to compare printheads.....	132
<b>Figure 5-11</b> Data processing to predict tensile strength.....	132
<b>Figure 5-12</b> Analysing the consistency of ink volume across printheads. Ink volume for Proton 60 are the manufacturer's claimed values.....	133
<b>Figure 5-13</b> Correlation between reflectance and UTS of parts made using a) gold lamp and b) coated lamp .....	134
<b>Figure 6-1</b> Input variables for the HSS energy density model.....	139
<b>Figure 6-2</b> Schematic of heat transfer in the HSS process.....	140
<b>Figure 6-3</b> Powder and ink particles within a voxel.....	142
<b>Figure 6-4</b> Effective irradiance of gold lamp x powder; the lamp power absorbed by the powder without ink .....	144
<b>Figure 6-5</b> Effective irradiance of coated lamp x powder; the lamp power absorbed by the powder without ink .....	145
<b>Figure 6-6</b> Effective irradiance of gold lamp x carbon black; the lamp power absorbed by the ink .	146
<b>Figure 6-7</b> Effective irradiance of coated lamp x carbon black; the lamp power absorbed by the ink .....	146
<b>Figure 6-8</b> Distribution of carbon black on printed area, seen as black blotches on white powder...	148
<b>Figure 6-9</b> Approximation of carbon black surface area as a function of ink volume.....	149
<b>Figure 6-10</b> The HSS <sub>ED</sub> model equation .....	150
<b>Figure 6-11</b> Energy distribution in HSS processing.....	152
<b>Figure 6-12</b> HSS energy density values of parts from the PA12 experiment .....	153
<b>Figure 6-13</b> Predicted correlation between HSS energy density and ultimate tensile strength.....	154
<b>Figure 6-14</b> Correlation between HSS energy density and ultimate tensile strength.....	155
<b>Figure 6-15</b> Energy gradient effect on the dimensional accuracy of parts in x, y, and z directions ..	156

# List of Tables

<b>Table 1-1</b> Typical tensile properties of polymers.....	9
<b>Table 1-2</b> Typical Shore hardness of polymers.....	9
<b>Table 1-3</b> High speed sintering machines and specifications.....	18
<b>Table 1-4</b> Definitions of HSS build parameters.....	19
<b>Table 1-5</b> Tensile properties of high speed sintered materials (to the nearest whole number).....	20
<b>Table 2-1</b> ALM TPE210-S and EOS PA2200 powder properties.....	37
<b>Table 2-2</b> Details of the TPE samples.....	42
<b>Table 2-3</b> HSS processing parameters for TPE samples.....	45
<b>Table 2-4</b> HSS key parameter optimisation for TPE processing.....	46
<b>Table 2-5</b> Test methods for TPE specimens.....	47
<b>Table 2-6</b> Surface roughness settings for TPE specimens.....	48
<b>Table 2-7</b> Lamp type and levels.....	55
<b>Table 2-8</b> Ink volume and levels.....	55
<b>Table 2-9</b> Lamp-ink combination matrix of PA12 builds.....	55
<b>Table 2-10</b> Details of PA12 samples.....	56
<b>Table 2-11</b> HSS processing parameters for PA12 samples.....	58
<b>Table 2-12</b> Test methods for PA12 specimens.....	59
<b>Table 2-13</b> ANOVA table to investigate the effect of parameters on PA12 part properties.....	62
<b>Table 2-14</b> Detectors used to measure the spectral irradiance of IR lamps.....	67
<b>Table 2-15</b> Properties of quartz cuvette.....	68
<b>Table 3-1</b> Vis and NIR regions on the electromagnetic spectrum.....	75
<b>Table 3-2</b> Properties of IR lamps.....	76
<b>Table 3-3</b> Properties of ink.....	77
<b>Table 4-1</b> Build time for TPE specimens.....	84
<b>Table 4-2</b> Dimensions of untreated TPE specimens.....	85
<b>Table 4-3</b> Shore A hardness of untreated TPE specimens.....	90
<b>Table 4-4</b> Tensile properties of untreated TPE specimens.....	91
<b>Table 4-5</b> Tear properties of untreated TPE specimens.....	92
<b>Table 4-6</b> Dimensions of PUSH TPE specimens.....	94
<b>Table 4-7</b> Shore A hardness of PUSH TPE specimens.....	99
<b>Table 4-8</b> Tensile properties of PUSH TPE specimens.....	100
<b>Table 4-9</b> Details of the HSS planned production systems and LS commercial systems used in the cost analysis.....	103

<b>Table 4-10</b> HSS cost analysis - machine and build details.....	104
<b>Table 4-11</b> HSS cost analysis - machine costs .....	105
<b>Table 4-12</b> HSS cost analysis - production overhead costs.....	105
<b>Table 4-13</b> HSS cost analysis - production labour costs .....	106
<b>Table 4-14</b> HSS cost analysis - LS material costs.....	106
<b>Table 4-15</b> HSS cost analysis - HSS material costs .....	107
<b>Table 4-16</b> HSS cost analysis - total cost per part.....	108
<b>Table 4-17</b> An example of HSS cost per part calculation – HSS small machine.....	109
<b>Table 5-1</b> Ink-lamp configuration for PA12 builds.....	117
<b>Table 5-2</b> ANOVA factors and levels .....	124
<b>Table 5-3</b> ANOVA table of means for UTS.....	124
<b>Table 5-4</b> ANOVA table for UTS .....	125
<b>Table 5-5</b> ANOVA table of means for dimensional accuracy .....	126
<b>Table 5-6</b> Summary ANOVA table for dimensional accuracy .....	126
<b>Table 5-7</b> Printhead and greyscale comparison between two sets of parts .....	131
<b>Table 6-1</b> Printhead parameters.....	147
<b>Table 6-2</b> Carbon black calculation.....	147
<b>Table 6-3</b> Initial conditions and material constants for powder .....	149
<b>Table 6-4</b> Material constants and build conditions for carbon black .....	150
<b>Table 6-5</b> Initial and build conditions for IR lamp.....	150
<b>Table 6-6</b> Properties to calculate energy-to-melt layer by Starr et al.....	151

# Dissemination

## Journal papers

1. Norazman, F., Smith, P., Ellis, A. & Hopkinson, N. 2017. Smoother and Stronger High Speed Sintered Elastomers through Surface Modification Process. *International Journal of Rapid Manufacturing*, 6(2-3), pp 155-169.
2. Norazman, F. & Hopkinson, N. 2014. Effect of Sintering Parameters and Flow Agent on the Mechanical Properties of High Speed Sintered Elastomer. *Journal of Manufacturing Science and Engineering*, 136(6), 061006.

## Conference proceedings

1. Norazman, F., Smith, P. & Hopkinson N. 2016. Spectral Analysis of Infrared Lamps for Use in the High Speed Sintering Process. *Proceedings of the 27<sup>th</sup> Solid Freeform Fabrication Symposium*.
2. Norazman, F., Beaumont, D., Zanten, J., Ellis, A. & Hopkinson, N. 2016. The Effect of Surface Modification on Mechanical Properties of High Speed Sintered Elastomers. *Proceedings of 2015 14<sup>th</sup> Rapid Design, Prototyping and Manufacturing conference*.

## Presentations

<u>Month/Year</u>	<u>Title &amp; Location</u>
Sep 2016	<b>Estimation of High Speed Sintered Nylon-12 Tensile Strength Using Visible Reflectance Spectroscopy.</b> Presented at the Printing for Fabrication Conference (NIP 32) Conference, The University of Manchester, UK.
Aug 2016	<b>Spectral Analysis of Infrared Lamps for Use in the High Speed Sintering Process.</b> Presented at the 27 <sup>th</sup> Annual International Solid Freeform Fabrication Symposium, The University of Texas in Austin, Texas, USA.
May 2016	<b>Development of a Novel Energy Equation for the High Speed Sintering Process</b> (Poster). Presented at the Department of Mechanical Engineering's PhD Poster Day, The University of Sheffield, UK.
Dec 2015	<b>The Effect of Surface Modification on Mechanical Properties of High Speed Sintered Elastomers.</b> Presented at the 14th Conference on Rapid Design, Prototyping & Manufacturing, Loughborough University, UK.

# Chapter 1 Introduction & Literature Review

This chapter begins with an introduction to the research covered in this thesis and its context. An introduction of the main themes of the thesis is given first before a full discussion is presented. This is followed by a review of literature on subject area, theoretical background, and related research.

## 1.1 Introduction

### 1.1.1 Research Context

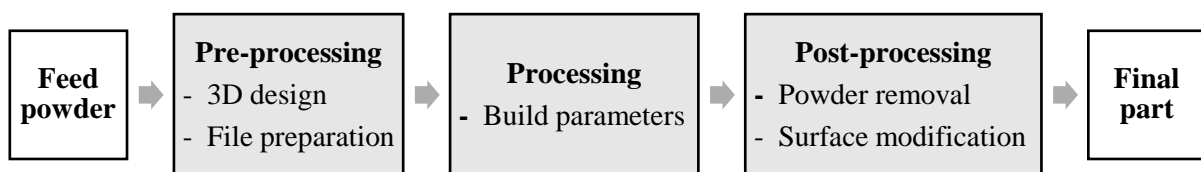
Additive Manufacturing (AM) is a group of technologies that transforms three-dimensional (3D) model data to 3D objects by consolidating materials layer upon layer. These technologies are in contrast to traditional subtractive technologies such as computer numerical control (CNC) machining, which shapes 3D objects by cutting away from a solid block of material. AM can complement traditional manufacturing, particularly for producing parts with high geometric complexity as AM does not require tooling and therefore enable rapid design iterations. However, one of the main challenges faced by most AM processes is their low production speed, due to the adoption of point-by-point consolidation techniques, such as the laser used in laser sintering (LS). These AM processes are therefore limited to one-off and small batch production runs, and are unattractive for use with mass manufacture, which demands high production rates.

A new AM process, High Speed Sintering (HSS) is fast and commercially attractive for high volume manufacturing. The consolidation process in HSS is done by area, making the process scalable at no cost to production time. HSS has the potential to compete with injection moulding to produce polymer consumer products (Hopkinson and Dickens, 2003). However, similar to most AM processes, HSS parts have low dimensional accuracy and repeatability compared to industrial parts manufactured using traditional manufacturing processes. In order to realise HSS's potential for commercialisation and industrial implementation, the part quality and repeatability issues first need to be addressed.

The research in this thesis focuses on the optimisation of the HSS process and the findings can be applied to all HSS applications. The research is divided into three main parts:

1. Investigation of the HSS process chain, identifying the steps that influence the dimensional accuracy of parts.
2. Evaluation of the effect of key processing parameters on part quality and repeatability.
3. Construction of a model as a systematic tool to correlate processing parameters to part quality and repeatability.

The first part of the research examines the HSS process chain, evaluating the steps that can affect the dimensional accuracy of parts. Figure 1-1 shows the HSS process chain and the steps involved to transform raw material into a final part.



**Figure 1-1** The HSS process chain, showing how polymer powder is transformed into the final part

The HSS process chain can be classed into three stages, pre-processing, processing, and post-processing, all of which are crucial to determine the final part quality. During the pre-processing stage, the conversion of a 3D computer-aided design model into a STereoLithography file, and further into bitmap image files results in a loss of feature resolutions. During processing, build parameters, particularly the temperature control, determine the quality of sintering. A lack, or excess, of thermal energy input from the heaters may result in damaged features, shrinkage, wall growth or difficult powder removal. During the post-processing stage, bead blasting is applied to remove excess powder from the part and different levels of surface finish can be achieved depending on the bead material and size, and duration of application. Surface modification techniques can also affect the dimensional accuracy of a finished part. The preliminary investigation suggested that the build parameters are fundamental to produce high quality HSS parts, and therefore formed the focus of the research.

The second part of this research involves investigating the effect of processing parameters on the part properties. Due to the low repeatability of parts, a quality assessment method to monitor repeatability and build quality was developed.

The third part of this research focuses on developing a model to correlate the energy density in HSS with part strength. The sintering process involves a complex interaction between the infrared (IR) sintering lamp, ink, and powder, which determines the quality and performance of manufactured parts. An increased understanding of this interaction will help to improve and utilise the technology especially when using different IR sintering lamps, inks, and powder. This model will be a useful tool to determine the suitability of an equipment and/or material for use on the HSS machine, consequently reducing down time and cost by removing the element of trial and error.

### **1.1.2 Research Novelty**

There is a great demand to take AM technologies to a larger scale for industrial applications and the HSS process is a great candidate for it. Wohlers Associates (2015) reported that the Factum project team at the University of Sheffield had received £900,000 to manufacture a 1 m<sup>3</sup> HSS machine capable of processing high temperature polymers and embedding multiple materials. This machine is expected to be ready at the end of 2017. Licensing contracts have also been completed for the manufacture and sale of HSS machines to various equipment suppliers.

HSS is a unique process and research work is currently exclusively done by The University of Sheffield (previously by Loughborough University) and its industrial partners. Limited work has been done on HSS process development, with previous research placing a large focus on material development, as reviewed in Section 1.4. The novelty of this thesis lies in the systematic characterisation of HSS parts and the development of an energy model to correlate processing conditions with final part properties, in readiness for industrial implementation. This research proposes a cost model for the HSS process and a novel method to assess its part quality. This research also explores new directions for HSS, such as the processing of a thermoplastic elastomer (non-standard material) and the application of a new surface modification process (PUSH process) for surface topography improvement.



### 1.1.3 Aims and Objectives

#### *Aims*

The overall aim of this research is to realise the potential of industrial implementation of HSS and its commercial aspects as a high volume AM production process. Optimisation of HSS machine parameters and development of novel monitoring and evaluation methods for high speed sintered parts are crucial in order to produce high quality parts and progress HSS to a higher technology readiness level.

#### *Objectives*

The objectives for each of the Results chapter are detailed as follows.

#### Chapter 4: Investigation of the HSS process chain and its influence on the dimensional accuracy of parts

- Manufacture non-standard elastomer parts using the HSS machine
- Measure dimensional accuracy and other properties of elastomer parts
- Apply PUSH post processing and examine its effect on the properties of elastomer parts
- Identify steps along the HSS process chain that can influence the dimensional accuracy of elastomer parts
- Develop a cost estimation model and build projection to analyse the commercial viability of HSS

#### Chapter 5: Evaluation of the effect of key processing parameters on part quality and repeatability

- Construct a design of experiments to assess the effect of lamp and ink print volume on the properties of nylon parts
- Manufacture nylon parts using the HSS machine
- Measure a range of physical and mechanical properties of nylon parts
- Evaluate the effect of key processing parameters on the properties of nylon parts
- Measure repeatability across build area and between build replicas
- Develop a method of quality assessment for batch production of HSS parts

## Chapter 6: Construction and analysis of the HSS energy density model

- Measure spectral irradiance of IR lamp and spectral absorbance of ink and powder
- Study the interaction between the lamp, ink, and powder at voxel surface
- Formulate an analytical model to calculate the energy density in HSS based on the spectral analysis of lamp, carbon black, and powder, alongside other parameters
- Synthesise data to establish whether correlation exists between the HSS energy density values and part properties
- Assess the suitability of HSS model to predict manufactured part properties

### **1.1.4 Thesis Structure**

Chapter 1 presents the introduction and literature review of the research. The literature search covers polymers and polymer sintering, AM benefits and challenges, HSS process overview, and heat transfer and energy models in AM.

Chapter 2 outlines the procedures for a series of experiments performed in the research. The experimental work covers powder characterisation, processing of elastomer and nylon, application of PUSH process, and characterisation of HSS equipment and materials.

Chapter 3 analyses the results from the characterisation of HSS equipment and materials.

Chapter 4 reports the results obtained from the investigation of steps along HSS process chain and their effect on the dimensional accuracy of high speed sintered elastomer parts.

Chapter 5 discusses the effect of key HSS processing parameters on the quality and repeatability of high speed sintered nylon parts. The use of reflectance spectroscopy as a HSS part quality assessment is proposed in this chapter.

Chapter 6 details the construction and evaluation of the HSS energy density model as a systematic tool to correlate HSS processing parameters with part quality and repeatability.

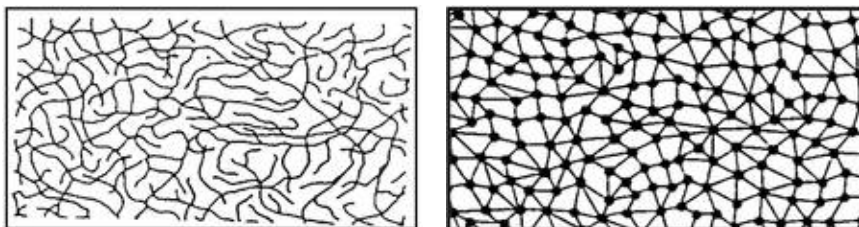
Chapter 7 summarises the research and provides recommendations for future work.

## 1.2 Polymers & Polymer Sintering

This section begins with an introduction to polymers, focusing on their structures and properties. Next, polyamides, the polymer of interest in this study, are explored in detail. This is followed by an overview of polymer processing, and then the sintering process that occurs during these processes.

### 1.2.1 Introduction to Polymers

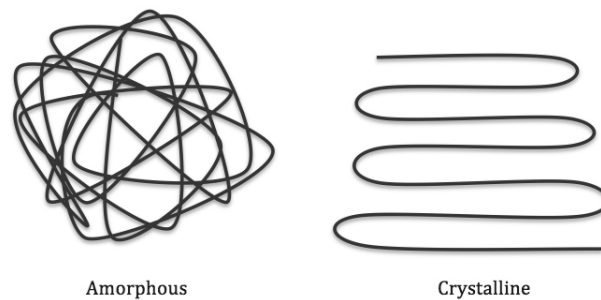
Polymers are long-chain molecules formed by many repeated smaller molecules called monomers, and can be either natural or synthetic. Synthetic polymers are artificially produced by chemically modifying natural polymers. For instance, natural rubber is used to make vulcanised rubber, which has a higher elasticity and is more durable. According to Fried (2014), classification of polymers can be made according to their thermal processing behaviour, chemical structure of their backbones, or the type of polymerisation mechanism. Based upon their characteristic behaviour, polymers can be divided into either thermoplastics or thermosets. Thermoplastics soften when heated and can be reshaped, while thermosets cannot be reshaped once heated. Figure 1-2 illustrates the difference in molecular structures between thermoplastics and thermosets (Ensinger, 2014).



**Figure 1-2** Chain structures of thermoplastics (left) and thermosets (right)

Thermoplastics have long, linear molecular chains that are bound by intermolecular van der Waals forces and mechanical entanglement between the chains. When they are heated above certain temperatures, these bonds are easily broken, resulting in viscous liquids that are easy to mould and process. This also allows repeated heating and moulding, which promotes high recyclability of thermoplastics. Thermosets, on the other hand, consist of cross-linked linear chains that do not flow under heat once processed. This prevents thermosets from being continuously reformed thus only suitable for simultaneous heating and moulding processes such as reaction injection moulding (Saldívar-Guerra and Vivaldo-Lima, 2013).

Thermoset materials include resins such as epoxy, polyester and phenolic. Examples of thermoplastics are polyethylene, polypropylene, polystyrene, and nylon. The molecular structures of thermoplastics change with temperature. When heated, thermoplastics undergo phase changes from a solid, glassy state into a soft, rubbery state, then into a viscous flow melt. The temperatures in which the transitions occur depend on the degree of order exhibited by the chains. In crystalline regions, the chains are highly ordered, while in amorphous regions the chains are tangled with no order, as shown in Figure 1-3 (Bates and Dean, 2017a).



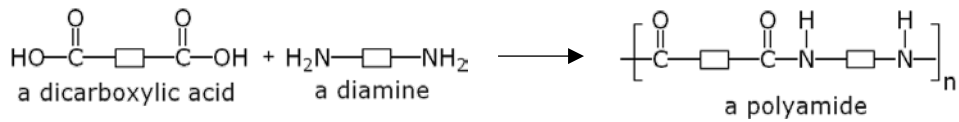
**Figure 1-3** Amorphous and crystalline structures

Polymers can consist of highly crystalline regions (crystalline), highly amorphous regions (amorphous), or a combination of crystalline and amorphous regions (semi-crystalline). Thermoplastics are typically amorphous (polystyrene) or semi-crystalline (nylon).

### 1.2.2 Polyamides

Polyamide (nylon) is a group of thermoplastic polymers where the individual monomers are held together by amide linkages. Polyamides have a good balance of properties - their strength, elasticity, toughness, and resistance to moisture make them suitable for a range of applications. For instance, they are used as an engineering material for car parts and packaging, and as fibres in tyre cords, ropes and clothes (Carragher, 2013).

Polyamides can be synthesised using polycondensation, a chemical reaction in which monomers are combined and a small molecule by-product is produced. The by-product is usually water, hydrochloric acid, or sometimes sodium chloride. Polyamides can be produced by reacting amines – usually diamines, with carboxylic acids – usually dicarboxylic acids. An example of the polycondensation reaction is shown in Figure 1-4, as illustrated by Bates and Dean (2017b).

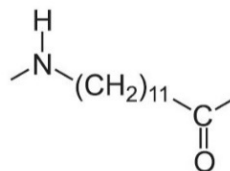


**Figure 1-4** Synthesis of a polyamide

A dicarboxylic acid reacts with a diamine to produce a polyamide with water as the by-product. Sometimes, cryogenic grinding is used on top of polymerisation to refine polymer particle size or to process elastomers that cannot be ground at room temperature. Liquid nitrogen is used to freeze polymer pellets prior to feeding them into a grinding mill, where a low temperature is maintained throughout the system (Harper, 2006). Goodridge et al. (2012) reported that polyamide particles produced by cryogenic grinding are irregular in shape compared to the near spherical particles produced by polymerisation. In AM processes, the irregular particles result in poor powder flow, which consequently creates a rough powder bed and poor surface finish of the final part.

### *Nylon 12*

An example of a commercial polyamide is nylon 12 (PA12). PA12 is made through ring-opening polymerisation of laurolactam monomers. During this reaction, one H<sub>2</sub>O molecule is removed from each monomer and turned into the water by-product. The chemical structure of one repeat unit of PA12 is shown in Figure 1-5.



**Figure 1-5** Chemical structure of nylon 12

The properties of PA12 are directly connected to its structure. According to Griehl and Ruestem (1970), the long aliphatic chain between the -CONH- groups contributes to low water absorption. The excellent dielectric properties of PA12 indicate that it is suitable for application in the electrical and electronics industry. PA12 also exhibits high toughness and impact strength, due to its polyamide structure. These properties enable PA12 to be used in the plastic industry to produce cogwheels, screws, injection syringes, and insulation materials.

### ***Thermoplastic Elastomer***

Thermoplastic elastomer (TPE) is a material that exhibits both thermoplastic and elastomeric properties. TPEs can be synthesised using a range of polymers as their base, including polyamides. One such way is by mixing ethylene-propylene rubber with the lauro lactam.

According to Harper (2002b), polyamide TPEs have high service temperature under load, good heat aging, and high solvent resistance. TPEs have high elasticity and can undergo deformation while retaining their properties. TPEs are widely used in the automotive industry for seals and gaskets, and in consumer industry, for example in athletic footwear soles.

### ***Mechanical Properties***

The mechanical properties of polymers aid users in selecting material based on the particular in-service application of the product. One of the most important properties of polymers is tensile strength. Table 1-1 shows the typical tensile values for polyamides and elastomers (Harper, 2006).

**Table 1-1** Typical tensile properties of polymers

<b>Material</b>	<b>Ultimate Tensile Strength, UTS (MPa)</b>	<b>Young's Modulus, E (MPa)</b>	<b>Elongation at Break, EaB (%)</b>
Polyamides	40 – 80	2,100 – 3,400	20 – 100
Elastomers	7 – 20	0.7 – 4.0	100 – 800

In general, polyamides have high strength, high ductility, and low elasticity, while elastomers are directly opposite. It is possible to enhance a material's tensile properties by using a composite material (Ward and Sweeney, 2004). For instance, a TPE inherits high elasticity from its elastomer unit and high ductility from its thermoplastic unit.

In some instances, polymers are also characterised by their hardness, or resistance to indentation. The two most common test methods for polymer hardness are Shore Type A for soft polymers and Shore Type D for harder polymers. Some typical hardness values are shown in Table 1-2 (Chanda and Roy, 2006).

**Table 1-2** Typical Shore hardness of polymers

<b>Material</b>	<b>Hardness</b>
Nylon (polyamide)	80 Shore D
Silicone rubber (elastomer)	30 – 80 Shore A

Unlike the hardness of metals, polymer hardness readings should only be taken after a fixed time interval, for example, five seconds after indentation. This is done to account for the time-dependent increase in strain in viscoelastic materials such as polymers. Therefore, it should be noted that Shore hardness values are not absolute and the range of hardness values should only be used as a guideline when choosing polymers.

### **1.2.3 Polymer Processing**

This section presents two conventional methods of producing polymer products.

#### ***Injection Moulding***

Injection moulding (IM) is the primary method for high volume production of thermoplastic parts, at 32 wt% of all plastics (Rosato et al., 2012). The process starts by feeding material pellets into a heated barrel via a hopper. Inside the temperature-controlled barrel, a rotating screw pressurises and injects the molten plastic into a mould. The high temperature weakens the Van der Waals forces of the intermolecular chain and forces the plastic to flow. As it flows inside the barrel, the plastic is subjected to a high shear rate from the screw. As the shear rate increases, the viscosity of the molten plastic decreases, resulting in a better flow. The plastic is left to cool and solidifies to the shape of the mould. Injection moulded parts have high strength as the parts are fully dense with no presence of pores.

#### ***Extrusion***

In this process, polymers are melted and extruded through a two-dimensional (2D) die to create products with a continuous profile. The extruded plastic is passed through a water bath to cool and solidify. Extruded parts are linear in shape, such as rods, tubes, films, and sheets. Applications of extruded plastics include pipes, window frames, and wire insulation (Harper, 2002a). According to Rauwendaal (2010), the two most significant cost factors in extrusion are resin cost and energy cost to melt the plastic.

### **1.2.4 Polymer Sintering**

The coalescence of polymer particles is fundamental in processes such as powder coating, rotational moulding, and AM powder bed fusion. German (1996) defines sintering as a consolidation technique that bonds adjacent powder particles to one another to form a solid structure, typically driven by the application of heat and/or pressure.

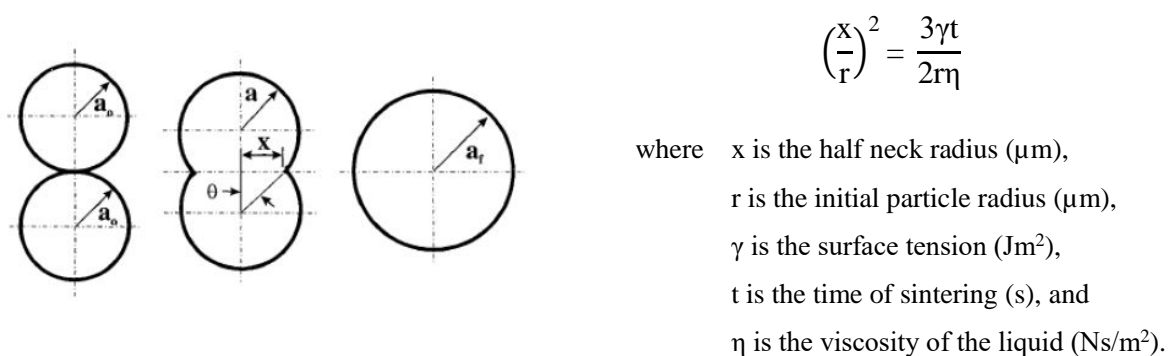
## Theory of Sintering

There are two types of sintering, which are solid-state and liquid phase. Solid state sintering occurs when particles are in direct contact and only solid phases are present, for example in ceramics sintering. In liquid phase sintering, liquid phase is present besides solid particles during sintering, usually at an elevated temperature. The latter type of sintering occurs in LS and HSS processes, and is further discussed below.

### Liquid Phase Sintering

The mechanisms of liquid phase sintering are explained by Kang (2005) as follows. When some of the solid particles melt during heating, their original sites become pores. The liquid phase promotes capillary action between the remaining solid particles. This liquid flow causes solid particles to rearrange themselves, depending on the particle size and distribution. Liniger and Raj (1987) reported that a powder compact made up of mono-sized spheres resulted in larger pores, when compared to different-sized spheres. The uncertainty in particle size and distribution causes non-uniform pore size and distribution in liquid phase sintering.

One of the earliest studies to describe liquid phase sintering was done by Frenkel (1945), who proposed that sintering is driven by viscous flow induced by surface tension. Figure 1-6 illustrates the Frenkel model of viscous sintering and its equation. Recently, many attempts have been made to refine the Frenkel model by taking into account the effect of viscoelasticity and the neighbouring particles (Bellehumeur et al., 1998; Asgarpour et al., 2011).

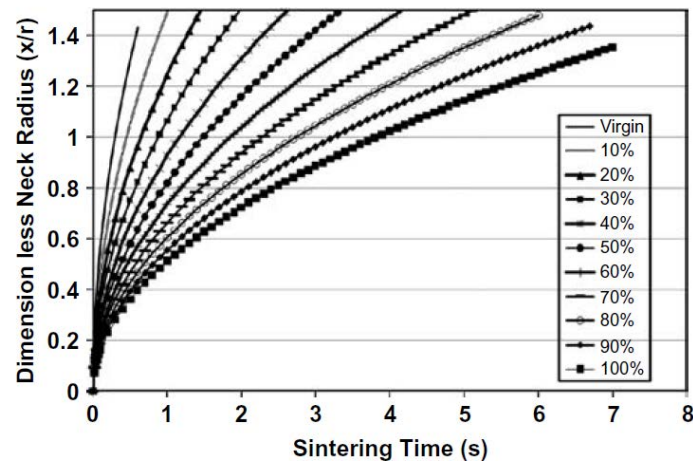


**Figure 1-6** Frenkel's model of viscous sintering

Based on the above equation, the ratio of half neck radius to the initial particle radius (sinter neck radius) is governed by the surface tension, sintering time, and viscosity. Building on this, Haworth et al. (2013) conducted a study to predict the sinter neck radius of PA12 powder as a



function of sintering time. The sinter neck radii for different levels of virgin/recycled powder mix are shown in Figure 1-7.



**Figure 1-7** Prediction of sinter neck radius ( $x/r$ ) against sintering time for PA12 powder (Haworth et al., 2013)

Figure 1-7 shows that in order to achieve an  $x/r$  ratio of one (full sintering), 100 percent virgin PA12 powder needs to be sintered for 0.2 s. It is believed that as an effect of the thermal cycle, the recycled powder have developed longer chain lengths and therefore have a higher viscosity compared to virgin powder. As more recycled powder is mixed in, the equivalent sintering time for the same  $x/r$  ratio increases.

These are the key reasons as to why IM parts are superior in mechanical properties compared to HSS parts. The IM parts are made of long polymer chains and are stronger than the shorter chains in HSS parts. Unlike in IM, the powder particles in HSS are not subjected to any high shear stress. The roller only imposes a low shear rate as it spreads the fresh powder particles across the build bed ( $x$ -direction). The sintering process is exclusively driven by the powder's melt viscosity and surface tension, as the HSS chamber is non-pressurised. In addition, the sintering mechanism in HSS is partial melting, instead of the fully melting in IM. The inherent pores created by the molten solid particles inhibit HSS parts from achieving full density.

## **1.3 Additive Manufacturing**

This section discusses additive manufacturing (AM), which is a group of technologies that transforms 3D model data to 3D objects by consolidating materials layer upon layer. The term additive is used to reflect the method of layer building and to contrast with subtractive technologies such as CNC machining, which creates objects by taking away materials from a larger block.

### **1.3.1 Introduction to Additive Manufacturing**

Also commonly known as 3D printing, AM dates back to the late 1980s, where it started out as rapid prototyping (RP) to produce scale models of products for visualisation purposes. Rapid tooling (RT) followed by using an RP machine to create master patterns or moulds for casting processes. The main advantage of adopting RT is the significant reduction of manufacturing time and cost by eliminating conventional tooling. These technologies subsequently developed into rapid manufacturing (RM) to fabricate end-use products with full functionality, which is what AM is today (Gibson et al., 2010).

According to Wohlers Associates (2017), the type of material operated by AM service providers in decreasing order is polymer only at 51%, both metal and polymer at 29.2%, and metal only at 19.8%. The use of AM is currently extended across many sectors, mainly for aerospace, automotive, and medical applications.

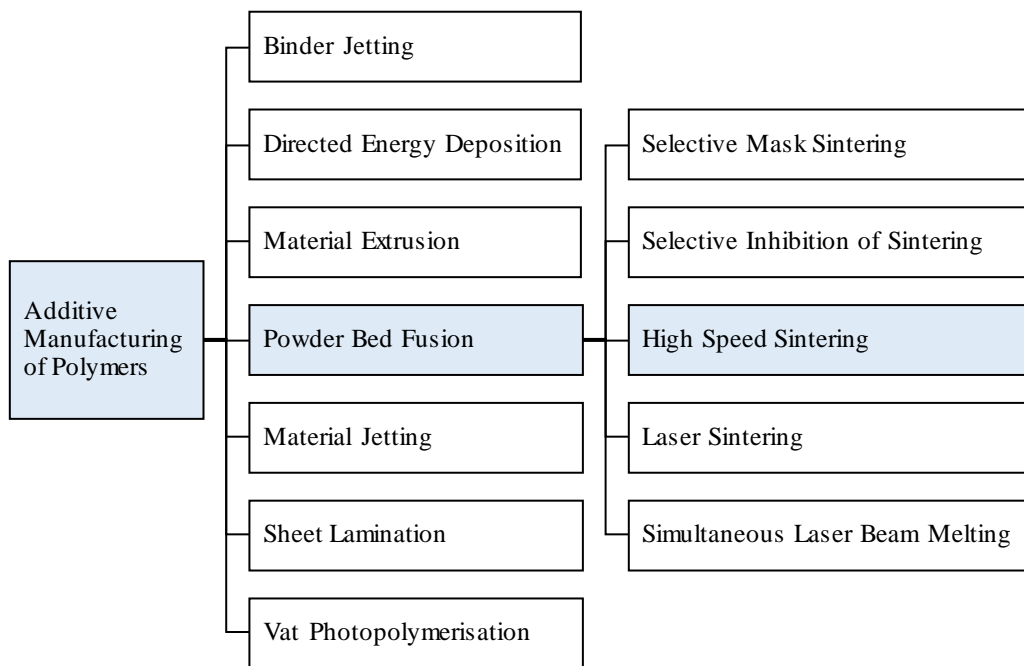
As a developing technology, AM comes with its benefits and limitations. The primary advantage of AM is the design freedom that comes with its tool-less and mould-free processes, enabling consumers to produce parts of almost any geometric shape or feature (Hopkinson et al., 2006). Design iteration is also made seamless and cost-effective with AM as it only takes place within the computer aided design (CAD) programme. AM eliminates many restrictions of conventional design for manufacture and assembly (DFMA) such as the need for undercuts, draft angles, and reduced part counts, thus improving the design process as a whole.

A study by Li et al. (2016) highlighted the main downsides to AM, one of which is poor data translation between CAD models and machines, which results in a discrepancy between the design and actual product. The quality and repeatability of AM processes are also low, often owing to poor real-time process control. The current slow production speed in AM processes,

which also includes lengthy manual pre- and post-processing, make them non-competitive against traditional processes such as injection moulding for use in high volume production.

### 1.3.2 Classification of Additive Manufacturing Technologies

There are numerous AM technologies currently available on the market, each with a different method of layer consolidation, hardware, and processible material. Several methods have been used to group the AM technologies. Hopkinson et al. (2006) classified them according to the physical state of raw material used; liquid-based (stereolithography), powder-based (laser sintering), and solid-based systems (fused deposition modelling). In 2012, ASTM International published a guideline to standardise the classification of AM technologies by their fundamental methodology. Figure 1-8 depicts ASTM's seven categories of AM technologies.



**Figure 1-8** ASTM categorisation of AM processes

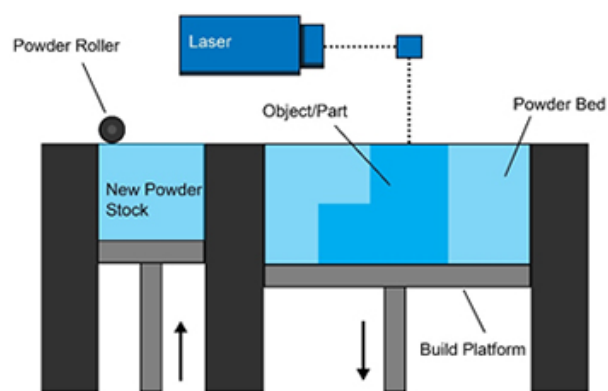
The process of interest in this work is High Speed Sintering (HSS), which falls under the powder bed fusion technology. Arguably, the process also has the characteristics of a binder jetting technology, due to its inkjet printing element. For simplicity, HSS is classified as powder bed fusion, since powder coalescence (sintering) is the main mechanism of joining the materials in the process.

### 1.3.3 Powder Bed Fusion Processes

This section discusses the powder bed fusion (PBF) technology and relevant AM processes laid out in Figure 1-8. By definition, a PBF process uses thermal energy to selectively fuse regions of a powder bed, with the energy source typically being a laser.

#### *Overview of Polymer Powder Bed Fusion*

The schematic of a PBF process is illustrated by Loughborough University (2017) in Figure 1-9. The main components of a PBF system, including a roller and an energy source (laser) are labelled accordingly.



**Figure 1-9** Schematic of a powder bed fusion process (Loughborough University, 2017)

The systematic process of PBF is described as follows. Firstly, a layer of powder is transferred from the powder platform and spread over the build platform using a roller. Then, the first cross section of the part is fused using a laser (or other energy source). A new layer of powder is spread over the previous layer, and the subsequent cross section is fused. The process is repeated until the whole part is finished. The loose, unfused powder in the surrounding support the part in-process, and are removed during post-processing.

The two main issues in PBF parts are high porosity and low dimensional accuracy caused by shrinkage. Mani et al. (2015) addressed the main areas for improvement in measurement techniques to achieve better process control. Amongst them are real time measurement of surface temperature and geometric accuracy. Additionally, Shanjani and Toyserkani (2008) highlighted the influence of roller geometry and parameters on the density of compacted powder and ultimately part quality.

## *Laser Sintering*

Besides HSS, other notable PBF processes include laser sintering (LS), selective mask sintering (Wendel et al., 2008), selective inhibition sintering (Asiabanpour et al., 2006), and simultaneous laser beam melting (Laumer et al., 2015). This section focuses solely on LS due to its high preference in the polymer AM industry, and its similarity to HSS.

The LS process selectively sinters successive layers of powder using a high power carbon dioxide (CO<sub>2</sub>) laser beam enclosed in an inert nitrogen chamber. The schematic of LS is identical to the PBF process in Figure 1-8. The key processing parameters in LS are as follows.

- *Bed temperature*: The temperature of powder on the build platform.
- *Fill laser power*: The applied laser power at which each 2D cross-section is scanned.
- *Layer thickness*: The vertical distance lowered by the bed platform between each layer.
- *Scan spacing*: The distance between adjacent scan vectors.
- *Scan speed*: The traversing speed of a laser beam over a scan vector.
- *Scan count*: The amount the laser beam traverses each scan vector on the same layer.

Many attempts have been undertaken to evaluate the influence of LS processing parameters on mechanical properties (Gibson and Shi, 1997; Caulfield et al., 2007; Starr et al., 2011). An energy density to predict the performance of LS parts has been formulated using these parameters, which is further discussed in Section 1.5.2.

Goodridge et al. (2012) had listed, through a literature review, the range of polymers compatible with LS. They are predominantly polyamides, in particular nylon 12 (PA12) (Vasquez et al., 2011a), or polyamide-based thermoplastic elastomer (TPE) like ALM TPE210-S (Vasquez et al., 2011b; Davidson, 2012). In 2010, Athreya et al. processed a carbon black-filled PA12 using LS. The study found that the composite parts showed increased electrical conductivity but decreased flexural modulus compared to PA12 parts. It is thought that the study had mimicked the HSS process, although the energy input by the CO<sub>2</sub> laser power is significantly higher than the infrared (IR) lamp in HSS.

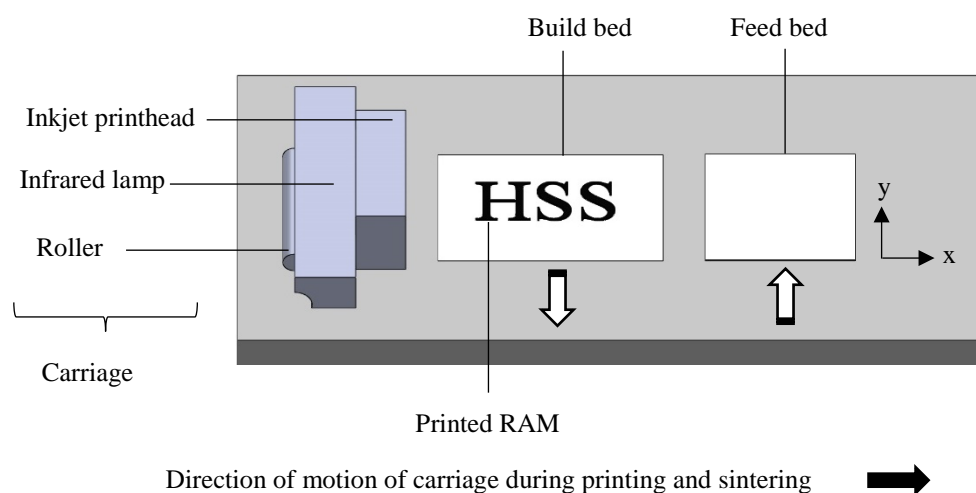
Many studies have likened the HSS process to LS, due to the similarity in the selective thermal energy deposition method. In reality, there is very little similarity between LS and HSS, other than that both processes belong to the same AM category (powder bed fusion). Details of the HSS process and its research and development are presented in the next section.

## 1.4 High Speed Sintering

HSS is a novel AM process developed at Loughborough University in 2004. The process has a high potential for commercialisation, due to its attractive speed and cost. In HSS, sintering time is determined per layer, and the layer time is constant irrespective of the geometry and size of the printed 2D cross-sections on each layer. This characteristic enables HSS to produce a higher output than AM processes that operate on a pointwise basis, within the same given time. The high output, combined with low equipment costs, translate into a low cost per part for HSS.

### 1.4.1 Introduction to High Speed Sintering

A schematic of the HSS process is shown in Figure 1-10.



**Figure 1-10** Schematic of the high speed sintering process

The key components in HSS are the inkjet printhead, infrared (IR) lamp, and roller. They are housed in the conveyor-operated carriage, which traverses the build platform in the x-direction. The build platform also holds the feed bed and build bed platforms, which move vertically (z-direction) during the build process. The build process starts with a new layer of powder spread across from the feed bed onto the build bed by the roller action. The inkjet printhead selectively deposits ink containing radiation absorbing material (RAM) to define the 2D cross-sections of a part. Carbon black is the main type of RAM currently used in HSS ink formulation. The IR lamp irradiates the entire surface area of the build bed. As the RAM has a higher absorptivity than the polymer powder, only the powder underneath the printed ink absorbs sufficient thermal energy to be sintered. The surrounding unsintered powder support the part in-process.

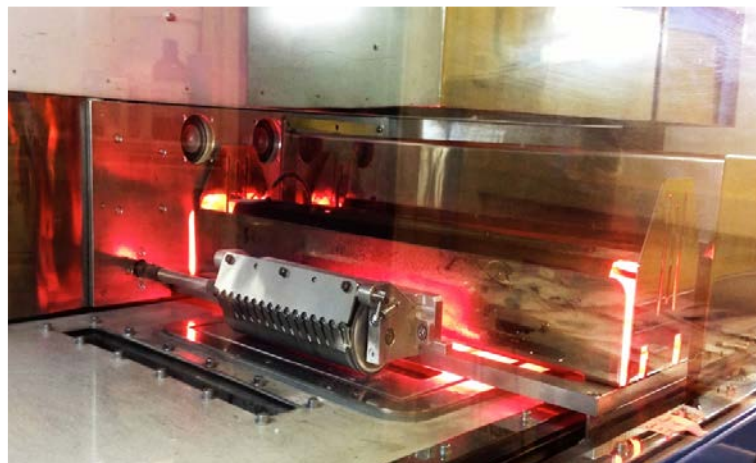
The first HSS test rig was created by modifying a 3D Systems' LS machine (Thomas et al., 2006). A number of purpose-built HSS machines have been built ever since. The specifications of three HSS machines that have been developed or licensed to equipment suppliers are listed in Table 1-3\*.

**Table 1-3** High speed sintering machines and specifications

<i>Machine name</i>	<b>HSS</b>	<b>Voxeljet VX200</b> (voxeljet, 2017)	<b>Velox 10<sup>9</sup></b> (Ellis, 2017)
<i>Year built</i>	2011	2017	2017
<i>Build bed size</i> <i>(L x W x D)</i>	145 mm x 50 mm x 200 mm	200 mm x 200 mm x 200 mm	1.6 m x 0.8 m x 0.75 m
<i>Materials</i>	Nylon 11, nylon 12, TPE210-S	No published data	Thermoplastics with embedded electronic circuits

\*At the time of writing

All work in this research was done on the first purpose-built HSS machine (HSS 2011). The voxeljet VX200 is a newly released HSS machine that was licensed from Loughborough University and Evonik. There is currently no published data on the materials supported by VX200. Velox 10<sup>9</sup> is a large volume HSS machine built for research purposes, funded by the Engineering and Physical Sciences Research Council (EPSRC) through the FACTUM project. Figure 1-11 shows the original HSS machine in operation.



**Figure 1-11** The IR lamp emits a bright red glow when it irradiates the build bed during preheat and sintering passes

#### **1.4.2 High Speed Sintering Build Process and Key Parameters**

The HSS build process involves a series of pre-processing, processing and post-processing steps. The process chain is discussed in details in Section 2.3.2 (page 44).

HSS build parameters are tailored according to the material properties and the desired application of finished parts. Each parameter is defined in Table 1-4.

**Table 1-4** Definitions of HSS build parameters

<b><i>HSS build parameter</i></b>	<b>Definition</b>
<i>Break out temperature</i>	The temperature of the environment where the finished parts are left to cool, either in or out of the machine
<i>Build bed jacket temperature</i>	The powder temperature at the base of the build bed platform
<i>Build bed overhead temperature</i>	The powder temperature on build bed surface
<i>Feed bed jacket temperature</i>	The powder temperature at the base of the feed bed platform
<i>Feed overhead temperature</i>	The powder temperature on feed bed surface
<i>Feed powder ratio</i>	The ratio between a feed bed layer height to a build bed layer height. This is determined by the volume of powder that needs to be transferred from the feed bed to enable full spreading of powder across the build bed
<i>Ink volume</i>	The volume of ink printed over an area of powder. The HSS printhead can generate variable ink volume to achieve greyscale effect in parts
<i>Lamp type</i>	The light bulb used for the build
<i>Layer thickness</i>	The vertical (z) height that the build bed platform drops between each layer to allow of new powder deposition
<i>Maintenance layers</i>	The number of layers between a printhead auto-maintenance to rid of any powder particles adhering to its nozzles
<i>Material</i>	The type of polymer material used as the feed
<i>Orientation</i>	The xyz orientation of parts on the build bed
<i>Powder ratio</i>	The ratio between virgin and recycled powder in the feed
<i>Powder temperature</i>	The temperature of powder at the start of each build. It is usually specified as room temperature (18°C) for the first build of the day, and pre-warmed for consequent builds
<i>Printhead type</i>	The printhead model used for the build
<i>Sintering lamp power</i>	The lamp power level on the sintering pass, between 0 to 100%
<i>Sintering lamp speed</i>	The travelling speed of the carriage on the sintering pass
<i>Surface preheat lamp power</i>	The lamp power level on the preheat pass, between 0 to 100%
<i>Surface preheat lamp speed</i>	The travelling speed of the carriage on the preheat pass
<i>Warm up time</i>	The machine warm up time before each build



### 1.4.3 High Speed Sintering Materials

The materials for HSS are mostly polyamide-based, which includes nylon 12, nylon 11, filled-nylon, and nylon TPE. Table 1-5 summarises the tensile properties of HSS parts. Duraform PA is a PA12 material supplied by 3D Systems. Duraform EX Natural is a high impact resistance nylon 11. ALM TPE210-S is a nylon elastomer, ideal for parts that require high flexibility. Duraform HST is a fibre-filled nylon composite. Its high stiffness at elevated temperatures makes it suitable for high performance parts.

**Table 1-5** Tensile properties of high speed sintered materials (to the nearest whole number)

Material	UTS (MPa)	E (MPa)	EaB (%)
<i>LS Duraform PA (Starr et al., 2011)</i>	40 – 55	1,600 – 2,000	4 – 18
Duraform PA (Rouholamin and Hopkinson, 2016)	45	2,000	32
Duraform EX Natural (Ellis et al., 2015b)	38	N/A	25
ALM TPE210-S (Norazman and Hopkinson, 2014)	2	5	265
Duraform HST (Ellis et al., 2014b)	42	3,933	5

The tensile properties of HSS parts in Table 1-5 are mostly comparable or higher than equivalent LS parts reported in other studies or claimed by the manufacturer. The most significant example can be seen for ALM TPE210-S, where EaB of 265% more than doubled the LS equivalent of 110%.

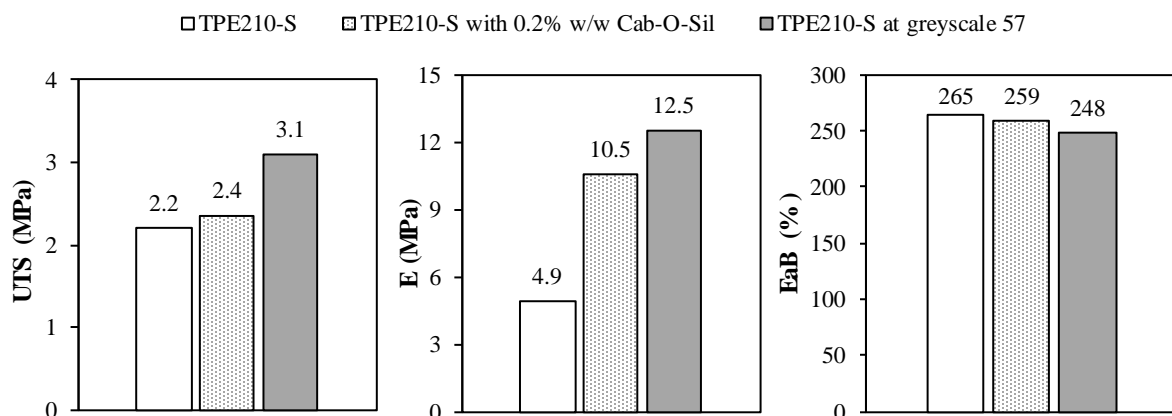
The superior mechanical properties of HSS parts can be explained by referring to the sinter neck radius vs time relationship displayed in Figure 1-7. As previously discussed, a sintering time of 0.2 second is needed for full sintering of virgin PA12. The actual laser interaction time in LS is 0.000066 second for a fast laser, which is 1/10,000<sup>th</sup> of the required time (Vasquez, 2012). On the other hand, the results in Section 6.3.3 (page 150) showed that the IR lamp exposure time in HSS is 0.0011 second, which is significantly longer than the laser interaction time. This allows for a fuller sintering to occur and contributes to higher tensile properties in HSS parts.

Existing HSS research focuses on processing PA12 material, and the dependence of its mechanical properties on build parameters. Thomas et al. (2006) investigated the effect of build bed temperature and lamp power on the hardness of surrounding unsintered powder. Majewski et al. (2007) extended the study by measuring the effect of similar parameters on the tensile properties of parts. Both studies suggested that there should be a trade-off between the two

heating components, which are overhead heater (build bed temperature) and sintering lamp (lamp power), in order to produce robust parts while maintaining easy powder removal. Majewski et al. (2008) also reported more pronounced shrinkage in all directions at higher lamp powers.

Several attempts have been made to quantify the influence of HSS ink type and volume. Fox et al. (2015) reported comparable mechanical performance when using an alternative ink from a different supplier rather than the standard HSS ink with carbon black RAM. It can be inferred that the two inks do not differ greatly in their RAM type or concentration, but this was not disclosed in the study. Alternatively, the amount of RAM in a part can be manipulated by applying a greyscale level on the BMP files, which prompts the printhead to deposit lower ink volume. Inkjet printing and greyscale are discussed in detail in the next Section 1.4.5. Ellis et al. (2014a) reported an improvement in tensile properties of parts with decreasing level of greyscale (increasing volume of ink) up until powder degradation occurs, by which the properties start to decline.

Existing ALM TPE210-S related research includes the addition of fumed silica to the feed powder composition (Norazman and Hopkinson, 2014). This was done to improve powder flow, as the morphology of TPE210-S powder particles greatly differed with PA12 (see page 74). In a separate study, Ellis et al. (2015a) also investigated the effect of greyscale on TPE210-S, where an optimum level of greyscale was determined at 57, which corresponds to 22% less ink volume. Figure 1-12 summarises the results from these two studies, showing the effect of greyscale (level 57) and fumed silica (Cab-O-Sil) on the tensile properties of TPE210-S parts. Both the addition of fumed silica and greyscale resulted in higher UTS and E, but lower EaB.



**Figure 1-12** Effect of build parameters on the tensile properties of TPE210-S

The literature on HSS lamp and ink discussed in this section are limited to measuring the effect of those parameters on mechanical properties exclusively, mostly tensile properties. There is insufficient discussion on the mechanism involved in the consequential change in properties. There is also a lack of focus on other assessments of part quality, such as feature resolutions and surface roughness. A number of these studies are specific to the HSS machine configuration at the time, which makes them trivial when the machine configuration changes.

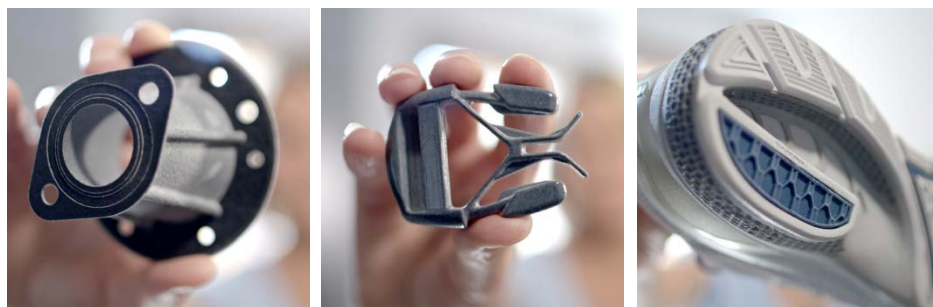
#### 1.4.4 High Speed Sintering Applications

The potential applications of HSS are discussed as follows.

Thompson et al. (2008) reported good dielectric properties in HSS parts. Compared to injection moulded PA12, the dielectric constant and dissipation factor were comparable, but the dielectric strength was lower. The printhead on the HSS machine can be made to print conductive ink, which enables the manufacture of polymer parts with embedded printed electronic circuits. Examples of this application includes sensors and wearable technology such as a smartwatch.

The ability to control the ink volume via greyscale enables the creation of a part with sections of varying densities, which corresponds to a change in properties. This mimics a functionally graded material (FGM) and has a vast application in different sectors, for instance in tennis rackets and skis (Mahamood and Akinlabi, 2017).

Figure 1-13 displays a few examples of parts made by the HSS process (High Speed Sintering Loughborough University., 2017).



**Figure 1-13** Examples of high speed sintering parts; a pipe fitting, a belt buckle, and the midsole of a running shoe

### 1.4.5 Inkjet Printing in High Speed Sintering

The HSS process incorporates inkjet printing to outline the 2D cross-section images on powder substrate in each layer. The printhead employed is a piezoelectric drop-on-demand (DOD). In DOD inkjet technology, ink drops are ejected only when required, and are formed by the creation of a pressure pulse (Magdassi, 2010). A piezoelectric printhead operates via a change in electric field, which creates mechanical pressure that ejects a drop from the nozzle. Hence, the printhead on a HSS machine can selectively deposit ink onto the desired sintering region and in a varying amount by controlling the voltage. Figure 1-14 illustrates the schematic of the printhead technology.

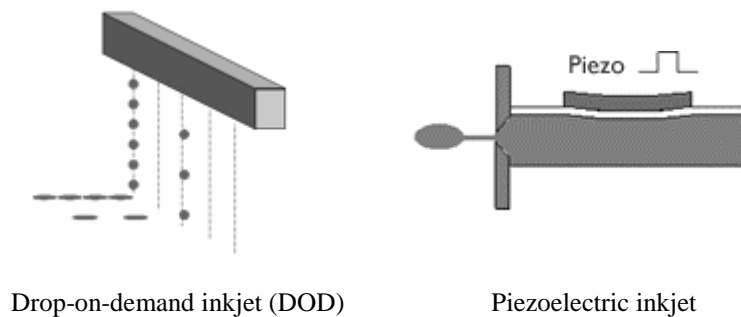


Figure 1-14 Piezoelectric drop-on-demand technology

#### *Rheological Properties of Inkjet Ink*

Inkjet printing is a complex process and it is critical that an inkjet ink has the physicochemical properties that match the requirements of a printhead. According to Hoath (2016), the two physical properties that dominate the behaviour of jetting and spreading are viscosity and surface tension. The ink density and the printhead nozzle diameter are also important to ensure successful drop formation.

The viscosity of the ink is particularly important during jetting, as it determines the jet's break-off length from the nozzle (Hoath et al., 2010). Inkjet inks are typically Newtonian, which means that their viscosity remain constant even at high shear rate. The viscosity required for piezo DOD printing is usually between 10 – 14 cP, depending on the printhead (Magdassi, 2010). The viscosity of ink increases when particles are added to the solvent, for instance the addition of carbon black as the RAM in HSS.

The surface tension of the ink primarily determines the spreading behaviour on the substrate. Jung and Hutchings (2012) reported slow spreading in the wetting phase for an ink with a high

surface tension. In piezo DOD, a static surface tension in the range of 22-36 dynes/cm is required (Magdassi, 2010).

The drop formation concerns the formation of a jet exiting through a nozzle in a single drop instead of disintegrating into many small droplets known as satellite drops. These satellite drops are detrimental to printing quality.

The tendency of drop formation can be determined using a relationship of ink properties, called the Ohnesorge number (Oh). Oh is a dimensionless constant that measures the ratio of viscous and inertial resistances to spreading, which relates the Weber number (We) to the Reynolds number (Re). The equation for Ohnesorge number is given in the following Equation 1-1.

$$Oh = \frac{\sqrt{We}}{Re} = \frac{\eta}{\sqrt{\rho\gamma r}} \quad \text{Equation 1-1}$$

where:

$\eta$  is the ink viscosity,  $\gamma$  is the ink surface tension, and  
 $\rho$  is the ink density,  $r$  is the characteristic length

In DOD inkjet printing, an Ohnesorge number of between 0.1 and 1 ( $0.1 < Oh < 1$ ) is required for a stable drop formation. At high values of Oh, the fluid will be too viscous to be ejected, whereas at low values satellite droplets will form alongside the primary drop. Derby (2010) plotted the printable region for DOD inkjet printing, in terms of parameter Z, where  $Z = 1/Oh$ , in Figure 1-15.

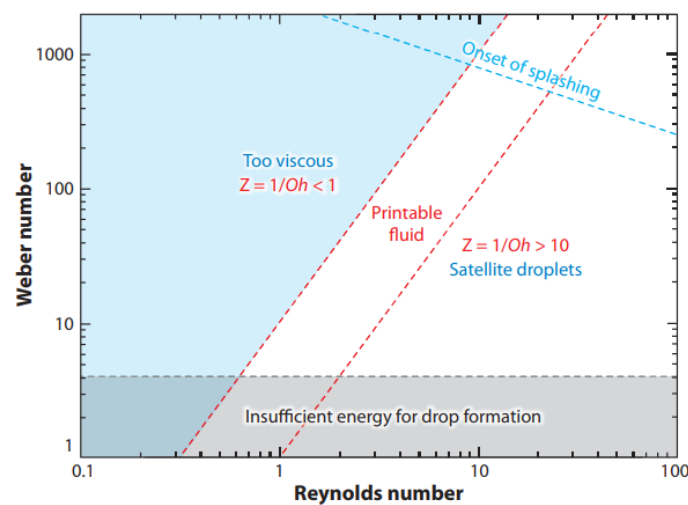
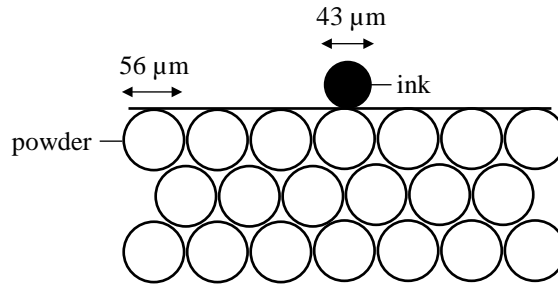


Figure 1-15 Oh range of printable fluid (Derby, 2010)

Figure 1-16 illustrates the ejected ink droplet on the HSS powder-filled build bed.



**Figure 1-16** Ink droplet impact on powder

The interaction between micrometer-sized droplets and powder in powder-based AM processes upon impact has been investigated by Tan (2016). Due to the comparable size between ink and powder particle and the interstitial spaces between the powder particles, the penetration of droplet produced by DOD inkjet printing is significantly different compared to the impact of a larger droplet size (millimeter). While the spreading of a droplet on a solid surface is dependent on the surface wettability, the interstitial spaces between the powder particles also result in new menisci to form, which in turns decelerate the penetrating droplet. The droplet size and impact velocity are two critical parameters that influence part quality. Jung and Hutchings (2012) reported that the maximum spreading diameter increases with speed. The droplet also spreads wider and penetrates deeper into the powder layers at a higher impact velocity (Tan, 2016).

### ***Greyscale in High Speed Sintering***

The employment of inkjet printing in HSS provides the process the capability to print in greyscale. Greyscale printing is advantageous to HSS as it allows the creation of density gradients in parts and controls the ink volume. HSS greyscale applies the 8-bit greyscale to print cross-section images in shades of grey. In 8-bit greyscale, 256 different shades of grey (2 to the power of 8) can be applied to an image. The scale goes from 0 to 255, where 0 is black and 255 is white. Figure 1-17 demonstrates the range of greyscale levels.



**Figure 1-17** 8-bit greyscale

Early HSS greyscale employed an image processing software to set the greyscale during file preparation stage. Recent development in DOD technology has enabled greyscale to be executed directly by the printhead, where different voltage can be delivered to release between 0 and 8 droplets per ejection event to achieve the desired greyscale.

### 1.4.6 PUSH process

PUSH process is a novel solvent polishing process developed by the University of Sheffield (2014) to post-process polymer AM parts. The process is exclusively licensed to a start-up company, Additive Manufacturing Technologies (AMT) in order to develop a scalable automated manufacturing system through the patent pending PostPro3D technology. The technology is being developed in collaboration with Xaar plc with a £624,000 grant awarded by Innovate UK in 2017 (Additive Manufacturing Technologies, 2018).

The PUSH process was developed to improve the surface roughness of polymer AM parts. The process utilises a simple chemical surface treatment technique and requires low labour with quick turnaround time. Solvent polishing is a common technique used to smooth plastics, and can be achieved by either immersing the plastic part in a solvent bath, or exposing the part to a vapourised solvent (Singh et al., 2016). In AM, the solvent polishing technique is especially popular for use on fused deposition modelling parts to remove the characteristic stair-step appearance (Priedeman and Smith David, 2012). The technique works by reflowing the plastic on the surface, thus making it smooth.

The PUSH process application is material specific instead of process specific, and it has had success with several nylon materials such as nylon 11 and nylon 12, and thermoplastic polyurethanes (Ellis et al., 2015b). The visual effect of the PUSH process on a test specimen can be observed in Figure 1-18.



**Figure 1-18** The PUSH process effect on test specimen. Before (top) and after (bottom)

It is evident that the PUSH process significantly changes the appearance of a part. The PUSH part is significantly darker than the original part. The process also changed the finish of the sample from matte to glossy. The colour change can be attributed to the carbon black (RAM) contained in the specimen, which is made prominent after the surface treatment.

## **1.5 Heat Transfer and Energy Models in Additive Manufacturing**

The basis of heat transfer is its physical mechanisms or modes, which are conduction, convection, and radiation. Conduction is the transfer of energy across a medium from the more energetic particles (higher temperature) to the less energetic particles (lower temperature). Convection is the heat transfer that occurs between a surface and a moving liquid when a temperature gradient exists. Radiation is the energy emitted by a matter without the presence of a medium.

Energy exists in many forms such as thermal, mechanical, kinetic and chemical (Çengel, 2011). The sum of the energy of a system can be constituted as total energy (E). The total energy of a system can be calculated by determining the mechanisms involved.

### **1.5.1 Heat Transfer in Additive Manufacturing**

Understandings of the heat transfer and energy distribution form a critical part of the AM process improvement. Many attempts have been made to simulate the AM processes through numerical, analytical, and empirical modelling approaches. A few examples of these simulation models, as constructed based on the LS process are discussed as follows.

- One-dimensional empirical sintering model  
Nelson (1993) proposed a simple equation to correlate the key LS process parameters to describe different scan conditions. The resultant value, the energy density, is then correlated with different mechanical properties. This model is further discussed in the next section.
- Two-dimensional numerical model  
Tontowi and Childs (2001) developed a two-dimensional numerical model to predict the density of sintered part. The model was validated against experimental results of PA12 processed at various powder bed temperatures.
- Three-dimensional transient finite element analysis  
Bugeda et al. (1999) developed a three-dimensional finite element model to simulate the temperature and density distribution in LS. The initial conditions considered in this model included bed temperature, powder density and solid fraction (packing density). The model was applied to polycarbonate and various material constants such as conductivity, specific heat, surface energy, and activation energy were used as input.



Moser et al. (2016) performed a study to compute the effective thermal conductivity of polymers in LS. The study defined the net heat transfer in a polymer particle to consist of three mechanisms. These mechanisms are particle–particle conduction ( $\dot{Q}_r$ ), particle–fluid–particle conduction ( $\dot{Q}_{pfp}$ ), and radiation ( $\dot{Q}_{rad}$ ). In a steady state, the relationship can be described by Equation 1-2.

$$\dot{Q}_r + \dot{Q}_{pfp} + \dot{Q}_{rad} = 0 \quad \text{Equation 1-2}$$

Meanwhile, Roberts et al. (2009) equated the laser flux in a metal LS process to the total of conduction, convection losses and radiation losses. The study established a model of the LS heat transfer mechanisms, as shown in Figure 1-19.

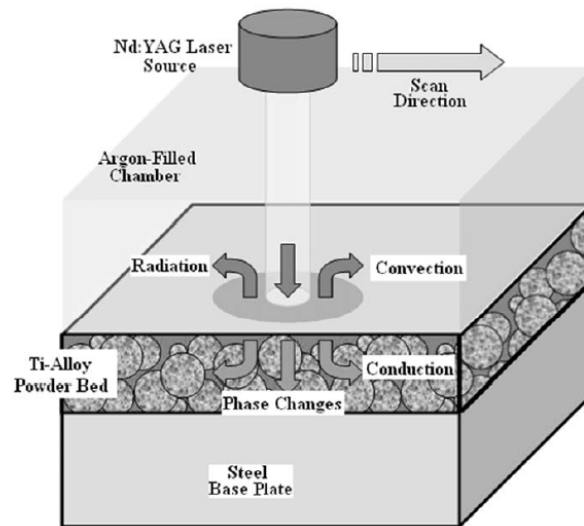


Figure 1-19 Schematic of heat transfer in laser sintering (Roberts et al., 2009)

## 1.5.2 Existing Energy Models in Additive Manufacturing

This section discusses several energy models that have been proposed as a quantitative measurement method to assess the quality of a build or part in AM.

### *Andrew's Number – Laser Sintering*

The first model is the Andrew's number developed by Nelson (1993). Also known as the energy density (ED) model, this model measures the energy density of a build as a function of its process parameters. The ED equation is given in Equation 1-3.

$$ED = \frac{\text{laser power}}{\text{laser speed} \times \text{scan spacing}} \quad \text{Equation 1-3}$$

The model is straightforward and relatively easy to use as a tool to compare different LS builds on different platforms. However, the exclusion of layer height makes it difficult to compare builds of different thicknesses.

### ***Energy Melt Ratio – Laser Sintering***

The energy-melt ratio (EMR) is a dimensionless parameter proposed by Starr et al. (2011) to compare the amount of energy deposited during laser scanning to the amount of energy needed to melt the powder. When the EMR is greater than one, the amount of laser energy incident on the powder bed is sufficient to melt the powder. This calculation assumes that the entire energy incident from the laser is absorbed within the layer of powder. However, this is only approximately true as some incident laser energy may be reflected, re-radiated or absorbed by the underlying previously melted layer. The EMR equation is given in Equation 1-4.

$$\text{EMR} = \frac{\text{laser power}}{[\text{specific heat}(\text{melt temp} - \text{bed temp}) + \text{heat of fusion}](\text{density})(\text{packing density}) \times \text{laser speed} \times \text{scan spacing} \times \text{layer thickness}}$$

Equation 1-4

The only criticism to the EMR model is that the density of bulk powder should have been used instead of sintered powder, as the melt energy of powder is calculated in powder state.

### ***Energy Absorption Value – High Speed Sintering***

Thomas (2009) proposed an energy absorption value (EAV) model to represent the theoretical energy value in a HSS part. The EAV value is calculated by integrating the product of IR lamp spectral output with the RAM spectral absorption. The EAV equation is given in Equation 1-5.

$$\text{EAV} = \int_{400}^{2,500} (\text{Spectral irradiance of IR lamp} \times \text{Spectral absorption of RAM}) \quad \text{Equation 1-5}$$

The EAV model only considers the lamp and ink, but not powder. Powder reflectivity and temperature gradient between sintered and unsintered powder are significant aspects of the HSS process and should not have been dismissed. Furthermore, the spectral absorption of RAM used in this model was a sum of absorbance and transmittance, which does not accurately represent the lamp-ink interaction during sintering.

## 1.6 Summary

HSS is a polymer AM process that combines powder bed fusion with inkjet printing technology. This chapter introduced the HSS research covered in this thesis and highlighted its novelty. The following themes are discussed throughout this thesis:

- Characterisation of raw materials and equipment used for HSS
- Characterisation of high speed sintered thermoplastic elastomer and nylon-12 parts
- Influence of HSS process chain on part properties
- Cost analysis of HSS for high volume manufacturing
- Quality assessment of HSS parts
- Development of an analytical model to correlate process parameters with part properties

The background theories and literature to the above themes were presented in this chapter.

Firstly, polymers and their properties were discussed. Thermoplastic polymers are suitable for HSS processing as they can be continuously reformed upon heating.

Next, AM technology and its processes were summarised. The group of technology of interest is powder bed fusion. The drawback of powder bed fusion parts, specifically the high porosity and shrinkage, were addressed. The AM process central to this thesis, the HSS process, was introduced. The mechanisms and variables pertaining to the process were defined. Polyamide and its derivatives were revealed as the preferred feed materials for HSS.

Previous research on HSS and LS energy models was reviewed. The literature review revealed a need for a deeper understanding of the fundamental interaction that occurs on the HSS build bed during processing.

The following chapter presents the materials and methods used to perform the experimental work in this thesis.

## 1.7 References

1. Additive Manufacturing Technologies. 2018. *Automated Post Processing for 3D Printing* [Online]. Available: <https://amtechnologies.co.uk/> [Accessed April 2nd 2018].
2. Asgarpour, M., Tcharkhtchi, F., Bakir, S., Khelladi, A. & Khavandi, A. 2011. Characterization and modeling of sintering of polymer particles. *Journal of Applied Polymer Science*, 119(5), 2784-2792.
3. Asiabanpour, B., Khoshnevis, B. & Palmer, K. 2006. Advancements in the selective inhibition sintering process development. *Virtual and Physical Prototyping*, 1(1), 43-52.
4. ASTM International (2012) Standard Terminology for Additive Manufacturing Technologies. *ASTM Standard F2792*. West Conshohocken, PA: ASTM International.
5. Athreya, S. R., Kalaitzidou, K. & Das, S. 2010. Processing and characterization of a carbon black-filled electrically conductive Nylon-12 nanocomposite produced by selective laser sintering. *Materials Science and Engineering: A*, 527(10–11), 2637-2642.
6. Bates, J. & Dean, J. (2017a) MAT1640 Nylon - mechanical properties. Lecture Notes. The University of Sheffield.
7. Bates, J. & Dean, J. (2017b) MAT1640 Nylon - making. Lecture Notes. The University of Sheffield.
8. Bellehumeur, C. T., Kontopoulou, M. & Vlachopoulos, J. 1998. The role of viscoelasticity in polymer sintering. *Rheologica acta*, 37(3), 270-278.
9. Bugada, G., Cervera, M. & Lombera, G. 1999. Numerical prediction of temperature and density distributions in selective laser sintering processes. *Rapid Prototyping Journal*, 5(1), 21-26.
10. Carraher, C. E. 2013. *Carraher's Polymer Chemistry, Ninth Edition*, Boca Raton, FL, Taylor & Francis.
11. Caulfield, B., McHugh, P. E. & Lohfeld, S. 2007. Dependence of mechanical properties of polyamide components on build parameters in the SLS process. *Journal of Materials Processing Technology*, 182(1–3), 477-488.
12. Çengel, Y. A. 2011. *Thermodynamics : an engineering approach*, New York, McGraw-Hill.
13. Chanda, M. & Roy, S. K. 2006. *Plastics Technology Handbook, Fourth Edition*, Boca Raton, FL, CRC Press.
14. Davidson, C. 2012. *Investigating the suitability of laser sintered elastomers for running footwear applications*. PhD Thesis, Loughborough University.

15. Derby, B. 2010. Inkjet Printing of Functional and Structural Materials: Fluid Property Requirements, Feature Stability, and Resolution. *Annual Review of Materials Research*, 40(1), 395-414.
16. Ellis, A. 2017. High Speed Sintering: The Next Generation of Manufacturing. *In: Magdassi, Shlomo & Kamyshny, Alexander (eds.) Nanomaterials for 2D and 3D Printing*. United Kingdom: Wiley-VCH Verlag GmbH & Co. KGaA.
17. Ellis, A., Noble, C. J. & Hopkinson, N. 2014a. High Speed Sintering: Assessing the influence of print density on microstructure and mechanical properties of nylon parts. *Additive Manufacturing*, 1-4(1), 48-51.
18. Ellis, A., Hartley, L. & Hopkinson, N. 2015a. Effect of Print Density on the Properties of High Speed Sintered Elastomers. *Metallurgical and Materials Transactions A*, 46(9), 3883-3886.
19. Ellis, A., Brown, R. & Hopkinson, N. 2015b. The effect of build orientation and surface modification on mechanical properties of high speed sintered parts. *Surface Topography: Metrology and Properties*, 3(3), 034005.
20. Ellis, A., Noble, C. J., Hartley, L., Lestrage, C., Hopkinson, N. & Majewski, C. 2014b. Materials for high speed sintering. *Journal of Materials Research*, 29(17), 2080-2085.
21. Ensinger. 2014. Available: <https://www.ensingerplastics.com/> [Accessed 29 October 2014].
22. Erasenthiran, P. & Hopkinson, N. 2005. *Method and apparatus for combining particulate material*.
23. Fox, L., Ellis, A. & Hopkinson, N. 2015. Use of an Alternative Ink in the High Speed Sintering Process. Proceedings of the 26th Solid Freeform Fabrication Symposium, 2015. Austin, Texas: The University of Texas at Austin, 456-463.
24. Frenkel, J. 1945. Viscous flow of crystalline bodies under the action of surface tension. *J. Phys.*, 9(1), 385-391.
25. Fried, J. R. 2014. *Polymer Science and Technology*, New Jersey, Prentice Hall.
26. German, R. M. 1996. *Sintering theory and practice*, New York ; Chichester, Wiley.
27. Gibson, I. & Shi, D. 1997. Material properties and fabrication parameters in selective laser sintering process. *Rapid Prototyping Journal*, 3(4), 129-136.
28. Gibson, I., Rosen, D. W. & Stucker, B. 2010. *Additive Manufacturing Technologies: Rapid Prototyping to Direct Digital Manufacturing*, New York, Springer.
29. Goodridge, R., Tuck, C. & Hague, R. 2012. Laser sintering of polyamides and other polymers. *Progress in Materials Science*, 57(2), 229-267.
30. Griehl, W. & Ruestem, D. 1970. Nylon-12-Preparation, Properties, and Applications. *Industrial & Engineering Chemistry*, 62(3), 16-22.

31. Harper, C. A. 2002a. Design and Processing of Plastic Parts. *In: Hull, John L. (ed.) Handbook of Plastics, Elastomers, and Composites, Fourth Edition.* London: McGraw-Hill Professional.
32. Harper, C. A. 2002b. Elastomeric Materials and Processes. *In: Margolis, James M. (ed.) Handbook of Plastics, Elastomers, and Composites, Fourth Edition.* London: McGraw-Hill Professional.
33. Harper, C. A. 2006. *Handbook of Plastic Processes*, Hoboken, New Jersey, John Wiley & Sons Inc.
34. Haworth, B., Hopkinson, N., Hitt, D. & Zhong, X. 2013. Shear viscosity measurements on Polyamide-12 polymers for laser sintering. *Rapid Prototyping Journal*, 19(1), 28-36.
35. High Speed Sintering Loughborough University. 2017. *High Speed Sintering* [Online]. Available: <https://www.highspeedsinteringtechnology.com/applications/industry-sector-gallery/> [Accessed 20 November 2017].
36. Hoath, S. D. 2016. *Fundamentals of Inkjet Printing: The Science of Inkjet and Droplets*, Weinheim, Germany, Wiley-VCH.
37. Hoath, S. D., Martin, G. D. & Hutchings, I. M. 2010. Effects of Fluid Viscosity on Drop-on-Demand Ink-Jet Break-Off. *NIP & Digital Fabrication Conference*, 2010(1), 10-13.
38. Hopkinson, N. & Dickens, P. 2003. Analysis of rapid manufacturing—using layer manufacturing processes for production. *Proceedings of the Institution of Mechanical Engineers, Part C: Journal of Mechanical Engineering Science*, 217(1), 31-39.
39. Hopkinson, N., Hague, R. & Dickens, P. 2006. *Rapid Manufacturing: An Industrial Revolution for the Digital Age*, Chichester, England, John Wiley & Sons.
40. Jung, S. & Hutchings, I. M. 2012. The impact and spreading of a small liquid drop on a non-porous substrate over an extended time scale. *Soft Matter*, 8(9), 2686-2696.
41. Kang, S. J. L. 2005. *Sintering : densification, grain growth, and microstructure*, Oxford, Elsevier Butterworth-Heinemann.
42. Laumer, T., Stichel, T., Gachot, A., Amend, P. & Schmidt, M. 2015. Realization of multi-material polymer parts by simultaneous laser beam melting. *Journal of Laser Micro/Nanoengineering*, 10(2), 140-147.
43. Li, J., Myant, C. & Wu, B. (2016) *The Current Landscape for Additive Manufacturing Research*. London: Imperial College London.
44. Liniger, E. & Raj, R. 1987. Packing and Sintering of Two-Dimensional Structures Made fro Bimodal Particle Size Distributions. *Journal of the American Ceramic Society*, 70(11), 843-849.

45. Loughborough University. 2017. *Powder Bed Fusion* [Online]. Available: <http://www.lboro.ac.uk/research/amrg/about/the7categoriesofadditivemanufacturing/powderbedfusion/> [Accessed 25 November 2017].
46. Magdassi, S. 2010. *The chemistry of inkjet inks*, New Jersey; London, World Scientific.
47. Mahamood, R. M. & Akinlabi, E. T. 2017. Introduction to Functionally Graded Materials. In: Mahamood, Rasheedat Modupe & Akinlabi, Esther Titilayo (eds.) *Functionally Graded Materials*. Cham: Springer International Publishing.
48. Majewski, C. E., Hobbs, B. S. & Hopkinson, N. 2007. Effect of bed temperature and infra-red lamp power on the mechanical properties of parts produced using high-speed sintering. *Virtual and Physical Prototyping*, 2(2), 103-110.
49. Majewski, C. E., Oduye, D., Thomas, H. R. & Hopkinson, N. 2008. Effect of infra-red power level on the sintering behaviour in the high speed sintering process. *Rapid Prototyping Journal*, 14(3), 155-160.
50. Mani, M., Feng, S., Lane, B., Donmez, A., Moylan, S. & Fesperman, R. 2015. *Measurement science needs for real-time control of additive manufacturing powder bed fusion processes*, US Department of Commerce, National Institute of Standards and Technology.
51. Moser, D., Pannala, S. & Murthy, J. 2016. Computation of Effective Thermal Conductivity of Powders for Selective Laser Sintering Simulations. *Journal of Heat Transfer*, 138(8), 082002.
52. Nelson, J. C. 1993. *Selective laser sintering: a definition of the process and an empirical sintering model*. PhD Thesis, University of Texas.
53. Norazman, F. & Hopkinson, N. 2014. Effect of Sintering Parameters and Flow Agent on the Mechanical Properties of High Speed Sintered Elastomer. *Journal of Manufacturing Science and Engineering*, 136(6), 061006.
54. Priedeman, J. W. R. & Smith David, T. 2012. *Smoothing method for layered deposition modeling*. United States,; patent application.
55. Rauwendaal, C. 2010. *Understanding extrusion*, Munich; Cincinnati, Ohio, Hanser.
56. Roberts, I. A., Wang, C. J., Esterlein, R., Stanford, M. & Mynors, D. J. 2009. A three-dimensional finite element analysis of the temperature field during laser melting of metal powders in additive layer manufacturing. *International Journal of Machine Tools and Manufacture*, 49(12), 916-923.
57. Rosato, D. V., Rosato, D. V. & Rosato, M. G. 2012. *Injection Molding Handbook*, USA, Springer US.
58. Rouholamin, D. & Hopkinson, N. 2016. Understanding the efficacy of micro-CT to analyse high speed sintering parts. *Rapid Prototyping Journal*, 22(1), 152-161.
59. Saldívar-Guerra, E. & Vivaldo-Lima, E. 2013. *Handbook of Polymer Synthesis, Characterization and Processing*, Hoboken, John Wiley and Sons.

60. Shanjani, Y. & Toyserkani, E. 2008. Material Spreading and Compaction in Powder-based Solid Freeform Fabrication Methods: Mathematical Modeling. Proceedings of the 19th Solid Freeform Fabrication Symposium, 2008. Austin, Texas: The University of Texas at Austin, 399-410.
61. Singh, R., Singh, S. & Singh, I. P. 2016. Effect of Hot Vapor Smoothing Process on Surface Hardness of Fused Deposition Modeling Parts. *3D Printing and Additive Manufacturing*, 3(2), 128-133.
62. Starr, T. L., Gornet, T. J. & Usher, J. S. 2011. The effect of process conditions on mechanical properties of laser-sintered nylon. *Rapid Prototyping Journal*, 17(6), 418-423.
63. Tan, H. 2016. Three-dimensional simulation of micrometer-sized droplet impact and penetration into the powder bed. *Chemical Engineering Science*, 153(1), 93-107.
64. The University of Sheffield. 2014. *PUSH Process* [Online]. Available: <http://www.pushprocess.technology/> [Accessed November 2nd 2015].
65. Thomas, H. 2009. *The construction and testing of an IR absorption metric for High Speed Sintering*. PhD thesis, Loughborough University.
66. Thomas, H. R., Hopkinson, N. & Erasenthiran, P. 2006. High Speed Sintering - Continuing research into a new Rapid Manufacturing process. Proceedings of the 17th Solid Freeform Fabrication Symposium, 2006. Austin, Texas: The University of Texas at Austin, 682-691.
67. Thompson, M. J., Whalley, D. C. & Hopkinson, N. 2008. Investigating Dielectric Properties of Sintered Polymers for Rapid Manufacturing. Proceedings of the 19th Solid Freeform Fabrication Symposium, 2008. Austin, Texas: The University of Texas at Austin.
68. Tontowi, A. E. & Childs, T. H. C. 2001. Density prediction of crystalline polymer sintered parts at various powder bed temperatures. *Rapid Prototyping Journal*, 7(3), 180-184.
69. Vasquez, M. 2012. *Analysis and Development of New Materials for Polymer Laser Sintering*. PhD thesis, Loughborough University.
70. Vasquez, M., Haworth, B. & Hopkinson, N. 2011a. Optimum sintering region for laser sintered nylon-12. *Proceedings of the Institution of Mechanical Engineers, Part B: Journal of Engineering Manufacture*, 225(12), 2240-2248.
71. Vasquez, M., Hopkinson, N. & Haworth, B. Laser Sintering Processes: Practical Verification of Particle Coalescence for Polyamides and Thermoplastic Elastomers 2011b. Society of Plastics Engineers, D41.
72. voxeljet. 2017. *Voxeljet unveils new 3D printing technology - high speed sintering process for the production of end-use parts* [Online]. Available: <https://www.voxeljet.com/company/news/voxeljet-introduces-high-speed-sintering-process/> [Accessed 14 October 2017].



73. Ward, I. M. & Sweeney, J. 2004. *An Introduction to the Mechanical Properties of Solid Polymers*, New York; Chichester, Wiley.
74. Wendel, B., Rietzel, D., Kühnlein, F., Feulner, R., Hülder, G. & Schmachtenberg, E. 2008. Additive Processing of Polymers. *Macromolecular Materials and Engineering*, 293(10), 799-809.
75. Wohlers Associates. 2015. *Wohlers report 2015 : 3D printing and additive manufacturing state of the industry annual worldwide progress report*, Colorado, Wohlers Associates Inc.
76. Wohlers Associates. 2017. *Wohlers report 2017 : 3D printing and additive manufacturing state of the industry : annual worldwide progress report*, Fort Collins, Colorado, Wohlers Associates.

# Chapter 2 Experimental Work

## 2.1 Introduction

Drawing on the literature presented in Chapter 1, a series of experiments was conducted to evaluate the quality and mechanical performance of parts manufactured by the high speed sintering (HSS) process. This chapter presents the procedures for these experiments.

This chapter can be divided into four main sections. The first section concentrates on the powder characterisation prior to HSS processing. The subsequent three sections form the primary part of the experimental work presented in this thesis. These comprise the experimental procedures for evaluating the dimensional accuracy of HSS elastomer parts, investigating the influence of build parameters on HSS nylon part properties, and constructing a systematic model that correlates HSS part properties with process parameters.

## 2.2 Powder Characterisation

Powder characterisation using differential scanning calorimetry (DSC) and scanning electron microscope (SEM) are usually carried out prior to HSS processing to assess the material's compatibility with the process. A DSC curve provides the key processing temperatures for a particular material, while SEM images reveal particle sizes and shapes.

### 2.2.1 Physical Properties of Feed Powder

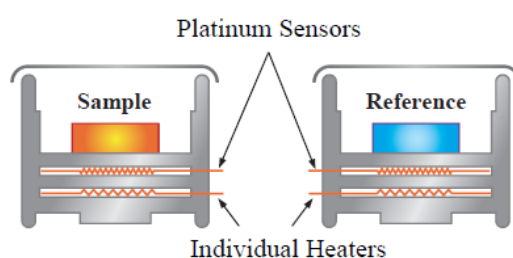
Two types of powder are used throughout this research – nylon thermoplastic elastomer, ALM TPE210-S (TPE) and nylon 12, EOS PA2200 (PA12). Table 2-1 lists a few of their physical properties as provided by the material suppliers. The data sheet for both materials are enclosed in the Appendices.

**Table 2-1** ALM TPE210-S and EOS PA2200 powder properties

<b>Commercial Name</b>	<b>ALM TPE210-S (TPE)</b>	<b>EOS PA2200 (PA12)</b>
Powder type	Nylon-based thermoplastic elastomer	Nylon 12
Mean particle size	85 $\mu\text{m}$	56 $\mu\text{m}$
Particle size range	20 – 130 $\mu\text{m}$	40 – 90 $\mu\text{m}$
Bulk density	0.37 $\text{g}/\text{cm}^3$	0.45 $\text{g}/\text{cm}^3$
Melting point	178°C	172 – 180°C

## 2.2.2 Differential Scanning Calorimetry

The properties of a material can be measured as a function of temperature using a wide range of thermal analysis techniques. According to Skoog (2007), the most used thermal analysis method is differential scanning calorimetry (DSC). It measures the difference in energy of a material as a function of temperature. This is achieved by measuring the difference in heat flow into a sample and a reference (usually air) during heating and cooling processes. A diagram of a PerkinElmer double-furnace DSC instrument is shown in Figure 2-1 (PerkinElmer, 2013).



**Figure 2-1** Sample and reference holders in a double-furnace DSC (PerkinElmer, 2013)

Both the sample and reference holders are housed in independent units with their individual heaters. The heaters are used to maintain both the sample and reference temperatures, which are regulated by the platinum sensors.

### *DSC Experimental Setup and Procedure*

A PerkinElmer DSC8500 double furnace instrument was used to perform the DSC test. Nitrogen was used as the purge gas during testing. The powder sample was tested against an empty aluminium sample pan as a reference. Both powders (TPE and PA12) were subjected to the DSC experimental procedures in accordance with ASTM D3418-15 (ASTM International, 2015). The procedures are outlined as follows.

Firstly, a small amount of between  $5.0 - 15.0 \pm 0.1$  mg of powder sample was weighed. The powder sample was then placed in an aluminium sample pan. A metal cover was placed over the pan with the powder sample sandwiched in between, and crimped. Another aluminium sample pan was not filled with powder and simply crimped with a metal cover to be used as a reference. To ensure good heat transfer during heating, the base of both the sample and reference pans were ensured to be flat and that the covers were completely sealed. The DSC test was performed by successively heating and cooling the sample in the following sequence:

1. Heat from 20°C to 210°C at a rate of 20°C/min.
2. Hold at 210°C for one minute.
3. Cool from 210°C to 20°C at a rate of 20°C/min.

The test was repeated for two cycles for each powder type. The results were analysed on Pyris software and DSC thermal plots were obtained. The DSC plots are presented in Section 3.2.2 (page 72).

### ***Setting HSS Process Parameters Using DSC***

The DSC quantified a material's enthalpy values, crystallisation temperatures ( $T_c$ ), melting temperatures ( $T_m$ ), and glass transition temperatures ( $T_g$ ). In HSS, the temperature range between melting and solidification is commonly known as the 'HSS processing window', an optimum range of temperatures for full sintering to occur. These temperature points were used to set the initial values for process parameters such as build bed and feed bed temperatures accordingly.

- The build bed jacket temperature was set at  $T_c$
- The build bed overhead temperature was set at  $T_g$  (for amorphous) or below  $T_m$  (for semi-crystalline)
- Both feed bed jacket and feed bed overhead temperatures were set below  $T_c$

As discussed in Section 1.2.1 (page 7), amorphous and semi-crystalline (thermoplastic) polymers behave differently when subjected to heat. This is caused by the difference in the amount of energy required to break the molecular bonds. Semi-crystalline polymers, which consist of molecules arranged in an orderly manner, require less energy to melt compared to the disorderly molecules in amorphous polymers. Consequently, an amorphous polymer requires more time to sinter. On the HSS machine, this is achieved by setting a low sintering lamp speed for amorphous polymers and the reverse for semi-crystalline. In both cases, the preheat lamp is usually set at the same speed, albeit at a lower power to discourage sintering of surrounding powder. The above parameters were then optimised using design of experiment.

The DSC results obtained were fed into setting the HSS processing parameters for TPE and PA12 powders in Sections 2.3.2 (page 45) and 2.4.2 (page 58), respectively. A more detailed analysis of the HSS processing window is discussed in Section 3.2.1 (page 71).

### 2.2.3 Scanning Electron Microscope

Scanning electron microscope (SEM) is a microscope that scans a specimen using a focused beam of high-energy electrons to create an image. Figure 2-2 shows a schematic drawing of a typical SEM instrument (The University of Iowa, 2018).

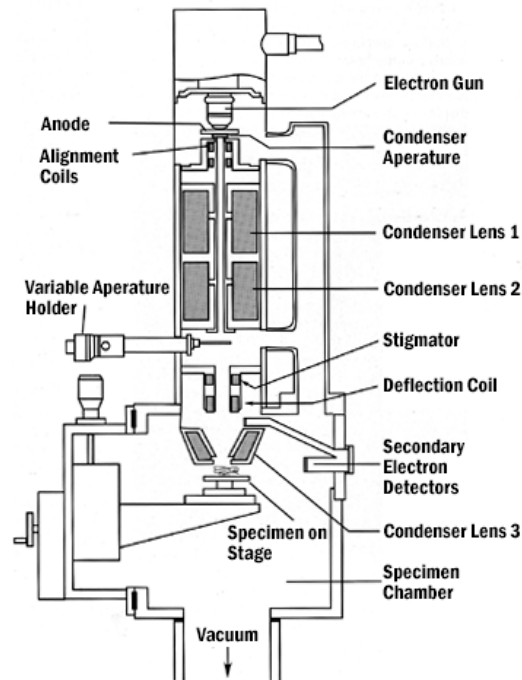


Figure 2-2 Schematic of SEM (The University of Iowa, 2018)

The two most common signals used to form an SEM image are made up of secondary and backscattered electrons (Khursheed, 2010). When the primary beam hits a specimen, electrons are scattered from near the surface (secondary) and from deeper locations within the specimen (backscattered).

#### *SEM Experimental Setup and Procedure*

In this work, SEM is used to determine powder particle size, shape, and texture. SEM examination was performed on the ALM TPE210-S and EOS PA2200 powder with a TESCAN VEGA3 SEM system. The powder samples were distributed on a 0.5-inch diameter aluminium stub. The samples were coated with gold coating on an Edwards Gold Sputter Coater S150B to reduce sample charging and improve secondary electron emission. The voltage was set to 20 kV. The images were captured using backscattered electron detector at two orders of magnification – low magnification at 500X and high magnification at 5,000X. The micrographs are presented and discussed in Section 3.3 (page 74).

## 2.3 Experiments to Evaluate the Dimensional Accuracy of High Speed Sintered TPE Parts

As discussed in Chapter 1, the processing of elastomers using AM is currently limited. The series of experiments discussed here attempts to manufacture ALM TPE210-S thermoplastic elastomer (TPE) samples using HSS and to evaluate the resulting part properties. Figure 2-3 shows the flowchart for the entire experimental procedures.

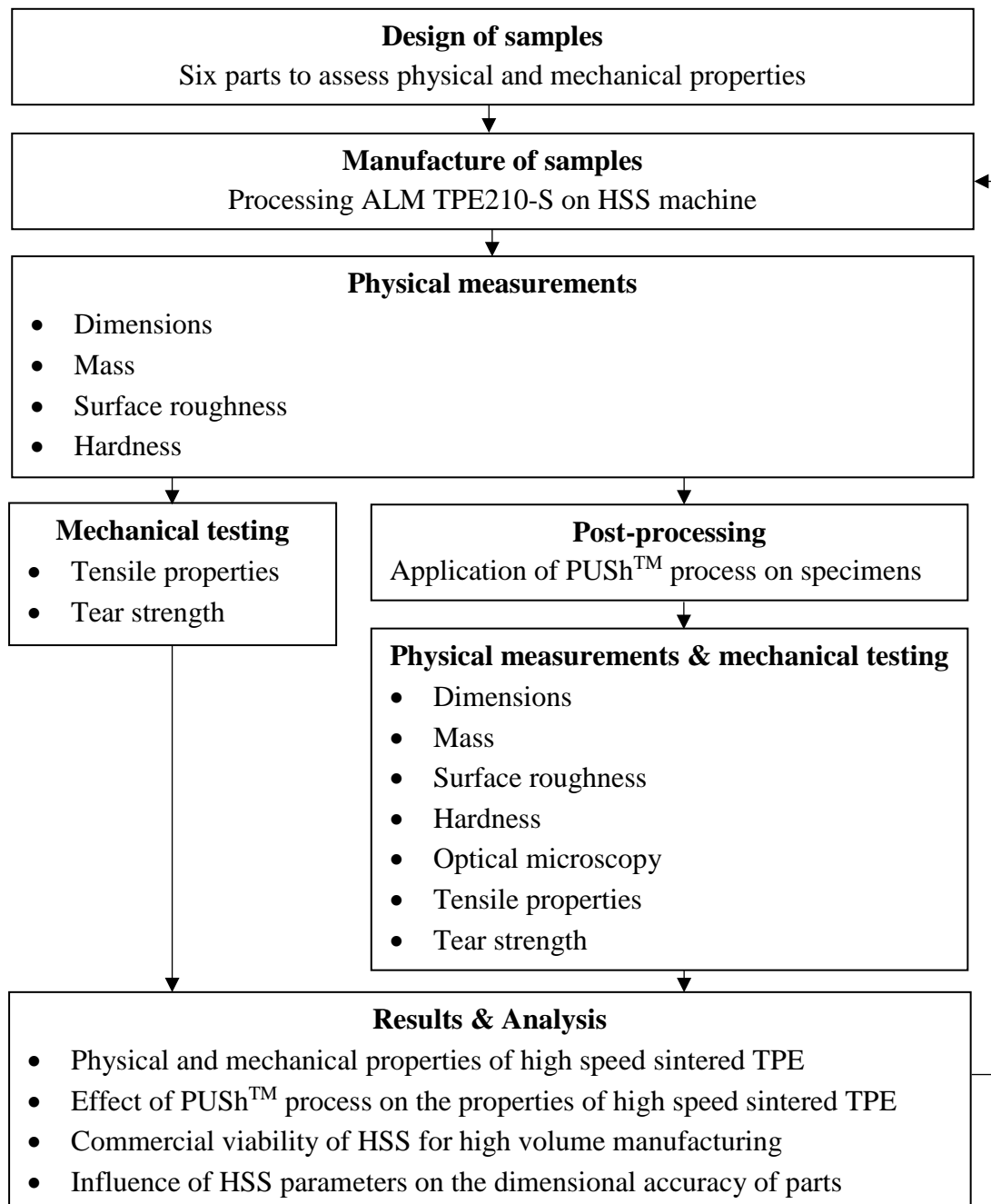



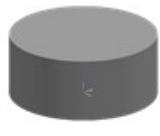

Figure 2-3 Flowchart of the experimental procedures to investigate the dimensional accuracy of HSS TPE parts

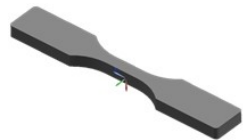

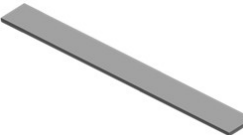
This series of experiments was performed in collaboration with an Original Equipment Manufacturer (OEM) as part of a feasibility study for manufacturing a specific product. The target product requires high flexibility and dimensional accuracy, hence ALM TPE210-S elastomer was chosen as the base material. The samples were designed by the OEM following recommendations on HSS feature resolutions and build bed size. The samples were manufactured on the prototype HSS machine using an optimised set of parameters. The manufactured samples were cleaned from excess powder, then characterised and divided into two sets. The first set was subjected to mechanical testing without further post-processing; while the second set was post-treated with a chemical process called the PUSH<sup>TM</sup> treatment, and then subjected to repeated physical measurements and the same mechanical testing. Experimental results and analysis are discussed in Chapter 4.

### 2.3.1 Design of Samples

Three-dimensional (3D) computer aided design (CAD) models of twelve samples were provided by the OEM for this experiment. The samples consisted of six design samples that incorporated features from the actual product and six test samples for characterisation purposes. Due to the confidentiality agreement, this thesis only considered the manufacturing of the latter samples. Details of the test samples, including pictures and xyz dimensions are provided in Table 2-2.

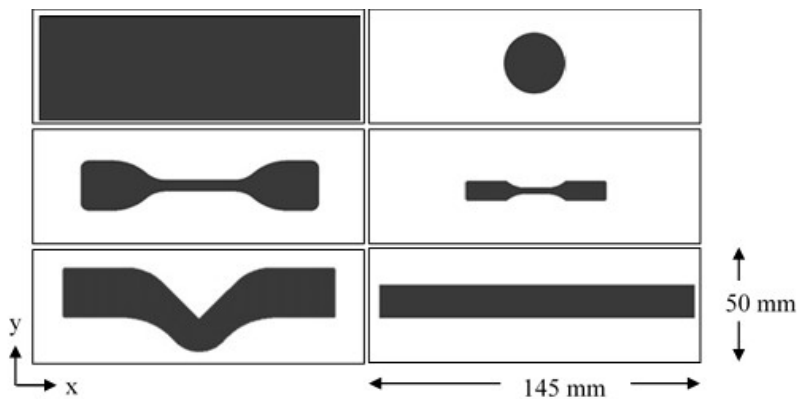
**Table 2-2** Details of the TPE samples

Sample details			Part dimensions (mm)			Part volume (cm <sup>3</sup> )	Quantity
Sample	Name	3D CAD model	Length (x)	Width (y)	Depth (z)		
1	Plate		140.00	45.00	0.40	2.52	10
2	Disc		28.00	28.00	12.00	7.40	10
3	Tensile bar (ISO 37)		115.00	25.00	2.00	3.60	10

4	Tensile bar (ASTM D638 Type V)		63.50	9.53	3.20	1.50	10
5	Tear test (ASTM D624 Type C)		102.00	19.00	2.30	4.30	10
6	Tear test (ASTM D624 Type T)		140.00	15.00	2.00	4.20	10

The set of samples ranged in sizes and shapes, consisting of one rectangular plate, one disc, two tensile bars, and two tear test pieces. The rectangular plate, sample 1, was designed to evaluate the printability of thin structures, having a thickness of only four build layers. The disc, sample 2 was chosen to assess the printability of curved surfaces. Two types of tensile bars, samples 3 and 4, were included as requested by the OEM to conform to their testing standards. Two types of tear test pieces, samples 5 and 6, were selected to test for different aspects of tear strength. Ten duplicates were manufactured for each sample and relevant tests as detailed in Section 2.3.3 (page 47) were performed.

Figure 2-4 shows the plan view of all samples positioned on the HSS build bed, illustrating their printing orientations and relative sizes to the build bed, which measures 145 mm x 50 mm. All samples were built on the xy (horizontal) plane. Tensile and tear test samples (samples 3 – 6) were built horizontally for maximum consolidation in the xy-direction. Each set of samples were built separately in a vertical stack. The blank spaces around samples 2, 4, and 6 were filled with their duplicates to reduce build time.



**Figure 2-4** Two-dimensional plan view of TPE samples on the HSS build bed



### **2.3.2 Manufacture of TPE Samples by HSS**

#### ***Pre-processing***

The pre-processing stage involved the preparation of three primary areas, which were build files, powder, and machine.

The preparation of HSS build files required an array of software. The 3D CAD models were drawn and converted into STereoLithography (STL) format in Solidworks 2013 software. The STL files were imported into Materialise Magics 18.0 software to be duplicated and arranged on the virtual HSS platform. All parts on the platform were merged then sliced into a vertical stack of 2D cross sectional layer files (SLC), each with a thickness of 100  $\mu\text{m}$ . The SLC files were consequently imported into CTools and converted into bitmap images (BMP). The BMP files were inverted to create negative images and blank layers were added to the top and bottom of the stack in Faststone Image Viewer software. The images were further manipulated by removing one pixel around the perimeter of the images and applying a greyscale level of 57 (optimised greyscale level for TPE210-S, page 21) using a custom plugin in the ImageJ software. The final BMP files were then transferred to the HSS machine.

Powder synthesis was not performed for this experiment. The TPE210-S powder from ALM was a commercially available material supplied as a laser sintering (LS) feed powder. Virgin powder was manually sifted to remove lumps in order to increase the spreadability of the powder. DSC test on the powder was carried out as outlined in Section 0 (page 38).

At the start of machine preparation, powder was filled into the powder feed chamber and spread over the build bed. An infrared camera that was mounted over the build bed was cleaned using acetone. Several pad layers were built to ensure that the build has a compact and flat base. Build parameters were set and all heaters were switched on. After a thirty-minute machine warm up, build files were loaded to start the build.

#### ***Processing***

To maintain consistency, the same set of parameters was used to manufacture all samples, including the design samples that were not discussed in this thesis. The processing parameters used are listed in Table 2-3. The definition of each parameter was previously discussed in detail in Table 1-4 (page 19).

**Table 2-3** HSS processing parameters for TPE samples

<b>Parameter</b>	<b>Value</b>
Break out temperature	Room Temperature
Build bed jacket temperature	60°C
Build bed overhead temperature	110°C
Feed bed jacket temperature	28°C
Feed bed overhead temperature	32°C
Feed powder ratio	3.2
Ink volume	2,340 pL/mm <sup>2</sup> (GS57)
Lamp type	2 kW Coated
Layer thickness	0.1 mm
Maintenance layers	1
Material	TPE210-S
Orientation	XYZ
Powder ratio	100% virgin
Powder temperature	Room & Pre-warmed
Printhead type	Xaar Proton 60
Sintering lamp power	60%
Sintering lamp speed	80 mm/s
Surface preheat lamp power	40%
Surface preheat lamp speed	80 mm/s
Warm up time	30 minutes

Break out temperature, layer thickness, orientation, powder temperature, and warm up time were set according to standard HSS practice. Feed powder ratio and the frequency of maintenance layers were higher than the standard PA12 parameters due to the larger size of the TPE polymer particles. Powder ratio was kept at 100% virgin to discount any effect that may derive from powder recycling. Lamp type, ink volume, and printhead type were predetermined by the components already in place.

Build bed jacket and overhead temperatures, feed bed jacket and overhead temperatures, sintering lamp power and speed, and surface preheat lamp power and speed were optimised for successful printing of all samples, by drawing on data from previous research and conducting preliminary experiments.

Optimisation data on the above eight key parameters is disclosed in Table 2-4.

**Table 2-4** HSS key parameter optimisation for TPE processing

Level	Key Parameters							
	Build bed temperatures		Feed bed temperatures		Sintering lamp		Surface preheat lamp	
	Jacket (°C)	Overhead (°C)	Jacket (°C)	Overhead (°C)	Power (%)	Speed (mm/s)	Power (%)	Speed (mm/s)
Initial	35	100	30	35	100	50	50	100
Low	35	90	28	28	60	50	0	80
Medium	50	100	30	32	80	80	40	90
High	60	110	32	35	100	110	80	100
Final	60	110	28	32	60	80	40	80

The initial set of parameters was based on the values obtained from the preliminary research, which yielded parts with high tensile strength (Norazman and Hopkinson, 2014). The build bed and feed bed temperatures were set according to the guidelines discussed in Section 2.2.2 (page 39).

Three levels were assigned to each parameter, which were low, medium, and high. Test builds were performed by varying one or two parameter values at a time. The responses were scored based on two outcomes. Firstly is the printability of parts, in that the parts could be printed successfully without causing any damage to the equipment, such as creating a melt pool or colliding with the printhead. Secondly is the powder removability, in which parts can be successfully retrieved from the powder cake during bead blasting (post-process). Under sintered parts might be damaged during this process, while over sintered parts result in a hard powder cake. A final set of parameters was obtained and applied to the main experiments.

### ***Post-processing***

Once building finishes, the parts were left to cool in the powder cake before being removed from the machine. Part cleaning was performed by removing unsintered powder on a Guyson Euroblast 4SF bead blasting station. The media used was Guyson Honite 13 glass bead with an average diameter of 106 – 212  $\mu\text{m}$ . Air was also used at a pressure of three bar. The average duration taken to clean each part was five minutes.

A number of test specimens were subjected to the PUSH surface finish process after the initial physical measurements. The process involved an application of a temperature-controlled

solvent onto the surfaces of the test specimens. The process was carried out in a temperature-controlled environment. Parts were suspended or placed on a support during application. In this experiment, the average application time was one minute per part, excluding preparation and drying time. The exact details of the process application cannot be disclosed due to the intellectual property restrictions.

### 2.3.3 Test Methods

This section provides an overview of all the testing methods and procedures used in this experiment. Table 2-5 shows the test matrix performed on each sample type.

**Table 2-5** Test methods for TPE specimens

Test Methods		Sample Number					
		1	2	3	4	5	6
<b>Physical Measurements</b>	Dimensions						
	Mass						
	Surface roughness						
	Hardness						
	Optical microscopy						
<b>Mechanical Testing</b>	Tensile						
	Tear						

Physical measurements were performed on almost all test specimens. In addition, samples 3 – 6 were subjected to their respective mechanical testing. The results of these measurements are discussed in Chapter 4.

#### *Dimensions*

The dimensions of each specimen were measured using a Senator SEN-331-2230K digital Vernier caliper with an accuracy of  $\pm 0.01$  mm. All measurements were repeated for five times and mean values were calculated.

#### *Mass*

The mass of each specimen was determined using an OHAUS Pioneer PA64C balance with an accuracy of  $\pm 0.0001$  g. All measurements were repeated for five times and mean values were calculated.

## Surface Roughness

The measured surface roughness of a material represents the quality of the surface. A lower number indicates a smoother surface finish. Figure 2-5 depicts a surface roughness profile and its associated parameters (Ark Novin, 2015).

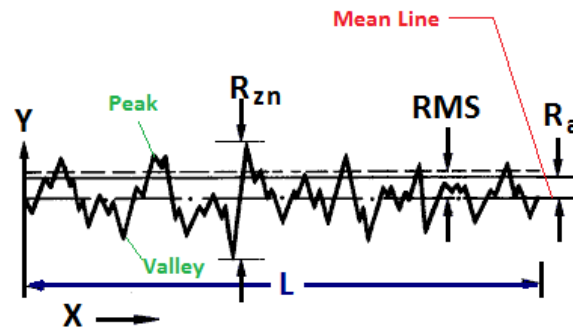


Figure 2-5 Surface roughness profile and parameters (Ark Novin, 2015)

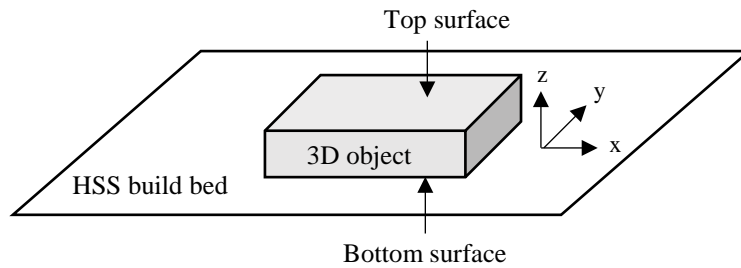
Arithmetic mean roughness ( $R_a$ ) is the most commonly quoted parameter for surface roughness.  $R_a$  is the arithmetic mean of peaks and valleys from the mean line. Ten-point mean roughness ( $R_z$ ) is the average of total distances between five highest peaks and five lowest valleys. Root mean square (RMS) is the square root of average height deviation from the mean line squared, and is an alternative way of calculating average surface roughness.

Surface roughness testing was performed on a Mitutoyo SurfTest contact profilometer rig. Table 2-6 lists two sets of evaluation settings applied for all test specimens. Both the sampling length and travelling speed were reduced for samples 2 and 4, due to their shorter lengths.

Table 2-6 Surface roughness settings for TPE specimens

Sample	Sampling length (mm)	Travel speed (mm/s)
Sample 1, 3, 5, 6	20.0	2.0
Sample 2, 4	15.0	1.0

In HSS, surfaces parallel to the xy-plane are commonly called top and bottom surfaces. A top surface faces upwards towards the surface of the build bed, while a bottom surface faces downwards towards the base of the build bed. Figure 2-6 illustrates the position of the two surfaces.



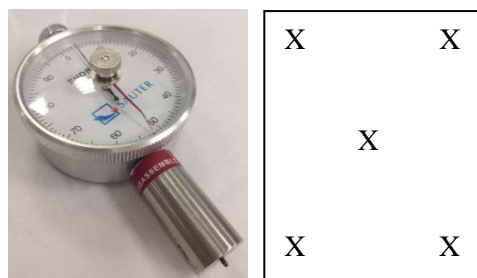
**Figure 2-6** The top and bottom surfaces of an HSS part

The test was performed on both top and bottom surfaces of samples 1 – 6. The test was carried out five times across each surface of each specimen to enable a calculation of mean values. Through this test, surface roughness values, average roughness,  $R_a$  and average maximum height,  $R_z$  were obtained.

### ***Hardness***

Shore A hardness measures the hardness of polymers, elastomers and rubbers by measuring the resistance of the material to indentation on a scale of 0 to 100. All test specimens, apart from sample 1 specimens were subjected to Shore A hardness test. The thickness of sample 1 specimens was below the required standard to be tested.

The test was performed using a Sauter HBA 100-0 handheld durometer according to ASTM D2240 (Standard Test Method for Rubber Property - Durometer Hardness) (ASTM International, 2005 (2010)). Figure 2-7 shows the durometer used in this test, and the distribution of measurement points on a sample.



**Figure 2-7** Durometer used to measure Shore A hardness of TPE specimens, and locations of measurement points

All specimens were measured on a hard flat surface. The durometer was placed perpendicularly to the specimen's surface. When a vertical force was applied, the indenter receded to the presser foot to give a hardness reading. The reading was taken after five seconds. Five measurements were taken across the surface of each specimen and a mean value was calculated.

### *Optical Microscopy*

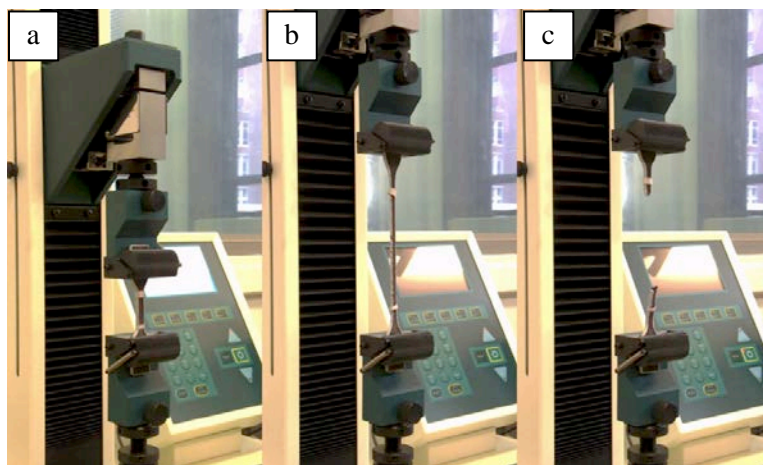
Optical microscopy was performed on selected parts to observe the effect of PUSH process at a microstructural level. The equipment used was a Zeiss Stemi 2000-C stereomicroscope with a Schott KL 200 cold-light source, shown in Figure 2-8. The images were viewed at 200- $\mu\text{m}$  resolution using an AxioVision 4.8 imaging software.



**Figure 2-8** Optical microscopy equipment

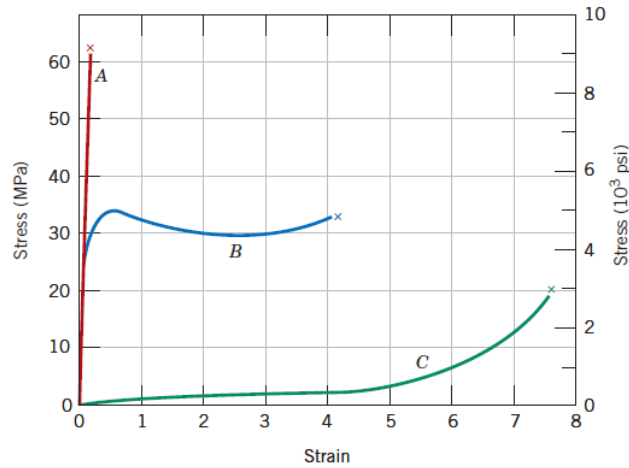
### *Tensile Tests*

Tensile testing is used to evaluate the strength and ductility of a solid material. The test determines the tensile properties of a material by applying a uniaxial load at a fixed displacement rate. Figure 2-9 demonstrates the three stages of deformation during a tensile test.



**Figure 2-9** Deformation stages during tensile testing a) elastic deformation, b) necking, and c) fracture

Different types of polymers behave differently under tensile loading. Figure 2-10 illustrates the three different stress-strain behaviours in polymers as described by Callister (2015).



**Figure 2-10** The stress-strain curves for brittle (A), plastic (B), and elastic (C) polymers

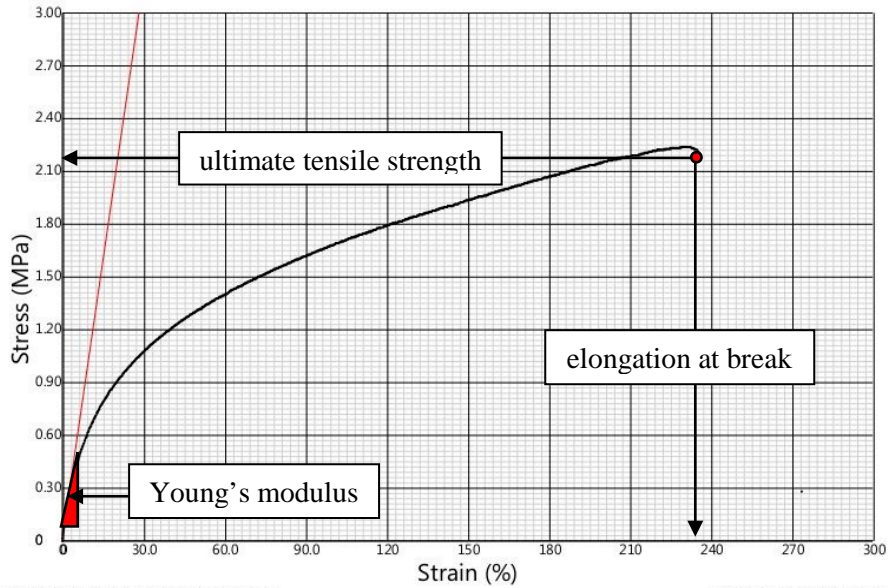
In a brittle polymer (A), fracture occurs alongside elastic deformation. In a plastic polymer (B), both elastic and plastic regions exist, in which yield and fracture happen independently. On the other hand, elastic polymer (C) continues to deform elastically at a high strain before fracture.

Callister (2015) states that the tensile properties of polymers are highly dependent on the measurement strain rate, temperature and the chemical environment. It is therefore important to maintain identical testing conditions when performing tensile testing.

In this set of experiments, tensile testing was conducted on an Instron universal testing machine, equipped with a video extensometer and 60-psi pneumatic grips. Specimens 3 were tested under 100 N load at a rate of 20 mm/min in accordance with ISO 37 test method (International Organization for Standardization, 2011). Specimens 4 were tested under 1,000 N load at a rate of 1 mm/min in accordance with ASTM D638 test method (ASTM International, 2014). Ten samples were tested for each set of tensile test type, and the average and standard deviations within each set were calculated.

The test specimen was prepared by marking its gage length using a strain marker, then loaded in between the grips and aligned vertically. The specimen was pulled at the chosen rate until it completely ruptured. A force-displacement curve was obtained from the tensile test. This curve was then converted to a stress-strain curve in Figure 2-11. The horizontal axis represents strain in percentage and the vertical axis represents stress in MPa.





**Figure 2-11** Example of a stress-strain curve showing the Young's modulus, ultimate tensile strength, and elongation at break

The three most important parameters extracted from a tensile test curve are the Young's modulus (E), ultimate tensile strength (UTS), and elongation at break (EaB). UTS is the tensile stress at fracture. EaB is the tensile strain at fracture. E is determined as the ratio between stress and strain in the elastic region, as given by the following equation.

$$E = \frac{\sigma}{\epsilon} = \frac{F/A}{\Delta l/l_0} \quad \text{Equation 2-1}$$

where:

E is the Young's modulus,

$\sigma$  is the nominal stress,

F is the force applied during testing,

A is the initial cross-sectional area of the sample,

$\epsilon$  is the measured strain,

$\Delta l$  is the change in length of the sample, and

$l_0$  is the initial length of the sample

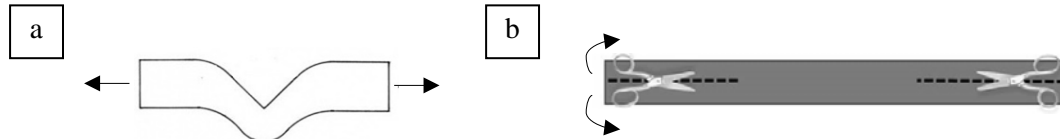
### ***Tear Tests***

Tear testing is used to measure the ability of a material to resist tearing. A tear test can be performed to measure the force required to initiate a tear in a specimen (crack initiation) and the force required to continually tear an existing cut in a specimen (crack propagation). These two measurements give the tear strength and tear force of a material. Tear strength is determined by dividing the maximum force with the specimen thickness. Tear force is

calculated by taking an arithmetic mean of the mean peak force and mean peak valley using the mean force analysis.

Tear resistance of the TPE parts was measured via two test methods, by measure of crack initiation (type C, sample 5) and crack propagation (type T, sample 6). All tests were performed at the OEM's in-house testing facilities on an Instron universal testing machine, equipped with a video extensometer and 60-psi pneumatic grips, at  $23 \pm 2^\circ\text{C}$ . Type C tear testing on sample 5 was conducted under 100 N load at a rate of 12 mm/min. Type T tear testing on sample 6 was conducted under 1,000 N at a rate of 50 mm/min.

Sample preparation and testing were done according to ASTM D624 (Standard Test Method for Tear Strength of Conventional Vulcanized Rubber and Thermoplastic Elastomers) (ASTM International, 2000 (2012)). Test specimen 5 was loaded onto the testing machine as manufactured, and the force required to initiate a crack from the corner of the centre of the specimen was measured. Meanwhile, an initial cut measuring  $40 \pm 5$  mm running through the centreline was introduced on test specimen 6. Figure 2-12 illustrates the direction of applied force in both samples (5 and 6) and the preparation of sample 6.



**Figure 2-12** a) Arrows showing the direction of applied force on specimen 5, and b) position of initial cuts and arrows showing the direction of applied force on specimen 6

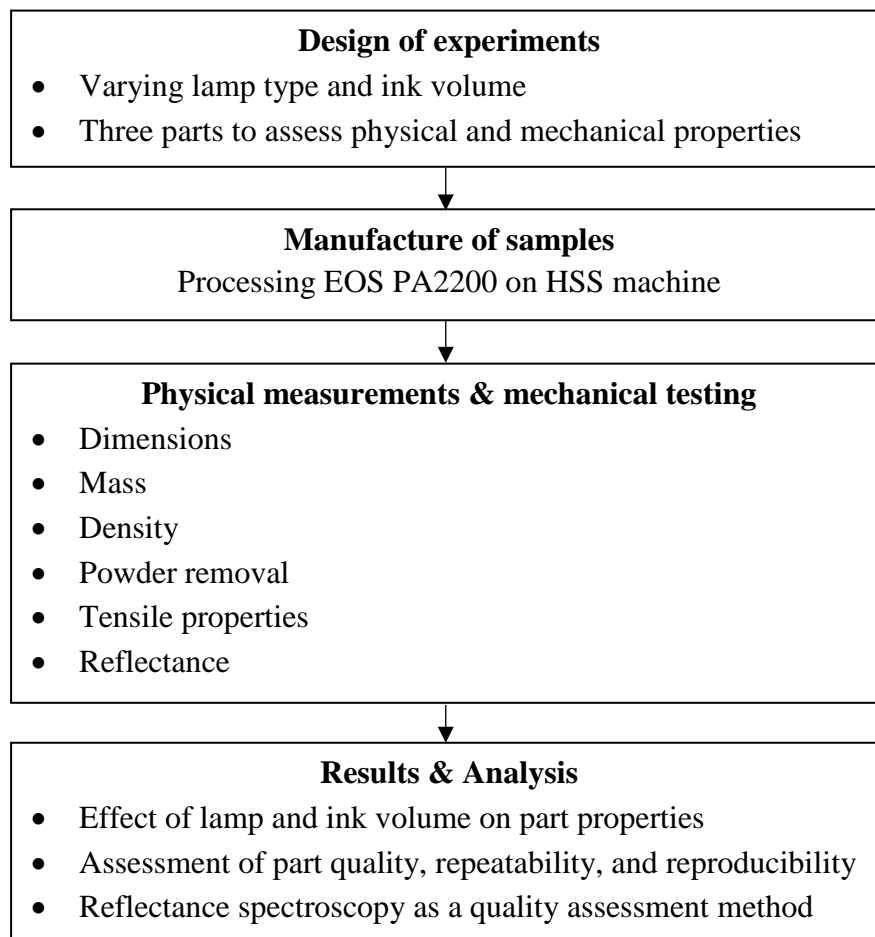
Forces were applied along the length of the specimens, which were parallel to the HSS printing direction of both samples. The force required to propagate the crack until rupture was measured.

### ***Test Methods for PUSH parts***

Five test specimens from each sample 2 – 6 were measured, treated by the PUSH process and then re-measured. Subsequent tensile and tear tests were performed on respective test specimens. In order to evaluate the effect of the PUSH process, the results were compared against untreated specimens and discussed in Section 0 (page 92).

## 2.4 Experiments to Investigate the Influence of HSS Parameters on the Properties of PA12 Parts

This section focuses on the HSS processing of nylon 12 (PA12) at different conditions to investigate the influence of key parameters on part properties. Figure 2-13 shows the flowchart for the entire experimental procedures.



**Figure 2-13** Flowchart of the experimental procedures to investigate the influence of HSS parameters on PA12 parts

A set of experiments was designed to evaluate the effect of two factors, the lamp type and ink volume, on the physical and mechanical properties of HSS parts. Three parts were designed and printed on the HSS machine using PA12 powder to assess these effects. Various testing methods were used to evaluate part properties. The experimental results and analysis are discussed in Chapter 5.

### 2.4.1 Design of Experiments

Two key processing parameters that contribute to HSS part consolidation were chosen as factors in this experiment. The two factors were lamp type and ink volume, and their respective levels are shown in Table 2-7 and 2-8.

**Table 2-7** Lamp type and levels

Level	Factor: Lamp Type
1	2kW gold infrared
2	2kW coated infrared

**Table 2-8** Ink volume and levels

Level	Factor: Ink Volume (pL/mm <sup>2</sup> )
1	1,500
2	3,000
3	4,500
4	6,000
5	7,500

Two levels were set for the type of sintering lamp used. Both lamps were commercially available 2 kW quartz halogen infrared (IR) lamps with a difference in reflector coating. Five levels of ink volume were chosen, ranging from 1,500 – 7,500 pL/mm<sup>2</sup>. The responses measured were the dimensional accuracy of parts, powder removal, and mechanical properties. Table 2-9 lists the ten build combinations obtained from the above lamp-ink experimental matrix.


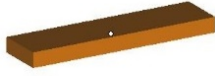
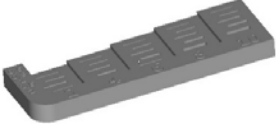
**Table 2-9** Lamp-ink combination matrix of PA12 builds

Lamp Type	Ink volume in pL/mm <sup>2</sup> (Ink Level)				
	1,500 (1)	3,000 (2)	4,500 (3)	6,000 (4)	7,500 (5)
2kW Gold IR lamp (G)	G1	G2	G3	G4	G5
2kW Coated IR lamp (C)	C1	C2	C3	C4	C5

The builds were denoted by alphanumeric strings to reflect the lamp type (G=Gold lamp, C=Coated lamp) and ink volume (1=1,500, 2=3,000, 3=4,500, 4=6,000, 5=7,500) used. Each build was completed in triplicate, which generated thirty builds in total. The replica builds were identified by assigning a suffix of one, two, or three following each build name, e.g. G1\_1, G1\_2, G1\_3...C5\_3. All builds were completed at a random sequence to reduce errors.

Each build consisted of three types of samples. Their images and xyz dimensions are provided in Table 2-10.

Table 2-10 Details of PA12 samples

Sample details			Part dimensions (mm)			Part volume (cm <sup>3</sup> )	Quantity per build
Sample	Name	3D CAD model	Length (x)	Width (y)	Depth (z)		Replicates
1	Tensile bar (ASTM D638 Type IV)		115.0	19.0	3.2	5.01	6
							18
2	Rectangular block		40.0	10.0	3.2	1.27	3
							9
3	Powder removal		130.0	41.5	10.8	38.06	1
							3

Sample 1 was a tensile bar conforming to ASTM D638 Type IV specifications. The rectangular block (sample 2) had the same thickness as sample 1 and positioned in between a pair of them. Sample 3 was designed to score the quality of powder removal by incorporating twenty-five rectangular slots of different volumes.

Each build consisted of six of sample 1, three of sample 2, and one of sample 3. In order to differentiate the tensile test specimens within each build, identifiers were designed into the side of each sample. Figure 2-14 depicts the build stack and the position of the identifiers.

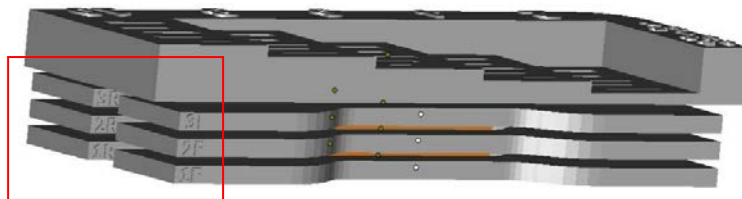
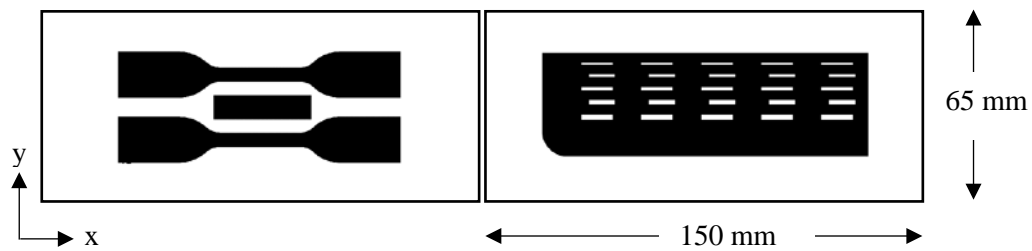


Figure 2-14 Identifiers on tensile test specimens

The identifiers were 3 mm x 3 mm in size. An alphanumeric string was used to uniquely identify the vertical (1 = bottom, 2 = middle, 3 = top) and horizontal (F = front, R = rear) placements of the sample in the HSS build chamber. These identifiers were needed to perform further analysis on the correlation between part location on build bed and part properties. No identifier was used on sample 2, as this would affect the density calculation of the blocks.

Figure 2-15 shows the plan view of all samples positioned on the HSS build bed, illustrating their printing orientations and relative sizes to the build bed (150 x 65 mm).



**Figure 2-15** Two-dimensional plan view of PA12 samples on the HSS build bed

The build bed envelope was wider than the previous HSS experiments (145 mm x 50 mm) due to a machine upgrade. All samples were built on the xy (horizontal) plane. Each set of samples were built separately in a vertical stack. Tensile test samples (sample 1) were built horizontally for maximum consolidation in the xy-direction.

## 2.4.2 Manufacture of PA12 Samples by HSS

### *Pre-processing*

The pre-processing stage for this experiment followed similar steps to the TPE pre-processing in Section 2.3.2 (page 44) with the following adjustments:

- Greyscale value of 0 (full black) was applied to the BMP in the ImageJ software
- The material used was virgin PA2200, a commercially available LS/HSS feed powder

The relevant IR sintering lamp was fitted prior to machine preparation according to the experimental matrix in Table 2-9.

### *Processing*

Table 2-11 shows the processing parameters used to manufacture the PA12 parts. All but two parameters were kept constant across all builds. These two parameters, lamp type and ink volume, are highlighted in the table.

**Table 2-11** HSS processing parameters for PA12 samples

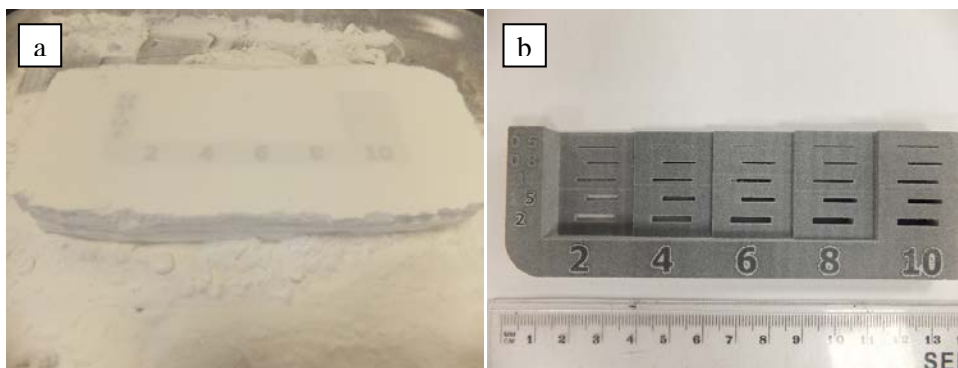
<b>Parameter</b>	<b>Value</b>
Break out temperature	Room Temperature
Build bed jacket temperature	156°C
Build bed overhead temperature	166°C
Feed bed jacket temperature	120°C
Feed bed overhead temperature	140°C
Feed powder ratio	1.7
Ink volume	1,500 pL/mm <sup>2</sup> 3,000 pL/mm <sup>2</sup> 4,500 pL/mm <sup>2</sup> 6,000 pL/mm <sup>2</sup> 7,500 pL/mm <sup>2</sup>
Lamp type	2 kW Gold IR lamp 2kW Coated IR lamp
Layer thickness	0.1 mm
Maintenance layers	500
Material	EOS PA2200
Orientation	XY
Powder ratio	100% virgin
Powder temperature	Room & Prewarmed
Printhead type	Xaar 1002 GS6
Sintering lamp power	100%
Sintering lamp speed	120 mm/s
Surface preheat lamp power	50%
Surface preheat lamp speed	150 mm/s
Warm up time	15/30 minutes

Break out temperature, feed powder ratio, layer thickness, maintenance layers, orientation, and powder temperature were set according to standard HSS practice. Powder ratio was kept at 100% virgin to discount any effect that may derive from powder recycling. Printhead type was predetermined by the component already in place. Lamp type and ink volume were varied according to the experimental matrix. Since PA12 was the standard powder for HSS and used by other colleagues in the research group, a joint effort was taken to establish the optimum processing parameters for this material. Build bed jacket and overhead temperatures, feed bed jacket and overhead temperatures, sintering lamp power and speed, and surface preheat lamp

power and speed were obtained through this optimisation. Warm up time was varied between fifteen and thirty minutes.

### ***Post-processing***

Once building finishes, the parts were left to cool in the powder cake before being removed from the machine. Part cleaning was performed by removing unsintered powder on a Guyson Euroblast 4SF bead blasting station. The media used was Guyson Honite 13 glass bead with an average diameter of 106 – 212  $\mu\text{m}$ . Air was also used at a pressure of three bar. The average duration taken to clean samples 1 and 2 was five minutes. A set time of ten minutes was allowed for bead blasting sample 3 before a powder removal score was taken. Figure 2-16 shows the powder removal part before and after going through bead blasting.



**Figure 2-16** a) Powder removal part in powder cake before bead blasting and b) part after bead blasting

### **2.4.3 Test Methods**

The test methods applied to each PA12 specimen are summarised in Table 2-12.

**Table 2-12** Test methods for PA12 specimens

<b>Test Method</b>		<b>Sample 1</b>	<b>Sample 2</b>	<b>Sample 3</b>
<b>Physical Measurements</b>	Dimensions			
	Mass			
	Density			
	Powder removal			
<b>Mechanical Testing</b>	Tensile			
	Reflectance			



All specimens were subjected to dimensions and mass measurements. Test specimens 1 were further used in tensile testing and reflectance spectroscopy. Test specimens 2 were subjected to density measurement. Test specimens 3 were used to obtain powder removal scores.

### ***Dimensions***

The dimensions of each specimen were measured using a Senator SEN-331-2230K digital Vernier caliper with an accuracy of  $\pm 0.01$  mm. All measurements were repeated for five times and mean values were calculated.

### ***Mass***

The mass of each specimen was determined using an OHAUS Pioneer PA64C balance with an accuracy of  $\pm 0.0001$  g. All measurements were repeated for five times and mean values were calculated.

### ***Density***

The apparent density of each sample 2 was determined using the following formula:

$$\rho = \frac{m}{v} \quad \text{Equation 2-2}$$

where  $\rho$  = apparent density of specimen, in  $\text{g/cm}^3$

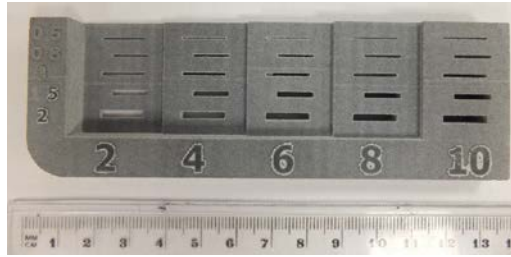
$m$  = mass of specimen, in g

$v$  = specimen volume from linear dimensions (length x width x depth), in  $\text{cm}^3$

Five measurements were taken for each specimen and an arithmetic mean was calculated.

### ***Powder Removal***

Figure 2-17 shows a powder removal sample. The sample has five numbers on the horizontal scale representing the depth of the rectangular slots, and five numbers on the vertical scale representing the width of the slots, both in mm. The length of each slot was approximately 10 mm and negligible in the determination of powder removal score.



**Figure 2-17** Rectangular slots incorporated into the powder removal part

The sample was held in front of a light to check if the slots had been cleared of powder. Each cleared slot was given a score of 1 while an uncleared slot was given a score of 0. Powder removal score, in percentage, was determined using the following formula:

$$\text{Powder removal score (\%)} = \frac{\text{Total number of cleared slots}}{\text{Total number of slots}} \times 100\% \quad \text{Equation 2-3}$$

A higher percentage indicates an easier powder removal, which is preferable.

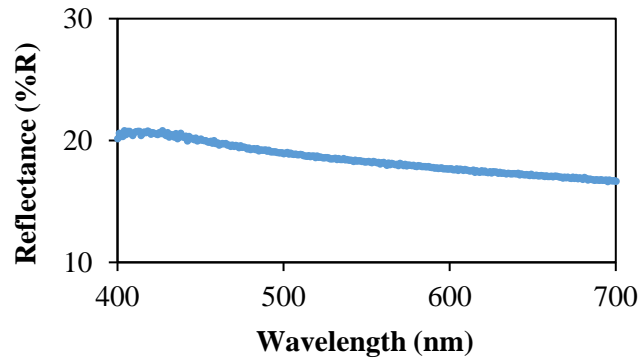
### ***Tensile Tests***

Tensile testing was conducted on a Tinius Olsen H5KS tensile test machine equipped with an H500L laser extensometer and HT36 grip under ambient conditions. The test was performed according to the ASTM D638 standard under 5 kN load at a crosshead speed of 5 mm/min for all specimens. Values of E, UTS, and EaB were determined from the stress-strain curves.

### ***Reflectance Spectroscopy***

As part of this experiment, reflectance spectroscopy was proposed as a non-destructive method to predict the UTS of PA12 parts based on part colorimetry. The spectroscopy was performed on a Perkin Elmer Lambda 40 UV-Vis Spectrophotometer. An integrating sphere was not used in this experiment.

The spectrometer was switched on thirty minutes before the test to allow the lamp to warm up. The measurement range was set to 400 – 700 nm, with data taken at every one nm interval. The output was set to percentage reflectance (%R) and a baseline correction mode of 100% T or 0 A was selected. A white disc was used as the blank reference, and a tensile bar was used as the sample. The reference disc was first placed in the sample compartment to calibrate the equipment to 100% R. Next, the sample was placed in and scanned for reflectance. This step was repeated until all samples were scanned. Figure 2-18 shows an example of a reflectance spectrum.



**Figure 2-18** Example of a reflectance measurement result

The horizontal axis represents wavelength in nm and the vertical axis represents reflectance in %R. The %R scale goes from 0 to 100% (0 = black, 100 = white). The black colouration in a HSS part originated from the carbon black in the ink. It was hypothesised that the ink volume deposited during printing influences UTS. Therefore, an investigation into whether a correlation between reflectance and UTS exists was undertaken.

**Statistical Analysis**

Analysis of variance (ANOVA) test at 5% significance level was carried out to investigate the effect of each parameter on part properties. The computations were performed using IBM SPSS Statistics 24 software. Table 2-13 is to be filled when the results are obtained.

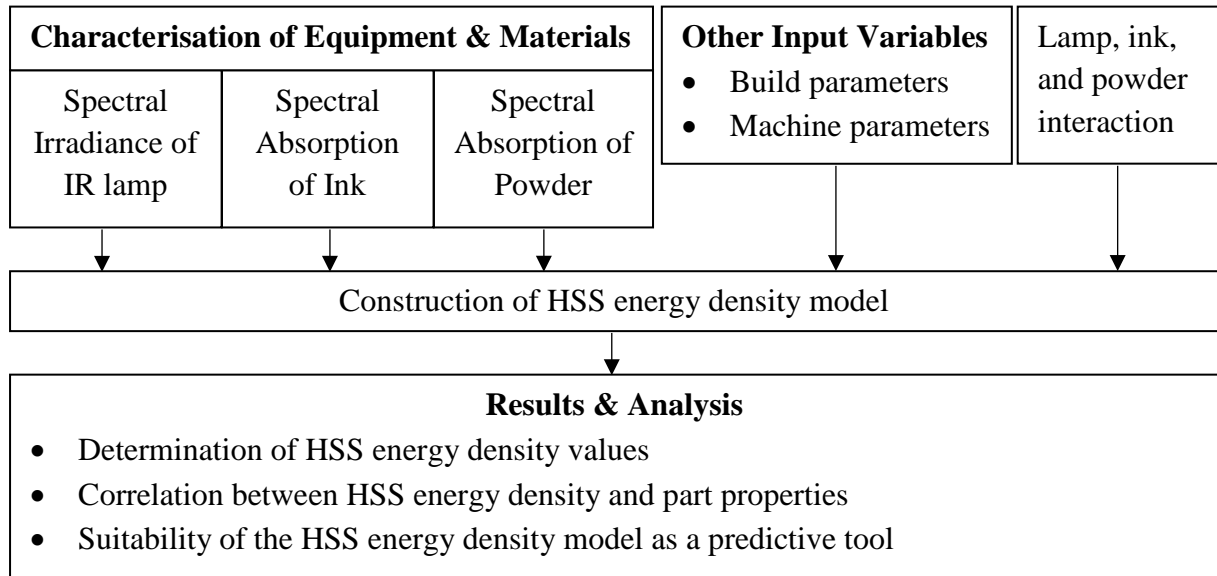
**Table 2-13** ANOVA table to investigate the effect of parameters on PA12 part properties

Source	Sum of squares	Degrees of freedom	Mean square	f value	p value
Model					
Ink					
Lamp					
Ink x Lamp					
Error					
Total					
Corrected Total					

From the table, significance of the main effects (lamp and ink) and the interaction (ink x lamp) can be determined, such that if the *p* value is less than 0.05, significance of the corresponding term is established. However, an insignificant *p* value is favoured for ‘total’, as that would indicate that any term left out of the model is insignificant, which means that the model is well fitted.

## 2.5 Experiments to Construct the HSS Energy Density Model

This section describes the key experimental work performed to construct a systematic model to quantify the energy density in HSS process. The HSS energy density model was developed to study the interaction between lamp, ink, and powder at voxel level. The suitability of the model to be used as a tool to correlate HSS parameters with part properties was assessed. Figure 2-19 outlines the procedures for the model development.



**Figure 2-19** Flowchart of the experimental procedures to construct the HSS energy density model

The characterisations of HSS equipment and materials (lamp, ink, and powder) via spectroscopy method formed the basis of the HSS energy density model. Near infrared (NIR) spectroscopy is an easy, non-destructive technique that can potentially be used for screening HSS-compatible equipment and materials. Spectral irradiance of IR lamp, spectral absorption of ink and spectral absorption of feed powder were performed across the NIR wavelength range.

The spectroscopy results and other parameters, such as ink volume and sintering speed, were incorporated into the HSS energy density model construction. The analytical approach taken for the model construction, including relevant assumptions and boundary conditions are further discussed in Chapter 6.

## 2.5.1 Theory of Molecular Spectroscopy

All bodies emit electromagnetic radiation (energy). Electromagnetic energy does not require a medium and travel through vacuum at the speed of light ( $3 \times 10^8$  m/s). As shown in Figure 2-20, the electromagnetic spectrum consists of a wide range of wavelengths and frequencies.

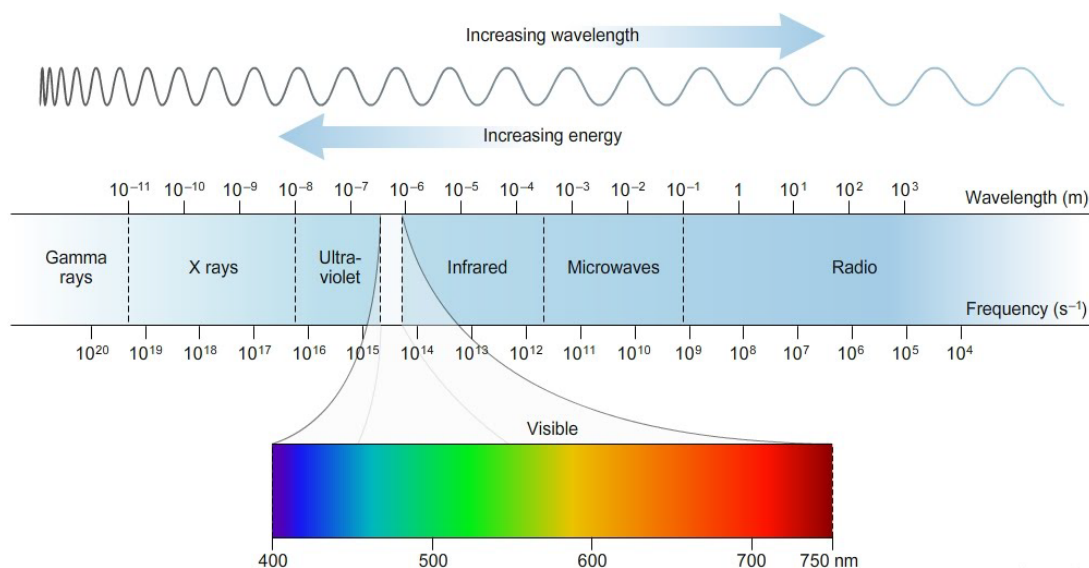


Figure 2-20 Electromagnetic spectrum

In this thesis, we are interested in two regions on the electromagnetic spectrum: primarily infrared (IR) and secondarily visible (Vis). The spectral region visible to the human eye is aptly named the Vis region, which spans between 400 nm to 750 nm. This region is followed by IR from 750 nm to 300,000 nm or 300  $\mu$ m, and can be further divided into near-infrared (NIR), mid-infrared (mid-IR), and far-infrared. Spectroscopic measurements, in particular molecular absorption spectroscopy, can be used in both regions (Vis and IR).

### *Absorption*

In NIR and mid-IR absorption spectroscopy, the intensity of light absorbed by a sample can be measured using a term called absorbance. The definition of absorbance, also expressed as the Beer's Law, is given by the following equation (Skoog, 2007):

$$A = \log \frac{P_0}{P} = abc \quad \text{Equation 2-4}$$

where  $A$  is the absorbance,

$P_0$  is the incident radiant power through the medium,

P is the transmitted power by the medium,  
 a is the absorptivity,  
 b is the path length, and  
 c is the concentration of the sample.

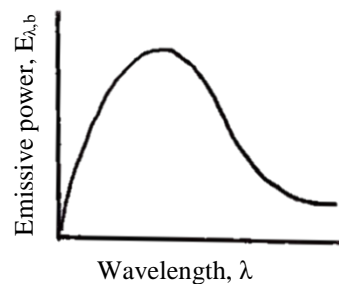
NIR spectroscopy has previously been used to study the effect of LS build parameters on parts (Beard et al., 2011) and to determine the mechanical strength of vulcanised rubber parts (Pornprasit et al., 2016).

### ***Irradiation***

The maximum achievable rate of radiation emitted by a surface is equal to the radiation emitted from an idealised surface that is a perfect absorber and emitter, called a blackbody. The properties of a blackbody is listed as follows (Incropera, 2007):

1. A blackbody absorbs all incident radiation at all wavelength and direction.
2. No surface can emit more energy than a blackbody at the same temperature and wavelength.
3. A blackbody is a diffuse emitter, where its emitted radiation is independent of direction.

Figure 2-21 illustrates a spectral blackbody emissive power.



**Figure 2-21** Spectral blackbody emissive power

The Stefan–Boltzmann law states that the area under the curve in Figure 2-21, which is the total amount of radiation emitted by a blackbody in all directions and over all wavelengths can be calculated from its temperature. The equation is given as below:

$$E_b = \sigma T^4 \quad \text{Equation 2-5}$$

where  $E_b$  is the total blackbody emissive power in  $\text{W m}^{-2}$ ,

$\sigma$  is the Stefan-Boltzmann constant, given as  $5.670 \times 10^{-8} \text{ W m}^{-2} \text{ K}^{-4}$ , and

$T$  is the temperature of the blackbody in K.

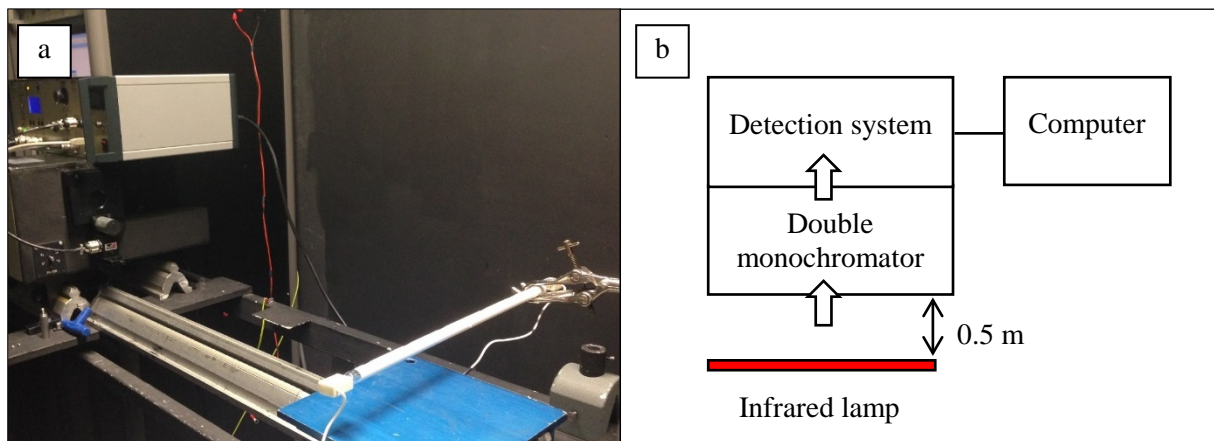
## 2.5.2 Spectral Irradiance of Infrared Lamp

The spectral irradiance of two IR sintering lamps were measured to obtain their spectral distributions. The measurements quantified the energy output of each lamp, which has a consequential effect on the sintering quality of powder.

An attempt was made to construct a light testing rig that uses an integrating sphere. However, the test light sources (IR lamps) were too wide to fit into the available integrating sphere. The test was then contracted externally. These measurements were executed by a metrologist at the Bentham Instruments headquarters in Reading, Berkshire, UK. The experimental setup and procedures for this test are provided as follows.

The irradiance measurements were performed in an enclosed dark room. The measurements were taken at a distance of 500 mm parallel to, and along the optical axis of the measurement plane. This resulted in a relative and not absolute irradiance. The absolute irradiance at any distance can then be calculated using the inverse square law. The lamps were tested in their original conditions and at full power level.

Figure 2-22 shows the equipment setup before a measurement was taken, alongside a drawn schematic plan view.



**Figure 2-22** a) Experimental setup and b) schematic plan view, showing how the lamp output is fed into the light detectors

The test lamp was clamped onto an adjustable rail at a distance from the light detectors. Light travelled from the lamp and into the double monochromator, which then passed it onto the detection system for filtering. The system was connected to a computer that processed the data and generated the spectral output.

The irradiance measurements were performed over the range 300 – 2,500 nm. An isolated power supply set to 240V was used for stable operation of the lamps. The monochromator used was a Bentham DM150 double monochromator, fitted with 600 and 1200 lines/mm gratings. A measurement bandwidth of 5nm was employed throughout the spectral range.

A calibrated quartz halogen standard lamp was used as a reference. This lamp had been calibrated in the same wavelength range used in this test. All calibrations are traceable to The National Metrology Institute of Germany. The input optic was positioned to measure a maximum signal at the required measurement distance.

For the measurement of irradiance, light was collected from the lamp under test using a Bentham D7 cosine response diffuser ( $f2 < 1\%$ ) attached to a randomised fibre bundle, coupled to a monochromator for spectral analysis. Two detector types were used in the test, as each detector was only sensitive to a specific range of wavelength. Table 2-14 displays the wavelength range of each detector, with some overlap to check for continuity.

**Table 2-14** Detectors used to measure the spectral irradiance of IR lamps

<b>Detector type</b>	<b>Wavelength range</b>	<b>Measurement bandwidth</b>
Silicon	300 – 1,100 nm	5 nm
Pyroelectric	1,000 – 2,500 nm	5 nm

At the end of the test, two irradiance curves were obtained for each lamp from the two detectors. The two curves collected were combined to produce one irradiance curve for each lamp.

### **2.5.3 Spectral Absorption of Ink**

The ink is responsible for conducting thermal energy to the underlying powder. In order to conduct heat efficiently, the RAM needs to have a high emissivity. The spectral absorption test was carried out to find the absorbance of ink and its spectral distribution across the Vis and NIR range.

Due to its high concentration, the preliminary absorption test encountered error from testing the ink in its original concentration. In order to gather comprehensive results, the ink was diluted to 0.1 wt% ink solution by mixing 1.00 g of ink (solute) with 999.00 g of petroleum ether 40-65 (solvent).



An Agilent Cary 5000 UV-Vis-NIR spectrophotometer was employed to perform the spectral absorption measurement. The solution was filled into a macro quartz cuvette, the properties of which can be found in Table 2-15.

**Table 2-15** Properties of quartz cuvette

<b>Name</b>	Hellma® absorption cuvette
<b>Material</b>	Suprasil® quartz
<b>Spectral range</b>	200 – 2,500 nm
<b>Path length</b>	10 mm
<b>Chamber volume</b>	3,500 µL

The sample cuvette was placed in the sample holder and another cuvette containing the solvent was used as the reference, or blank sample. A wavelength scan with baseline correction was performed from 400 nm to 2,500 nm, at an interval of five nm. The data was analysed on the supplementary Cary WinUV software Scan application.

#### **2.5.4 Spectral Absorption of Powder**

The spectral absorption of powder was carried out using the experimental procedures described below. In order to mimic real absorption behaviour during sintering, PA2200 powder was tested in its solid form instead of being transformed into a solution. This required the spectroscopy to be conducted in diffuse reflectance mode instead of transmission.

The test was performed using the same spectrophotometer from the ink test. An additional equipment, called the Agilent Praying Mantis accessory was attached to the spectrophotometer to enable measurement in diffuse reflectance mode.

A wavelength scan with baseline correction was performed from 400 nm to 2,500 nm on the Cary WinUV software Scan application. The baseline was measured using a blank disc. Both of the reference and sample discs were covered with polytetrafluoroethylene (PTFE) tape before being mounted on the sampling cup. This was done to ease sample preparation, as the PTFE tape can be easily removed before each measurement, instead of cleaning the sample disc that might have been contaminated with other samples. Sample measurement was then run for approximately 10 minutes per scan. Absorbance data, between a minimum of zero and a maximum of two, was plotted against the wavelength at every five nm interval.

## 2.6 Summary

This chapter detailed the experimental plans and testing procedures for three main sets of experiments. Two powder types were used in the research, which were ALM TPE210-S elastomer (TPE) and EOS PA2200 polyamide (PA12).

Differential scanning calorimetry (DSC) was used to determine the range of material processing temperatures, called the HSS process window. The systematic procedures to operate the high speed sintering (HSS) machine were presented.

In the TPE experiments, 60 parts of six different designs were manufactured. The same set of parameters was used to manufacture all parts to ensure consistency and link between printability and properties. A novel post-processing method, the PUSH process was introduced to the experiment. TPE parts were tested for physical and mechanical properties before and after the PUSH process, and its effect was analysed. The results from this set of experiments are discussed in Chapter 4.

In the PA12 experiments, 180 parts of three different designs were manufactured. Two lamp types and five levels of ink volume were used in this experiment. The build combinations of lamp type and ink volume were detailed. The procedures for a novel quality assessment method using reflectance spectroscopy was discussed. A framework for statistical analysis through analysis of variance (ANOVA) was designed. The results from this set of experiments are discussed in Chapter 5.

The experimental procedures performed to obtain input data for the construction of HSS energy density model (HSS<sub>ED</sub> model) were given. The infrared (IR) lamp was tested for spectral irradiance, while the ink and the powder were subjected to spectral absorption tests through IR spectroscopy. The results from this set of experiments can be found in Chapter 3.

## 2.7 References

1. Ark Novin. 2015. *Surface Roughness* [Online]. Available: <http://www.arknovin.com/en/quality-control/surface-quality/surface-roughness.html> [Accessed 1st December 2017].
2. ASTM International (2000 (2012)) Standard Test Method for Tear Strength of Conventional Vulcanized Rubber and Thermoplastic Elastomers. *ASTM Standard D624*. West Conshohocken, PA: ASTM International.

3. ASTM International (2005 (2010)) Standard Test Method for Rubber Property - Durometer Hardness. *ASTM Standard D2240*. West Conshohocken, PA: ASTM International.
4. ASTM International (2014) Standard Test Method for Tensile Properties of Plastics. *ASTM Standard D638*. West Conshohocken, PA: ASTM International.
5. ASTM International (2015) Standard Test Method for Transition Temperatures and Enthalpies of Fusion and Crystallization of Polymers by Differential Scanning Calorimetry. *ASTM Standard D3418*. West Conshohocken, PA: ASTM International.
6. Beard, M. A., Ghita, O. R. & Evans, K. E. 2011. Monitoring the effects of selective laser sintering (SLS) build parameters on polyamide using near infrared spectroscopy. *Journal of Applied Polymer Science*, 121(6), 3153-3158.
7. Callister, W. D. 2015. *Materials science and engineering : an introduction*, Hoboken, NJ, Wiley.
8. Incropera, F. P. 2007. *Fundamentals of heat and mass transfer*, Hoboken, NJ, John Wiley.
9. International Organization for Standardization (2011) Rubber, vulcanized or thermoplastic — Determination of tensile stress-strain properties. *ISO 37*. International Organization for Standardization.
10. Khursheed, A. 2010. *Scanning electron microscope optics and spectrometers*, World Scientific Pub Co Pte.
11. Norazman, F. & Hopkinson, N. 2014. Effect of Sintering Parameters and Flow Agent on the Mechanical Properties of High Speed Sintered Elastomer. *Journal of Manufacturing Science and Engineering*, 136(6), 061006.
12. PerkinElmer (2013) Open your eyes to a world of opportunity in thermal analysis. PerkinElmer Inc.,.
13. Pornprasit, R., Pornprasit, P., Boonma, P. & Natwichai, J. 2016. Determination of the Mechanical Properties of Rubber by FT-NIR. *Journal of Spectroscopy*, 2016(1), 7.
14. Skoog, D. A. 2007. *Principles of instrumental analysis*, Belmont, C.A., Thomson/Brooks-Cole.
15. The University of Iowa. 2018. *Central Microscopy Research Facility* [Online]. Available: <https://cmrf.research.uiowa.edu/scanning-electron-microscopy> [Accessed April 1st 2018].

# Chapter 3 Characterisation of High Speed Sintering Equipment and Materials

## 3.1 Introduction

In this chapter, the characteristics of the HSS sintering lamp, ink, and powder are explored. The first two sections present the thermal characteristics and powder morphology of both powder types used throughout this thesis. The third section discusses the spectra of the infrared (IR) lamp, ink, and powder obtained through near infrared spectroscopy.

## 3.2 Thermal Characteristics

DSC is a quick and simple thermal method widely used to measure the amount of heat absorbed or liberated during heating and cooling of materials (Skoog, 2007). In this work, the DSC curve of a polymer is used to determine its optimum sintering region, which is known as the HSS processing window.

### 3.2.1 HSS Processing Window

Figure 3-1 shows a typical DSC curve for a polymeric material. The curve illustrates the heat flow through a powder sample as a function of temperature.

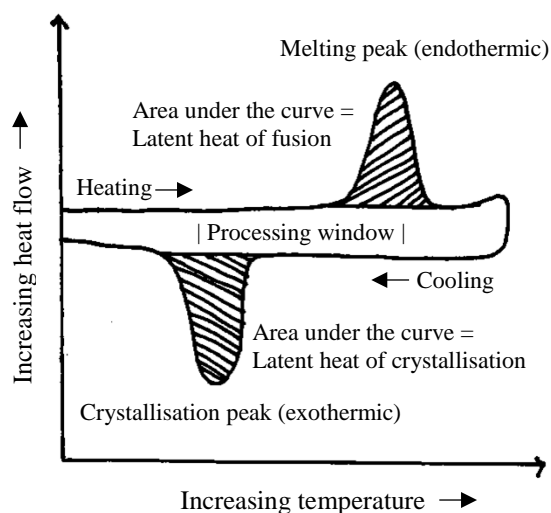


Figure 3-1 A typical DSC curve for a polymeric material

A DSC curve displays the endothermic and exothermic events occurring within a material during the heating and cooling process (Höhne, 1996). These events are observed as peaks, which are melting (endothermic) and crystallisation (exothermic) peaks. Melting temperature ( $T_m$ ) and crystallisation temperature ( $T_c$ ) are defined as the temperatures at the peaks. The enthalpy of melting or crystallisation is calculated by integrating the area under the respective peaks. The HSS processing window is defined as the range of temperature between  $T_m$  and  $T_c$ .

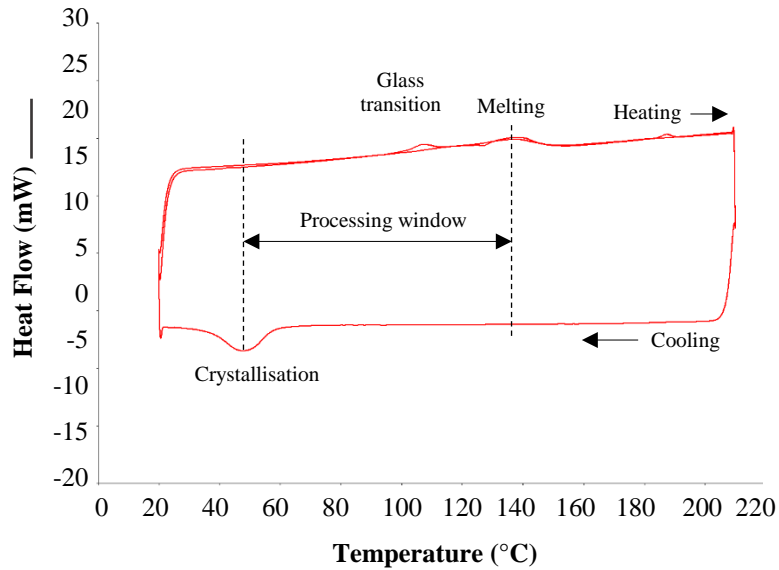
The clarity of the peaks are dependent on the material's crystallinity. Semi-crystalline materials have clearly defined peaks whereas amorphous materials undergo gradual phase changes. In amorphous materials, glass transition occurs before melting, where the material goes from glassy to rubbery. No heat is absorbed or released during this transition; therefore, there is no peak evident. The glass transition temperature ( $T_g$ ) is either taken in the middle of the transition or defined as a temperature range.

In order to be viable for HSS processing, a material needs to have a relatively large processing window. This is to ensure that the polymer does not recrystallise in between consecutive sintering layers. A wide processing window is desirable to allow longer cooling of the molten polymer, i.e. to promote slow recrystallisation. Conversely, a narrow processing window lead to rapid recrystallisation, which result in shrinkage and geometrical distortions in parts (Kruth et al., 2007).

By performing DSC on the polymer, the bed temperatures and lamp exposure time can be adjusted according to the processing window. For example, the overhead temperature for a semi-crystalline material with a wide HSS processing window can be set close to its  $T_m$ . On the other hand, the overhead temperature for an amorphous material needs to be set closer to its  $T_g$  to prevent over sintering.

### **3.2.2 DSC Curves**

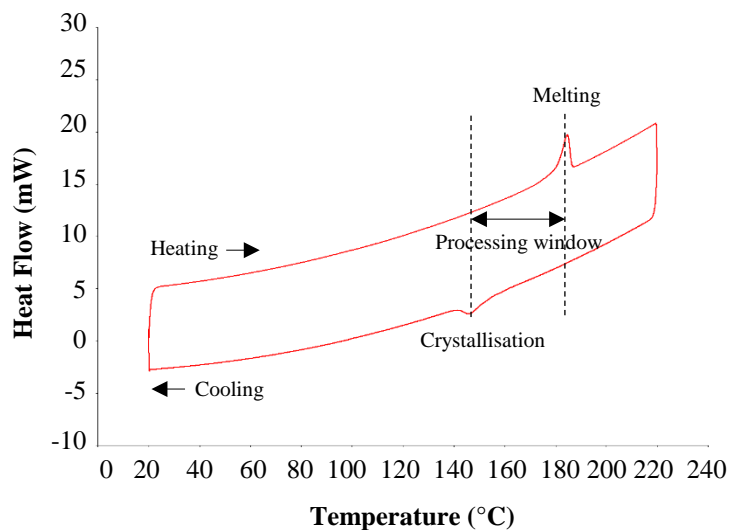
Two polymer materials were tested, TPE210-S thermoplastic elastomer (ALM, Texas) and PA2200 nylon 12 (EOS, Germany). Their DSC curves are shown in Figure 3-2 and Figure 3-3. The vertical axis represents the amount of heat flow to the powder sample in mW and the horizontal axis represents the temperature in °C. Peaks of crystallisation, glass transition, and melting, and the processing window are labelled accordingly. The heating and cooling directions of the powder sample are indicated using arrows.



**Figure 3-2** ALM TPE210-S DSC curve

From Figure 3-2, the characteristic temperatures of TPE210-S were observed as follows:  $T_c = 50^\circ\text{C}$ ,  $T_g = 110^\circ\text{C}$ , and  $T_m = 135^\circ\text{C}$ . The processing window was wide and extended over  $85^\circ\text{C}$ . However, the real processing window is significantly narrower if taking into account the presence of glass transition. TPE210-S satisfies the criteria for HSS processing ( $T_m > T_c$ ).

There was a lack of definition in the temperature peaks, which is characteristic of an amorphous material. This implies that TPE210-S undergoes gradual melt over the range of temperature between  $T_g$  and  $T_m$ . Hence, the polymer will be in the gradual softening/hardening region for most of the sintering process.



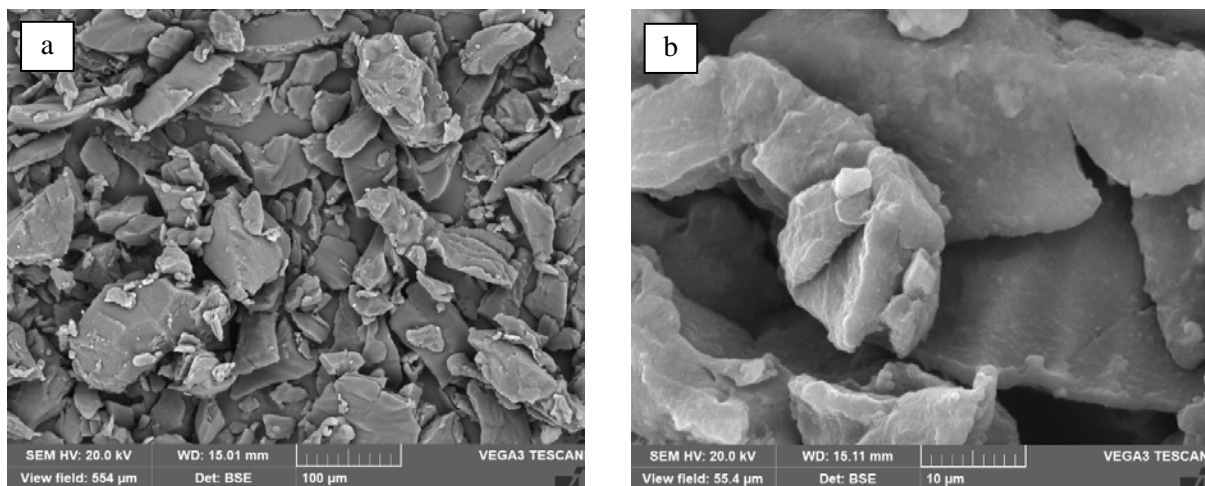
**Figure 3-3** EOS PA2200 DSC curve

From Figure 3-3,  $T_c$  was observed at 150°C and  $T_m$  at 185°C for PA2200. The peak temperatures are corroborated with previously reported values for virgin nylon 12 powder (Hopkinson et al., 2006; Athreya et al., 2010). The processing window stretched for 35°C, which is still considered wide and good for sintering, even though not as wide as TPE210-S. PA2200 also satisfies the criteria required for HSS processing.

The high enthalpy of fusion ensures that the surrounding powder will not be sintered. The sharp temperature peaks illustrate the sharp phase transition from solid to liquid or vice versa, which reflect the semi-crystalline regions present in the polymer. The molecules pack in an orderly configuration, thus promoting them to melt at the same temperature. The wide processing window in nylon 12 encourages good melt flow and contributes to its high sinterability (Hashmi, 2014).

### 3.3 Powder Morphology

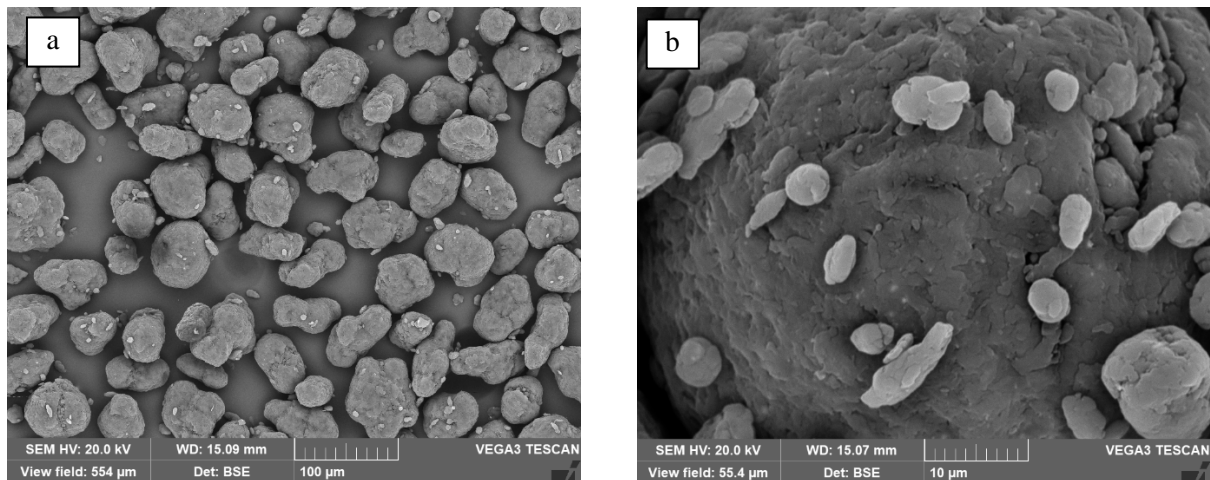
Goodridge et al. (2012) recommended that the optimum LS powder particles should measure in between 45 – 90  $\mu\text{m}$  and have high sphericity to facilitate flow, reduce the surface area to volume ratio, and improve packing efficiency. Figure 3-4 and Figure 3-5 show the particle morphologies of virgin TPE210-S and PA2200 powders, respectively.



**Figure 3-4** Micrographs of ALM TPE210-S powder at a) low magnification and b) high magnification

The TPE210-S particles are irregular in shape and the edges are coarse. There also seems to be a wide distribution of particle size. These are characteristics of powder produced by cryogenic grinding. Dadbakhsh et al. (2016) reported similar powder morphology for a new grade thermoplastic polyurethane (TPU) powder that has been cryogenically ground for LS. Their

study found that coarse TPU powder was more difficult to process than fine TPU powder with added flow additive, despite having the same DSC curve.



**Figure 3-5** Micrographs of PA2200 powder at a) low magnification and b) high magnification

In the case of PA2200, the powder particles are near spherical and slightly elongated (potato-shaped). Beard et al. (2011) reported similar morphology for this material, and the particle shape and size are closer to the ideal sintering powder characteristics than TPE210-S.

### 3.4 Spectral Analysis

Spectral data over the visible (Vis) and near infrared (NIR) spectrum, between 400 – 2,500 nm, was collected to determine the spectral matching between lamp irradiance and ink and powder absorption. The wavelength range tested was selected based upon the emissivity of the IR lamp, which is known to have a peak irradiance in the NIR region.

Table 3-1 shows the position of the relevant wavelength on the electromagnetic spectrum.

**Table 3-1** Vis and NIR regions on the electromagnetic spectrum

Gamma	X-Ray	Ultraviolet	Visible	Infrared			Microwave	Radio
				Near-Infrared	Mid-Infrared	Far-Infrared		
< 0.01 nm	0.01 – 10 nm	10 – 380 nm	380 – 780 nm	780 – 2,500 nm	2.5 – 25 μm	25 – 1,000 μm	750 μm – 375 mm	> 10 mm

In this section, each HSS component was characterised individually. The interaction between these components is further analysed to compute the HSS energy density values, as discussed in Chapter 6.



### 3.4.1 Spectral Irradiance of the Infrared Lamp

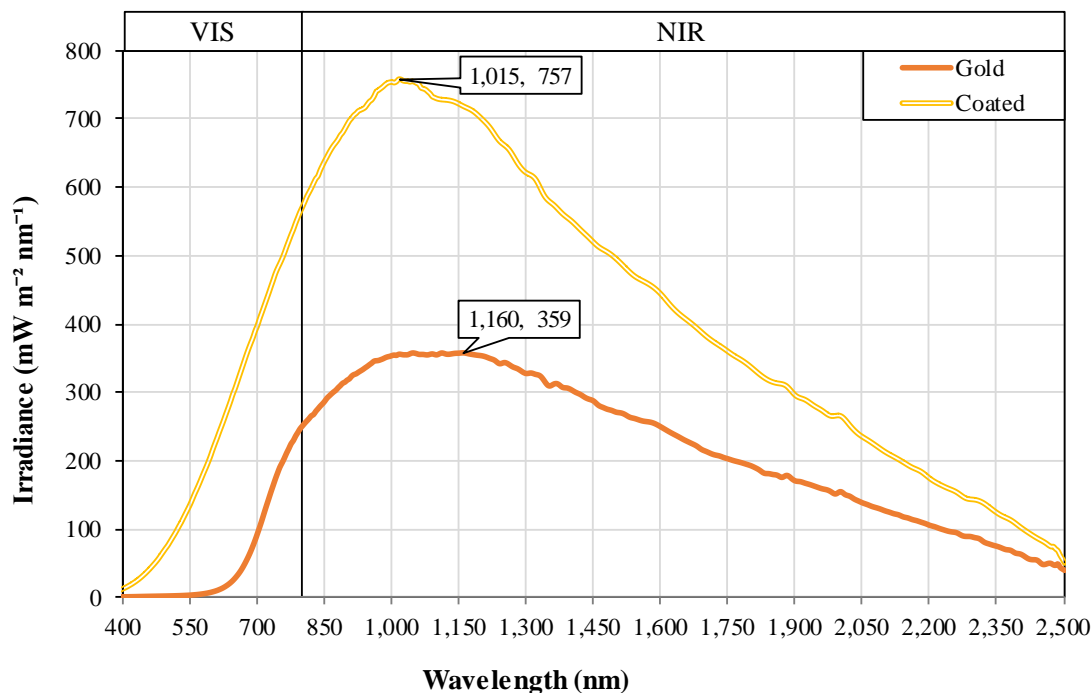
The IR lamps selected for this experiment were both manufactured by Philips and sourced from Victory Lighting (2016). The lamp properties are listed in Table 3-2 below.

**Table 3-2** Properties of IR lamps

Properties	Gold Lamp	Coated Lamp
Manufacturer's product code	64242070	64242056
Length	353 mm	353 mm
Diameter	10 mm	10.5 mm
Voltage	235 V	240 V
Power	2,000 W	2,000 W

Both lamps were 2 kW rated IR quartz halogen lamp with tungsten filament. The main difference between the two lamps was the material used for their reflector coating. Lamp coating serves different purposes, mainly applied for anti-glare, or sometimes as a filter to block certain wavelengths.

Figure 3-6 shows the measurement results, with the peak irradiances and their corresponding wavelengths labelled.



**Figure 3-6** Irradiance spectra of the gold and coated IR lamps

Figure 3-6 shows how the difference in the reflector coating resulted in a difference in irradiance. Both spectra exhibited the characteristic of a blackbody radiation curve. The two spectra differed by approximately a factor of two at all wavelengths. Both spectra peaked in the NIR region, with the coated lamp having a peak twice as high as the gold. The peaks were observed at 1,160 nm and 1,015 nm for the gold and coated lamp respectively. The gold lamp was thought to have a wavelength filter fitted, as there was no radiation from wavelengths less than 600 nm. It was assumed that this was done to reduce glare.

The irradiance in this wavelength range was determined for both lamps using first order numerical integral described by the following equation.

$$E = \sum_{i=400}^{2500} \frac{(E_{\lambda_i} + E_{\lambda_j})}{2} \times (\lambda_j - \lambda_i) \quad \text{Equation 3-1}$$

where  $E$  is the irradiance in  $\text{W m}^{-2}$ ,

$E_{\lambda}$  is the spectral irradiance in  $\text{W m}^{-2} \text{nm}^{-1}$ , and

$\lambda$  is the wavelength in nm.

The total irradiance was calculated as  $402 \text{ W m}^{-2}$  for the gold lamp and  $818 \text{ W m}^{-2}$  for the coated lamp. This indicates that the coated lamp radiates over double the amount of energy when compared to the gold lamp if applied over the same area and exposure time.

Based on the uncertainty in the calibrated standard and in the repeatability of the measurement, the uncertainty in the spectral irradiance measurements was estimated not to exceed  $\pm 5\%$  over the spectral range 400 – 1,100 nm and  $\pm 10\%$  over the spectral range 1,100 – 2,500 nm.

### 3.4.2 Spectral Absorption of Carbon Black

The physical properties of the ink used in this experiment are listed in Table 3-3 below.

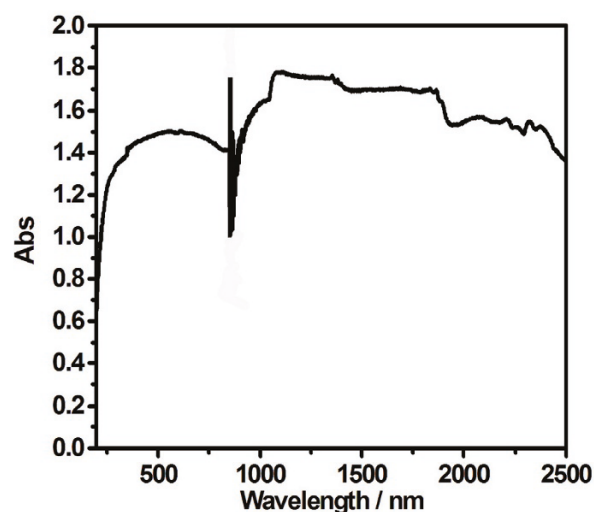
**Table 3-3** Properties of ink

<b>Properties</b>	
Product name	SunChemical Jetstream PCO 7774
Boiling point	90°C
Kinematic viscosity @ 40°C	<20 cSt (equivalent to 17 mPa-s)
Weight percentage of carbon black	10 wt%

This is a commercial ink predominantly made up of hydrocarbon and 10 wt% carbon black as the radiation absorbing material (RAM). The carbon black weight percentage was optimised for this ink formulation in a study done by Thomas (2009).

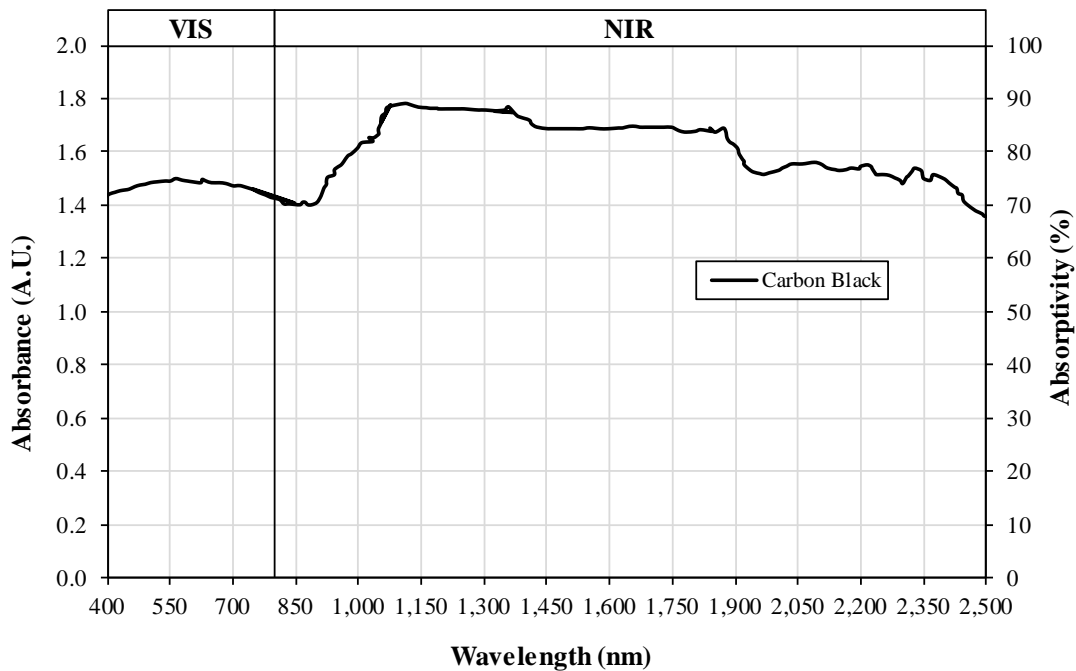
The spectrum obtained through the spectroscopy of ink planned in Section 2.5.3 (page 67) was found to be inconclusive. It was deduced that the spectral absorption of ink did not reflect the spectral absorption of carbon black as anticipated. This can be attributed to the fact that the ink is essentially a compound made of different individual particles. As carbon black is the only active ingredient required and present on the build bed during sintering (other ink constituents are vaporised), it is crucial that the absorption of carbon black is considered on its own. It could be that the hydrocarbon particles have a high reflectivity, or low absorbance, and as they make up the majority of the ink, their absorbance overpowered that of carbon black. Dahm and Dahm (2007) associated such effect with the presence of void and the random distribution of particles in different sizes within the ink.

The ink used in this study is a commercial ink and therefore its formulation is confidential. It was not possible to ascertain the type of carbon black used in the ink. To solve this problem, the spectral absorption of a commercial N115 carbon black powder was adopted from a study by Han et al. (2011). In their study, the spectral absorption of the carbon black powder was measured on an identical spectrophotometer between 200 – 2,500 nm wavelength range. Figure 3-7 shows the spectral absorption of carbon black as reported in the literature. A fluctuation can be observed around 800 – 950 nm due to the change of light source as the wavelength shifts from Vis to NIR region.



**Figure 3-7** Original absorption spectrum of carbon black powder (Han et al., 2011)

Figure 3-7 was replotted using Plot Digitizer 2.6.8 programme to obtain a spectrum within the wavelength range relevant to the study, which is between 400 – 2,500 nm. The original fluctuation between 800 – 950 nm was removed. The resultant absorption spectrum of carbon black powder is shown in Figure 3-8. The spectrum was plotted in absorbance and percentage absorptivity, the latter for use in constructing the HSS energy model.



**Figure 3-8** Absorption spectrum of carbon black powder

The carbon black had high absorptivity across the relevant wavelength range. The peak absorbance was observed at 1,110 nm. This is incident to the irradiance peak of the IR lamps in Figure 3-6 (1,015 nm for coated and 1,160 nm for gold). This shows that the carbon black (ink) is spectrally matched to the IR lamp, which is advantageous for sintering.

### 3.4.3 Spectral Absorption of Powder

Figure 3-9 shows the absorption spectrum for PA2200 powder obtained from the spectroscopy in Section 2.5.4 (page 68). Similar to the carbon black spectrum, the absorbance was also converted to percentage absorptivity on a scale of 0 to 100%.

The absorbance of PA2200 was uniform with a few peaks. According to Dahm and Dahm (2007), absorbance in the Vis range is broad due to the electronic transition, while in the NIR range, absorbed energy is changed to molecular vibrational energy. Peaks can be observed in the NIR range at around 1,700 nm and increasingly higher after 2,300 nm. Neither peaks

matched the peaks of the IR lamp spectra and carbon black. This spectral mismatch is desirable for HSS process, as the powder surrounding the printed area will not absorb the radiated energy as efficiently as the carbon black. The difference in energy absorption between the two regions constitutes to a good definition along the perimeter of a printed part.

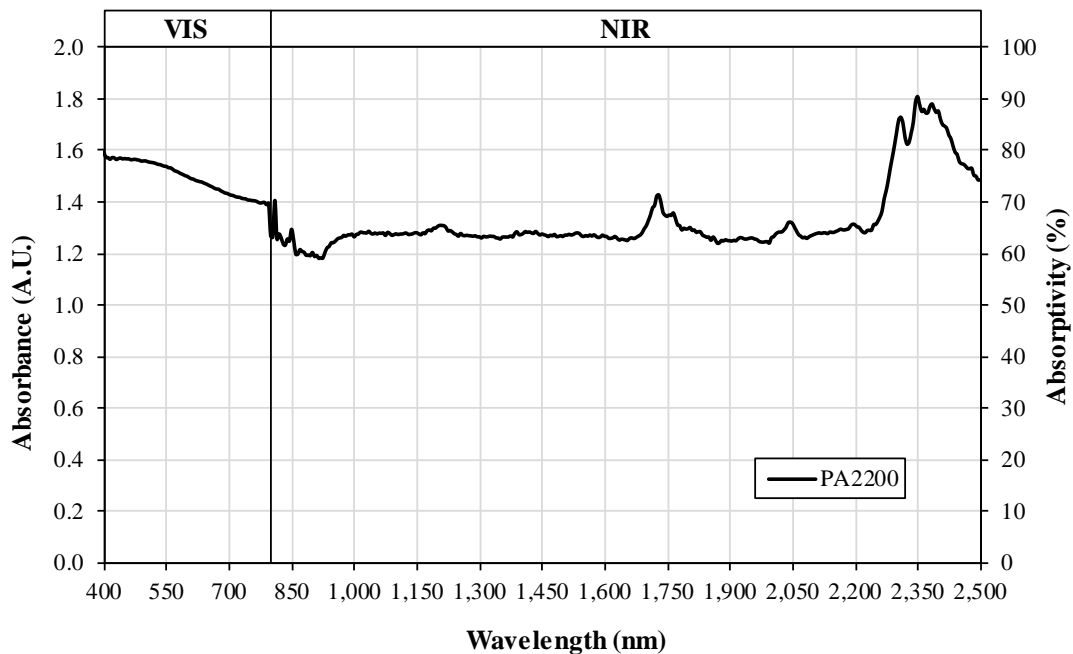


Figure 3-9 Absorption spectrum of PA2200 powder

### 3.5 Summary

ALM TPE210-S is an amorphous material with a very wide HSS processing window. The material gradually softens and hardens over a large temperature range. EOS PA2200 is a semi-crystalline material with a wide HSS processing window and clear transition peaks. A wide HSS processing window is essential to promote slow recrystallization and achieve better part properties. The processing temperatures of both materials were set according to the characteristic temperatures presented, according to the guidelines provided on page 39.

SEM images revealed the difference in particle morphology between the two materials studied in this thesis. TPE210-S particles were irregular with rough edges, while PA2200 particles were shaped like potatoes and had smooth texture. Based on the DSC and SEM results, it was expected that the TPE210-S would be more difficult to process on the HSS machine.

The spectral irradiance of the two test lamps conformed to the characteristic of a blackbody. The total irradiance of the coated lamp was higher than the gold lamp by a factor of two. The

absorbance of carbon black could not be obtained through IR spectroscopy of ink. The absorbance of PA2200 powder was presented.

### 3.6 References

1. Athreya, S. R., Kalaitzidou, K. & Das, S. 2010. Processing and characterization of a carbon black-filled electrically conductive Nylon-12 nanocomposite produced by selective laser sintering. *Materials Science and Engineering: A*, 527(10–11), 2637-2642.
2. Beard, M. A., Ghita, O. R. & Evans, K. E. 2011. Monitoring the effects of selective laser sintering (SLS) build parameters on polyamide using near infrared spectroscopy. *Journal of Applied Polymer Science*, 121(6), 3153-3158.
3. Dadbakhsh, S., Verbelen, L., Vandeputte, T., Strobbe, D., Van Puyvelde, P. & Kruth, J.-P. 2016. Effect of Powder Size and Shape on the SLS Processability and Mechanical Properties of a TPU Elastomer. *Physics Procedia*, 83(971-980).
4. Dahm, D. J. & Dahm, K. D. 2007. *Interpreting diffuse reflectance and transmittance : a theoretical introduction to absorption spectroscopy of scattering materials*, Chichester, UK, NIR Publications.
5. Goodridge, R., Tuck, C. & Hague, R. 2012. Laser sintering of polyamides and other polymers. *Progress in Materials Science*, 57(2), 229-267.
6. Han, D., Meng, Z., Wu, D., Zhang, C. & Zhu, H. 2011. Thermal properties of carbon black aqueous nanofluids for solar absorption. *Nanoscale Research Letters*, 6(1), 457.
7. Hashmi, S. 2014. *Comprehensive materials processing*, USA, Newnes.
8. Höhne, G. W. H. 1996. *Differential scanning calorimetry : an introduction for practitioners*, Berlin; London, Springer.
9. Hopkinson, N., Hague, R. & Dickens, P. 2006. *Rapid Manufacturing: An Industrial Revolution for the Digital Age*, Chichester, England, John Wiley & Sons.
10. Kruth, J. P., Levy, G., Klocke, F. & Childs, T. H. C. 2007. Consolidation phenomena in laser and powder-bed based layered manufacturing. *CIRP Annals - Manufacturing Technology*, 56(2), 730-759.
11. Skoog, D. A. 2007. *Principles of instrumental analysis*, Belmont, C.A., Thomson/Brooks-Cole.
12. Thomas, H. 2009. *The construction and testing of an IR absorption metric for High Speed Sintering*. PhD thesis, Loughborough University.
13. Victory Lighting. 2016. *Victory Lighting Infrared heaters and UV lamps* [Online]. Available: <http://www.victorylighting.co.uk/> [Accessed 1 December 2016].

# **Chapter 4 High Speed Sintering of Elastomer - Influence of Process Chain on the Dimensional Accuracy of Parts**

## **4.1 Introduction**

This chapter consists of four main sections. In the first section, the high speed sintering (HSS) of thermoplastic elastomers (TPEs) are reported and their properties are presented. In the second section, the effect of PUSH post-processing technique on the physical and mechanical properties of high speed sintered TPE are evaluated. In the third section, the commercial viability of HSS as a high volume production process is assessed. In the last section, the influences of HSS process steps on part quality are examined.

## **4.2 Processing of TPE by High Speed Sintering**

This section discusses the justification for parameter selection and general experimental observations as noted during the processing of ALM TPE210-S on the HSS machine.

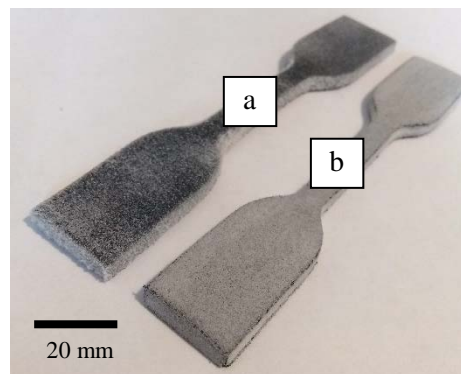
### **4.2.1 HSS Build Parameters**

It is important to note that the optimisation of parameters specified in Table 2-4 was a simplified version of the Design of Experiments (DOE) method. Ideally, a preliminary experiment would have been executed to perform a complete DOE to enable the final experiments to be performed using an optimised set of parameters. However, it can be justified that a previous study on the same material (Norazman and Hopkinson, 2014) can serve as the preliminary investigation. The study identified the key HSS parameters and evaluated their effect on part properties. The factors investigated were build bed temperature, lamp speed, and weight percentage of flow additive. All three parameters proved to be significant on the tensile properties and surface roughness of TPE2 parts. The literature is attached in the Appendices for further reference.

Some HSS build parameters can significantly influence part strength and surface finish quality, especially the key parameters related to thermal energy input (e.g. build bed temperature). If the thermal energy input by the infrared lamp is too high, the powder particles adjacent to the

printed area will absorb the excess energy. This will partially sinter the undesired surrounding powder and result in a hard powder cake. The powder cake, which contains the printed part and used powder, needs to be post-processed in order to retrieve the parts. This is done through a process called powder removal in a bead blasting machine. Post-processing a hard powder cake is time-consuming and usually produces parts with low dimensional accuracy and surface roughness. A soft powder cake sometimes results in damaged parts.

The complex geometries and intricate features of the six undisclosed OEM design samples manufactured as part of this experiment require a soft powder cake for easy powder removal. Hence, the build parameters were optimised for a trade-off between part strength and part quality to fulfill the part specifications. The test samples were printed at the same set of optimised parameters throughout to match the properties of the design samples. The difference in surface roughness achieved through this trade-off parameter optimisation is evident in Figure 4-1.



**Figure 4-1** Part a) has high strength and high surface roughness, while part b) has medium strength and medium surface roughness

In Figure 4-1, it can be seen that part b), which was manufactured using the optimised parameters, had a smoother surface compared to part a) taken from a preliminary study. Preliminary studies on high speed sintered TPE were only mainly concerned with the mechanical strength of parts (Norazman and Hopkinson, 2013; Hartley, 2014). The manufactured parts in these studies were exclusively test specimens, hence low surface roughness was not essential, as illustrated above. The TPE experiments in this thesis were performed with parameters that are a trade-off between part strength and part quality. The result was an improvement of surface roughness and dimensional accuracy, though it is to be expected that the parts would not perform as well as previous studies in terms of mechanical strength, due to the reason stated above.



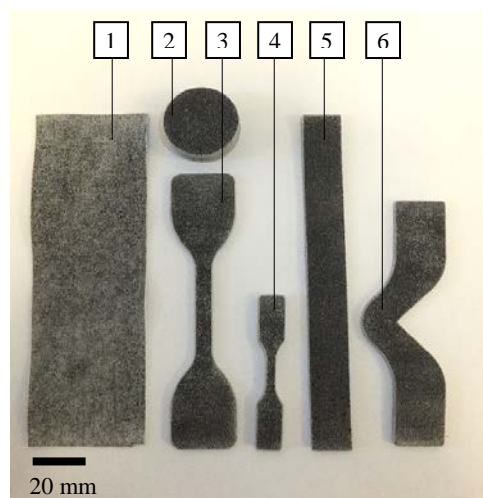
## 4.2.2 Experimental Observations

Table 4-1 lists the build time, excluding pre-processing and post-processing time, for each specimen. The number of layers per part (excluding blank) corresponds to the thickness of each part. Each build contains ten blank layers or 1 mm vertical gap between each specimen, and ten blank layers for both underneath and over the stack. The layer cycle time was 40 seconds.

**Table 4-1** Build time for TPE specimens

Specimen number	Replicates per build	Number of layers		Build time (minute)	
		per part (excluding blank)	per build (including blank)	per build	per part
1	10	4	150	100	10
2	10	120	270	180	18
3	10	20	310	207	21
4	10	32	94	63	6
5	10	23	340	227	23
6	10	20	160	107	11

Figure 4-2 shows the printed specimens after they had been retrieved from the powder cake and cleaned through bead blasting. These geometries were selected for the reasons discussed in Section 2.3.1 (page 43). In general, powder removal was easy for all parts as the powder cake was soft. However, not all powder came off and this was visible on the part surfaces. The parts had a consistent dark grey coloration with a dusting of white powder and a consistently rough texture.



**Figure 4-2** Printed TPE specimens 1 – 6

### 4.3 Physical and Mechanical Properties of High Speed Sintered TPE

This section discusses the dimensions, mass, surface roughness, hardness, tensile properties and tear properties of the manufactured TPE parts.

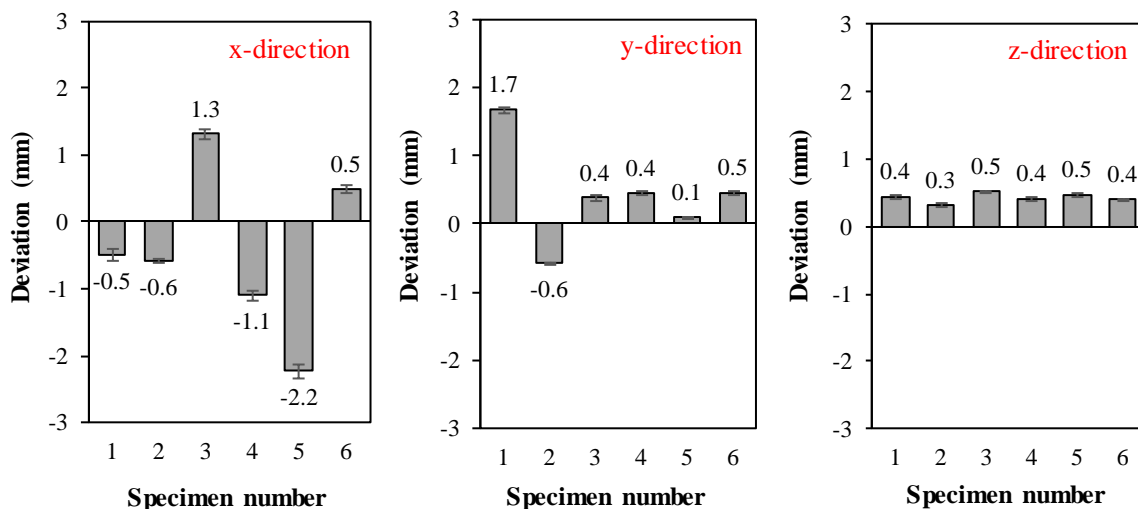
#### 4.3.1 Part Dimensions

Table 4-2 shows the average part dimensions. These parts are also referred as “untreated” to differentiate them from the parts that are further surface finished using the PUSH process.

**Table 4-2** Dimensions of untreated TPE specimens

Specimen	x dimensions (mm)		y dimensions (mm)		z dimensions (mm)	
	Target	Measured	Target	Measured	Target	Measured
1	140.00	144.50	45.00	46.67	0.40	0.84
2	28.00	27.42	28.00	27.42	12.00	12.31
3	115.00	116.31	25.00	25.38	2.00	2.51
4	63.50	62.40	9.53	9.98	3.20	3.63
5	102.00	99.77	19.00	19.09	2.30	2.78
6	140.00	140.49	15.00	15.46	2.00	2.39

The measured dimensions were compared to their respective nominal values to obtain the dimensional accuracy. Figure 4-3 shows the dimensional accuracy of TPE specimens along the x-, y-, and z-directions. The mean absolute deviation in mm is plotted against the specimen number. The error bars represent one standard error (SE).



**Figure 4-3** Dimensional accuracy of high speed sintered TPE specimens along x-, y-, and z-directions ( $\pm 1$  SE)

From Figure 4-3, it can be observed that the TPE parts showed most significant deviation along x-direction. All parts deviated between -2.2 and 1.3 mm along this direction, where most of the specimens shrunk with the exception of specimens 3 and 6.

Along y-direction, all but one set of specimens (specimen 2) deviated positively, up to 1.7 mm. This phenomenon is called wall growth, where surrounding unsintered powder fuse to the part due to excess thermal energy input or poor ink drop formation. Most excess powder can be removed via bead blasting, though it might be difficult for a particularly thin section.

On the other hand, all parts were oversized within 0.5 mm or less the nominal dimensions along z-direction. This is the direction in which layer lamination occurs. Although these values are lowest compared to other directions, when taking into consideration the layer height of 0.1 mm and the powder particle size of 0.085 mm, this value is approximately five layers of powder in excess. It can be speculated that the constant ~0.5 mm tolerance in z-direction is attributed to the sintering depth, where the absorbed thermal energy penetrated through consecutive layers of powder. Majewski et al. (2008) reported a sintering depth of 0.20 – 0.25 mm for a single layer part made from PA12 with a powder particle size of 0.056 mm, which translated into similar five layers of excess powder.

The dimensional deviations were also plotted as relative percentages to their nominal dimensions to assess the directional shrinkage or wall growth, as shown in Figure 4-4.

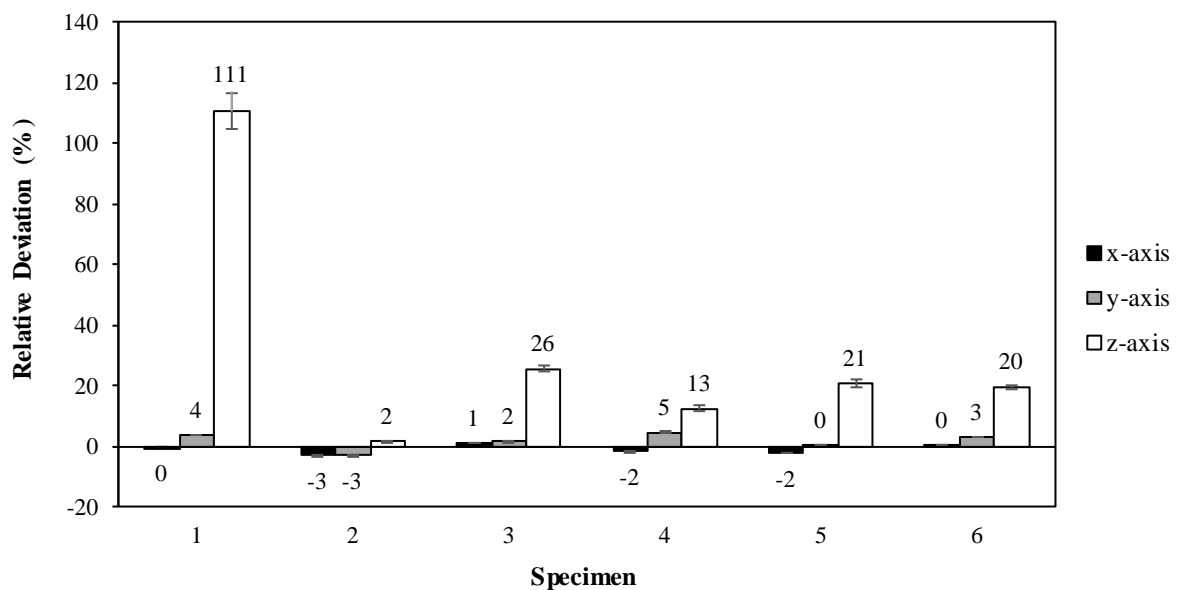


Figure 4-4 Relative deviation of TPE specimens in percentage ( $\pm 1$  SE)

Part shrinkage is commonplace for additive manufactured parts, with reported values of up to 4% in laser sintering (LS) and 1% in binder jetting (Dimitrov et al., 2006; Grimm, 2004). Figure 4-4 shows good dimensional accuracy in x- and y-directions, where deviations were less than 5%. However, this was not the case in z-direction, as deviation soared up to 111% in specimen 1 (very thin part). When compared to the nominal deviations in Figure 4-3, it can be concluded that the deviation in z-direction is independent of part thickness, and instead is constant with a value of ~0.5mm.

Note that as specimen 2 has a circular profile, it was presumed that the part had shrunk equally along both x- and y- directions. It can be speculated that the specimen's shrinkage along x-direction influenced shrinkage in y-direction, which agrees with the directional shrinkage interdependence reported in LS (Raghunath and Pandey, 2007).

It is interesting to note that the x-direction of the HSS build bed is the direction of the carriage movement, i.e. direction of inkjet printing and powder spreading. High part shrinkage is not desirable as it encourages part warpage, which is shown in Figure 4-5. It is particularly dangerous when warpage occurs on a HSS machine, as the raised section of the specimen might hit the printhead as it traverses above the build bed.

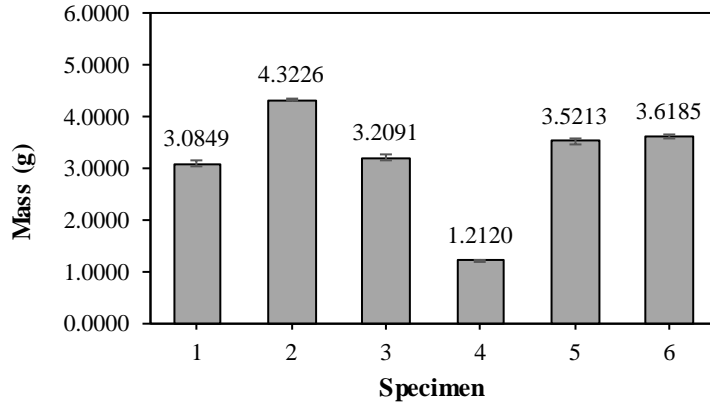


**Figure 4-5** The ends of a TPE part were lifted and created shadows, indicating part warpage

### 4.3.2 Mass

The repeatability of parts within a build can be assessed through density measurement via pycnometry. However, due to the unavailability of the equipment, repeatability was evaluated through mass measurement.

The average mass of each specimen is displayed in Figure 4-6.

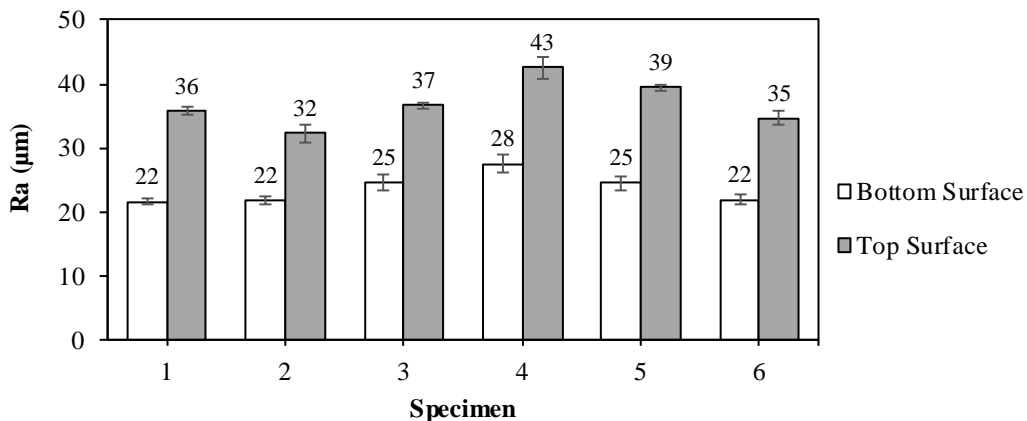


**Figure 4-6** Average mass of high speed sintered TPE specimens ( $\pm 1$  SE)

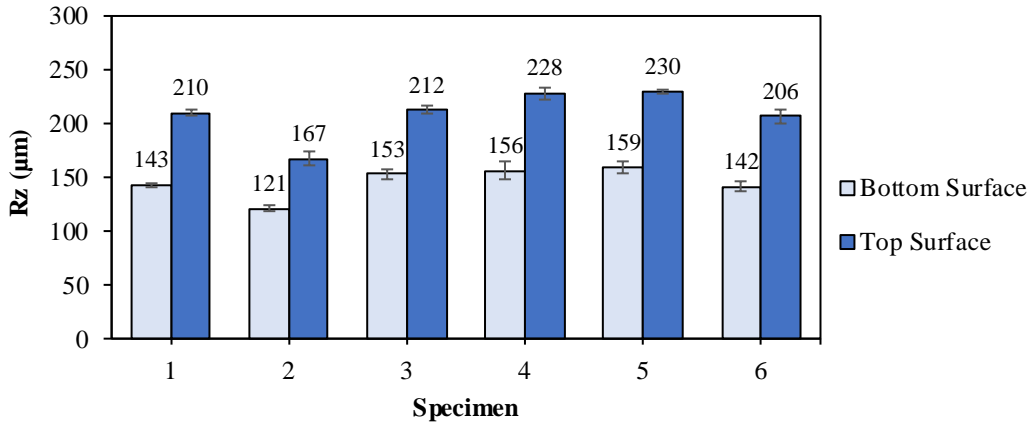
The average mass differs for each specimen type due to the difference in part volume. The standard error in each set of specimen (specimen 1, 2, 3...) were consistently low. The low error in mass, combined with the low error in dimensional measurements, suggests a high repeatability of parts within a build.

### 4.3.3 Surface Roughness

A high quality part requires a low overall surface roughness. Of the utmost importance are the surfaces parallel to the xy-plane, as this is the most common orientation used for building HSS parts. The surface roughness results presented in this section are given in terms of two measurements, average surface roughness,  $R_a$  (Figure 4-7) and ten-point mean roughness,  $R_z$  (Figure 4-8).



**Figure 4-7** Average surface roughness of high speed sintered TPE specimens on bottom and top surfaces ( $\pm 1$  SE)



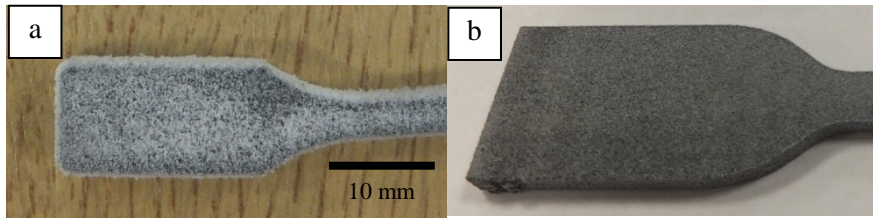
**Figure 4-8** Mean surface roughness of high speed sintered TPE specimens on bottom and top surfaces ( $\pm 1$  SE)

The  $R_a$  ranged from 20 – 30  $\mu\text{m}$  on bottom surfaces and 30 – 45  $\mu\text{m}$  on top surfaces. This is higher compared to the 9 – 20  $\mu\text{m}$  reported for LS PA12 parts (Kruth et al., 2003). However, if taking into account the 34 % difference in powder particle size between TPE210-S and PA2200, these HSS values are still comparable to LS.

Based on Figure 4-7, the bottom surfaces had lower  $R_a$  (smoother) than the top surfaces. This trend agrees with previous surface roughness analysis of TPE210-S and nylon 11 parts (Norazman and Hopkinson, 2014; Ellis et al., 2015). In common with most AM powder bed processes, the  $R_a$  values of HSS parts vary between different part surfaces. However, the position of the smoother surface may vary between AM processes. In HSS's case, the bottom surface is generally smoother than the top surface. The rougher top surface may be attributed to the distribution of a new layer of powder on top of the top surface, where undesired unsintered powder at an elevated temperature may adhere. Alternatively, the smoother bottom surface can be caused by the meniscus that formed on the surface of the underlying powder.

$R_z$  values of 120 – 160  $\mu\text{m}$  and 165 – 230  $\mu\text{m}$  were recorded for the bottom and top surfaces, respectively. The bottom surfaces, again, proved smoother than the top. The  $R_z$  is high compared to the complementary  $R_a$ . This can be explained by the presence of extreme peaks and valleys along an otherwise smooth profile on the surfaces, as  $R_z$  only averages the maximum peak-to-valley distances. The extreme peaks can be made up of stacked up unsintered powder particles that are inherent on the surfaces. This theory is further investigated using optical microscopy.

The level of surface finish achievable with the HSS process is highly dependent on the type of material used. Figure 4-9 compares the surface finish of a TPE210-S part compared to a PA12 (PA2200) part from Chapter 5.



**Figure 4-9** Loose white powder evident on a) TPE specimen 4, compared to b) PA12 specimen 1

#### 4.3.4 Hardness

On a Shore A hardness scale of 0 – 100, with higher values indicating harder materials, the average Shore A hardness for untreated TPE specimens are given in Table 4-3.

**Table 4-3** Shore A hardness of untreated TPE specimens

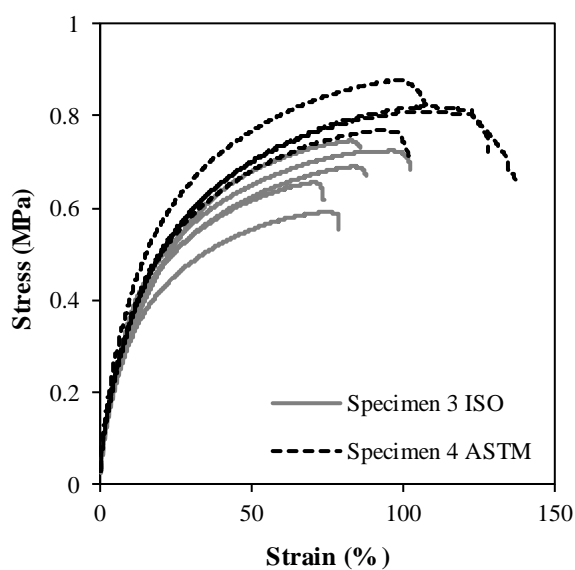
Specimen	Shore A hardness
2	52 ± 0.2
3	57 ± 0.5
4	56 ± 0.3
5	58 ± 0.3
6	57 ± 0.5

The average hardness is significantly higher than the manufacturer quoted value for laser sintered TPE at 40 Shore A. For comparison, the hardness of a laser sintered PA12 is a lot higher at 75 Shore D, surpassing the maximum value of 100 on the Shore A scale.

The disparity is believed to stem from the presence of carbon black particles, or RAM, in between the TPE powder particles in the part. The carbon black acts as a filler to reinforce the polymer, in what is called the polymer-filler interaction. The reinforcing effect can be attributed to the Van der Waal forces between the carbon black and the polymer.

### 4.3.5 Tensile Properties

Figure 4-10 shows the stress-strain curves of untreated TPE specimens. Two sets of data are presented in this graph, obtained using ISO 37 and ASTM D638 test methods on specimens 3 and specimens 4, respectively. The vertical axis represents the stress in MPa, and the horizontal axis represents the strain in percentage. One specimen 4 was damaged before the test, therefore only results from four specimens 4 are compared against the average of five specimens 3. Table 4-4 summarises the key tensile properties; the ultimate tensile strength (UTS), Young's modulus (E), and elongation at break (EaB) for each set of test.



**Table 4-4** Tensile properties of untreated TPE specimens

Tensile Properties	Test Method	
	ISO	ASTM
UTS (MPa)	$0.68 \pm 0.02$	$0.82 \pm 0.02$
E (MPa)	$3.80 \pm 0.15$	$3.93 \pm 0.20$
EaB (%)	$86 \pm 4$	$119 \pm 7$

**Figure 4-10** Stress-strain curves of untreated TPE specimens

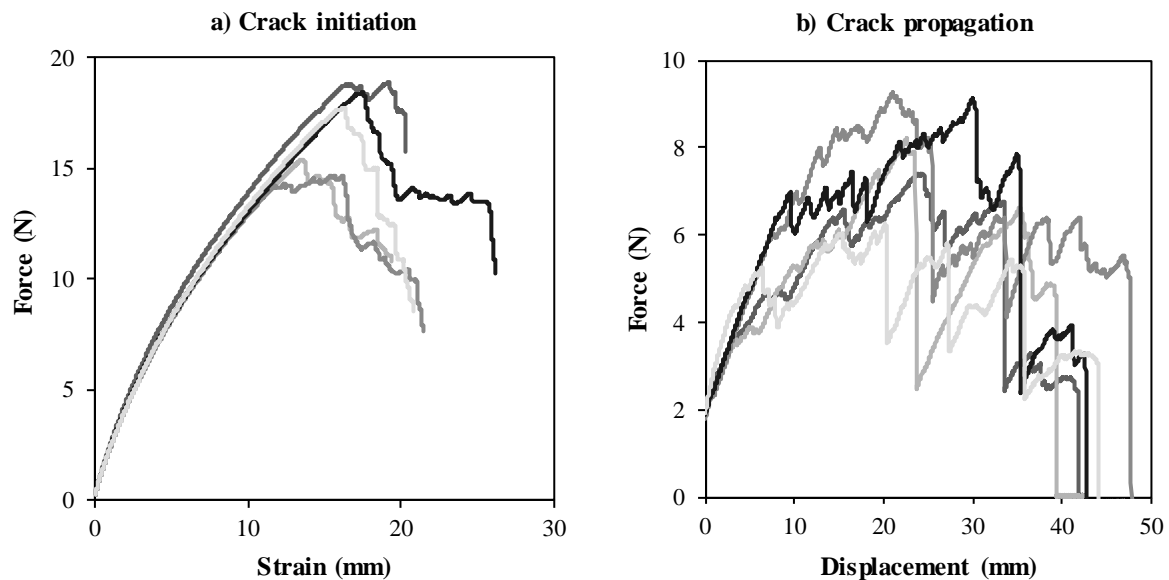
It can be seen from figure above that the two set of curves are similar in shape and failure occurred in the same way. The UTS, YM, and EaB of parts from both sets were comparable to each other.

As discussed in Section 1.4.3 (page 20), the HSS part in the Norazman and Hopkinson study exhibits superior mechanical properties compared to an equivalent LS part due to the longer sintering time in HSS. However, as stressed in Section 4.2.1 (page 83), there is a trade-off between tensile properties and dimensional accuracy. This experiment had to consider both part strength and accuracy due to the high geometric complexity of parts manufactured, whereas previous studies only focussed on achieving the best mechanical strength. Even though the properties in Table 4-4 are lower than previously reported for HSS TPE, they are still within quoted range and are also comparable to the LS TPE210-S obtained by Vasquez (2012).



### 4.3.6 Tear Properties

Figure 4-11 depicts the force-displacement curves from two modes of tear testing – crack initiation (a, specimens 5) and crack propagation (b, specimens 6).



**Figure 4-11** a) Crack initiation and b) crack propagation curves of untreated TPE specimens

From Figure 4-11, it can be seen that the parts failed in the same mode, as the curves were all similar in shape. The curves were grouped together, which suggests a good consistency within the build. The calculated tear properties are shown in Table 4-5.

**Table 4-5** Tear properties of untreated TPE specimens

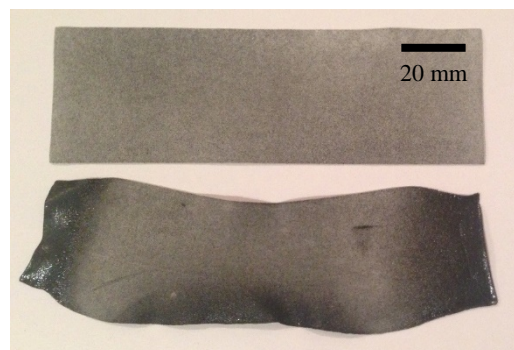
<b>Tear properties</b>	<b>Value</b>
Average tear strength	$6.09 \pm 0.26$ kN/m
Average tear force	$6.36 \pm 0.38$ N

The TPE specimens exhibited good average tear strength and the value was slightly higher than the manufacturer-claimed for LS (6 kN/m). As an elastomer, however, the tear strength is lower than both silicone (10 kN/m) and rubber (20 kNm). It can be seen from Figure 4-11b that the crack did not propagate at a steady rate. This type of crack propagation can be characterised as knotty (or stick-slip) instead of smooth. Gent and Kim (1978) reported that a knotty tear is inherent in filler-reinforced elastomers, especially if the filler is carbon black. Donnet (1993) summarised the effect of carbon black on the reinforcement of amorphous polymers, evidently through enhancing the molecular orientation of the polymer in a stress-strain field.

#### 4.4 Effect of PUSH Process on the Physical and Mechanical Properties of High Speed Sintered TPE

The main goal of the PUSH process is to improve the surface quality of HSS parts by reducing their surface roughness. However, it is crucial to ensure that this aesthetics improvement is not being achieved at the expense of other part properties, especially mechanical properties. In order to investigate the effect of PUSH on physical properties, half of each set of test specimens were measured, finished with PUSH process then remeasured. The mechanical properties of PUSH parts were directly compared to untreated parts, as it was impossible to repeat destructive testing on the same specimen.

As a new technique, the process has its limitation on the size and geometry suitable for treatment, due to its current application method and setup. It is not yet capable of achieving successful smoothing with thin structures. Five samples from specimen 1, which had an average thickness of 0.8 mm, were damaged during the smoothing process. Figure 4-12 depicts the transformation of the damaged specimen 1, where the top specimen in the picture is the original and the bottom specimen is PUSH treated.



**Figure 4-12** Damaged PUSH test specimen 1 (bottom) compared to the original specimen (top)

It can be seen that the treatment distorted the shape of the specimen. The high surface area of the specimen also made it difficult to obtain an even application of the chemical. As a result, PUSH specimens 1 were excluded from this study, and only results for PUSH specimens 2 – 6 were discussed in this section. The test results for the PUSH specimens are first presented separately before a comparison is made with respective initial results from Section 4.3 (page 85).

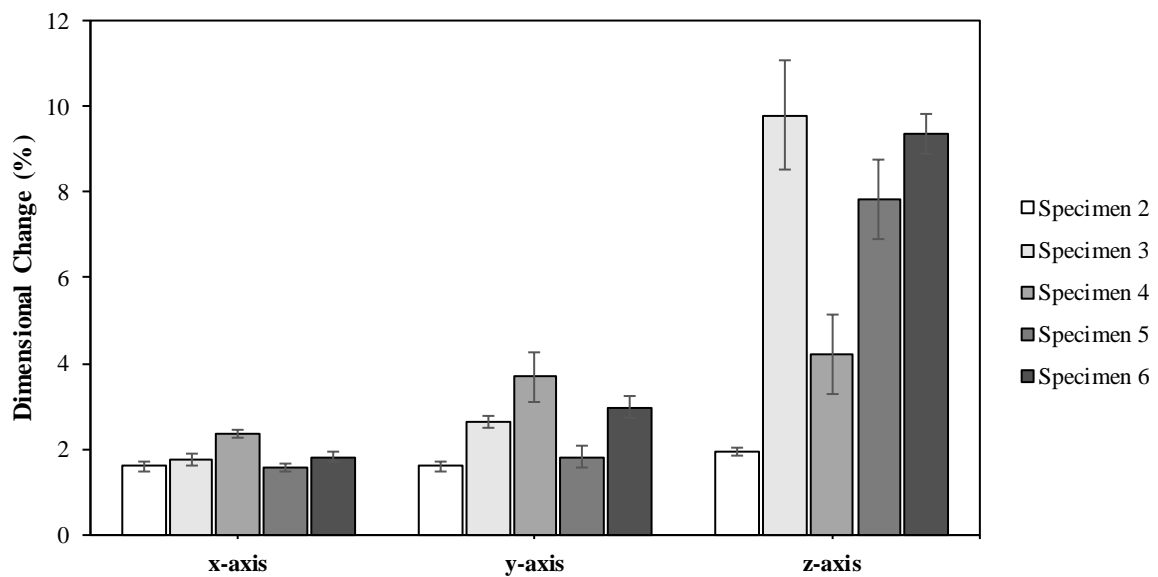
#### 4.4.1 Part Dimensions

The average dimensions of five PUSH specimens from each specimen type are presented in Table 4-6 below.

**Table 4-6** Dimensions of PUSH TPE specimens

Specimen	PUSH Dimensions (mm)		
	x	y	z
2	26.96	26.96	12.04
3	114.24	24.65	2.25
4	60.90	9.58	3.47
5	98.43	18.79	2.64
6	138.03	15.02	2.17

In order to assess the dimensional changes caused by the PUSH process, the dimensions of the PUSH parts were compared against their initial values from Table 4-2. Figure 4-13 illustrates the dimensional changes, expressed in percentage, for each specimen in x-, y- and z-directions.



**Figure 4-13** Effect of PUSH on the physical dimensions of TPE specimens ( $\pm 1$  SE)

A negative dimensional change was observed for all specimens in all directions. The magnitude of change was lowest along x-direction, averaging around 2 %, followed by y-direction and highest in z-direction with up to 11 %.

Specimens 2 and 4 experienced a consistent reduction in size across all axes. On the other hand, the dimensional change in specimens 3, 5, and 6 were more random across the different axes. The high error along z-direction can be caused by the non-symmetrical way of which the treatment was applied, and can be improved by introducing a better setup.

The difference in the degree of dimensional change can be attributed to the geometry of the test specimens. Specimens 2 and 4 are compact in shape, whereas specimens 3, 5 and 6 are more slender with bigger surface areas. The solvent polishing process works by minimising the surface area of a part by dissolving and reflowing the material. Therefore, parts with lower surface areas are more favourable to receive a uniform PUSH treatment across all directions.

The dimensional change in a part indicates the removal of its top surface layers as part of the mechanism of PUSH process. Loose unsintered powder tend to cling more on the top and bottom surfaces of a specimen (xy-plane) due to the direction of powder compaction and layer lamination. These powder particles are more easily dissolved than the sintered powder that form the specimen, which might explain the greater dimensional change along z-direction. This mechanism is further supported by the colour transformation of a PUSH part. The excess powder is dissolved into a translucent glossy layer, revealing the darker colour on the inside of a part, which originated from the black pigments in the ink (see Figure 4-14).



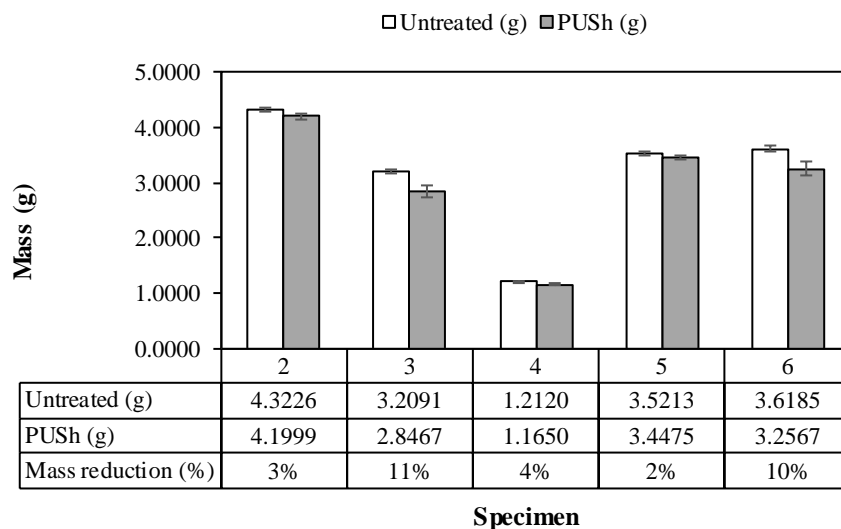
**Figure 4-14** The cross-sectional view of a PUSH specimen 2 (left) and an untreated specimen 2 (right)

Ideally, it is desirable to have a surface treatment that maintains a part's dimensions. The dimensional change caused by the PUSH process further reduces the dimensional accuracy of parts along x-direction. However, in the y-and z-directions, the size reduction helps to compensate for the wall growth. If the dimensional change is reproducible in every PUSH

application, then an appropriate scaling factor can be applied when manufacturing parts subjected to the PUSH process to compensate for the dimensional loss.

#### 4.4.2 Mass

A change in specimen mass was measured in place of a change in specimen volume, which was more difficult to measure. Figure 4-15 compares the average mass of TPE specimens before and after the PUSH process.



**Figure 4-15** Effect of PUSH on the mass of TPE specimens ( $\pm 1$  SE)

Based on Figure 4-15, the mass of specimens was reduced between 2 and 11 percent. The two specimens with the highest mass changes, specimens 3 and specimens 6, also had the highest dimensional changes. An unpublished study showed that no chemical residue was left in the specimen after the PUSH process. It is possible that mass loss occurs while handling the parts when wet, for example, when transferring the parts from the application area to the drying area. Wet handling can lead to the dissolved material sticking to the support or other apparatus.

#### 4.4.3 Surface Roughness

The PUSH process was chiefly developed to overcome the poor surface roughness of parts manufactured by powder bed fusion AM processes. In this section, the effectiveness of PUSH process is measured. The average roughness on the bottom and top surfaces of PUSH specimens are compared against untreated specimens. Figure 4-16 shows the  $R_a$  values while Figure 4-17 shows the  $R_z$  values.

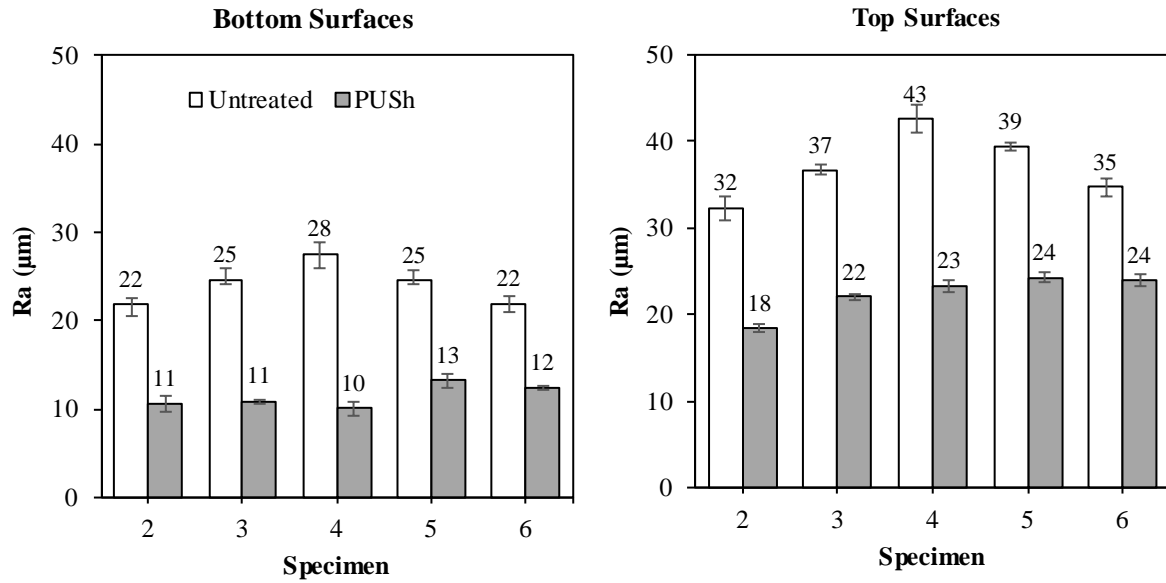


Figure 4-16 Effect of PUSH on the  $R_a$  of TPE specimens ( $\pm 1$  SE)

The effect of PUSH process is highly significant in Figure 4-16. The process reduced  $R_a$  values on both surfaces by an average of 50 %. The treatment offered a more aesthetically pleasing part, where the surfaces are smooth and not fuzzy to the touch.

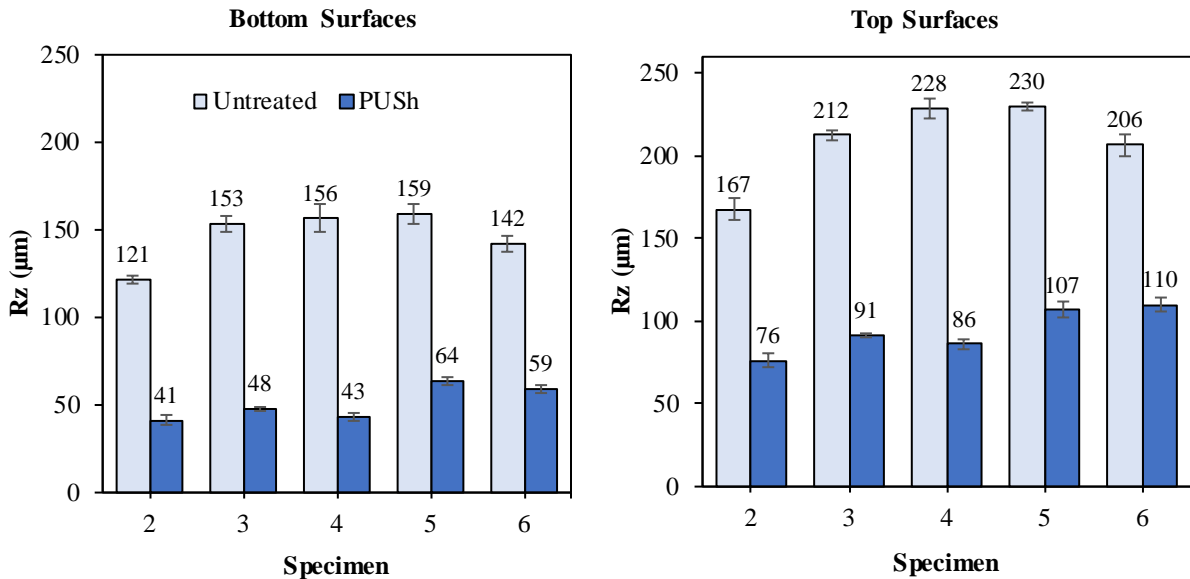
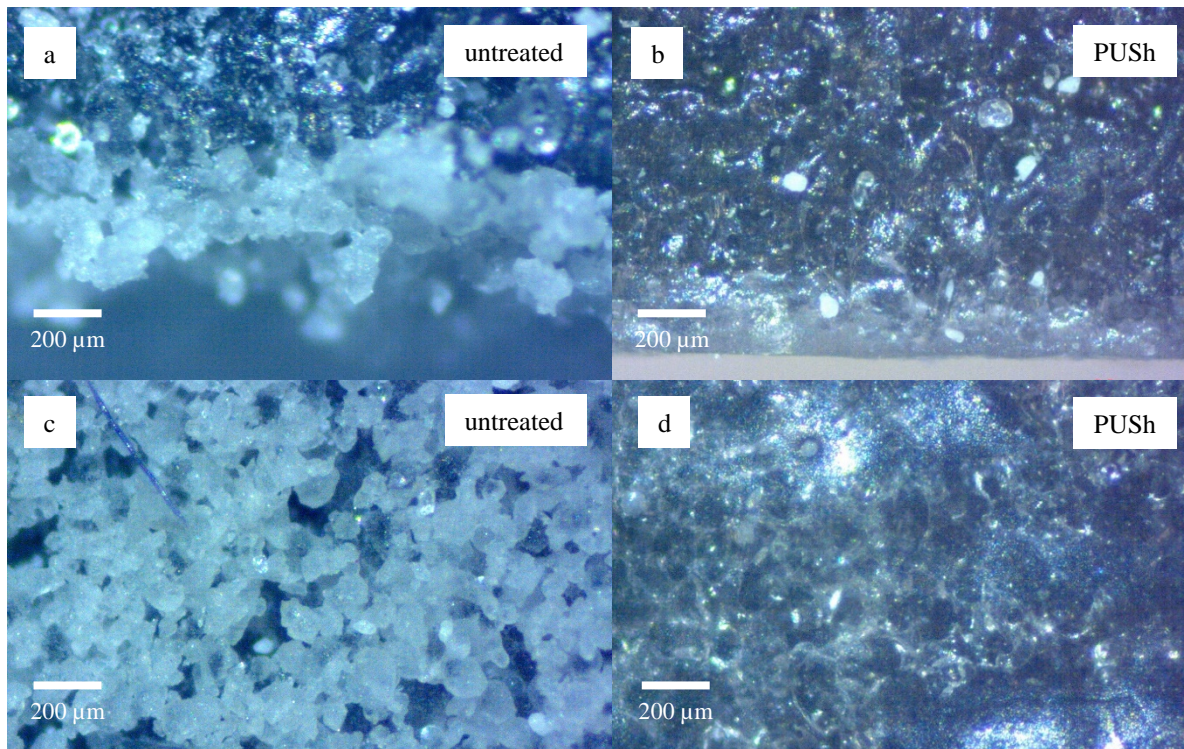


Figure 4-17 Effect of PUSH on the  $R_z$  of TPE specimens ( $\pm 1$  SE)

The  $R_z$  values of PUSH specimens were similarly lowered, at even a higher rate than the  $R_a$ . The  $R_z$  values dropped by at least 50 % in both surfaces. This pronounced decrease can be explained by the removal of the extreme peaks that originally contributed to the high  $R_z$ .

In order to validate the postulation of PUSH mechanisms discussed above, optical microscopy was performed on the specimens to observe the transformations on part surface. The images are presented below.

Figure 4-18a and Figure 4-18b are cross-sectional views at the edge of the specimens, while Figure 4-18c and Figure 4-18d are plan views of the specimens' bottom surfaces.



**Figure 4-18** Optical microscope images of untreated (a & c) and PUSH (b & d) specimens

Figure 4-18a and Figure 4-18c reveal the powder particles (white) that fused to the sintered part surface (black). The irregular height of the powder cluster contributed to the extreme profiles in  $R_z$ . The great transformation from a) to b), and similarly from c) to d), shows how the chemical treatment completely dissolved the excess powder layer.

Low surface roughness values represent smooth surfaces and are desirable in manufacturing consumer products. The achieved values in Figure 4-16 and Figure 4-17 are still inferior in the manufacturing industry environment. As a comparison, an injection moulded plastic has an achievable  $R_a$  of  $1 \mu\text{m}$  (Bacchewar et al., 2007). In order to improve surface roughness, AM powder needs to be produced through polymerisation and not cryogenic grinding, as the latter method forms non-spherical powder particles with jagged edges.



#### 4.4.4 Hardness

Table 4-7 summarises the average Shore A hardness of PUSH TPE specimens.

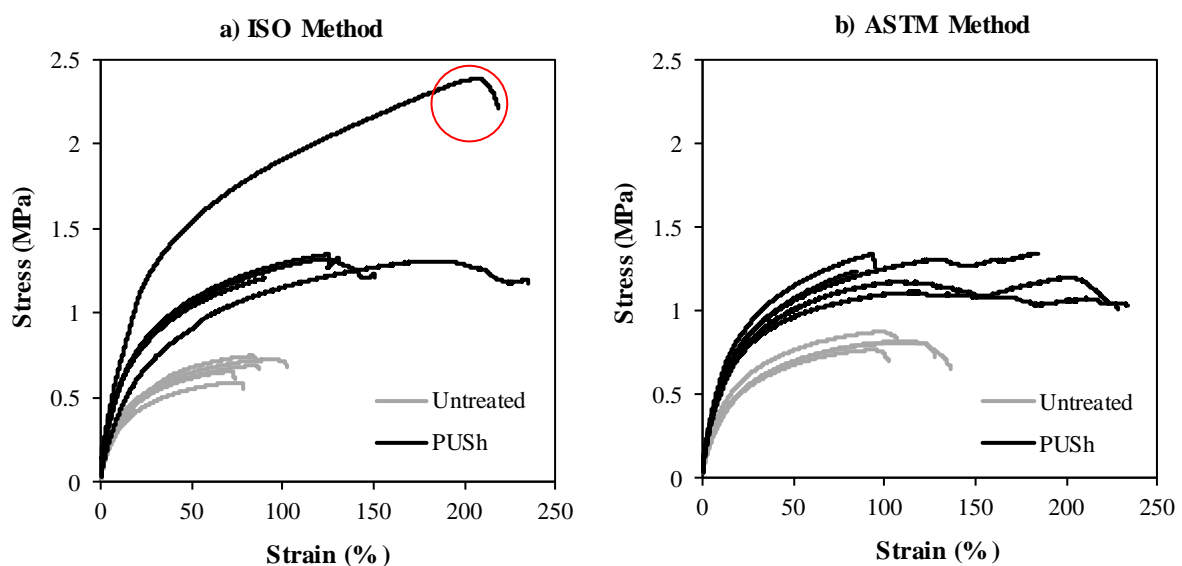
**Table 4-7** Shore A hardness of PUSH TPE specimens

Specimen	Shore A hardness
2	$53 \pm 0.2$
3	$60 \pm 1.3$
4	$57 \pm 0.3$
5	$59 \pm 0.5$
6	$58 \pm 0.5$

In comparison with the values listed in Table 4-3, a consistent increment of one was observed for all specimens. Considering hardness is a material characteristic, no change was to be expected on the account of post-processing. The slight change can be attributed to the high error associated with the test method itself, where the effect of viscoelasticity in polymers is too dominant to generate a meaningful hardness data. The change is disregarded and it can be assumed that the PUSH process does not affect the Shore A hardness of specimens.

#### 4.4.5 Tensile Properties

Figure 4-19 shows the stress-strain curves of PUSH TPE against untreated specimens, obtained through two different tensile test methods.



**Figure 4-19** Effect of PUSH on the tensile properties of TPE specimens using a) ISO method and b) ASTM method



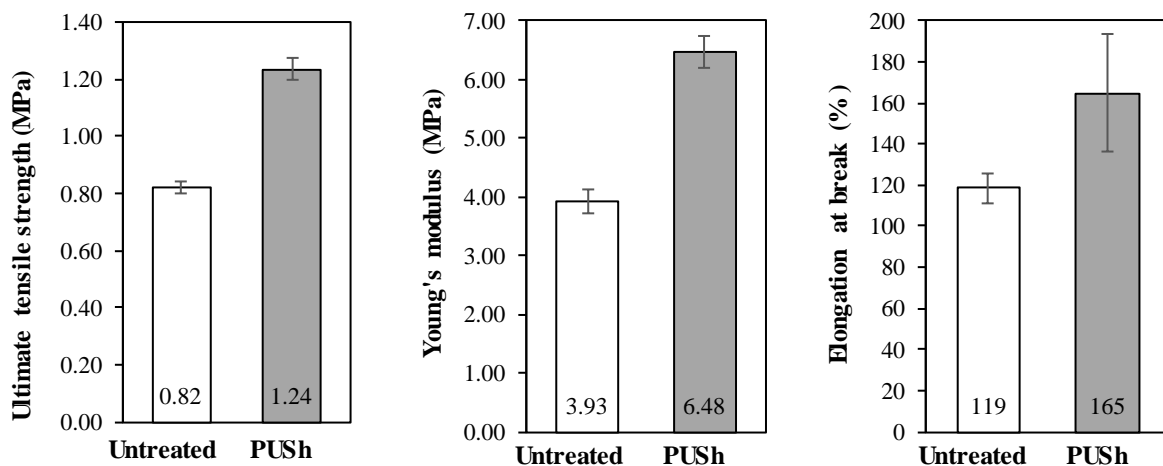
By disregarding one PUSH curve from specimen 3 as an outlier (circled), it can be seen that the curves from the two test sets are very similar in shape. The brittle failure of the untreated specimens in Figure 4-19a reflects the amorphous chain configuration of TPE210-S. On the other hand, the PUSH specimens seem to be sufficiently ductile to exhibit necking and experience a delayed fracture.

The tensile properties were highly improved through the PUSH process. Table 4-8 summarises the UTS, E, and EaB values for each tensile set.

**Table 4-8** Tensile properties of PUSH TPE specimens

Tensile Properties	Test Method	
	ISO	ASTM
UTS (MPa)	1.52 ± 0.19	1.24 ± 0.04
E (MPa)	6.77 ± 0.83	6.48 ± 0.27
EaB (%)	165 ± 24	165 ± 29

ASTM tensile test method is more widely used in the literature, and in this experiment, the ASTM method also incurred lower error. Therefore, only the ASTM tensile values were considered for the comparison between untreated and PUSH specimens shown in Figure 4-20.



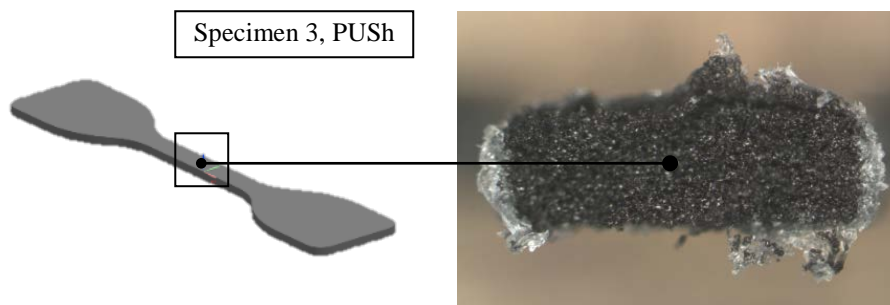
**Figure 4-20** Effect of PUSH on the UTS, E and EaB of TPE specimens ( $\pm 1$  SE)

The results showed that the average UTS for PUSH specimens was greater than the untreated by 51 %. The PUSH specimens were also stiffer, with a modulus greater by 64 % than the untreated. Similar trend can be observed with EaB where it was improved by 38 % in PUSH specimens. The similar results between the two set of specimens agree with Majewski and

Hopkinson (2011) study that section thickness does not affect the tensile properties of parts. By testing bigger specimens, however, the error that stems from measurement accuracy can be minimised.

As discussed in Section 4.3.1 (page 85), untreated TPE specimens 3 and 4 were oversized in y- and z-directions, which is where the cross sectional area of a tensile test piece is measured. A percentage of this wall growth is present in terms of layers of loose fused powder over the sintered part as illustrated in Figure 4-18a. This suggests that the linear dimensional measurements and consequently area determinations of these specimens include these excess powder layers to obtain what is deemed as an “apparent area”. The “apparent area” can be defined as the sum of area exclusively made of sintered material and the area generated by the layers of loose fused powder on top of the sintered material. As the “apparent area” is higher than the actual area of the sintered material, the tensile specimen therefore has a high area but low in volume/density, likening it to a porous structure. Since engineering stress is obtained by dividing the force with initial area, this error in measurement results in a lower stress value.

After PUSH application, the excess powder layers on a part surface are mostly dissolved by the solvent. This leaves behind a structure made up of the sintered powder and carbon black (grey) in the middle and a layer of dissolved powder (translucent), as shown in Figure 4-21. It is possible that the skin formed by the PUSH process acts as a protective layer, which improves the elasticity of the specimen during tensile testing.



**Figure 4-21** Cross-sectional view of a fractured PUSH specimen

Alternatively, the size reduction from the PUSH process yields a specimen with dimensions closer its nominal dimensions, therefore the measured area is now exclusively made of sintered material. Hence, the tensile test measured the real strength of the sintered material without the added error from unsintered powder.

#### 4.4.6 Tear Properties

Figure 4-22 and Figure 4-23 present the tear properties of TPE before and after PUSH. The tear curves illustrate the change in tear forces and tear profiles. The bar charts compare the magnitude of tear strength and average tear force between the untreated and PUSH specimens.

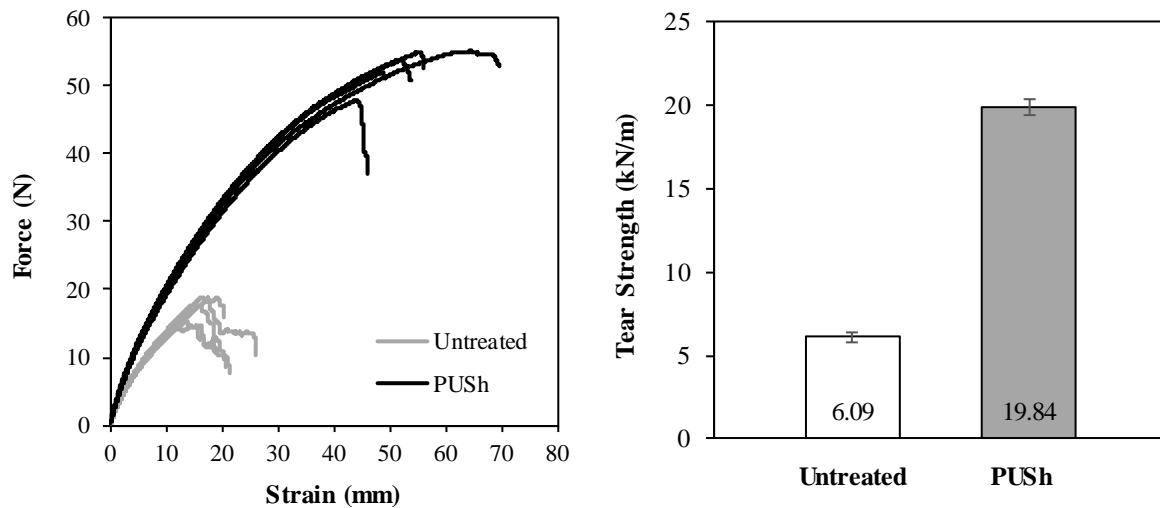


Figure 4-22 Effect of PUSH on crack initiation in TPE specimens ( $\pm 1$  SE)

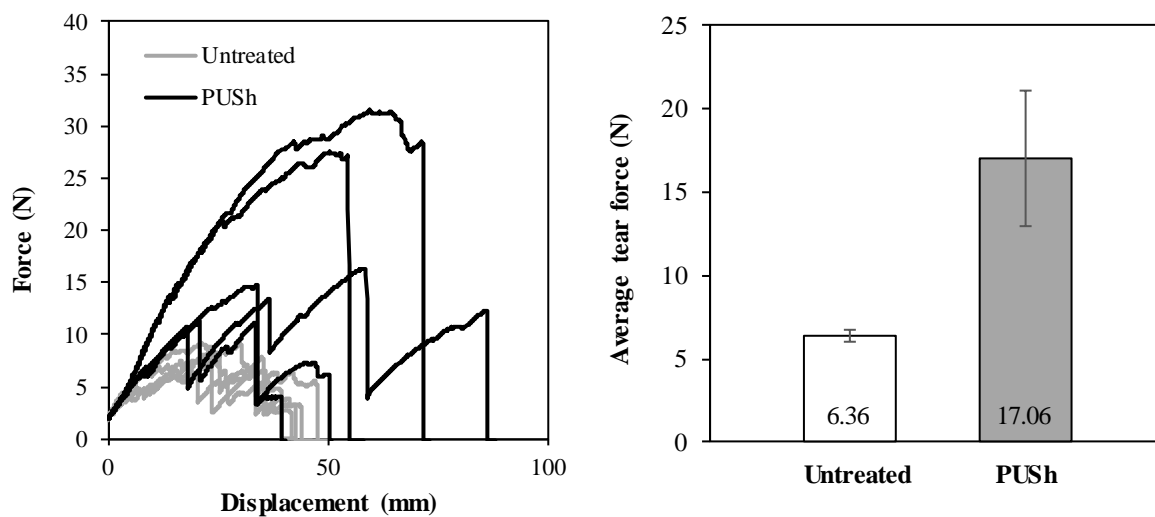


Figure 4-23 Effect of PUSH on crack propagation in TPE specimens ( $\pm 1$  SE)

Figure 4-22 shows that a higher force was required to initiate tear in a PUSH specimen. The crack propagation profile was consistently knotty, but with a higher tear force. The tear strength of PUSH specimens was superior by 225 % and the average tear force by 168 %, implying that the PUSH process had enhanced the tear properties of TPEs. Similar reasoning discussed in Section 4.4.5 can be used to explain the improvement of tear properties in PUSH specimens.

## 4.5 Cost Estimation for HSS High Volume Production

This section evaluates the suitability of HSS machines to be used commercially for high volume manufacturing. This was achieved by projecting production volume and developing a cost model to estimate the cost per part in a high volume production setting. The existence of economies of scale in AM as suggested by Baumann et al. (2016) puts HSS at an advantage. The HSS build volume is highly scalable and its production speed is already disruptive amongst other AM processes.

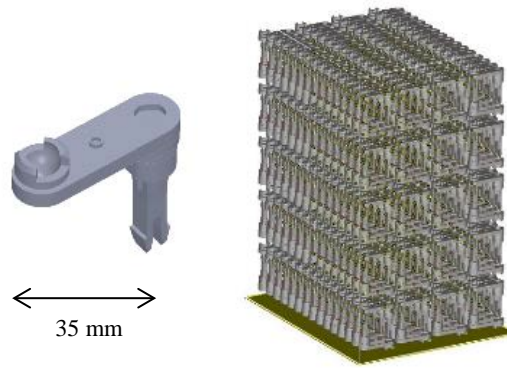
This cost model is developed based on the Hopkinson and Dickens (2003) cost model for rapid manufacturing processes and Ruffo et al. (2006) cost model for LS. This is the first cost model developed for HSS to assess its commercial viability. Only one cost category (HSS material cost) was specifically formulated in this research. Other cost categories were refined from the Hopkinson and Dickens model, and updated with current values.

The goal of this study is to compare the cost per part made using HSS against LS. The cost model is applied to six machines from three different size categories, which are small, medium, and large. The LS machines are EOS Germany commercial printers. The HSS machines are speculative printers that will be released in the market in the future. Table 4-9 shows the details of each machine.

**Table 4-9** Details of the HSS planned production systems and LS commercial systems used in the cost analysis

Type of Process	Machine Size, Name, and Bed Dimensions (mm)		
	Small	Medium	Large
High Speed Sintering	Projected 200 x 200 x 200	Projected 400 x 625 x 625	Projected 500 x 800 x 800
Laser Sintering	EOS P110 200 x 250 x 330	EOS P395 340 x 340 x 620	EOS P760 700 x 380 x 580

The part selected for the cost analysis is the same as used in the above literature. The part is a small lever that has a 35 mm length and measures 4.30 cm<sup>3</sup> in part volume. Figure 4-24 illustrates the lever part alongside an example of how the parts are duplicated and nested on the build bed using Materialise Magics software.



**Figure 4-24** The lever part used in the cost analysis and 600 parts nested on a LS EOS P110 build platform

The part costs can be broken down into four main categories. The cost categories are machine, production overhead, production labour and material costs. Table 4-11 – Table 4-14 list the cost model elements for each cost category and the summation of costs. All monetary cost data used in this research are expressed in euro (€) with an exchange rate £/€= 1.17.

Table 4-10 summarises the machine production parameters. The number of parts per build is obtained by nesting the parts with a 2 mm vertical and horizontal gap on each machine platform. The layer cycle time in HSS is constant per layer height and the build time is worked out by multiplying the layer cycle time with the number of layers.

**Table 4-10** HSS cost analysis - machine and build details

<b>Machine and build details</b>	<b>Notation</b>	<b>Details</b>
Build bed dimensions	<i>BD</i>	Volume of machine build platform (width × depth × height)
Number of parts per build	<i>N</i>	Obtained from nesting parts in Materialise Magics software
Build time	<i>T</i>	From EOS build time estimator (LS) or projected using layer cycle time (HSS)
Production rate per hour	<i>R</i>	$N / T$
Machine utilisation	<i>P</i>	Machine up time
Hours per year in operation	<i>H</i>	365 days x 24 hours/day x <i>P</i> % = 7,884 hours
Production volume total per year	<i>PV</i>	$R \times H$
Machine depreciation	<i>D</i>	Machine and equipment life time

The detailed breakdown of machine costs is presented in Table 4-11.

**Table 4-11** HSS cost analysis - machine costs

<b>Machine costs</b>	<b>Notation</b>	<b>Details</b>
Machine purchase	<i>M</i>	Cost of machine purchase
Machine purchase cost per year	<i>MY</i>	$M / D$
Machine maintenance per year	<i>MMY</i>	Covers preventive maintenance visit, repair work, spare and wearing parts
Software purchase per year	<i>SY</i>	Cost of purchase and renewal of Magics Materialise software licence
Hardware purchase	<i>E</i>	Cost of bead blaster and powder processing equipment
Hardware purchase cost per year	<i>EY</i>	$E / D$
Total machine cost per year	<i>TMY</i>	$MY + MMY + SY + EY$
Machine cost per hour	<i>MCH</i>	$TMY / T$
Machine cost per part	<i>MCP</i>	$MCH / R$

The machine costs include the purchase of machine, software, and hardware spread over the machine's lifetime. Machine maintenance is provided by the manufacturer as an annual service contract. The number of software licences and equipment required are subject to the size of the business. Machine cost per part is determined by dividing the annual cost with production rate.

The method for calculating production overhead cost is shown in Table 4-12.

**Table 4-12** HSS cost analysis - production overhead costs

<b>Production overhead costs</b>	<b>Notation</b>	<b>Details</b>
Yearly rent rate per m <sup>2</sup>	<i>RY</i>	Building rent inclusive of bills
Building area	<i>A</i>	Recommended installation area for one machine and relevant equipment
Total rent per year	<i>RT</i>	$RY \times A$
Consumables per year	<i>C</i>	Consumables cost
Energy consumption per hour	<i>PH</i>	Machine and equipment electricity usage
Production overhead per hour	<i>OCH</i>	$((RT + C) / H) + PH$
Production overhead cost per part	<i>OCP</i>	$OCH / R$

The rental cost is computed based on the rental cost of a space in an industrial business park. Consumables include office stationeries and personal protective equipment. The electricity cost is estimated from machine and equipment power consumption and the size of business, based on the guideline provided by the Department for Business (2017).

Table 4-13 relates the part build time from start to finish to its associated labour costs.

**Table 4-13** HSS cost analysis - production labour costs

<b>Production labour costs</b>	<b>Notation</b>	<b>Details</b>
Machine operator cost per hour	$O$	Annual salary of machine operator divided by operation hours
Set-up time	$TS$	Machine warm up and file preparation
Post-processing time per build	$TP$	Post-processing time per part $\times N$
Labour cost per build	$L$	$O \times (TS + TP)$
Labour cost per part	$LCP$	$L / N$

The operator salary is calculated based on the University of Sheffield's pay grade level 5. Set-up time covers prepping the machine with powder feed and preparing the build files in relevant software packages. The powder removal time is approximated at 30 seconds per part.

Calculations of production overhead, production labour and machine costs are identical for both HSS and LS machines. Material costs are formulated differently due to the addition of ink in HSS. Table 4-14 shows the calculation for LS material costs.

**Table 4-14** HSS cost analysis - LS material costs

<b>Material costs for LS</b>	<b>Notation</b>	<b>Details</b>
Powder cost per kg	$PC$	Obtained from material supplier
Mass of each part	$W$	Mass of finished part
Volume of each part	$V$	Calculated in Magics software
Total build volume	$TBV$	Effective building volume
Recycling rate	$RR_{LS}$	Recycling rate of unsintered powder, 50 %
Powder density	$PD$	Density of bulk powder
Mass of sintered material per build	$MS_{LS}$	$N \times W$
Mass of unsintered material per build	$MU_{LS}$	$(TBV - V \times N) \times PD / 1000$
Cost of material used in one build	$MC_{LS}$	$(MS_{LS} + ((1 - RR_{LS}) \times MU_{LS}) \times PC)$
Material cost per part (LS)	$MCP_{LS}$	$MC_{LS} / N$

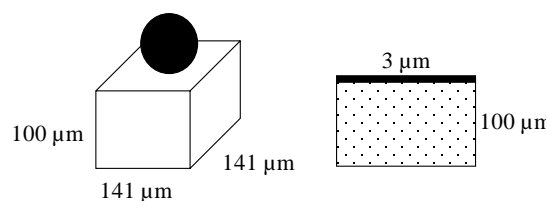
The references for powder cost and part volume are similar to that of HSS. However, the LS material costs are directly contributed by the powder cost. The recycling rate in LS is set lower than HSS, at 50 % due to the thermal degradation of the powder feed.

Table 4-15 shows the cost elements and material properties required to formulate the material cost per part for HSS machines.

**Table 4-15** HSS cost analysis - HSS material costs

Material costs for HSS	Notation	Details
Powder cost per kg	$PC$	Obtained from material supplier
Ink cost per litre	$IC$	Obtained from material supplier
Mass of each part	$W$	Mass of finished part
Volume of sintered powder per part	$V_P$	Part volume as calculated in Magics
Volume of printed ink per part	$V_I$	$3 \% \times V_P$
Total build volume	$TBV$	Effective build volume
Recycling rate	$RR_{HSS}$	Recycling rate of unsintered powder = 90 %
Powder density	$PD$	Density of bulk powder
Mass of sintered material per build	$MS_{HSS}$	$N \times W$
Mass of unsintered material per build	$MU_{HSS}$	$(TBV - (V_P \times N)) \times PD / 1,000$
Cost of material used in one build	$MC_{HSS}$	$(MS_{HSS} + ((1 - RR_{HSS}) \times MU_{HSS}) \times PC) + (V_I \times IC \times N) / 1,000$
Material cost per part (HSS)	$MCP_{HSS}$	$MC_{HSS} / N$

The raw cost of powder and ink provided by the material suppliers are €70.20/kg for PA12 or €12.20/kg for TPE, and €6.41 for ink. The sintered powder volume is the same as the part volume calculated in Magics software. The ink volume is determined as follows. The calculation is based on a Xaar Proton 60 print head with 60 pL droplet volume and 141 μm nozzle pitch. Figure 4-25 shows an ink droplet on a single voxel with a layer height of 100 μm. The height of an ink layer is obtained by dividing the droplet volume with the voxel area. The calculated ink height is 3 μm, which is three percent the total volume of the voxel/powder.



**Figure 4-25** Ink volume calculation



Recycling rate of unsintered HSS powder is approximated as 90 %, due to the low temperature used in HSS and as no negative effect was found from using recycling polymer powder (Plummer et al., 2012). Density of bulk PA12 powder is 0.475 g/cm<sup>3</sup>. The material cost per part is the total of sintered material cost, un-recyclable unsintered material cost and printed ink cost, divided by the number of parts per build.

Table 4-16 shows how to calculate the total cost per part.

**Table 4-16** HSS cost analysis - total cost per part

<b>Total cost per part (TCP) in euro</b>	<b>Formula</b>
HSS	$TCP_{HSS} = MCP + OCP + LCP + MCP_{HSS}$
LS	$TCP_{LS} = MCP + OCP + LCP + MCP_{LS}$

The total cost per part (*TCP*) for HSS and LS is given by the sum of machine cost per part (*MCP*), overhead cost per part (*OCP*), labour cost per part (*LCP*) and respective material cost per part (*MCP<sub>HSS</sub>* or *MCP<sub>LS</sub>*).

Table 4-17 gives an example of the cost analysis as performed on the small HSS machine. The unit cost calculation for other machines can be found in the Appendices.

**Table 4-17** An example of HSS cost per part calculation – HSS small machine

		<b>Unit</b>	<b>HSS Small (2013)</b>
<b>Machine parameters</b>	Build bed dimensions (W x D x H)	mm	200 x 200 x 200
	Number of parts per build		288
	Build time	h	5.55
	Production rate per hour	h <sup>-1</sup>	51.89
	Machine utilisation	%	80
	Hours per year in operation	h	7,008
	Production volume total per year		363,658
	Machine depreciation	year	8
<b>Machine costs</b>	Machine purchase	euro	80,000.00
	Machine purchase cost per year	euro	10,000.00
	Machine maintenance per year	euro	15,000.00
	Software purchase cost per year	euro	3,348.00
	Hardware purchase	euro	10,000.00
	Hardware purchase cost per year	euro	1,250.00
	Total machine cost per year	euro	29,598.00
	Machine cost per hour	euro	4.22
	Machine cost per part	euro	0.08
<b>Overhead costs</b>	Yearly rent rate per m <sup>2</sup>	euro	160.00
	Building area	m <sup>2</sup>	11.20
	Total rent per year	euro	1,792.00
	Consumables per year	euro	1,000.00
	Energy consumption per hour	euro	0.60
	Production overhead cost per hour	euro	1.00
	Production overhead cost per part	euro	0.02
<b>Labour costs</b>	Machine operator cost per hour	euro	11.20
	Set-up time to control machine	min	120
	Post-processing time per build	min	144
	Labour cost per build	euro	49.28
	Labour cost per part	euro	0.17
<b>Material costs</b>	Powder cost per kg	euro	70.20
	Ink cost per litre	euro	96.41
	Mass of each part	kg	0.0036
	Volume of sintered nylon per part	cm <sup>3</sup>	4.30
	Volume of printed ink per part	cm <sup>3</sup>	0.13
	Total build volume	cm <sup>3</sup>	8,000
	Recycling rate	%	90
	Powder density	g/cm <sup>3</sup>	0.475
	Mass of sintered material per build	kg	1.0368
	Mass of unsintered material per build	kg	3.2118
	Cost of material used in one build	euro	98.91
	Material cost per part	euro	0.34
<b>Total cost per part</b>		<b>euro</b>	<b>0.62</b>

Figure 4-26 plots the part cost for each machine (HSS and LS). These were compared to the costs reported by Hopkinson and Dickens (LS and injection moulding)<sup>a</sup> and Ruffo et al (LS)<sup>b</sup>.

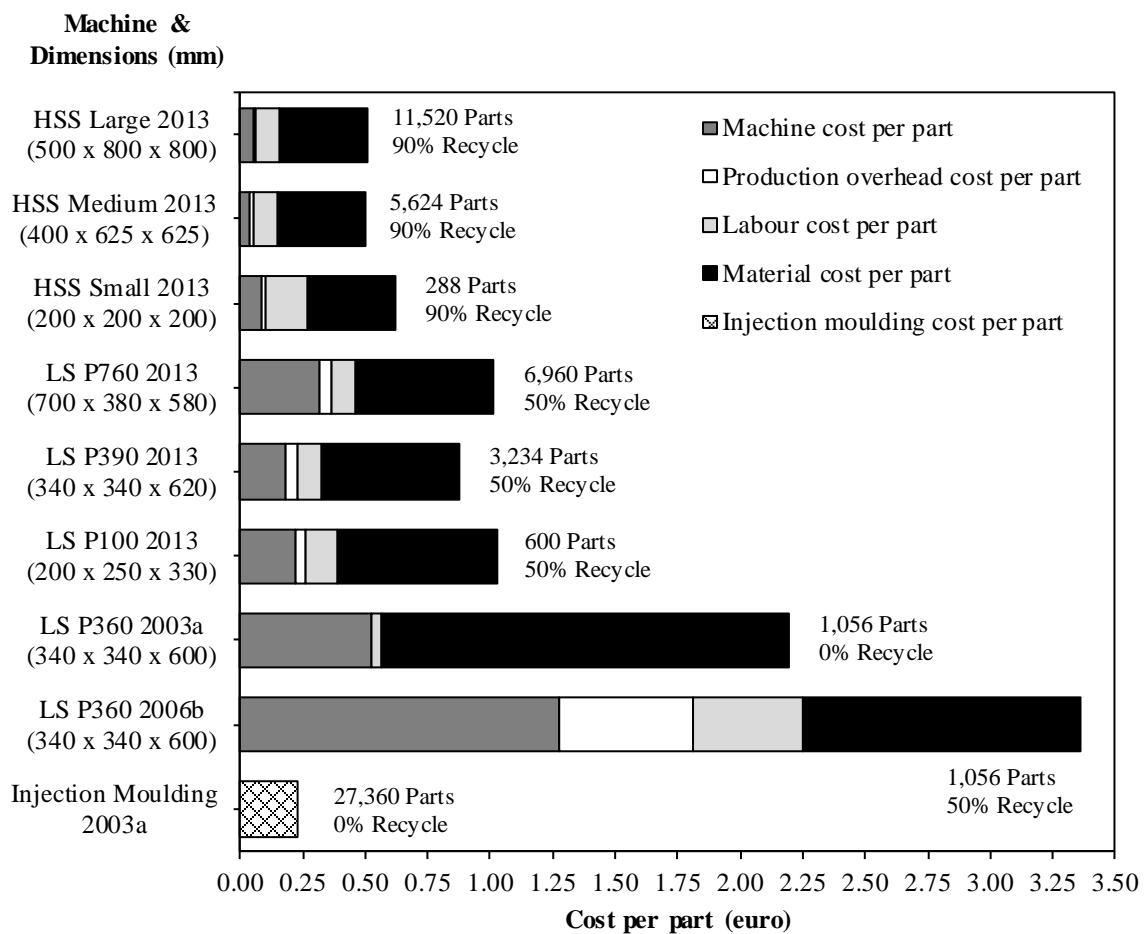


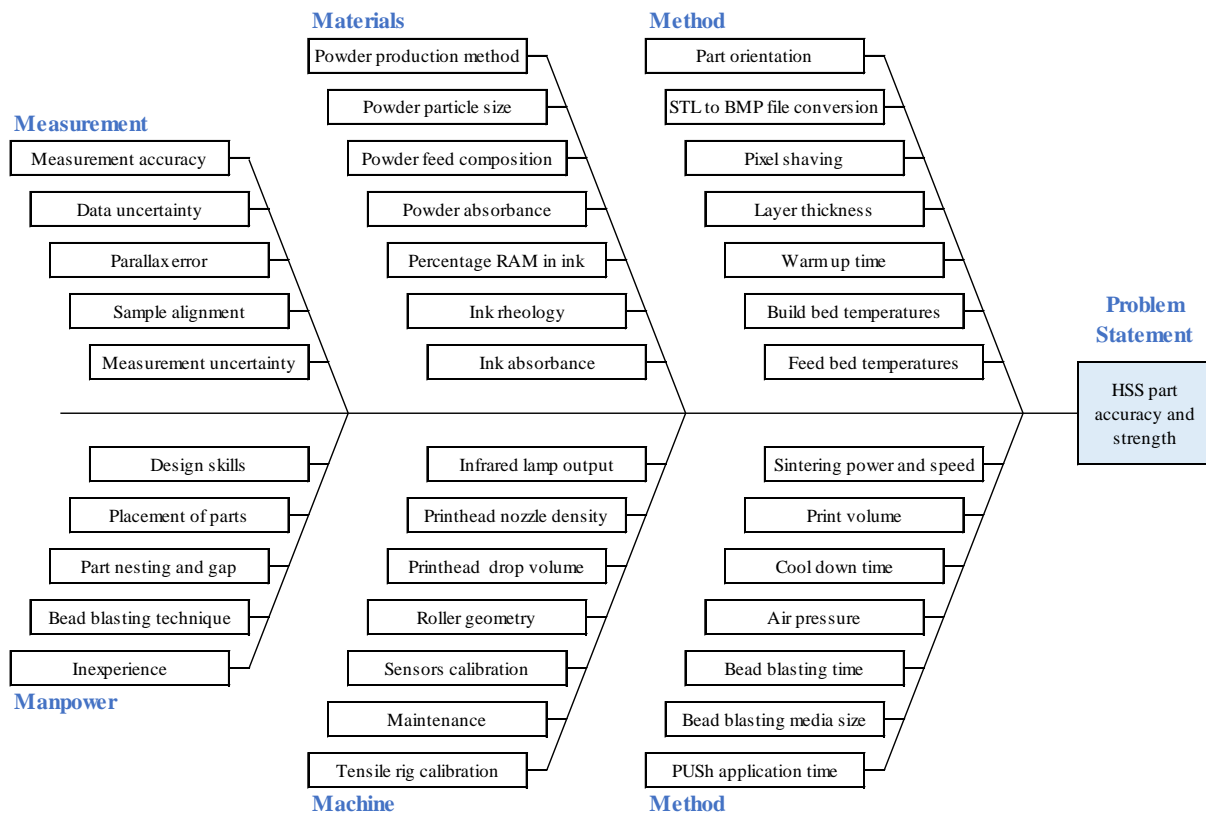
Figure 4-26 Comparison of cost per part between HSS and LS

The results showed that the cost per part for HSS was lower than for LS at all machine sizes. The cost for HSS reduced with increased machine size, but this was not the case for LS. In overall, material cost still dominated the part cost. In HSS, material cost per part was the highest contributor to the total cost, followed by labour, machine, and then overhead. In LS, however, the machine cost per part was higher than labour. The high material cost per part associated with Hopkinson and Dickens (2003) model stems from the absence of powder recyclability. They also did not consider any overhead cost, even though its effect would be minute.

The cost analysis proved that HSS parts could be manufactured at a low cost. However, the cost is still twice as high as the equivalent part made by injection moulding (IM). Taking into consideration the high cost of tooling in IM, HSS is still better suited for low volume production of personalised parts, especially parts with complex geometries that are unachievable using IM.

## 4.6 Influence of HSS Process Chain on the Dimensional Accuracy and Strength of HSS Parts

Figure 4-27 is the constructed fishbone diagram showing root causes along the HSS process chain that can affect final part accuracy and strength.



**Figure 4-27** Fishbone diagram showing the factors that contribute to HSS part properties

The main causes can be categorised into five, which are measurement, manpower, materials, machine, and method. The possible causes in each category are not in chronological order and can happen at any stage across the HSS process chain (pre-process, process, and post-process).

The measurement category covers causes associated with data measurement and measurement techniques. The need for accurate data measurement is crucial when dealing with fine features and tolerances. Errors in measuring finished parts, for example in linear dimensional measurements and tensile tests, can directly affect the calculation of part accuracy and strength. The selection of measurement tools is also of importance to obtain high accuracy and precision.

The manpower category concerns the skills possessed and techniques used by the HSS part designer and machine operator. The designer needs to factor in the machine and software

capability when designing parts to be printed on the HSS machine. The different approach taken in AM means that the design methodology used for other manufacturing techniques needs to be optimised for AM. This includes the skills required to design parts with the correct fit and tolerance, applying lattice structures, creating appropriate channels for removal of powder cake and so on. The operator's experience in preparing the powder feed and retrieving the part from a powder cake is particularly critical to the finished part properties. Shared responsibilities between the designer and operator include nesting of parts and their placements on the build bed, which if done incorrectly can induce thermal stresses and cause part distortions.

The materials category focuses on the fundamentals of polymer sintering and its behaviour. The constituents are feed powder and ink, and their characteristics. Powder characteristics include the method of powder production, which determines the shape of the powder particles. The ink's capillary action during printing influences the print resolution and ink bleeding fuses undesired powder, which results in difficult powder removal and low dimensional accuracy.

The machine category mainly comprises the HSS machine and its employed equipment. This includes the mainframe, sintering lamp, printhead and ink delivery system, roller, and electronics. The lamp energy output combined with the ink drop volume makes up the energy supplied to the underlying powder. Roller geometry affects powder spreading and compaction which in turns affect relative powder density (Shanjani and Toyserkani, 2008). Regular maintenance and calibration of equipment, for example the infrared camera and sensors, are essential to ensure validated process control and monitoring are in place.

The root causes in the method category are critical to the part properties as they cover the methods used in the pre-processing, processing and post-processing stages in HSS. When preparing and converting build files, feature resolutions may be lost from one software to another. This problem needs to be addressed by software developers to generate a seamless software to hardware system. The selection of machine parameters definitely plays an important role in mitigating wall growth and shrinkage phenomena. In post-processing stage, a range of surface finish can be achieved through the bead blasting process, depending on the duration of cleaning and selection of media. There is no standard in place to achieve repeatability across all samples and operators.

This root cause analysis pinpoints the area within HSS that needs improving. The subsequent part of this thesis will now focus on a few important causes; specifically the IR lamp output

and ink volume to measure their effects on part quality. Ink and powder absorbance will be incorporated to establish a material guideline to produce high quality high speed sintered parts.

## 4.7 Summary

TPE210-S powder is an amorphous material with gradual softening and hardening temperature regions. The properties of high speed sintered TPE are detailed as follows. The parts had the highest dimensional accuracy in z-direction and lowest in x-direction (printing direction). The dimensional accuracies were determined as 2.0 mm in x- and y-directions, and 0.5 mm along z-direction. The specimens had low  $R_a$  and high  $R_z$ , which implied a smooth profile with extreme peaks. The bottom surfaces were smoother than the top. Shore A hardness was measured between 50 – 60 for all specimens. Tensile properties (UTS, E and EaB) were lower than literature high speed sintered TPE due to lower input energy but matched the laser-sintered equivalent. The specimens had a low tear strength and knotty crack propagation.

The PUSH post-processing improved aesthetics and strength at the expense of dimensional change. The process forms a film surrounding the treated parts. All specimens' dimensions changed by an average of 2 %, 3 %, and 7 % in x-, y-, and z-directions respectively. The overall dimensional change was below 10 %. The average specimen mass was reduced between 2 to 11 % because of the volumetric change. Surface roughness was significantly improved, where  $R_a$  and  $R_z$  were reduced by an average of 50 %. There was a negligible change in Shore A hardness. In tensile properties, PUSH parts had a 51 % higher UTS, 64 % higher E, and 38 % higher EaB compared to untreated parts. The average tear strength of PUSH specimens was 225 % higher than the untreated; meanwhile the average tear force was 168 % higher.

The cost per part manufactured using HSS was lower than LS. In HSS, the importance of cost category in decreasing order was material, labour, machine, and overhead. In LS, it was material, machine, labour, and overhead. The attractive cost of HSS secures its commercial viability, on the premise that part quality can be improved.

The consequential parameters in HSS were mapped out in the root cause analysis. The analysis pinpointed areas in HSS that need improving in order to boost the dimensional accuracy and strength of parts, two of which were powder removal and energy input.

The following chapter discusses the effect of two main parameters that contribute to energy input, which are lamp power and ink volume, on the finished part properties.

## 4.8 References

1. Bacchewar, P. B., Singhal, S. K. & Pandey, P. M. 2007. Statistical modelling and optimization of surface roughness in the selective laser sintering process. *Proceedings of the Institution of Mechanical Engineers, Part B: Journal of Engineering Manufacture*, 221(1), 35-52.
2. Baumers, M., Dickens, P., Tuck, C. & Hague, R. 2016. The cost of additive manufacturing: machine productivity, economies of scale and technology-push. *Technological Forecasting and Social Change*, 102(1), 193-201.
3. Department for Business, Energy & Industrial Strategy. 2017. Prices of fuels purchased by manufacturing industry.
4. Dimitrov, D., Wijck, W. v., Schreve, K. & Beer, N. d. 2006. Investigating the achievable accuracy of three dimensional printing. *Rapid Prototyping Journal*, 12(1), 42-52.
5. Donnet, J. B. 1993. *Carbon Black: Science and Technology, Second Edition*, USA, Taylor & Francis.
6. Ellis, A., Brown, R. & Hopkinson, N. 2015. The effect of build orientation and surface modification on mechanical properties of high speed sintered parts. *Surface Topography: Metrology and Properties*, 3(3), 034005.
7. Gent, A. N. & Kim, H. J. 1978. Tear Strength of Stretched Rubber. *Rubber Chemistry and Technology*, 51(1), 35-44.
8. Grimm, T. 2004. *User's guide to rapid prototyping*, USA, Society of Manufacturing Engineers.
9. Hartley, L. 2014. *Investigating the effect of print density/greyscale on High Speed Sintered elastomer products' mechanical properties*. Masters Thesis, The University of Sheffield.
10. Hopkinson, N. & Dickens, P. 2003. Analysis of rapid manufacturing—using layer manufacturing processes for production. *Proceedings of the Institution of Mechanical Engineers, Part C: Journal of Mechanical Engineering Science*, 217(1), 31-39.
11. Kruth, J. P., Wang, X., Laoui, T. & Froyen, L. 2003. Lasers and materials in selective laser sintering. *Assembly Automation*, 23(4), 357-371.
12. Majewski, C. & Hopkinson, N. 2011. Effect of section thickness and build orientation on tensile properties and material characteristics of laser sintered nylon-12 parts. *Rapid Prototyping Journal*, 17(3), 176-180.
13. Majewski, C. E., Oduye, D., Thomas, H. R. & Hopkinson, N. 2008. Effect of infra-red power level on the sintering behaviour in the high speed sintering process. *Rapid Prototyping Journal*, 14(3), 155-160.

14. Norazman, F. & Hopkinson, N. 2013. Effect of Sintering Parameters and Flow Agent on the Mechanical Properties of High Speed Sintered Elastomer. Proceedings of the 24th Solid Freeform Fabrication Symposium, 2013. Austin, Texas: The University of Texas at Austin, 368-379.
15. Norazman, F. & Hopkinson, N. 2014. Effect of Sintering Parameters and Flow Agent on the Mechanical Properties of High Speed Sintered Elastomer. *Journal of Manufacturing Science and Engineering*, 136(6), 061006.
16. Plummer, K., Vasquez, M., Majewski, C. & Hopkinson, N. 2012. Study into the recyclability of a thermoplastic polyurethane powder for use in laser sintering. *Proceedings of the Institution of Mechanical Engineers, Part B: Journal of Engineering Manufacture*, 226(7), 1127-1135.
17. Raghunath, N. & Pandey, P. M. 2007. Improving accuracy through shrinkage modelling by using Taguchi method in selective laser sintering. *International Journal of Machine Tools and Manufacture*, 47(6), 985-995.
18. Ruffo, M., Tuck, C. & Hague, R. 2006. Cost estimation for rapid manufacturing - laser sintering production for low to medium volumes. *Proceedings of the Institution of Mechanical Engineers, Part B: Journal of Engineering Manufacture*, 220(9), 1417-1427.
19. Shanjani, Y. & Toyserkani, E. 2008. Material Spreading and Compaction in Powder-based Solid Freeform Fabrication Methods: Mathematical Modeling. Proceedings of the 19th Solid Freeform Fabrication Symposium, 2008. Austin, Texas: The University of Texas at Austin, 399-410.
20. Vasquez, M. 2012. *Analysis and Development of New Materials for Polymer Laser Sintering*. PhD thesis, Loughborough University.



# **Chapter 5 High Speed Sintering of Nylon 12 – The Effect of Key Processing Parameters on Part Quality and Repeatability**

## **5.1 Introduction**

This chapter discusses the properties of high speed sintered nylon 12 (PA12). The first section reports the experimental observations of PA12 processing. The second section details the physical and mechanical properties of PA12 parts manufactured using different combinations of lamp type and ink volume. Additionally, the correlations between these parameters and part properties calculated through analysis of variance (ANOVA) are reported. The next section evaluates the repeatability and reproducibility of parts. This is followed by the feasibility study of reflectance spectroscopy as a quality control for HSS process.

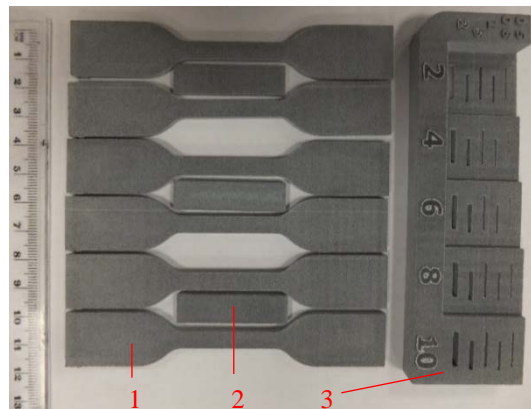
## **5.2 Processing of PA12 by High Speed Sintering**

Following on from the polyamide-based thermoplastic elastomer (TPE) experimentation in Chapter 4, the powder feed was switched to PA12 in this experiment for the following reason. PA12 is the standard feed material for HSS and has been proven to build parts successfully with a selected set of parameters. As the experiment in this chapter aims to correlate key parameters and part properties, the switch was necessary to ensure the effect could be measured accurately without the uncertainty resulting from processing a non-standard material.

In the preliminary experiments, alphanumeric identifiers were originally debossed into sample 1 (tensile bar) and sample 2 (rectangular block) on the surfaces parallel to the z-axis. The debossed text measured 3 mm x 3 mm in height and width, equivalent to a text size 9pt. Even though the features appeared sharp, it was difficult to distinguish the parts instantly due to the shadow formed in the text. For these reasons, the identifiers were instead embossed on the surfaces parallel to the y-axis. Additionally, the text on sample 2 caused a significant change in mass. As this would affect the calculation of apparent density, the design was revised to exclude identifiers on sample 2. The text size was kept constant at 9pt across all parts to ensure minimal effect on physical properties.

When embossing or debossing text onto HSS PA12 parts, it is advised that the text size is kept at a minimum of 9pt to ensure high legibility. However, a larger text size is required when using feed powder with larger particle size.

Each build consisted of 275 layers and took 90 minutes to complete. The cycle time is worked out at 20 seconds per layer. Figure 5-1 shows parts from one set of build, post powder removal.



**Figure 5-1** PA12 specimens 1 (6 replicates), 2 (3 replicates), and 3 (1 replicate)

The above parts had excellent powder removal with very little powder residue on the surfaces. The surfaces were smooth to touch and all parts within the set appeared to be of a consistent grey shade. However, it was noted that the hardness of the powder cake in this experiment varied extensively between builds. A few builds had to be repeated due to the unsuccessful extraction of parts from the hard powder cake.

### 5.3 Physical and Mechanical Properties of High Speed Sintered PA12

This section reports on the part dimensions, density, powder removal, and tensile properties of PA12 parts. These parts were built using ten different ink-lamp configurations shown in Table 5-1. The builds were denoted by alphanumeric strings to reflect the lamp type and ink volume used, for example G1 = gold lamp, ink level 1. Further details were discussed in Section 2.4.1.

**Table 5-1** Ink-lamp configuration for PA12 builds

Lamp Type	Ink volume in $\mu\text{L}/\text{mm}^2$ (Ink Level)				
	1,500 (1)	3,000 (2)	4,500 (3)	6,000 (4)	7,500 (5)
2kW Gold IR lamp (G)	G1	G2	G3	G4	G5
2kW Coated IR lamp (C)	C1	C2	C3	C4	C5

### 5.3.1 Part Dimensions

All of the tensile test specimens were fabricated to the same dimensional specifications. Mean values from 18 individual specimens were taken for each set. The deviation from nominal length, width, and depth were calculated and plotted separately in terms of plane direction x, y, and z respectively, as shown in Figure 5-2. The results for both lamp types were plotted as two separate curves with fitted trendlines. The error bars represent one standard error (SE) within each set.

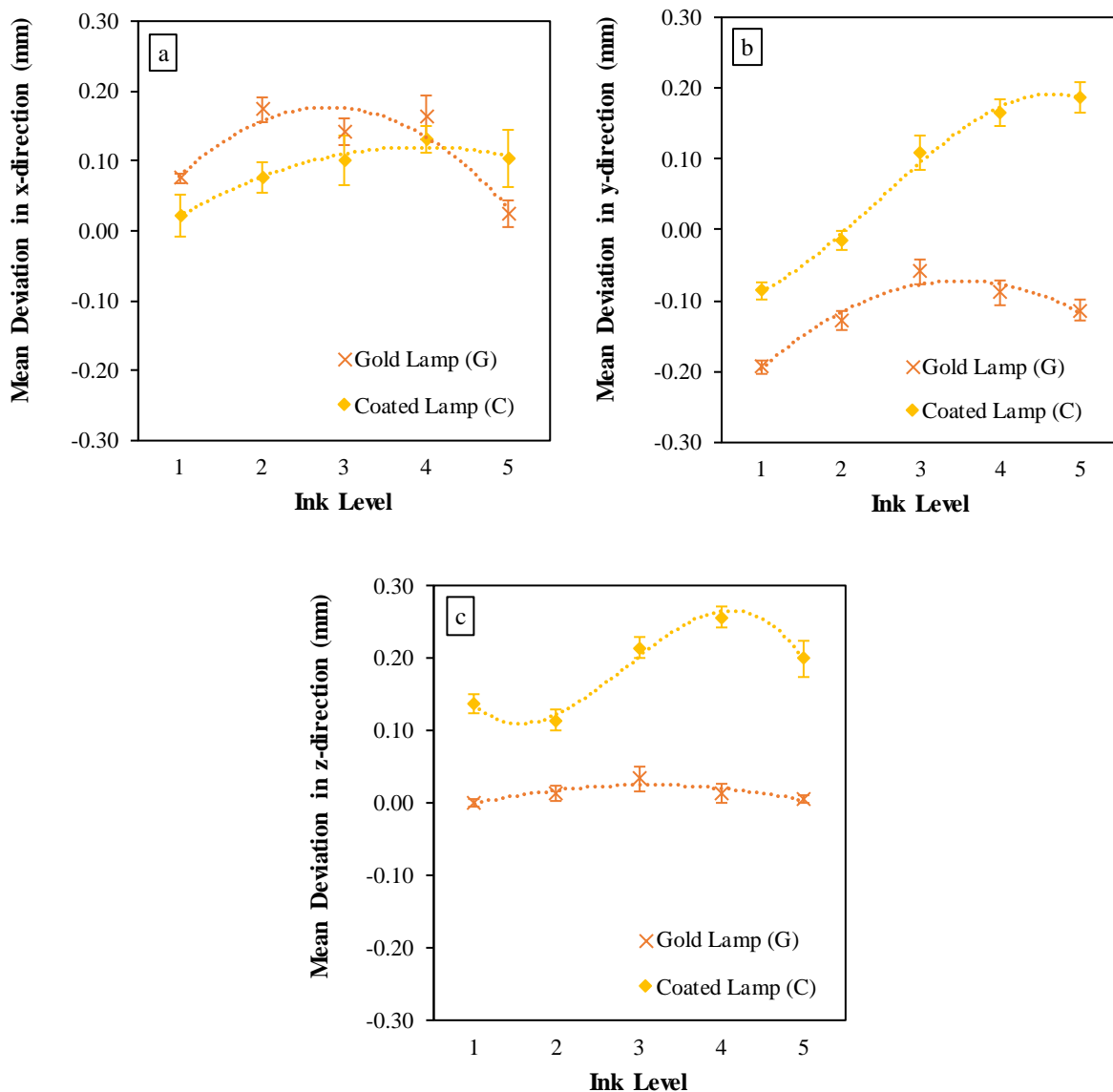


Figure 5-2 Dimensional accuracy of high speed sintered PA12 specimens along x-, y-, and z-directions ( $\pm 1$  SE)

A high dimensional accuracy, which is indicated by minimal deviation from the nominal dimensions, is desirable in manufactured parts. No real trend was observed between the two different types of lamp. In general, a low mean deviation of  $\pm 0.20$  mm was observed for all specimens in all directions. The deviations were consistent across all directions despite the great variation in the nominal dimensions ( $x = 115.00$  mm,  $y = 19.00$  mm,  $z = 3.20$  mm). The tight error bars across all specimens indicated good repeatability of parts. In comparison, Caulfield et al. (2007) reported a dimensional accuracy of up to  $\pm 0.80$  mm in all directions when processing Duraform PA on a DTM Sinterstation 2500<sup>plus</sup>. This suggests that the HSS parts manufactured in this experiment have a higher dimensional accuracy than LS parts.

Figure 5-2b shows that part shrinkage was evident in y-direction, except for parts built at higher energy density (high ink level, high lamp power), which are C3, C4, and C5. The disparity can be attributed to the excess thermal energy absorbed by these parts that led to powder aggregation on the surfaces. The part shrinkage can be caused by rapid cooling of powder cake, especially as PA12 was processed at a high temperature. In the case of the coated lamp, the y dimensions moved closer towards the nominal dimensions as ink level rose. Parts sintered using the gold lamp, however, peaked midway where the deviations were at their lowest, as seen in G3 parts.

Most parts were oversized in x-direction (Figure 5-2a) and all parts were oversized in z-direction (Figure 5-2c). Parts built at higher ink level developed further wall growth as they accumulated more loose powder, which was more pronounced in parts manufactured with coated lamp. At higher ink levels, more carbon black is present. The increasing carbon black results in a greater energy absorption, and this effect is magnified by the higher thermal output supplied by the coated lamp.

The difference in directional dimensional accuracy agrees with the study by Senthilkumaran et al. (2009), where non-uniformity can be observed between longitudinal and transverse directions relative to the sintering direction.

### 5.3.2 Apparent Density

Figure 5-3 depicts the mean density of sample 2 (rectangular block) against increasing ink level. Each data point represents a mean of nine specimens with an error bar of one SE.

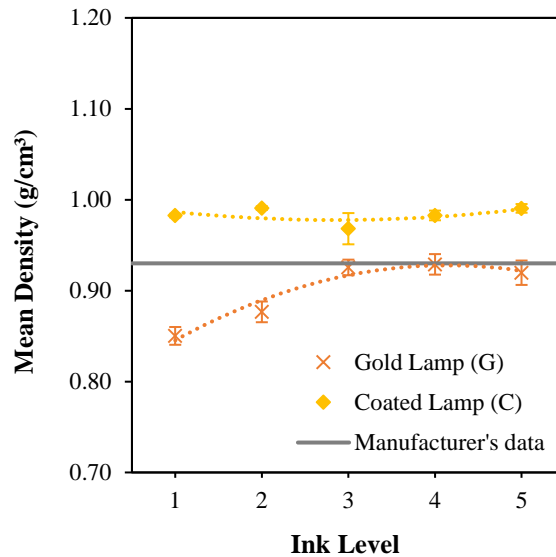


Figure 5-3 Mean density of high speed sintered PA12 ( $\pm 1$  SE)

A density of 0.85 – 0.93 g/cm<sup>3</sup> was determined for parts printed using the gold lamp. Higher density was observed for coated lamp parts at 0.98 – 0.99 g/cm<sup>3</sup>. The small error bars in all samples implied high repeatability of parts. The LS powder manufacturer claimed an achievable part density of 0.93 g/cm<sup>3</sup> in optimum processing conditions. Higher part density is preferable as it indicates a less porous structure, which leads to better mechanical properties.

The increased densification in parts sintered using the coated lamp can be attributed to better sintering. With the gold lamp, there was a marginal increase in part density with increasing ink level. In contrast, no effect was observed in the coated lamp parts. It can be speculated that at a higher lamp irradiance (coated lamp), maximum density had been achieved by these parts.

### 5.3.3 Powder Removal

Figure 5-4 shows the mean powder removal for all PA12 parts. Each data point represents a mean of three specimens with an error bar of one SE within each set. A higher percentage of powder removal is desirable to conserve the intricate geometries and features during post-processing.

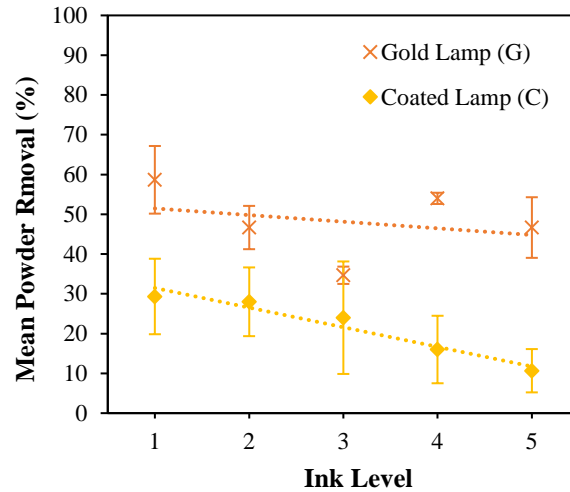


Figure 5-4 Mean powder removal of high speed sintered PA12 ( $\pm 1$  SE)

Powder removal was generally better in parts sintered by the gold lamp. Approximately 35 – 60 % of powder was removed from the gold lamp parts, but only 10 – 30 % was for the coated lamp parts. The poor powder removal in coated lamp parts agreed with the wall growth discussed in Section 5.3.1. The amount of powder removed from the parts decreased with increasing ink level, which is more evident in coated lamp parts than gold.

The large error present in the above data suggests low repeatability for the powder removal part. The error can be attributed to uneven heat distribution across builds, which can be caused by the variation in feed powder temperature, dependent on the sequence of the build within the day. It can also be caused by poor thermal control in the HSS chamber.

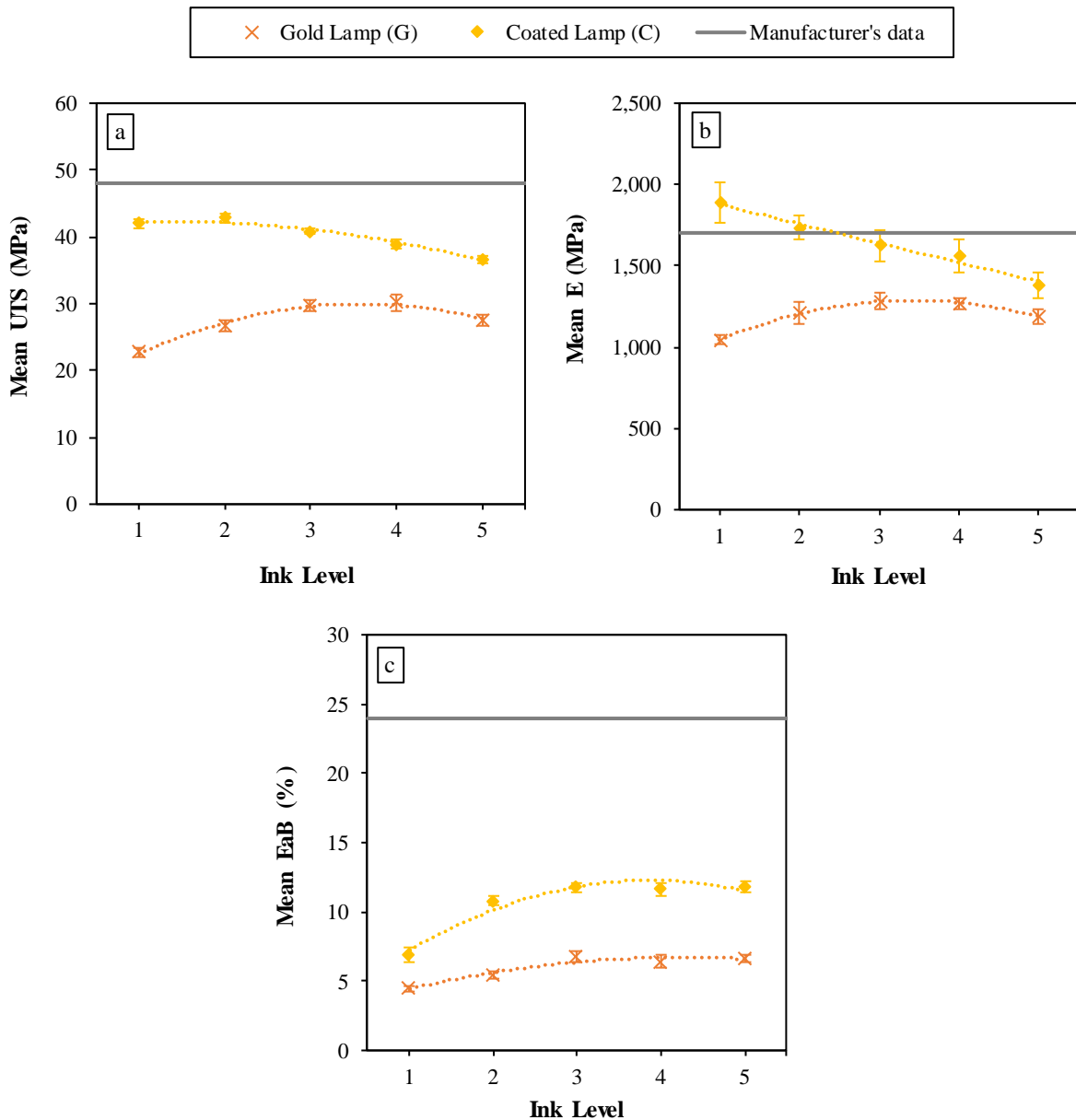
The issue is more prominent in the powder removal part (sample 3) compared to other parts (sample 1 and 2) due to its geometry. This part is a high volume rectangular solid with very few incorporated holes, as shown in Figure 5-5. This type of geometry is not preferable in self-supporting powder bed sintering processes due to the high retention of thermal energy in the part. As the part retains more heat during sintering, the risk of shrinkage and fusing of unsintered powder are higher, together of which result in poor powder removal.



Figure 5-5 The printed area of a powder removal part covers 60% of the build bed area

### 5.3.4 Tensile Properties

Figure 5-6 summarises the ultimate tensile strength (UTS), Young’s modulus (E), and elongation at break (EaB) as a function of lamp type and ink level. Each data point is a mean value of 18 individual specimens, with an error bar of one SE within each set.



**Figure 5-6** Tensile properties of high speed sintered PA12 ( $\pm 1$  SE)

EOS (2009) claims an achievable UTS of 48 MPa, E of 1,700 MPa, and EaB of 24 % when processed with LS. However, literature reveals that most of the reported LS tensile values are much lower than the values claimed above (Kruth et al., 2003). Similarly, in the experiment, all but two of the tensile values shown in Figure 5-6, the E of C1 and C2 parts, were also lower

than the target. This suggests that the material supplier's claimed values are unrealistic for real applications. The coated lamp values were good and comparable to LS values, while the gold lamp values were quite low, signifying poor mechanical strength.

In the case of the gold lamp, all three properties were enhanced by the ink level increment. An increase in ink volume translates to an increase in carbon black particles deposited on the build bed. The higher the amount of carbon black, the more heat is absorbed from the sintering lamp and radiated to the underlying layer of nylon powder. It is known that exposing polymer to an elevated temperature can introduce changes in its molecular weight. The molecular weight of a polyamide increases with increasing thermal history, as evidenced in the molecular weight study of used PA12 powder by Haworth et al. (2013). Zarringhalam et al. (2006) reported that an increase in molecular weight contributes to increased mechanical performance. This behaviour can be explained by an increase in long-chain molecules, which further forms the entanglement networks of the polymer (Swallowe, 2013). Therefore, an increase in temperature causes an increase in molecular weight, which increases the tensile properties of polymer parts.

However, the above argument of increasing tensile strength with temperature is not valid at very high temperatures. In the case of the coated lamp, a different set of trends can be observed for the variation of properties with ink level. Both the UTS and E decline, while EaB improves with increasing ink level. A similar trend can be observed in the study conducted by Ellis et al. (2014), although the study suggested that the decline in properties starts at much lower ink level than that presented in Figure 5-6. This difference can be attributed to the fact that higher build bed temperatures were used in their study, which is believed to accelerate the onset of the decline.

The decline in mechanical performance is not directly caused by the carbon black particles themselves but the associated thermal effect. Athreya (2010) reported no negative effect by the carbon-black induced localised heating on the molecular weight of nylon 12-carbon black composite. The high thermal load, however, might have caused the pyrolysis of the polyamide, where polymers decompose at high temperatures. Vasquez et al. (2011) reported that at 428°C, PA12 powder experiences peak loss in mass (peak decomposition) and suggested that mechanical properties start deteriorating at much lower temperatures. It is possible that the combination of high lamp irradiance and high carbon black absorption result in an elevated temperature close to the decomposition temperature. This consequently causes breaking of weak C-N bonds, which is the first stage of the pyrolysis.



## 5.4 Analysis of Variance

A two-way analysis of variance (ANOVA) was conducted to examine the effect of ink volume and lamp type on the UTS and dimensional accuracy of PA12 parts. Table 5-2 lists the factors and corresponding levels used in this analysis.

**Table 5-2** ANOVA factors and levels

Design Factors	Level 1	Level 2	Level 3	Level 4	Level 5
Ink volume (pL/mm <sup>2</sup> )	1,500	3,000	4,500	6,000	7,500
Lamp type	Gold	Coated			

### 5.4.1 Ultimate Tensile Strength

The means and *p* values of each factor are presented as follows. Table 5-3 compares the means and standard deviations (SD) of UTS, where higher UTS indicates better mechanical strength. The important values are highlighted in bold.

**Table 5-3** ANOVA table of means for UTS

Lamp Type	Ink Volume	Mean	Standard Deviation	N
Gold	1,500	22.72	3.243	18
	3,000	26.67	3.763	17
	4,500	29.72	3.798	17
	6,000	30.13	4.558	15
	7,500	27.54	3.992	18
	Total		<b>27.24</b>	4.633
Coated	1,500	41.98	2.511	16
	3,000	42.82	3.510	18
	4,500	40.85	2.224	18
	6,000	38.87	3.023	18
	7,500	36.69	2.312	18
	Total		<b>40.20</b>	3.506
Total	1,500	<b>31.78</b>	10.171	34
	3,000	<b>34.98</b>	8.935	35
	4,500	<b>35.45</b>	6.411	35
	6,000	<b>34.90</b>	5.785	33
	7,500	<b>32.12</b>	5.644	36
	Total		<b>33.83</b>	7.676

The grand mean for UTS was 33.83 MPa. By increasing ink volume, the means ranged between 31.78 – 35.45 MPa. By lamp type, the means were 27.24 MPa for gold lamp and 40.20 MPa for coated lamp.

The ANOVA table (Table 2-13) was filled in with the results. Table 5-4 shows the corresponding ANOVA results for UTS. The  $p$  value was used to check for the significance of the examined factors, where if  $p$  value is less than 0.05 (i.e. 95% confidence interval), then the examined factor is significant to the measured response.

**Table 5-4** ANOVA table for UTS

Source	Sum of squares	Degree of freedom	Mean square	F value	p value
Model	8302.228*	9	922.470	82.060	< .0001
Lamp	7151.244	1	7151.244	636.151	< .0001
Ink	298.040	4	74.510	6.628	< .0001
Lamp x Ink	729.780	4	182.445	16.230	< .0001
Error	1832.352	163	11.241		
Total	208165.591	173			
Corrected Total	10134.580	172			

\* $R^2 = .819$ , adjusted  $R^2 = .809$

The two-way ANOVA identifies the effect of ink volume and lamp type on the UTS. The  $p$  values showed that all parameters tested were significant. The ink level was significant ( $F_{4,173} = 6.628$ ,  $p < .0001$ ). When the ink level was kept constant, the lamp type was also significant ( $F_{1,173} = 7,151.244$ ,  $p < .0001$ ), with the coated lamp parts having higher UTS than the gold lamp. There was a statistically significant interaction between the effects of ink volume and lamp type on the UTS ( $F_{4,163} = 16.230$ ,  $p < .0001$ ).

As evident in the means (Table 5-3), the UTS was 47.5 % higher for the coated lamp compared to the gold lamp. The UTS was within a range of 5 MPa between all of the ink volumes. Between the two factors, it can be concluded that the lamp type has a more significant contribution to the tensile properties of parts than the ink volume.

#### 5.4.2 Dimensional Accuracy

Table 5-5 shows the dimensional accuracy means in x, y, and z directions. A positive value indicates that the part is oversized, and a negative value indicates that the part is undersized.

**Table 5-5** ANOVA table of means for dimensional accuracy

Lamp Type	Ink Volume	x-direction		y-direction		z-direction		N
		Mean	SD	Mean	SD	Mean	SD	
Gold	1,500	0.0750	0.03258	-0.1939	0.04354	0.0000	0.01815	18
	3,000	0.1735	0.07945	-0.1282	0.06217	0.0124	0.04409	17
	4,500	0.1424	0.08235	-0.0594	0.07075	0.0335	0.07297	17
	6,000	0.1627	0.12606	-0.0887	0.07249	0.0133	0.04806	15
	7,500	0.0239	0.08548	-0.1144	0.06483	0.0056	0.02684	18
	Total	<b>0.1128</b>	0.10101	<b>-0.1185</b>	0.07685	<b>0.0127</b>	0.04599	85
Coated	1,500	0.0224	0.12333	-0.0856	0.04939	0.1369	0.05003	16
	3,000	0.0761	0.09344	-0.0144	0.05680	0.1139	0.06381	18
	4,500	0.1017	0.15685	0.1078	0.10675	0.2144	0.06510	18
	6,000	0.1311	0.08731	0.1661	0.08346	0.2561	0.06563	18
	7,500	0.1028	0.17898	0.1878	0.09353	0.1989	0.10932	18
	Total	<b>0.0883</b>	0.13481	<b>0.0759</b>	0.13160	<b>0.1851</b>	0.08928	88
Total	1,500	<b>0.0502</b>	0.09040	<b>-0.1429</b>	0.07137	<b>0.0644</b>	0.07821	34
	3,000	<b>0.1234</b>	0.09887	<b>-0.0697</b>	0.08223	<b>0.0646</b>	0.07485	35
	4,500	<b>0.1214</b>	0.12617	<b>0.0266</b>	0.12345	<b>0.1266</b>	0.11420	35
	6,000	<b>0.1455</b>	0.10610	<b>0.0503</b>	0.15032	<b>0.1458</b>	0.13553	33
	7,500	<b>0.0633</b>	0.14390	<b>0.0367</b>	0.17256	<b>0.1022</b>	0.12556	36
	Total	<b>0.1003</b>	0.11970	<b>-0.0196</b>	0.14540	<b>0.1004</b>	0.11197	173

From Table 5-5, it can be concluded that the highest deviation between measured and nominal dimensions occurred at ink volume 6,000 pL/mm<sup>2</sup>.

The ANOVA results for dimensional accuracy in all directions are summarised in Table 5-6 to show the *p* value of each factor. The full ANOVA tables can be found in the Appendices.

**Table 5-6** Summary ANOVA table for dimensional accuracy

Source	<i>p</i> value   x-direction	<i>p</i> value   y-direction	<i>p</i> value   z-direction
Lamp	.095	< .0001	< .0001
Ink	.001	< .0001	< .0001
Lamp x Ink	.019	< .0001	< .0001

All factors were found to be significant in y- and z- directions, where *p* < .0001. In x-direction, however, only the ink volume was significant to the dimensional accuracy, but not the lamp.

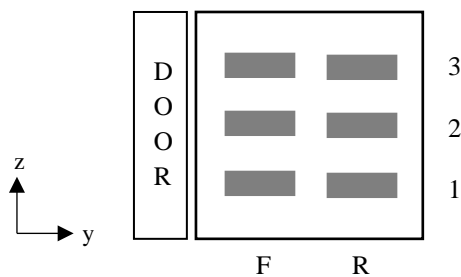
## 5.5 Robustness, Repeatability and Reproducibility

The properties of HSS parts presented in Sections 4.3 and 5.3 demonstrate the capability of the HSS process to produce high quality parts. Together with the cost analysis in Section 4.5, the process possesses a high potential for commercialisation. In order to improve the quality of parts manufactured through the HSS process, a repeatability and reproducibility study was conducted.

This section discusses the in-batch and batch-to-batch repeatability of the HSS process. Process reproducibility across HSS systems is briefly discussed and presented in Section 5.6. The evaluation is made on the PA12 parts presented earlier in this chapter. The parts were manufactured using ten different set of build parameters, with three replicate batches for each set.

### 5.5.1 Process Robustness

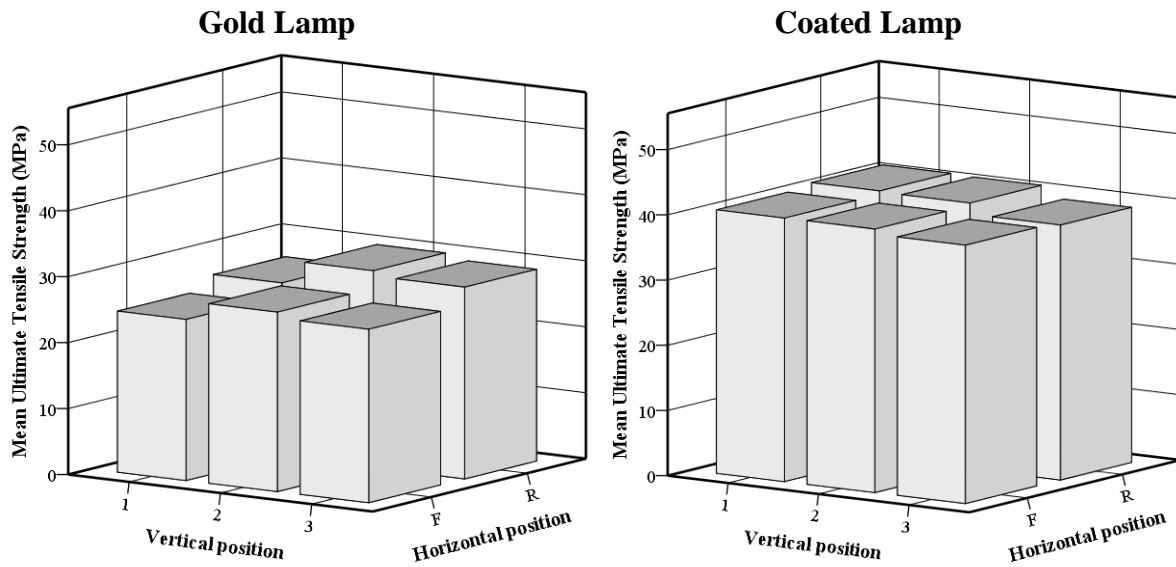
Six ASTM standard type IV tensile parts were built in each batch. Figure 5-7 illustrates their horizontal and vertical positions in the HSS build chamber.



**Figure 5-7** Side view of the tensile parts in the build chamber, configured in a matrix of 3 x 2

The build bed was divided as front and back sections in y-axis. The section closest to the door was assigned as Front (F), and the section further away from the door was Rear (R). The z-axis was divided into three levels. The numeric denomination started from 1 at the base of the build bed and increased along the height of the build chamber.

In order to assess the robustness of parts produced within a batch, the mean UTS of 18 specimens was determined at each position. Figure 5-8 shows the distribution of UTS over different positions in the HSS build chamber.



**Figure 5-8** UTS of PA12 parts against position in the build chamber

In the case of the gold lamp, the UTS was constantly higher in the rear position when compared to its counterpart. Conversely, the build position had a marginal effect on the UTS in parts built using the coated lamp. Parts that were built in the centre of the build chamber were found to be the strongest in both cases.

Uneven temperature distributions in the build chamber has been widely reported as the cause of inconsistencies in the mechanical properties of laser sintered parts. Tontowi and Childs (2001) reported large variations in the density of PA12 parts, subject to their positions on the LS build bed. Arguably, Goodridge et al. (2012) stated that the effect of position in PA12 parts is not as significant as in other polymers.

In this experiment, images from the infrared camera attached over the build bed indicated that build bed temperatures were higher towards the rear of the build bed. The middle section of the build chamber also retained a lot of heat during sintering. This is supported by a previous study done by Majewski et al. (2007), where powder hardness was found to be the highest in the centre of the build bed.

There was a considerable amount of variation in UTS at lower lamp power (gold lamp). An ANOVA test was performed to assess the effect of position on the UTS. The results showed that the part position is in fact significant in this experiment, where  $p = 0.039$ .

## 5.5.2 Process Repeatability

Figure 5-9 shows the variation in UTS across replicate builds, where identical set of parameters were used in each set of three builds. Standard deviations are given above each group of replicates.

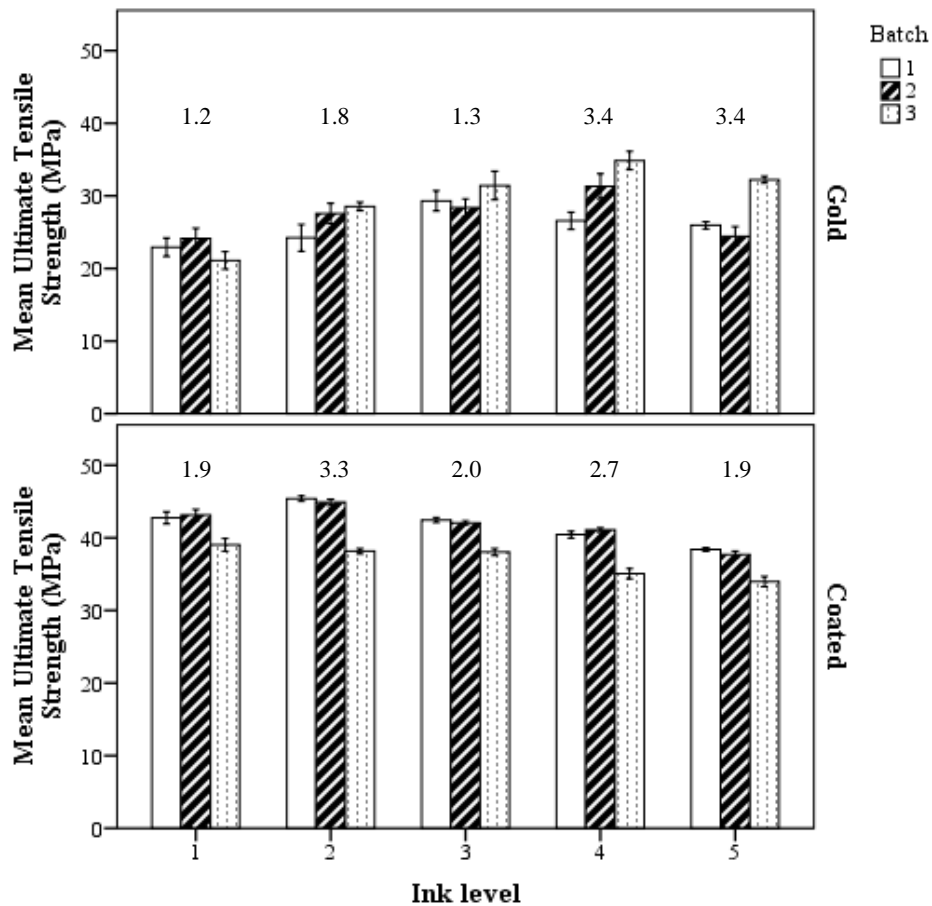


Figure 5-9 Batch-to-batch variation of UTS of PA12 parts

The standard deviations for all parts ranged between 1.2 – 3.4 MPa. The low standard deviations imply a good batch-to-batch repeatability. The error may be attributed to slight variation in machine temperatures, especially induced by residual heat when switching between parameters.

## 5.5.3 Process Reproducibility

Process reproducibility could not be identified due to limited access to the Voxeljet HSS machine. However, reproducibility across printhead systems was successfully measured and formed part of the findings presented in the following section.

## **5.6 Reflectance Spectroscopy as a Quality Assessment Method**

### **5.6.1 Overview**

Spectroscopy has never been used to assess HSS parts. This novel study, which was carried out at the end of the PhD, initially aimed to adopt reflectance spectroscopy for HSS quality management. There are two parts to this study, firstly where the reflectance is used to check for print consistency across builds and printheads, and secondly to predict the UTS of high speed sintered parts.

### **5.6.2 Hypotheses**

Since reflectance spectroscopy quantifies the greyness of a part, it is thought that the method can be used to quantify real greyscale in a part and compare it against the set value. This can be useful as the method of applying greyscale changes over time and across different build file preparation softwares and printhead technologies, and ultimately different HSS machines. Throughout this thesis, the greyscale application method has evolved from manipulating the bitmaps using an image processing software (TPE experiment) to varying the ink volume on the built-in HSS software on the machine (PA12 experiment). This is due to a printhead upgrade with dithering capabilities. A different machine, for example the Voxeljet HSS machine, allows the user to set the greyscale level between one and eight on the built-in HSS software during printing. These variations make it difficult to compare processing parameters and parts manufactured across different printheads and machines. Reflectance spectroscopy is therefore proposed to systematically measure the reproducibility from one system to another.

More importantly, it is critical that parts within the same system are replicated to the same quality. As discussed in Section 5.5.1, slight variation intra-build is to be expected dependent on the location of parts within the build envelope. High batch-to-batch repeatability is of primary concern and is desired in batch production. For this reason, reflectance spectroscopy is recommended as a quality control method to check for consistencies intra- and inter-build.

It can be inferred that the UTS of a part can be predicted based on its reflectance, if the correlation between ink volume and the UTS of PA12 parts is known.

The hypotheses for this study are listed as follows:

- There is a slight variation in reflectance values between parts within the same build
- There is a good consistency in reflectance values between replica builds
- The reflectance value is directly proportional to the print ink volume
- The UTS is directly proportional to the reflectance value

These hypotheses were made with the following assumptions:

- All parts have an equal level of surface finish
- The errors associated with tensile testing are low or negligible
- The errors associated with the printhead are low or negligible
- The errors associated with the spectrophotometer are reduced by taking repeat measurements
- The resolutions of the reflectance values can provide enough information for the analysis

### 5.6.3 Materials and Methods

The first part of this study measures the consistency across two printheads with two different approaches to greyscale. Two sets of PA12 tensile parts were used, which were manufactured according to the parameters listed in Table 5-7.

**Table 5-7** Printhead and greyscale comparison between two sets of parts

Parameters	Printhead name	
	1002	Proton
Lamp type	Coated	Coated
Printhead type	Xaar 1002 GS6	Xaar Proton 60
Greyscale type	Ink volume	8-bit greyscale
Ink volume (pL/mm <sup>2</sup> )	1,500, 3,000, 4,500, 6,000, 7,500	
Greyscale level	227, 198, 170, 142, 113, 85, 57, 28, 0	

1002 parts were taken from Section 5.3, while Proton parts were preliminary parts printed before the printhead upgrade. 1002 parts were printed in a range of absolute ink volume, while Proton parts had the greyscale applied to the build files during the pre-processing stage.

The systematic process taken to perform the reflectance analysis is illustrated in Figure 5-10.



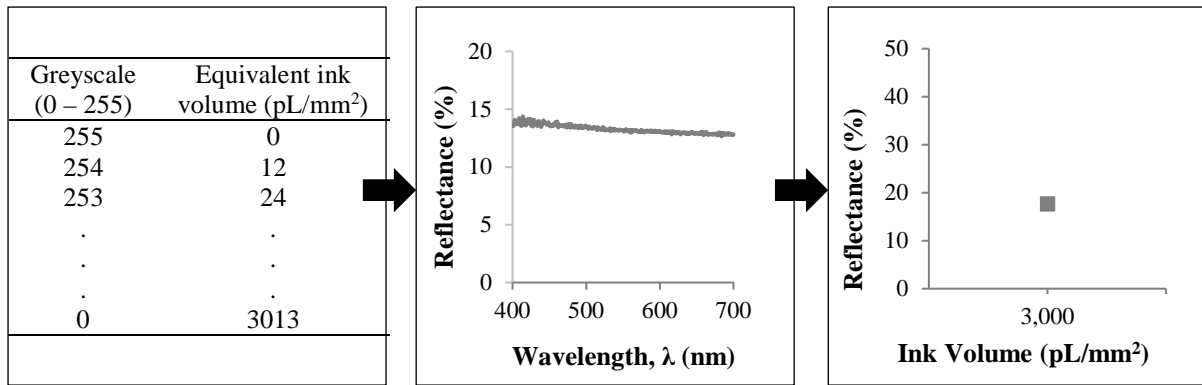


Figure 5-10 Data processing to compare printheads

Firstly, the Proton greyscale levels were converted to the equivalent ink volume of 1002 printhead. A spectrum was obtained by scanning a part in reflectance mode within the visible light region (400 – 700 nm) on a UV/Vis spectrophotometer. The average reflectance was calculated by averaging the data points. Average reflectance, in percentage, was plotted against ink volume, in pL/mm<sup>2</sup>. The above steps were repeated for all parts.

The second part of this study evaluates the feasibility of reflectance spectroscopy to predict the tensile strength of parts. Parts from Section 5.3, which were all printed with 1002 printhead at five different ink levels, were used in this analysis. Figure 5-11 illustrates how the spectral data was transformed to obtain the correlation.

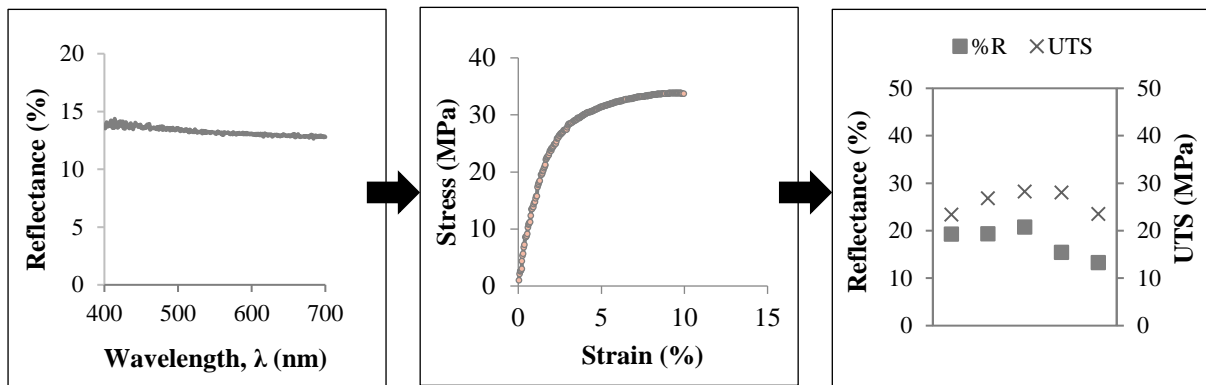
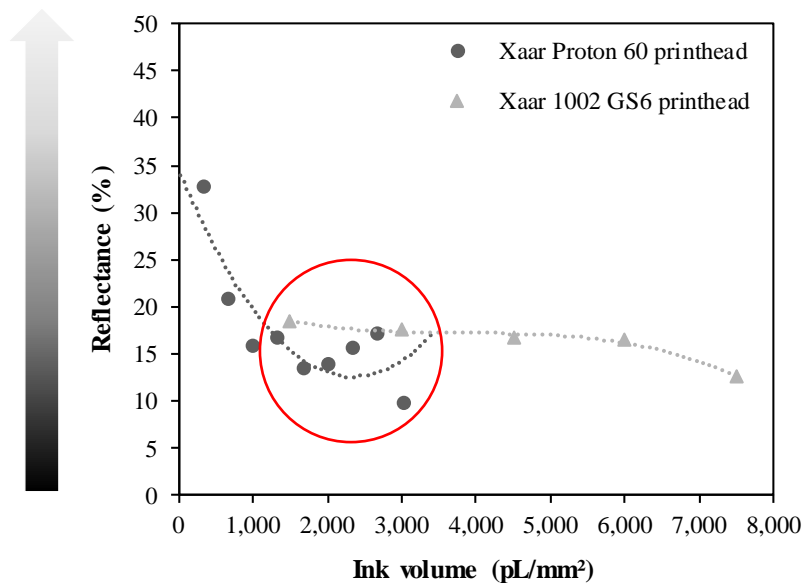


Figure 5-11 Data processing to predict tensile strength

The spectrum and average reflectance were obtained through the same method as above. Next, the UTS was determined from the stress-strain curve obtained through tensile testing. Average reflectance, in percentage, was plotted against UTS, in MPa, on opposite axes. The above steps were repeated for all parts. The correlation between reflectance and UTS was analysed.

## 5.6.4 Results & Discussion

Figure 5-12 shows the average reflectance plotted against ink volume. Due to the difference in scale between the two sets of data, the ink volume in this section will be expressed using absolute ink volume in pL/mm<sup>2</sup> unit, and not ink level or greyscale level. The full average reflectance scale ranges from 0 % to 100 %, going from black to white.



**Figure 5-12** Analysing the consistency of ink volume across printheads. Ink volume for Proton 60 are the manufacturer's claimed values

The Proton printhead had a limited range of printable ink volume, with a maximum of 3,013 pL/mm<sup>2</sup>. Its successor, the 1002 printhead had a higher capability that extends the ink volume range of up to 16,000 pL/mm<sup>2</sup>. The data set from both printheads overlapped between 1,500 – 3,000 pL/mm<sup>2</sup>. The overlapping region is circled in the figure and is of primary concern in this analysis.

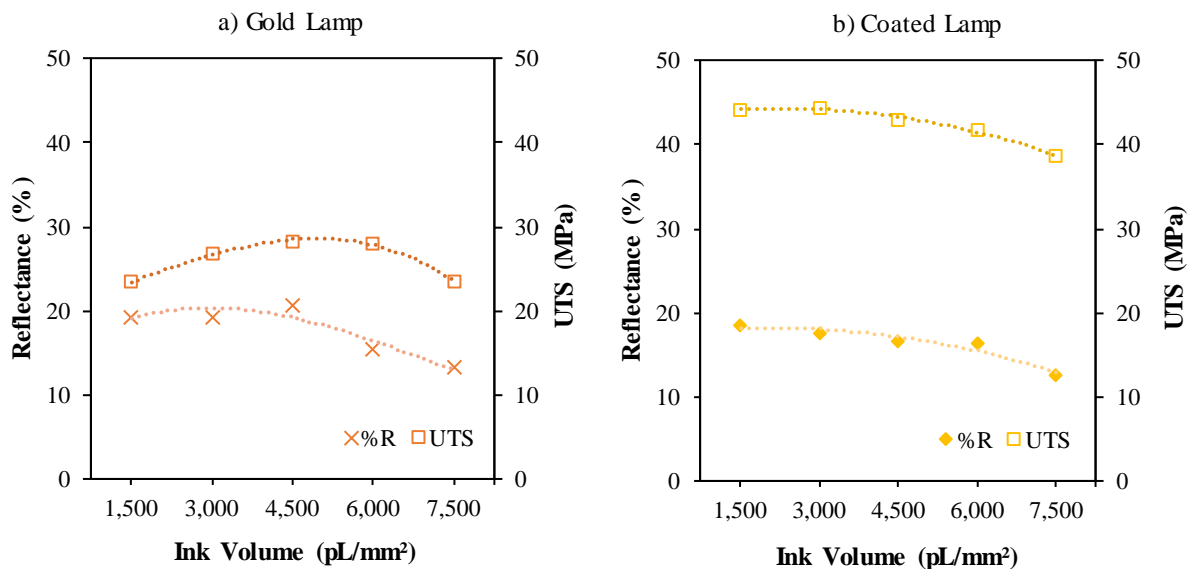
From Figure 5-12, it can be observed that the reflectance of the Proton parts showed no correlation to the ink volume. The reflectance trend was generally erratic, especially in the overlapping region. There was, however, a distinct variation between the lowest and the highest ink volume. This is because the Proton printhead was not capable of printing absolute ink volume in pL/mm<sup>2</sup>. The bitmap files of a part were pre-processed by setting a greyscale level to set its colour. The Proton printhead then decoded the colour into a corresponding ink volume using the printhead's built-in software. The absence of correlation between reflectance and ink

volume in the above figure suggested that the Proton printhead was not reliable in dispensing the correct ink volume as required.

Meanwhile, the parts made using the 1002 printhead showed an inverse correlation between reflectance and ink volume. This correlation, which indicates that parts appear darker at higher ink volume, agrees with the proposed hypothesis. The 1002 printhead was an upgrade of the Proton printhead and allows HSS users to set specific ink volume in-process as required.

In the overlapping region, there was a disparity in both reflectance values and reflectance-ink volume correlation between both sets of parts. It was arguable that the reflectance might not match due to the difference in operating temperatures. However, a similarity in correlation or trend was expected between the two sets with increased absorption of thermal energy. This suggested that the parts manufactured using equivalent ink volume across different printheads did not have the same reflectance.

In order to gain better understanding, a second analysis was performed to find correlation when the printhead was kept constant. Figure 5-13 shows the average reflectance and the UTS against increasing ink volume of parts manufactured using the 1002 printhead.



**Figure 5-13** Correlation between reflectance and UTS of parts made using a) gold lamp and b) coated lamp

Both Figure 5-13a and Figure 5-13b display a clear distinction in reflectance values between the lowest and the highest ink volume in each case.

In Figure 5-13a, the reflectance of gold lamp parts was not proportional to the ink volume. This trend is similar to the Proton parts shown in Figure 5-12. A slight similarity can be observed between the reflectance trend and the UTS trend in Figure 5-13a, in that both values raised to a peak before slowly declining. It can be concluded that no clear correlation exists between reflectance and UTS of parts made using the gold lamp.

On the other hand, Figure 5-13b shows a positive correlation between reflectance and UTS of coated lamp parts. A downward trend can be observed for both properties as the ink volume increases. This provides great confidence in the study, and as parts made using the coated lamp were stronger than the gold lamp, the former is more preferable for use on the HSS machine. Therefore, based on these preliminary results, reflectance spectroscopy has shown its potential to predict the UTS of parts based on their reflectance values.

There are a few possibilities for why similar positive result was not obtained in the other dataset. The range of reflectance might have been too small to detect any changes between the different ink volumes. The samples were within 6,000 pL/mm<sup>2</sup> in ink volume between each other but only ranged within 20% in reflectance. The change in reflectance is more obvious when comparing it between the lowest and the highest ink volume.

However, the low confidence in reflectance data probably stems from the measurement technique itself. Reflectance is obtained by measuring the difference between incident and reflected light after being scattered on a sample. In this case, the sample is a porous structure with excess powder covering its surfaces. The high reflectivity of loose nylon powder on the part surface causes random scattering of light. This suggests that the real reflectance could not be measured due to the high error caused by the overlying powder. Polishing methods such as sanding or chemical surface treatment can be applied to the parts to obtain results that are more meaningful.

The results can be improved by doing repeat measurements across different locations on multiple parts within each set. As previously mentioned, this is a preliminary study done at the end of the PhD, and consequently only managed to obtain limited data. In this study, only one sample from each set was measured to obtain the reflectance data. An increase in sample size will likely generate data with a higher confidence.

## 5.7 Summary

This chapter summed up the quality of nylon-12 (PA12) parts manufactured using the high speed sintering (HSS) process and its associated methods of assessment.

The parts were oversized in x- and z-directions, and undersized in y-direction. The parts had good dimensional accuracy of  $\pm 0.2$  mm in all directions. Part density varied between 0.85 – 0.99 g/cm<sup>3</sup>. Powder removal was generally inferior, which can partly be attributed to poor specimen design. Tensile properties were comparable to reported laser sintered values.

The effect of two main parameters, lamp type (power) and ink volume, on part properties were investigated. The coated lamp, which has a higher energy output, produced parts of superior properties compared to the gold lamp. However, the superior properties were obtained at the expense of poor powder removal. The effect of ink volume varied on the different measured output. The analysis of variance (ANOVA) showed that both parameters were significant ( $p < 0.05$ ) on the ultimate tensile strength (UTS) and dimensional accuracy of parts, except for dimensional accuracy in x-direction, where the lamp had no significant effect.

The UTS of a part was influenced by its position in the build chamber, with the central back position being the hot spot. The parts had good batch-to-batch repeatability, which was indicated by low standard deviations.

Greyscale is applied to HSS parts to vary the part density like functionally graded materials. As a result, parts are typically grey in colour, due to the combination of black ink and white powder. A quality assessment method to measure colorimetry of a part using reflectance spectroscopy was proposed. Preliminary results from the study indicated high suitability for reflectance to be used to predict UTS based on the reflectance of parts.

## 5.8 References

1. Athreya, S. R. 2010. *Processing and characterization of a carbon black-filled electrically conductive Nylon-12 nanocomposite produced by selective laser sintering*. PhD Thesis, Georgia Institute of Technology.
2. Caulfield, B., McHugh, P. E. & Lohfeld, S. 2007. Dependence of mechanical properties of polyamide components on build parameters in the SLS process. *Journal of Materials Processing Technology*, 182(1–3), 477-488.
3. Ellis, A., Noble, C. J. & Hopkinson, N. 2014. High Speed Sintering: Assessing the influence of print density on microstructure and mechanical properties of nylon parts. *Additive Manufacturing*, 1-4(1), 48-51.
4. EOS. 2009. *EOS Material Data Center* [Online]. Available: <https://eos.materialdatacenter.com/> [Accessed 1 December 2017].
5. Goodridge, R., Tuck, C. & Hague, R. 2012. Laser sintering of polyamides and other polymers. *Progress in Materials Science*, 57(2), 229-267.
6. Haworth, B., Hopkinson, N., Hitt, D. & Zhong, X. 2013. Shear viscosity measurements on Polyamide-12 polymers for laser sintering. *Rapid Prototyping Journal*, 19(1), 28-36.
7. Kruth, J. P., Wang, X., Laoui, T. & Froyen, L. 2003. Lasers and materials in selective laser sintering. *Assembly Automation*, 23(4), 357-371.
8. Majewski, C. E., Hobbs, B. S. & Hopkinson, N. 2007. Effect of bed temperature and infra-red lamp power on the mechanical properties of parts produced using high-speed sintering. *Virtual and Physical Prototyping*, 2(2), 103-110.
9. Senthilkumaran, K., Pandey, P. M. & Rao, P. V. M. 2009. Influence of building strategies on the accuracy of parts in selective laser sintering. *Materials & Design*, 30(8), 2946-2954.
10. Swallowe, G. M. 2013. *Mechanical Properties and Testing of Polymers: An A-Z Reference*, Dordrecht, Springer Netherlands.
11. Tontowi, A. E. & Childs, T. H. C. 2001. Density prediction of crystalline polymer sintered parts at various powder bed temperatures. *Rapid Prototyping Journal*, 7(3), 180-184.
12. Vasquez, M., Haworth, B. & Hopkinson, N. 2011. Optimum sintering region for laser sintered nylon-12. *Proceedings of the Institution of Mechanical Engineers, Part B: Journal of Engineering Manufacture*, 225(12), 2240-2248.
13. Zarringhalam, H., Hopkinson, N., Kamperman, N. F. & de Vlieger, J. J. 2006. Effects of processing on microstructure and properties of SLS Nylon 12. *Materials Science and Engineering: A*, 435–436(1), 172-180.

# **Chapter 6 High Speed Sintering Energy Density – The Construction and Validation of an Analytical Model**

## **6.1 Introduction**

This chapter reports the construction of an analytical model that represents the energy density of a high speed sintered part. The chapter begins by analysing the HSS process and modelling the in-service processing of polymeric material. Various input variables are considered, followed by the formulation of an equation based on heat transfer and sintering theory. The energy density model is validated by experimental work and correlation between energy density and manufactured part properties is investigated.

## **6.2 Construction of HSS Energy Density Model**

The multiphase interaction between the components in a complex process like HSS is challenging to examine empirically. As such the amount of energy that goes into processing a part has never been quantified. In this chapter, a new model called the HSS energy density (HSS<sub>ED</sub>) model was developed to quantify the energy density in HSS, in a similar way that the Andrew number or energy density (ED) does for laser sintering (Nelson, 1993).

The development of the HSS<sub>ED</sub> model aimed to improve understanding of the interactions that occur during the HSS process. This initial model quantifies energy input from a range of variables to ensure sufficient energy is added to the system to sinter the polymer particles. Secondary focus was given on measuring the difference in energy input between the unsintered and sintered areas in order to improve powder removability and dimensional accuracy.

## 6.2.1 Consideration of Input Variables

In order to formulate the HSS<sub>ED</sub> model, a list of variables that were thought to contribute to the energy balance were identified. The variables were categorised according to the three main components of HSS, which are lamp, ink/carbon black, and powder, as listed in Figure 6-1.

IR Lamp	Ink / Carbon Black	Powder
<ul style="list-style-type: none"> <li>• Traversing speed on preheat</li> <li>• Traversing speed on sintering</li> <li>• Height from build bed</li> <li>• Power on preheat</li> <li>• Power on sintering</li> <li>• <b>Spectral irradiance</b></li> </ul>	<ul style="list-style-type: none"> <li>• Weight percentage of carbon black in ink</li> <li>• Spectral absorption of carbon black</li> <li>• <b>Ink volume</b></li> </ul>	<ul style="list-style-type: none"> <li>• Particle size</li> <li>• Density</li> <li>• Specific heat capacity</li> <li>• Spectral absorption</li> <li>• Build bed temperature</li> </ul>

**Figure 6-1** Input variables for the HSS energy density model

The model was validated using the nylon 12 (PA12) experiment in Chapter 5. In this experiment, the spectral irradiance of lamp and the ink volume (the bold terms) were the only independent variables. All of the other variables were kept constant.

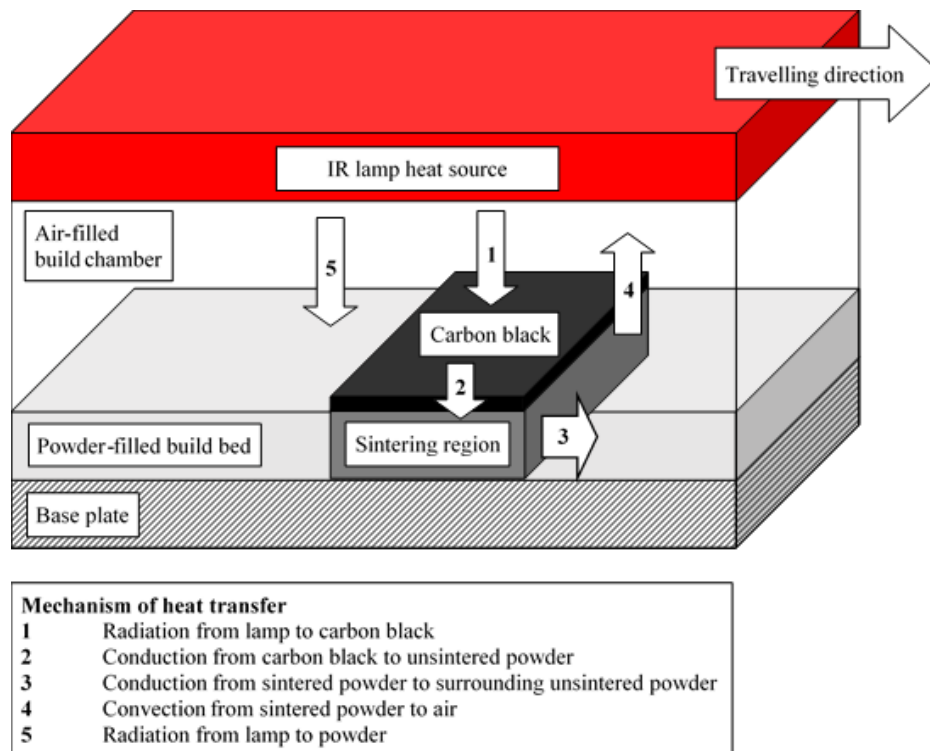
As the experiment used two different lamp types, two spectral irradiance curves were available for comparison. The infrared (IR) lamp speed was used to determine lamp exposure time on the build bed during both preheat and sintering passes. The lamp's distance from the build bed and its power level enabled real lamp power to be calculated from its spectral irradiance.

The influence of ink during sintering was primarily dependent on its Radiation Absorbing Material (RAM) element, as the hydrocarbon carrier was lost in evaporation in flight. The RAM used in this experiment was carbon black. As the same ink type was used throughout the experiment, the carbon black weight percentage and its spectral absorption were kept constant. The increasing ink volume, however, meant that more carbon black particles (higher mass and surface area) were deposited onto the build bed, which ultimately absorbed more heat to be transferred to the underlying powder.

By keeping the powder type constant, the physical properties of powder such as particle size, density, and specific heat capacity were also controlled. The spectral absorption of powder was used to quantify the energy absorbed by the surrounding unsintered powder. The build bed temperature represented the initial temperature of powder before both preheat and sintering.



A schematic diagram to model the heat transfer in HSS was developed. Figure 6-2 illustrates the heat transfer model and the mechanisms involved.



**Figure 6-2** Schematic of heat transfer in the HSS process

During the HSS process, the IR lamp traverses the build bed twice to construct a single layer. The build bed is heated during the first pass (preheat pass), and reheated after ink deposition (sintering pass). The thermal energy added to the sintering region is provided by one main source (the IR lamp) through two different mechanisms, which are the radiation from lamp to unsintered powder, followed by the conduction from carbon black (ink) to the underlying unsintered powder. The build bed temperature is higher than the boiling point of the ink, hence the solvent vaporises upon impact. The sintering region losses heat to the surrounding unsintered powder and the air within the chamber. By taking the sintering region as a control volume, the conservation of energy within the system is given as follows:

$$Q_{\text{Total}} = Q_{\text{Lamp}} + Q_{\text{CB}} - Q_{\text{P}} - Q_{\text{A}} \quad \text{Equation 6-1}$$

where  $Q_{\text{Lamp}}$  is the thermal energy provided by the lamp,  
 $Q_{\text{CB}}$  is the heat absorbed by the carbon black and conducted to the powder,  
 $Q_{\text{P}}$  is the heat loss to the surrounding unsintered powder, and  
 $Q_{\text{A}}$  is the heat loss to the air.

## 6.2.2 Assumptions and Boundary Conditions

The following assumptions were made for the derivation of equations in this chapter.

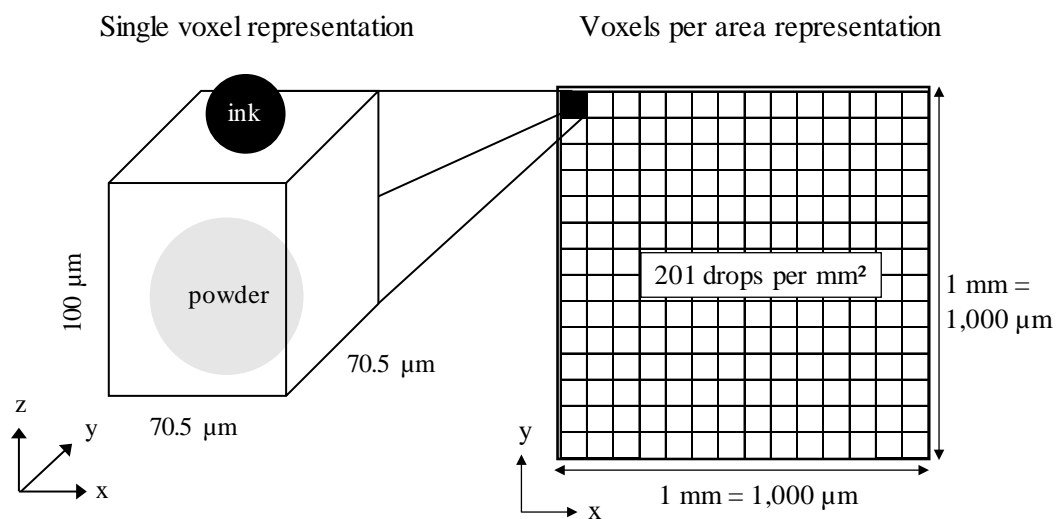
1. The air in the build chamber is kept at a constant temperature. Therefore, heat loss to the air is negligible.
2. There is no heat loss to the metal base plate.
3. The energy balance is computed on the surface area of one voxel as the control system.
4. The IR lamp irradiates the whole surface of the powder build bed.
5. Powder is treated as a discrete element.
6. The powder particles are assumed perfect spheres.
7. The powder particles are uniformly distributed in size.
8. The contact area between two spherical powder particles is a single point. Therefore, heat loss between particles in the sintering region and the surrounding is negligible.
9. Most of the hydrocarbon carrier in the ink vaporise in flight and upon heating. Only carbon black remains on the powder bed during sintering.
10. Carbon black is randomly dispersed across the printed area.

Based on the above assumptions, the total energy can be simplified to the following equation.

$$Q_{\text{Total}} = Q_{\text{Lamp}} + Q_{\text{CB}} \quad \text{Equation 6-2}$$

### 6.2.3 The High Speed Sintering Energy Density Equation

The basis of formulating the  $HSS_{ED}$  equation lies in the consideration of thermal energy input into a single voxel. Powder particles were arranged in simple cubic packing within voxels that correspond to the printhead nozzle pitch ( $70.5 \mu\text{m}$ ). This approach was taken to simplify the calculation of ink droplet size. The size of the voxel was  $70.5 \mu\text{m} \times 70.5 \mu\text{m} \times 100 \mu\text{m}$  (single layer z-height). Figure 6-3 illustrates the positions of powder particle and ink droplet within each voxel, and the number of voxels within a one square millimetre HSS build bed area.



**Figure 6-3** Powder and ink particles within a voxel

Centrally placed within each voxel is a powder particle with a diameter of  $56 \mu\text{m}$  and an ink droplet of varying size. Using the nozzle density, a maximum of 201 voxels can fit within an area of  $1 \text{ mm}^2$ , which is a matrix of  $14.18 \times 14.18$  voxels. Individual ink droplet size can be determined by dividing the ink volume, in  $\text{pL}/\text{mm}^2$  by 201. The drop volume achievable with Xaar 1002 GS6 printhead is between  $6 - 42 \text{ pL}$ . This relationship is employed to calculate the corresponding surface area covered by carbon black at each ink volume used in the PA12 experiment. This calculation is further discussed in Section 6.3.2.

The general equation to calculate the energy,  $Q$  was developed as the following Equation 6-3.

$$Q = \int_{\lambda_1}^{\lambda_2} E_{\lambda} d\lambda \times P \times \left( \frac{r_1^2}{r_2^2} \right) \times A \times \frac{W}{V} \quad \text{Equation 6-3}$$

where  $Q$  is the energy in J,

$E_{\lambda}$  is the effective spectral irradiance in  $\text{W m}^{-2} \text{ nm}^{-1}$ ,

- $\lambda$  is the wavelength in nm,
- $P$  is the lamp power at preheat ( $P_p$ ) or sintering ( $P_s$ ) in %,
- $r_1$  is the distance between the lamp and the detector during test in m,
- $r_2$  is the distance between the lamp and the HSS build bed in m,
- $A$  is the area of powder ( $A_p$ ) or carbon black ( $A_{cb}$ ) at the voxel surface in  $m^2$ ,
- $w$  is the width of a single voxel in m, and
- $v$  is the lamp speed at preheat ( $v_p$ ) or sintering ( $v_s$ ) in m/s.

Irradiance across the visible (VIS) and near infrared (NIR) region was worked out by integrating the area under the curve of effective spectral irradiance. Effective irradiance was used instead of the measured irradiance to mimic the real interaction in HSS. This was achieved by integrating the product curve of the spectral irradiance of lamp with the spectral absorption of powder or carbon black, as presented in Section 6.3.1.

The irradiance was proportionated to the power level of the lamp during operation and its distance from the build bed. According to the inverse square law, the intensity per unit area is inversely proportional to the square of the distance of the point source. Finally, the total irradiance was determined by multiplying it with radiated area and lamp exposure time.

Equation 6-3 was modified into Equation 6-4 and Equation 6-5, to calculate the energy input from the lamp and the heat transfer by the carbon black respectively. The total energy from the lamp can be separated into two parts, which were energy during preheat ( $Q_p$ ) and sintering ( $Q_s$ ).

$$Q_{\text{Lamp}} = Q_p + Q_s = \left[ \left( \int_{\lambda_1}^{\lambda_2} E_{1\lambda} d\lambda \right) \left( \frac{r_1^2}{r_2^2} \right) (A_p) \left( P_p \frac{w}{v_p} + P_s \frac{w}{v_s} \right) \right] \quad \text{Equation 6-4}$$

$$Q_{\text{CB}} = \left( \int_{\lambda_1}^{\lambda_2} E_{2\lambda} d\lambda \right) (P_s) \left( \frac{r_1^2}{r_2^2} \right) (A_{cb}) \left( \frac{w}{v_s} \right) \quad \text{Equation 6-5}$$

Based on Equation 6-2, the total energy input is the sum of  $Q_{\text{Lamp}} + Q_{\text{CB}}$  (Equation 6-4 and Equation 6-5). Hence, the  $\text{HSS}_{\text{ED}}$  equation can be written as follows.

$$\text{HSS}_{\text{ED}} = \overbrace{\left[ \left( \int_{\lambda_1}^{\lambda_2} E_{1\lambda} d\lambda \right) \left( \frac{r_1^2}{r_2^2} \right) (A_p) \left( P_p \frac{w}{v_p} + P_s \frac{w}{v_s} \right) \right]}^{Q_{\text{Lamp}}} + \overbrace{\left[ \left( \int_{\lambda_1}^{\lambda_2} E_{2\lambda} d\lambda \right) (P_s) \left( \frac{r_1^2}{r_2^2} \right) (A_{cb}) \left( \frac{w}{v_s} \right) \right]}^{Q_{\text{CB}}}$$

Equation 6-6

### 6.3 Determination of Input Data

This section reports the methodology used to obtain the values of variables required to calculate the  $HSS_{ED}$  values.

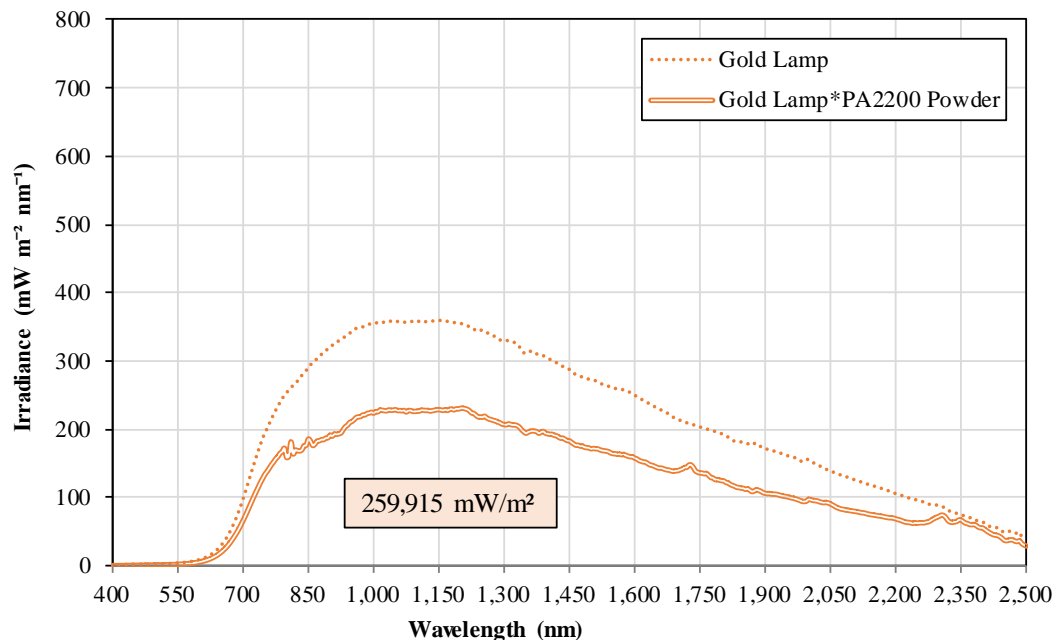
#### 6.3.1 Effective Spectral Irradiance

The spectral data used in this section was obtained from Section 3.4.

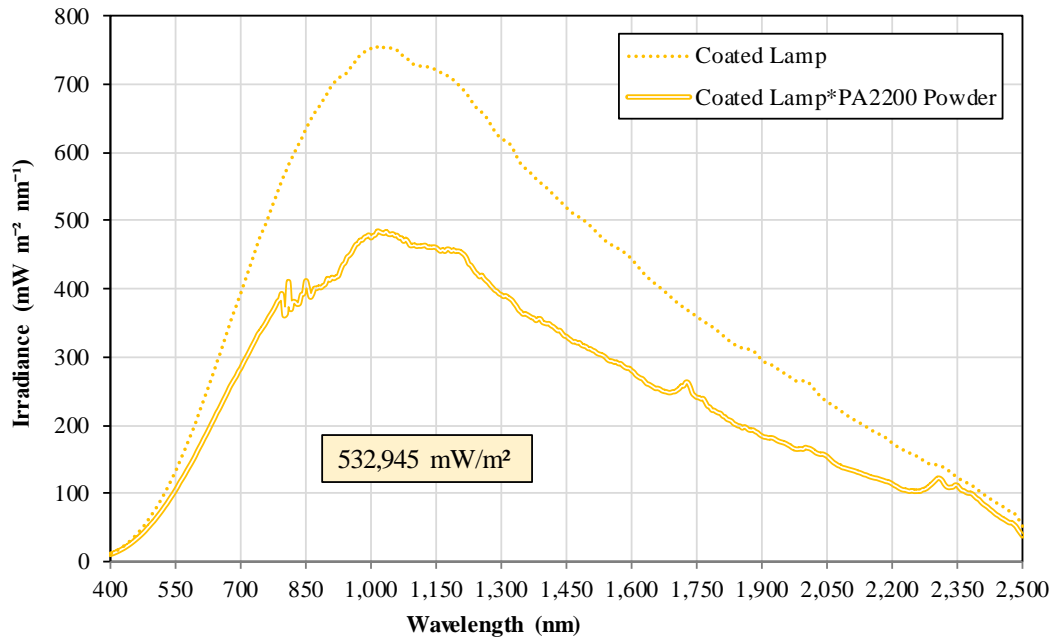
The spectral irradiance of both gold and coated lamps were multiplied with the percentage spectral absorption of PA2200 powder (see Figure 3-9). The resultant curves are plotted as double lines (lamp\*PA2200 powder) in Figure 6-4 and Figure 6-5, respectively. The area under the double line was determined using a first order numerical integration using the following equation.

$$E_1 = \sum_{i=400}^{2500} \frac{(E_{1\lambda_i} + E_{1\lambda_j})}{2} \times (\lambda_j - \lambda_i) \quad \text{Equation 6-7}$$

For the irradiance of lamp multiplied by powder, the area was calculated at a wavelength interval of 5 nm. The area under the curve is shown on the figure, in  $mW\ m^{-2}$  unit.



**Figure 6-4** Effective irradiance of gold lamp x powder; the lamp power absorbed by the powder without ink



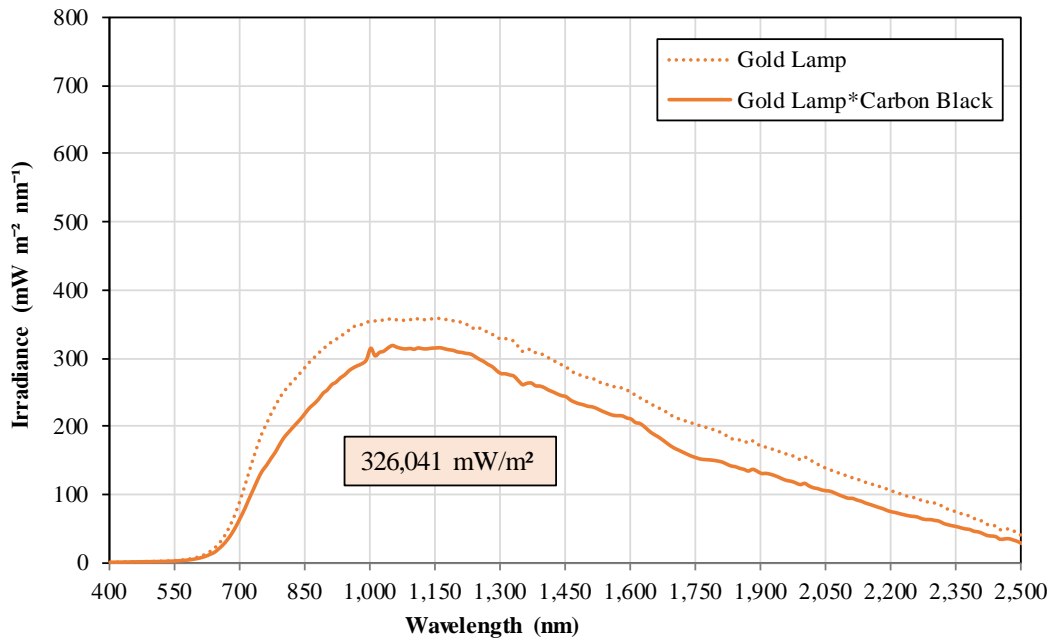
**Figure 6-5** Effective irradiance of coated lamp x powder; the lamp power absorbed by the powder without ink

In Figure 6-4, the effective irradiance of gold lamp\*PA2200 powder was approximately 260 W/m<sup>2</sup>, which was around 65% the original irradiance. The spectral curve had maintained its shape and the wavelength at which peak irradiance occurred. The powder was absorbent towards the end of the NIR region, at around 2,300 nm and above. Similar trends can be observed for coated lamp in Figure 6-5. The effective irradiance of coated lamp\*PA2200 powder was higher at 533 W/m<sup>2</sup>.

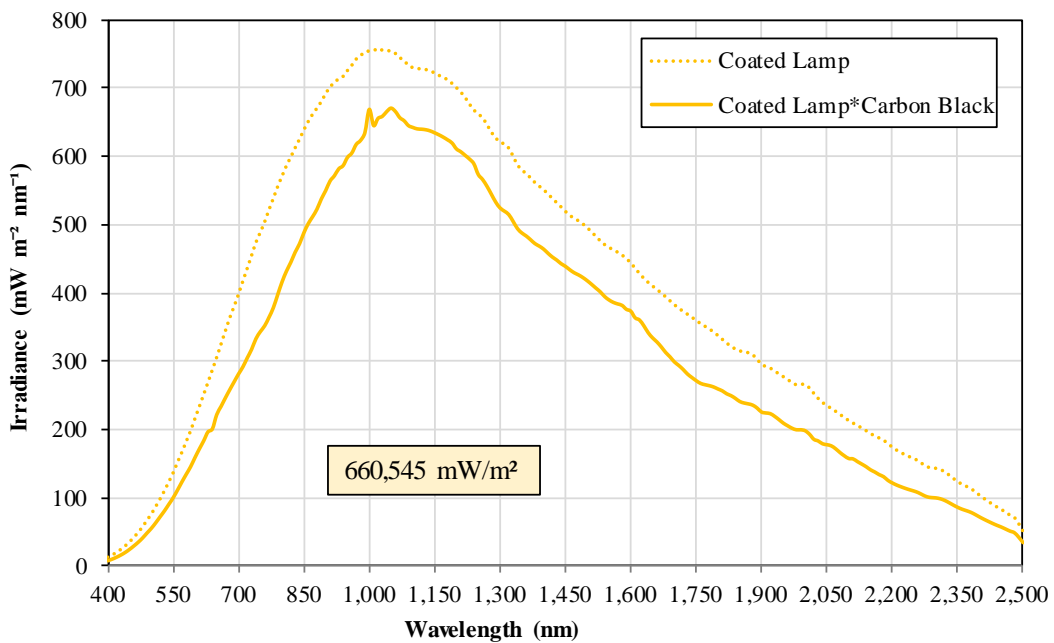
Next, the spectral irradiance of both the gold and coated lamps were multiplied with the percentage spectral absorption of carbon black powder (Figure 3-8). The resultant curves are plotted in Figure 6-6 and Figure 6-7, respectively. The area under the double line was determined using a first order numerical integration in the following Equation 6-8.

$$E_2 = \sum_{i=400}^{2500} \frac{(E_{2\lambda_i} + E_{2\lambda_j})}{2} \times (\lambda_j - \lambda_i) \quad \text{Equation 6-8}$$

Due to the difference in data collection techniques between the two curves, the area was calculated at a bigger wavelength interval of 10 nm. The area under the curve is shown on the figure, in mW m<sup>-2</sup> unit.



**Figure 6-6** Effective irradiance of gold lamp x carbon black; the lamp power absorbed by the ink



**Figure 6-7** Effective irradiance of coated lamp x carbon black; the lamp power absorbed by the ink

Carbon black had maximum absorptivity at around 1,000 – 1,150 nm, which was similar to the peak irradiance of both lamps. From Figure 6-6 and 6-7, it can be observed that the curves had kept their characteristic shape and only shifted slightly lower. The irradiance was 326 W/m<sup>2</sup> for gold lamp\*carbon black, and 661 W/m<sup>2</sup> for coated lamp\*carbon black. These areas translated into 81% heat transfer efficiency between the lamp and the carbon black.

### 6.3.2 Properties of Carbon Black

The HSS<sub>ED</sub> model concerns the influence of carbon black exclusively. The physical properties of carbon black were calculated from the ink and printhead. Table 6-1 lists the parameters for the drop-on-demand Xaar 1002 GS6 printhead used in the experiment.

**Table 6-1** Printhead parameters

<b>Xaar 1002 GS6 printhead</b>	<b>Value</b>	<b>Source</b>
Nozzle density (nozzles per inch)	360	Manufacturer's data sheet
Nozzle density (nozzles per mm <sup>2</sup> )	201	Calculated. 1 inch ~ 25 mm
Ink drop volume	6 – 42 pL	Manufacturer's data sheet
Range of ink volume	1,205 – 8,435 pL/mm <sup>2</sup>	Calculated

The nozzle density per square millimetres was obtained through unit conversion as shown in Figure 6-3. The range of ink volume was the product of the nozzle density per mm<sup>2</sup> and the drop volume. In HSS printing, the ink volume was the input parameter and the printhead adjusted its drop volume accordingly. Conversely, the drop volume can be determined by the ink volume.

Theoretically, the surface area of carbon black can be determined from the ink drop volume, ink density, weight percentage of carbon black and its statistical thickness surface area (STSA) using the following equation.

$$\text{Area of carbon black} = \frac{\text{Ink drop volume} \times \text{Ink density} \times \text{Carbon black wt\%} \times \text{STSA}}{(100 - \text{Carbon black wt\%})}$$

Equation 6-9

where ink density = 850 kg/m<sup>3</sup> and STSA = 123 m<sup>2</sup>/g. The results are shown in Table 6-2.

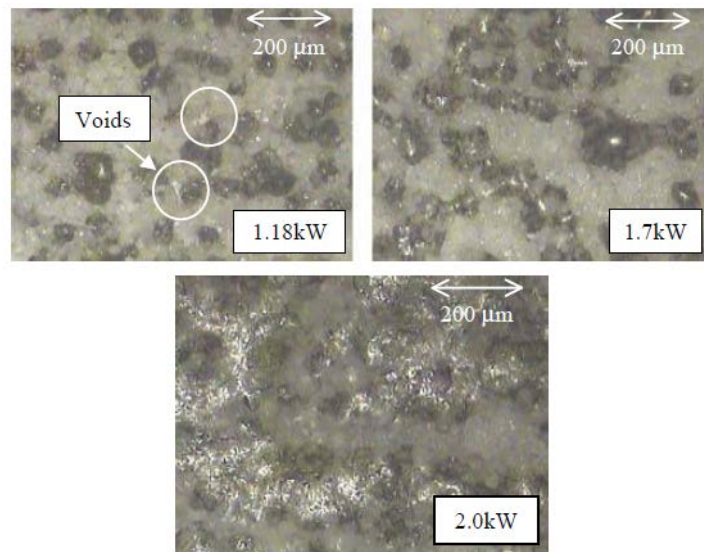
**Table 6-2** Carbon black calculation

<b>Ink volume (pL/mm<sup>2</sup>)</b>	<b>Ink drop volume (pL)</b>	<b>Surface area of carbon black (m<sup>2</sup>)</b>
1,500	7	8.67E-08
3,000	15	1.73E-07
4,500	22	2.60E-07
6,000	30	3.47E-07
7,500	37	4.34E-07



However, the surface area alone cannot be used for this model, as the surface area is a function of particle size, porosity and degree of aggregation. Carbon black has a high surface area to volume; hence, the surface area will not accurately represent the dispersion of carbon black over the area.

Previous study by Majewski et al. (2008) also reported that the carbon black does not provide a full coverage of the printed area, but form discrete aggregates instead. Figure 6-8 illustrates the dispersion of ink with 80 pL drop volume on nylon 12 powder bed (Majewski et al., 2008).



**Figure 6-8** Distribution of carbon black on printed area, seen as black blotches on white powder

The  $HSS_{ED}$  model only considers the interaction on the surface area of the voxel and as such, the relative carbon black area cannot be accurately determined with the data available. For the above reasons, a different method was employed to estimate the surface area of carbon black on the voxel surface, which assumes a direct proportionality between drop volume and surface area. It was assumed that carbon black completely covers the surface area of the voxel at the maximum droplet size of 42 pL or maximum ink volume of 8,435 pL/mm<sup>2</sup>. The surface area of carbon black at other ink volumes can be interpolated from this relationship. Figure 6-9 plots the relationship for a voxel size of 70.5 x 70.5 μm.

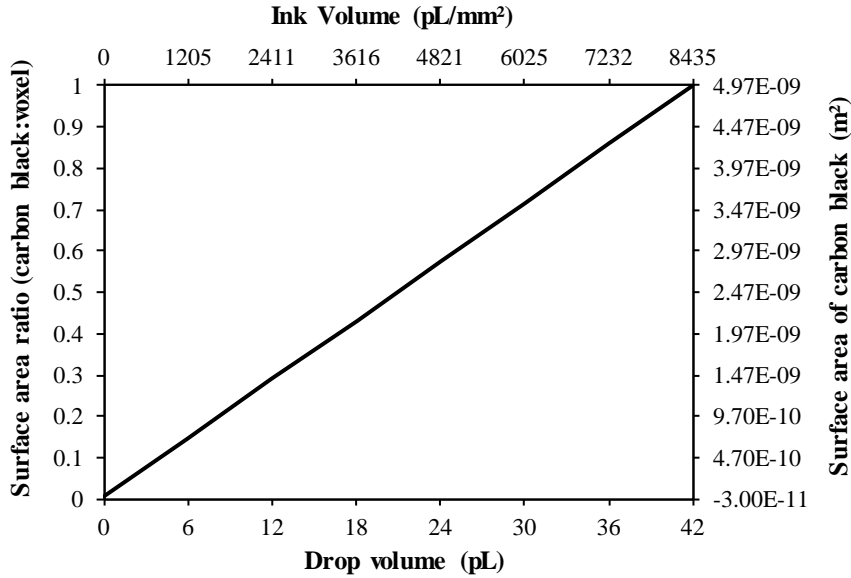


Figure 6-9 Approximation of carbon black surface area as a function of ink volume

The carbon black surface area at each ink level is listed in Table 6-4.

### 6.3.3 Other Input Data

Table 6-3 – 6.5 summarise the input data used to derive the  $HSS_{ED}$  equation. The  $HSS_{ED}$  values are calculated and reported in Section 6.4.2.

Table 6-3 Initial conditions and material constants for powder

	Input variable	Value	Source/Formula
<b>Powder</b>	Particle size, $d_p$	$5.6 \times 10^5$ m	Manufacturer's data sheet
	Surface area, $A_p$	$2.46 \times 10^{-9}$ m <sup>2</sup>	$A = \pi(d_p/2)^2$
	Volume, $V$	$9.20 \times 10^{-14}$ m <sup>3</sup>	$V = \frac{4}{3}\pi(d_p/2)^3$
	Bulk density, $\rho$	450 kg/m <sup>3</sup>	Manufacturer's data sheet
	Specific heat capacity, $C_p$	2,350 J/kg°C	Manufacturer's data sheet
	Melting temperature, $T_m$	185°C	DSC curve
	Preheat build bed temperature, $T_p$	171°C	Reading on HSS machine
	Initial build bed temperature, $T_b$	166°C	Build parameters
	Enthalpy heat of fusion, $\Delta h_f$	52,363 J/kg	Integration of DSC curve
	Irradiance gold lamp*powder, $E_{1,gold}$	260 W/m <sup>2</sup>	Integration of irradiance curve
	Irradiance coated lamp*powder, $E_{1,coated}$	33 W/m <sup>2</sup>	Integration of irradiance curve

**Table 6-4** Material constants and build conditions for carbon black

	<b>Input variable</b>	<b>Value</b>	<b>Source/Formula</b>
<b>Carbon Black</b>	Percentage of carbon black in ink, %CB	10 wt%	Manufacturer's data sheet
	Irradiance gold lamp*carbon black, $E_{2,gold}$	326 W/m <sup>2</sup>	Integration of irradiance curve
	Irradiance coated lamp*carbon black, $E_{2,coated}$	661 W/m <sup>2</sup>	Integration of irradiance curve
	Width of voxel, w	7.05 x 10 <sup>-5</sup> m	Manufacturer's data sheet
	Surface area of voxel, $A_v$	4.90 x 10 <sup>-9</sup> m <sup>2</sup>	Calculated
	Dispersed area @ 1,500 pL/mm <sup>2</sup> , $A_{cb,1500}$	8.84 x 10 <sup>-10</sup>	Calculated from ink volume
	Dispersed area @ 3,000 pL/mm <sup>2</sup> , $A_{cb,3000}$	1.77 x 10 <sup>9</sup>	Calculated from ink volume
	Dispersed area @ 4,500 pL/mm <sup>2</sup> , $A_{cb,4500}$	2.65 x 10 <sup>9</sup>	Calculated from ink volume
	Dispersed area @ 6,000 pL/mm <sup>2</sup> , $A_{cb,6000}$	3.54 x 10 <sup>9</sup>	Calculated from ink volume
	Dispersed area @ 7,500 pL/mm <sup>2</sup> , $A_{cb,7500}$	4.42 x 10 <sup>9</sup>	Calculated from ink volume

**Table 6-5** Initial and build conditions for IR lamp

	<b>Input variable</b>	<b>Value</b>	<b>Source/Formula</b>
<b>Lamp</b>	Distance between lamp and detectors, $r_1$	0.5 m	Spectral irradiance test
	Distance between lamp and build bed, $r_2$	0.012 m	Measured on HSS machine
	Speed on preheat pass, $v_p$	0.15 m/s	Build parameters
	Speed on sintering pass, $v_s$	0.12 m/s	Build parameters
	Power on preheat pass, $P_p$	0.5	Build parameters
	Power on sintering pass, $P_s$	1	Build parameters
	Exposure time during preheat, $t_p$	4.7 x 10 <sup>-4</sup> s	$t_p = w/v_p$
	Exposure time during sintering, $t_s$	5.88 x 10 <sup>-4</sup> s	$t_s = w/v_s$

Again, the HSS<sub>ED</sub> equation is given as follows.

$$HSS_{ED} = \left[ \left( \int_{\lambda_1}^{\lambda_2} E_{1\lambda} d\lambda \right) \left( \frac{r_1^2}{r_2^2} \right) (A_p) \left( P_p \frac{w}{v_p} + P_s \frac{w}{v_s} \right) \right] + \left[ \left( \int_{\lambda_1}^{\lambda_2} E_{2\lambda} d\lambda \right) (P_s) \left( \frac{r_1^2}{r_2^2} \right) (A_{cb}) \left( \frac{w}{v_s} \right) \right]$$

**Figure 6-10** The HSS<sub>ED</sub> model equation

## 6.4 Validation of HSS Energy Density Model

The HSS<sub>ED</sub> values were validated against theoretical energy values required to melt powder. The experimental builds from previous Chapter 5 were assigned their corresponding HSS<sub>ED</sub> values. Correlations were established between HSS<sub>ED</sub> and part properties. Next, the energy difference between the unsintered and sintered region was analysed.

### 6.4.1 Energy Needed to Melt Powder

A study by Starr et al. (2011) introduced the energy-melt ratio (EMR) as the ratio of energy density (Andrew Number) to the energy needed to melt one layer of powder in LS. EMR values of higher than one is desirable to achieve full mechanical properties. The energy-to-melt layer was calculated using Equation 6-10 and based on the material specific properties in Table 6-6 (Starr et al., 2011).

$$E_{LS} = [c_p(T_m - T_b) + h_f](\delta_s)(\delta_d) \quad \text{Equation 6-10}$$

**Table 6-6** Properties to calculate energy-to-melt layer by Starr et al.

<b>Nylon 12 powder</b>	<b>Symbol</b>	<b>Value</b>
Specific heat capacity	C <sub>p</sub>	4,040 J/kg °C
Melt temperature	T <sub>m</sub>	186°C
Build bed temperature	T <sub>b</sub>	166°C
Enthalpy of fusion	h <sub>f</sub>	108,000 J/kg
Bulk density	δ <sub>s</sub>	970 kg/m <sup>3</sup>
Packing density	δ <sub>d</sub>	0.5
Energy-to-melt layer		0.091 J/mm <sup>3</sup>

The energy-to-melt layer considers a layer of continuous power particles packed in simple cubic facing arrangement. While this method is sufficient for the LS process, the addition of carbon black complicates the selection of control volume in HSS. The energy input in HSS was also split between preheat and sintering passes.

In accordance with the HSS<sub>ED</sub> model approach, the energy required to melt a single powder particle in HSS was determined as follows.

$$\sum E_{\text{HSS}} = E_a + E_b + E_c = (\rho)(V)[c_p(T_m - T_b) + \Delta h_f] \quad \text{Equation 6-11}$$

where

$E_a$  is the energy required to raise the powder temperature during preheat, in J,

$E_b$  is the energy required to raise the powder temperature during sintering, in J, and

$E_c$  is the enthalpy required for phase change, in J.

The material properties used to calculate this energy can be found in Table 6-3. The individual formula to calculate  $E_a$ ,  $E_b$ , and  $E_c$  are given as follows.

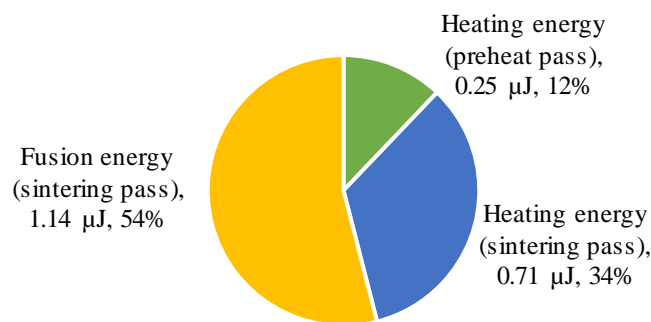
$$m = \rho \times V \quad \text{Equation 6-12}$$

$$E_a = m \times c_p \times (T_p - T_b) \quad \text{Equation 6-13}$$

$$E_b = m \times c_p \times (T_m - T_p) \quad \text{Equation 6-14}$$

$$E_c = m \times \Delta h_f \quad \text{Equation 6-15}$$

The energy distribution is illustrated as a percentage of the total energy in Figure 6-11.



**Figure 6-11** Energy distribution in HSS processing

More than half the energy was required for phase change. The total energy required to melt a powder particle was found to be  $2.10 \times 10^{-6}$  J, or simply 2.10 μJ. The energy needed to melt one voxel packed with powder was 11.4 μJ. An equivalent energy-to-melt value from the EMR model was calculated as 51.5 μJ, which is significantly higher. It is noted that the material properties used in the EMR model was higher than in this experiment. For example, the density of sintered powder was used instead of bulk density in their study. Their enthalpy of fusion was also double the area under the melt peak obtained from the DSC curve in this experiment.

### 6.4.2 Determination of HSS Energy Density for PA12 Experiment

Figure 6-12 plots the HSS<sub>ED</sub> values against the ten HSS builds from the PA12 experiment. A legend of build names and their corresponding parameters is provided on the right side of the chart. The total energy density for each build was split into two parts, the energy radiated by the IR lamp and the energy conducted by the carbon black.

The energy required to melt a powder particle was indicated by a horizontal line at 2.10 μJ. If the energy density surpasses this line, then it can be assumed that a full sintering was achieved. The lamp energy on its own must not exceed the energy required for sintering, as this implies that all powder will be sintered in the absence of carbon black (or any other type of RAM).

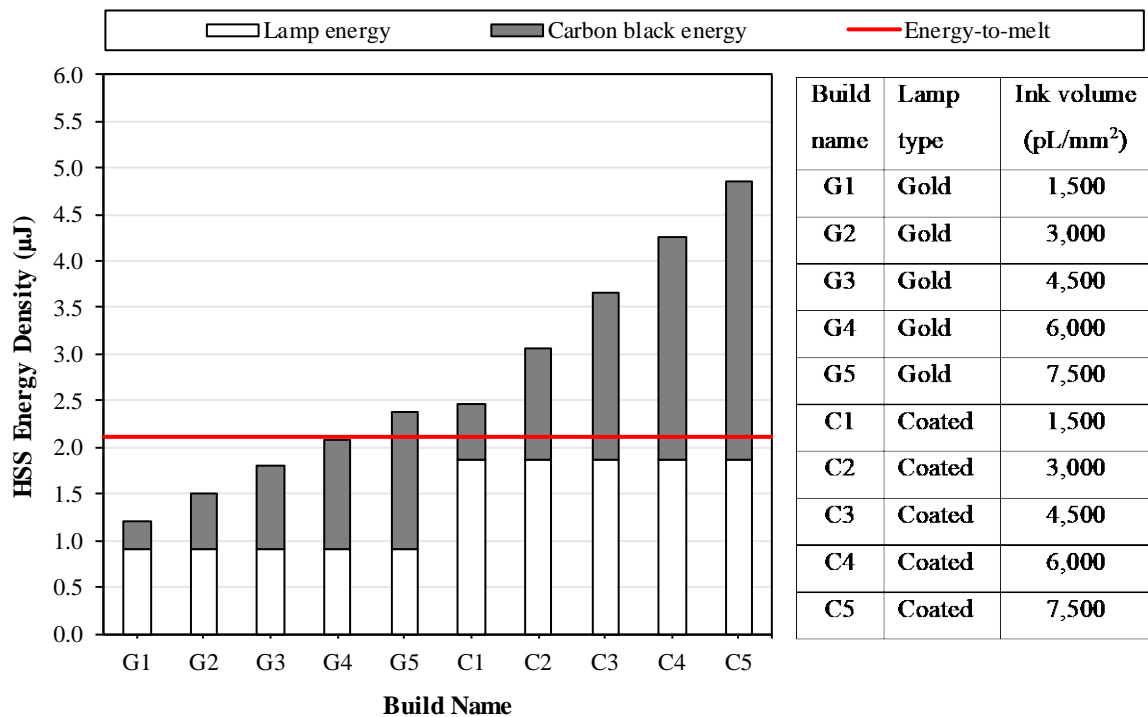


Figure 6-12 HSS energy density values of parts from the PA12 experiment

From the above figure, it can be seen that the energy contributed by the lamp was constant for each lamp configuration, as it was derived from the lamp spectral output and constant machine parameters. The irradiance of coated lamp was twice as high as the gold lamp, and this was translated into the amount of energy radiated from them. The energy output from the gold and coated lamp were calculated to be 0.91 μJ and 1.87 μJ, respectively. The lamp energy in all builds was lower than the theoretical energy required for powder melting. This proves that the

heat transfer from the carbon black is crucial to melt the printed area and create the energy difference needed between the sintered and unsintered regions.

The increment in ink volume resulted in an increased energy transfer from the carbon black particles in the ink. In general, the energy from carbon black made up between 24 – 60 percent of the total energy density. Six out of ten builds had sufficient energy to overcome the energy required to heat and melt the powder (threshold). These builds were all coated lamp builds except for one. This indicates that the coated lamp is better suited for HSS processing with this set of parameters, delivering up to 2.3 times the required amount of energy at the highest ink level.

### 6.4.3 Correlation between HSS Energy Density and Ultimate Tensile Strength

Figure 6-13 shows the predicted correlation between the HSS<sub>ED</sub> values and ultimate tensile strength (UTS).

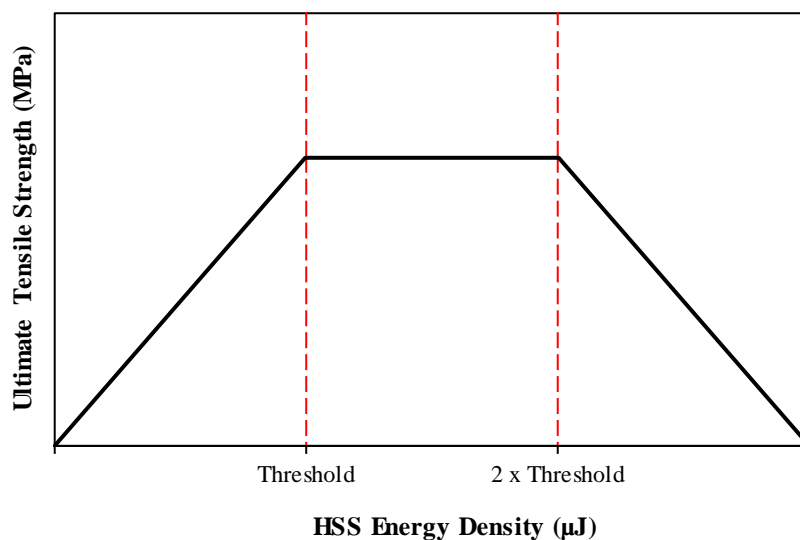
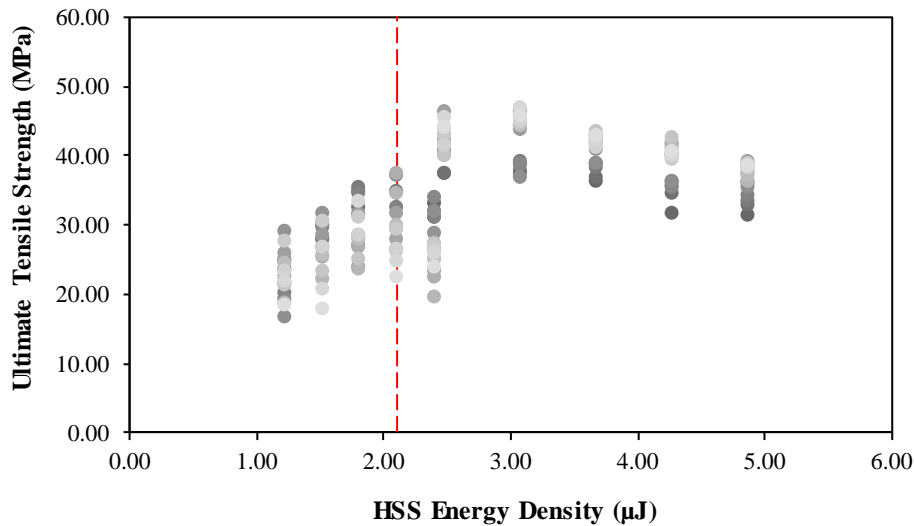


Figure 6-13 Predicted correlation between HSS energy density and ultimate tensile strength

A linear correlation is predicted between HSS<sub>ED</sub> and UTS up to the threshold point. By taking into consideration the heat loss to the surrounding, it is expected that the powder will continue to absorb enough energy in the area between threshold energy and up to twice the amount. As the powder temperature draws closer to the onset of polymer degradation, the UTS will start to decline.

Figure 6-14 plots the measured UTS of 172 parts against  $HSS_{ED}$ . The dotted line represents the calculated energy threshold for optimum sintering of PA12 powder ( $2.10 \mu J$ ).



**Figure 6-14** Correlation between HSS energy density and ultimate tensile strength

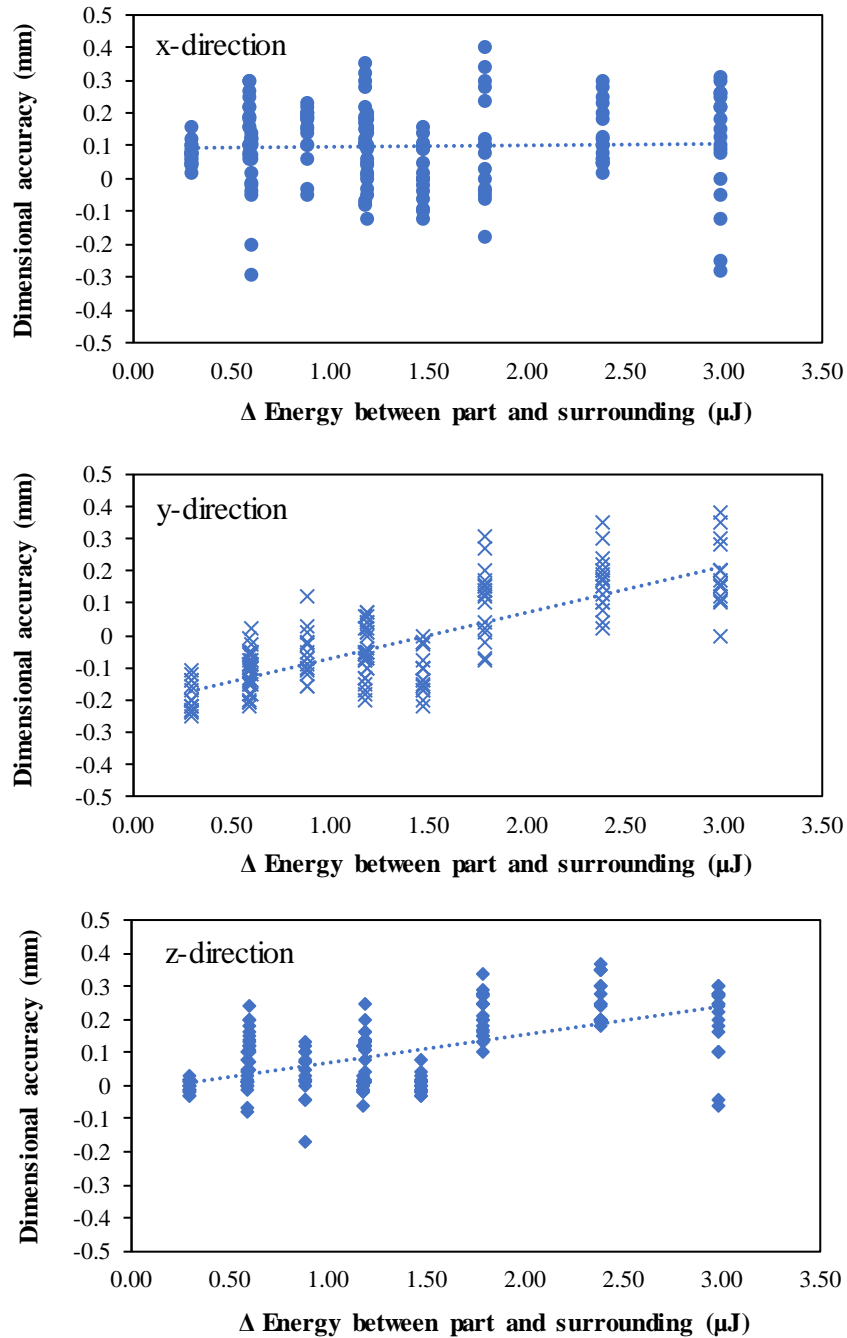
A linear region existed up to the threshold line as predicted. It is interesting to note that the UTS dipped just after the threshold, before rising again. It can be inferred that polymer degradation occurs at higher energy density levels, leading to lower UTS. However, it is not obvious from this dataset where the turning point is.

#### 6.4.4 Correlation between Energy Gradient and Dimensional Accuracy

The energy difference between the unsintered and sintered region in HSS is primarily contributed by the thermal energy conducted by the carbon black at sintering. This energy difference has been quantified as the carbon black energy in Figure 6-12, and it creates a temperature gradient on the perimeter of a part.

The correlation between the energy difference and dimensional accuracy is plotted in Figure 6-15. There were more parts built at the lower energy difference levels compared to the higher end in the experiment. This makes for a less dense plot at the further end of the chart.





**Figure 6-15** Energy gradient effect on the dimensional accuracy of parts in x, y, and z directions

Positive correlation can be seen between the energy difference and the dimensional accuracy in y- and z- directions. The higher the temperature gradient between the part and surrounding powder, the more positive the deviation. The correlation is more evident in wall growth than shrinkage, and is more pronounced in parts towards the higher end of the energy difference.

Optimum energy difference, where a deviation of 0 mm can be achieved, was observed at 1.50  $\mu\text{J}$  for y-direction, and at 0.30  $\mu\text{J}$  for z-direction. In both directions, an energy difference

between 0.60 and 1.50  $\mu\text{J}$  resulted in the highest dimensional accuracies of parts. A higher temperature gradient drives heat transfer by conduction from the printed region to the powder surrounding. If the excess energy is sufficiently high to overcome the energy to melt, excess powder is sintered, resulting in positive deviation.

Similar to the ANOVA result in Table 5-6, dimensional accuracy in x-direction is not affected by the lamp power or energy. It can be speculated that the dimensional accuracy in x-direction is influenced by the mechanisms of ink droplet formation and spreading, as it is in the same direction as carriage motion and sintering.

## 6.5 Summary

An analytical model, the  $\text{HSS}_{\text{ED}}$  model was developed to quantify the energy density of a part. Findings from this study can be further developed into computational models such as a three-dimensional transient heat transfer finite element analysis to simulate heat distribution on the HSS build bed. The  $\text{HSS}_{\text{ED}}$  model was validated empirically using the data from Chapter 5.

The  $\text{HSS}_{\text{ED}}$  model equation was formulated based on the heat transfer calculated on a voxel surface. The interaction between the infrared (IR) lamp, carbon black in ink, and powder was studied. Input data was obtained through HSS build parameters and various characterisation techniques, some of which were discussed in Chapter 3. The amount of energy irradiated by the IR lamp alone must not exceed the amount of energy required to melt powder, i.e. threshold energy. The additional energy conducted by the carbon black to the underlying powder surpassed the threshold energy. Positive correlation was found between energy density and measured UTS. Positive correlation was also found between the energy gradient on part perimeter and its dimensional accuracy.

## 6.6 References

1. Majewski, C. E., Oduye, D., Thomas, H. R. & Hopkinson, N. 2008. Effect of infra-red power level on the sintering behaviour in the high speed sintering process. *Rapid Prototyping Journal*, 14(3), 155-160.
2. Nelson, J. C. 1993. *Selective laser sintering: a definition of the process and an empirical sintering model*. PhD Thesis, University of Texas.
3. Starr, T. L., Gornet, T. J. & Usher, J. S. 2011. The effect of process conditions on mechanical properties of laser-sintered nylon. *Rapid Prototyping Journal*, 17(6), 418-423.

# Chapter 7    Conclusions and Recommendations for Future Work

## 7.1 Conclusions

The aim of the research was to optimise the HSS process for commercialisation. The findings had explored the HSS process chain and provided an understanding of the effect of parameters on manufactured part properties. This research had also established the commercial viability of the HSS process and developed novel methods to evaluate and monitor part quality and process repeatability, which are highly essential in a batch production setting.

This section discusses the conclusions for the work presented in the thesis.

1. The DSC analysis of a feed material provided its HSS processing window, which is an optimum processing temperature range between melting and crystallisation. The technique also illustrated the crystallinity of a material (i.e. amorphous or semi-crystalline).
2. SEM reveals the different particle morphology between the cryogenically milled elastomer and the commercial nylon powder produced through precipitation.
3. A systematic study of the HSS process chain mapped out the relevant areas that can affect the properties of manufactured parts. The properties of interest were dimensional accuracy and tensile strength, and the relevant factors identified include thermal energy input during sintering and powder removal during post-processing.
4. There was a trade-off between dimensional accuracy and tensile strength in high speed sintered parts. The build parameters need to be optimised when manufacturing parts that require a good balance of both properties.
5. ALM TPE210-S, a nylon thermoplastic elastomer, was successfully processed on the HSS machine using an optimised set of parameters. Consequently, the surface roughness was better but tensile properties were lower than previously reported values. A summary of the properties is given as follows:  $R_a = 20 - 45 \mu\text{m}$ ,  $UTS = 0.82 \text{ MPa}$ ,  $E = 3.93 \text{ MPa}$ , and  $EaB = 119 \%$ .

6. The dimensional accuracy of TPE parts was better in z-direction at  $\pm 0.50$  mm than in x- and y- directions at  $\pm 2.00$  mm. Wall growth was observed in y- and z-directions, whereas both wall growth and shrinkage were evident in x-direction.
7. A novel post-processing technique, the PUSH process was introduced to improve powder removal. The process was effective at improving surface roughness and incidentally mechanical properties by at least 50 %, but it reduced the part dimensions by an average of 5 %. The directional dimensional effect of PUSH was inconsistent throughout the analysis, which was attributed to the geometrical difference between the parts.
8. A cost analysis model for HSS was successfully developed by formulating the HSS material cost category and implementing it into an existing LS cost analysis model by Hopkinson and Dickens (2003). The cost per part for three sizes of HSS machines were half the LS equivalent, but still twice as high as an injection-moulding equivalent. Material cost was constituted as the highest cost category, both in HSS and LS.
9. Nylon-12 parts were manufactured using EOS PA2200 powder. Wall growth was prevalent in x- and z-directions, while shrinkage was consistently exhibited in y-direction. The dimensional accuracy was  $\pm 0.20$  mm in all directions. The effect of lamp type (power) on dimensional accuracy was more significant than the ink volume.
10. Tensile strength of parts made using the coated lamp (40.20 MPa) were superior than the parts made using the gold lamp (27.24 MPa). Consequently, the coated lamp parts had a low powder removal score, at only 10 – 30 %.
11. Variability in tensile strength was observed between parts depending on where they were located within the HSS build chamber during sintering. The central rear section of the chamber was found to produce parts with the highest tensile strength.
12. A quality assessment method was developed by measuring the reflectance of a part using visible spectroscopy. Positive correlation was found between reflectance and tensile strength. This technique can be used to assess inter-batch and intra-batch repeatability non-destructively, and to predict a part's tensile strength based on its reflectance.
13. The HSS<sub>ED</sub> model was another novel development within the framework of quality assessment and improvement. The model was validated using input data collected from

the characterisation of materials and equipment via IR spectroscopy and the characterisation of parts through mechanical testing. When a part absorbs sufficient energy to surpass the energy needed to melt the powder (threshold energy), a range of high tensile strength was observed. There was a positive correlation between energy gradient and the achieved dimensional accuracy, where an optimum energy gradient of 1.50  $\mu\text{J}$  can be interpolated.

14. The HSS<sub>ED</sub> model needed more iteration in order to simulate the complete heat transfer in HSS. Further development required for the model and other recommendations for future work are discussed in the following section.

## **7.2 Recommendations for Future Work**

1. For the HSS<sub>ED</sub> model, the analysis can be performed by considering the whole bed area instead of within one voxel. By doing so, the powder bed can be assumed as being continuous. The deposition of carbon black over the powder bed and its effective surface area need to be studied. By working out the thermal conductivity of air, heat convection within the build chamber can be calculated. The findings from this analytical model can be fed into a computational modelling to better simulate the process in transient phase.
2. The feasibility study of reflectance was conducted using a small sample size. A further development of the technique can be achieved by using a larger sample size, with repeated measurements across different locations on the parts.
3. The cost per part made using an AM process can be significantly reduced if the material cost can be lowered. Currently, most AM machine vendors dictate the powder that can be processed with their machines. An open supply chain can not only reduce the material cost, but also drive the development of AM to be implemented for industrial application.
4. The dimensional change in PUSH parts are unavoidable but should be made more consistent across all directions and different part geometries. If the percentage of change is known and dependable, the correct scale factor can be applied to the build files before part manufacturing. Current limitation in the process is the unidirectional application technique. The process would greatly benefit from an automation process, both to increase the quality of application and to reduce application time.

# Appendices

<i>Appendix A</i>	Material data sheet for ALM TPE210-S
<i>Appendix B</i>	Material data sheet for EOS PA2200
<i>Appendix C</i>	Cost analysis calculations (Chapter 4)
<i>Appendix D</i>	Preliminary work on high speed sintered TPE210-S
<i>Appendix E</i>	ANOVA tables for dimensional accuracy (Chapter 5)

## MATERIAL SPECIFICATIONS

# TPE 210-S

### HIGHLIGHTS

- Soft, white parts out of the machine
- Extreme elongations achievable without permanent deformation
- Easy to infiltrate to obtain maximum properties
- 100% recyclable

### APPLICATIONS

- Footwear prototyping
- Automotive gaskets and seals
- Cushioning applications
- Ideal for applications requiring softer parts with excellent ductility and surface finish

## TYPICAL PHYSICAL PROPERTIES

PROPERTY	TEST METHOD	U.S. STANDARD	METRIC
Colour/Appearance	Visual	White	White
Bulk Density	ASTM D1895	0.214 oz/in <sup>3</sup>	0.37 g/cm <sup>3</sup>
Elongation at Break	ASTM D638	110%	110%
Flexural Modulus (-40°C)	ASTM D790	3,336 psi	23 MPa
Flexural Modulus (23°C)	ASTM D790	1,885 psi	13 MPa
Flexural Modulus (100°C)	ASTM D790	435 psi	3 MPa
Initial Tear Resistance, Die C, 23°C	ASTM D624	7.4 lbf	33 N
Abrasion Resistance, Taber H-18 Wheel	ASTM D4060	0.012 oz	535 mg
Shore Hardness, Shore "A"	ASTM D2240	40	40
Tensile Modulus	ASTM D638	1,160 psi	8 MPa
Average Particle Size (D50)	Laser Diffraction	0.003 inches	85 microns
P article Size Range (D10-D90)	Laser Diffraction	0.001 - 0.005 inches	20 - 130 microns
Sintered Part Density	ASTM D792	0.595 oz/in <sup>3</sup>	1.03 g/cm <sup>3</sup>

For reference use only. Actual properties may vary significantly from those listed above based on processing parameters, operating conditions and end use applications. The above properties were based on virgin ALM TPE 210-S using normal processing parameters on a 2500+ platform as outlined in the ALM Material Processing Guide. Advanced Laser Materials, LLC makes no warranties of materials for any application, nor does it make a warranty of any type, expressed or implied, but not limited to, the warranties of merchantability for a particular purpose.



RP Support Ltd.  
14 Bridgegate Business Park  
Gatehouse Way  
Aylesbury  
Buckinghamshire  
HP19 8XN  
United Kingdom  
+44 (0)1296 425665  
+44 (0)1296 425665  
support@rpsupport.co.uk



ALM TPE 210-S: 02.04.2013



## Material data sheet

### PA 2200

#### 1 General

Typical applications of the material are fully functional parts with high end finish right from the process, which easily withstand high mechanical and thermal load.

PA 2200 is suitable for processing on the following systems:

- EOSINT P 730, P 700
- EOSINT P 390, P 385, P 380i, P 380, with or without powder conveying system  
EOSINT P 360, P 350/2 with upgrade 99
- FORMIGA P 100

#### 2 Technical data

##### General material properties

Average grain size	ISO 13320-11	56	µm
	Laser diffraction	2.20	mil
Bulk density	EN ISO 60	0.45	g/cm <sup>3</sup>
Density of laser-sintered part	EOS method	0.93	g/cm <sup>3</sup>
		58	lb/ft <sup>3</sup>

##### Mechanical properties

Tensile modulus	EN ISO 527	1700	MPa
	ASTM D638	247	ksi
Tensile strength	EN ISO 527	48	MPa
	ASTM D638	6962	psi

##### EOS GmbH - Electro Optical Systems

Robert-Stirling-Ring 1  
D-82152 Krailling / München

Telephone: +49 (0)89 / 893 36-0  
Telefax: +49 (0)89 / 893 36-285  
Internet: [www.eos.info](http://www.eos.info)





## Material data sheet

Elongation at break	EN ISO 527	24	%
Elongation at break	ASTM D638	24	%
Flexural modulus	EN ISO 178	1500	MPa
	ASTM D790	217	ksi
Flexural strength	EN ISO 178	58	MPa
	ASTM D790	8412	psi
Charpy - Impact strength	EN ISO 179	53	kJ/m <sup>2</sup>
Charpy - Notched impact strength	EN ISO 179	4.8	kJ/m <sup>2</sup>
Izod – Impact strength	EN ISO 180	32.8	kJ/m <sup>2</sup>
Izod – Notched impact strength	EN ISO 180	4.4	kJ/m <sup>2</sup>
Ball indentation hardness	EN ISO 2039	78	N/mm <sup>2</sup>
Shore D - hardness	ISO 868	75	-
	ASTM D2240	75	-

The mechanical properties depend on the x-, y-, z-position and on the exposure parameters used.

### Thermal properties

Melting point	EN ISO 11357-1	172 - 180	°C
Vicat softening temperature B/50	EN ISO 306	163	°C
	ASTM D1525	325	°F
Vicat softening temperature A/50	EN ISO 306	181	°C
	ASTM D1525	358	°F

The data are based on our latest knowledge and are subject to changes without notice. They do not guarantee properties for a particular part and in a particular application.

© 2009 EOS GmbH – Electro Optical Systems. All rights reserved.

		Unit	HSS Small (2013)	HSS Medium (2013)	HSS Large (2013)
<b>Machine parameters</b>	Build bed dimensions (W x D x H)	mm	200 x 200 x 200	400 x 625 x 625	500 x 800 x 800
	Number of parts per build		288	5,624	11,520
	Build time	h	5.55	26.04	44.44
	Production rate per hour	h <sup>-1</sup>	51.89	215.98	259.23
	Machine utilisation	%	80	80	80
	Hours per year in operation	h	7,008	7,008	7,008
	Production volume total per year		363,658	1,513,556	1,816,655
	Machine depreciation	year	8	8	8
<b>Machine costs</b>	Machine purchase	euro	80,000.00	250,000.00	400,000.00
	Machine purchase cost per year	euro	10,000.00	31,250.00	50,000.00
	Machine maintenance per year	euro	15,000.00	25,000.00	40,000.00
	Software purchase cost per year	euro	3,348.00	3,348.00	3,348.00
	Hardware purchase	euro	10,000.00	10,000.00	10,000.00
	Hardware purchase cost per year	euro	1,250.00	1,250.00	1,250.00
	Total machine cost per year	euro	29,598.00	60,848.00	94,598.00
	Machine cost per hour	euro	4.22	8.68	13.50
	Machine cost per part	euro	0.08	0.04	0.05
<b>Overhead costs</b>	Yearly rent rate per m <sup>2</sup>	euro	160.00	160.00	160.00
	Building area	m <sup>2</sup>	11.20	16.80	23.00
	Total rent per year	euro	1,792.00	2,688.00	3,680.00
	Consumables per year	euro	1,000.00	1,000.00	1,000.00
	Energy consumption per hour	euro	0.60	1.80	2.00
	Production overhead cost per hour	euro	1.00	2.33	2.67
	Production overhead cost per part	euro	0.02	0.01	0.01
<b>Labour costs</b>	Machine operator cost per hour	euro	11.20	11.20	11.20
	Set-up time to control machine	min	120	120	120
	Post-processing time per build	min	144	2,812	5,760
	Labour cost per build	euro	49.28	547.31	1,097.60
	Labour cost per part	euro	0.17	0.10	0.10
<b>Material costs</b>	Powder cost per kg	euro	70.20	70.20	70.20
	Ink cost per litre	euro	96.41	96.41	96.41
	Mass of each part	kg	0.0036	0.0036	0.0036
	Volume of sintered nylon per part	cm <sup>3</sup>	4.30	4.30	4.30
	Volume of printed ink per part	cm <sup>3</sup>	0.13	0.13	0.13
	Total build volume	cm <sup>3</sup>	8,000	8,000	156,250
	Recycling rate	%	90	90	90
	Powder density	g/cm <sup>3</sup>	0.475	0.475	0.475
	Mass of sintered material per build	kg	1.0368	1.0368	20.2464
	Mass of unsintered material per build	kg	3.2118	3.2118	62.7317
	Cost of material used in one build	euro	98.91	98.91	1,931.62
	Material cost per part	euro	0.34	0.34	0.34
<b>Total cost per part</b>		<b>euro</b>	<b>0.62</b>	<b>0.49</b>	<b>0.50</b>

	Unit	LS P360 (2003)	LS P110 (2013)	LS P395 (2013)	LS P760 (2013)	
<b>Machine parameters</b>	Build bed dimensions (W x D x H)	mm	340 x 340 x 600	200 x 250 x 330	340 x 340 x 620	700 x 380 x 580
	Number of parts per build		1,056	600	3,234	6,960
	Build time	h	59.78	24.00	60.00	120.00
	Production rate per hour	h <sup>-1</sup>	17.66	25.00	53.90	58.00
	Machine utilisation	%	90	90	90	90
	Hours per year in operation	h	7,884	7,884	7,884	7,884
	Production volume total per year		139,269	197,100	424,948	457,272
	Machine depreciation	year	8	8	8	8
<b>Machine costs</b>	Machine purchase	euro	340,000.00	190,000.00	400,000.00	800,000.00
	Machine purchase cost per year	euro	42,500.00	23,750.00	50,000.00	100,000.00
	Machine maintenance per year	euro	30,450.00	14,880.00	24,050.00	40,750.00
	Software purchase cost per year	euro	-	3,348.00	3,348.00	3,348.00
	Hardware purchase	euro	-	10,000.00	10,000.00	10,000.00
	Hardware purchase cost per year	euro	-	1,250.00	1,250.00	1,250.00
	Total machine cost per year	euro	72,950.00	43,228.00	78,648.00	145,348.00
	Machine cost per hour	euro	9.25	5.48	9.98	18.44
	Machine cost per part	euro	0.52	0.22	0.19	0.32
<b>Overhead costs</b>	Yearly rent rate per m <sup>2</sup>	euro	-	160.00	160.00	160.00
	Building area	m <sup>2</sup>	-	11.20	16.80	23.00
	Total rent per year	euro	-	1,792.00	2,688.00	3,680.00
	Consumables per year	euro	-	1,000.00	1,000.00	1,000.00
	Energy consumption per hour	euro	-	0.60	1.80	2.00
	Production overhead cost per hour	euro	-	0.95	2.27	2.59
	Production overhead cost per part	euro	-	0.04	0.04	0.04
<b>Labour costs</b>	Machine operator cost per hour	euro	5.30	11.20	11.20	11.20
	Set-up time to control machine	min	120	120	120	120
	Post-processing time per build	min	360	300	1,617	3,480
	Labour cost per build	euro	42.40	78.40	324.24	672.00
	Labour cost per part	euro	0.04	0.13	0.10	0.10
<b>Material costs</b>	Powder cost per kg	euro	70.20	70.20	70.20	70.20
	Mass of each part	kg	0.0036	0.0036	0.0036	0.0036
	Volume of each part	cm <sup>3</sup>	4.30	4.30	4.30	4.30
	Total build volume	cm <sup>3</sup>	69,360	16,500	71,672	154,280
	Recycling rate	%	-	50	50	50
	Powder density	g/cm <sup>3</sup>	0.475	0.475	0.475	0.475
	Mass of sintered material per build	kg	3.8016	2.1600	11.6424	25.0560
	Mass of unsintered material per build	kg	30.7891	6.6120	27.4388	59.0672
	Cost of material used in one build	euro	2,428.27	383.71	1,780.40	3,832.19
	Material cost per part	euro	2.30	0.64	0.55	0.55
<b>Total cost per part</b>	<b>euro</b>	<b>2.86</b>	<b>1.03</b>	<b>0.88</b>	<b>1.01</b>	

# Effect of Sintering Parameters and Flow Agent on the Mechanical Properties of High Speed Sintered Elastomer

**Farhana Norazman<sup>1</sup>**

Department of Mechanical Engineering,  
The University of Sheffield,  
Sheffield S1 3JD, UK  
e-mail: fnorazman1@sheffield.ac.uk

**Neil Hopkinson**

Department of Mechanical Engineering,  
The University of Sheffield,  
Sheffield S1 3JD, UK

*High speed sintering (HSS) is an additive manufacturing (AM) process that creates parts by sintering powder particles using inkjet and infrared (IR) lamp technology rather than laser systems employed in laser sintering (LS). This research investigated the effects of machine parameters (lamp speed, bed temperature) and the addition of fumed silica flow agent on the tensile properties of thermoplastic elastomer (TPE) parts processed using HSS. The results showed improved elongation at break (EaB) values by a factor of more than 2× compared to reported values for LS of the same TPE. At constant parameters, improved tensile strength and tensile modulus were observed with the addition of flow agent into the sintering mixture. [DOI: 10.1115/1.4028482]*

*Keywords: high speed sintering, powder sintering, thermoplastic elastomer, tensile properties, lamp speed, flow agent*

## 1 Introduction

AM is defined as “the process of joining materials to make objects from 3D model data, usually layer upon layer, as opposed to subtractive manufacturing technologies” [1]. There are currently over 20 recognized rapid prototyping (RP) processes based on the “additive” principle, though method of layers consolidation may differ from one another. Classification is made according to the physical state of raw material used in the process; liquid-based systems (e.g., stereolithography), solid-based systems (e.g., fused deposition modeling), and powder-based systems (e.g., LS, HSS) [2]. Depending on the type of process and hardware, a range of metal, polymer, and ceramic materials can be used with AM to create end-use parts with minimal postprocessing.

The main advantage of AM is the design freedom that comes with its tool-less and mold-free processes, enabling consumers to produce parts of almost any geometric shape or feature [3]. Design customization is also made easy and cost-effective with AM as it only takes place within the CAD design. This eliminates many restrictions of conventional design for manufacture and assembly such as the need for undercuts, draft angles, reduced part counts, etc., and therefore improves the design process as a whole [2].

LS is a popular additive process used for making polymer parts. It uses a high power CO<sub>2</sub> laser to sinter powder raw material on a surface bed to create desired shape. Nylon-based materials have been widely used with LS for many years in both RP and rapid manufacturing, particularly the nylon polyamide (Nylon-12) for its superior properties [4]. Material suppliers such as 3D systems and Advanced Laser Materials (ALM) specialize in materials development and have manufactured a range of polyamides (e.g., filled and unfilled nylon) and elastomers (e.g., TPE) to be used with LS [5].

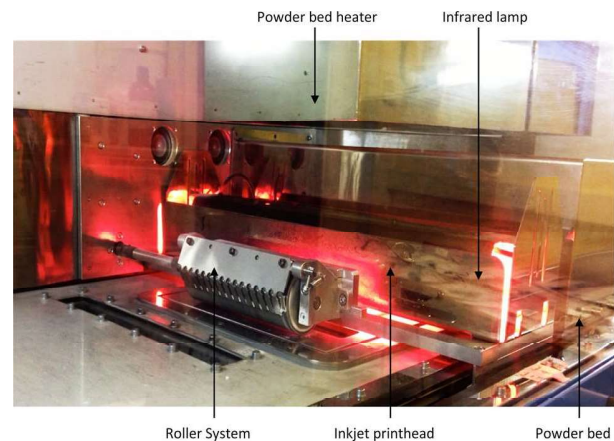
HSS is a relatively new AM process invented at and patented by Loughborough University in the UK, with its process developments detailed by Hopkinson et al. [2]. It utilizes inkjet print head and IR technology to manufacture products layer by layer from

polymer powder material. The process incorporates the same technique as LS with the exclusion of the laser. The process instead uses an IR lamp as the heating source and an inkjet print head defines the part geometry. HSS has several advantages over LS—reduced machine cost by laser elimination and reduced build time as it sinters layer by layer. In common with all AM processes, HSS is capable of producing complex geometry parts with superior mechanical properties. The disadvantage of HSS part, similar to LS part, is the high porosity of the finished part surfaces.

Application of AM is widespread across aerospace, automotive, and consumer industry. LS is used to manufacture air ducts for Boeing F-18 military jets. New Balance, a major footwear manufacturer has adopted LS in producing high-performance customized running shoes for elite athletes.

## 2 HSS

Figure 1 shows the HSS machine and its key parts: powder bed heater, IR lamp, roller system, inkjet printhead, and powder bed. The build procedure on the HSS machine can be broken down into three main stages: preprocessing, building, and postprocessing.



**Fig. 1 HSS machine and key parts**

<sup>1</sup>Corresponding author.

Contributed by the Manufacturing Engineering Division of ASME for publication in the JOURNAL OF MANUFACTURING SCIENCE AND ENGINEERING. Manuscript received April 12, 2014; final manuscript received August 25, 2014; published online October 24, 2014. Assoc. Editor: Joseph Beaman.

**Table 1 Sintering parameters**

Material variables	Process variables
<i>Layer thickness</i> The thickness of each powder layer is determined by the lowering of build platform	<i>Build bed jacket and overhead temperatures</i> The base and overhead temperatures of bed which determines the powder temperature at sintering
<i>Powder ratio</i> The composition of powder material which may include additives or fillers	<i>Sintering power</i> The sintering rate is determined by both lamp power and speed <i>Surface preheat</i> The rate at which powder is preheated before sintering

In this work, the preprocessing involves modeling of 3D part on a CAD software (SOLIDWORKS) then subsequently sliced into a stack of 2D layer files or slice files, each of 100  $\mu\text{m}$  thickness in preparation for the HSS machine. The layer files were transferred to the machine where build parameters were set.

Once the prepared powder was fed into the feed chamber and build parameters were set, the building process began with deposition of a layer of raw powder onto the part bed by roller action, with an IR preheat stroke to warm up the powder prior to sintering. Monochromatic bitmap images of desired part were printed onto the powder bed using a radiation absorbent material, which upon heating by IR lamp absorbed thermal energy and thus melted and sintered the powder underneath. Unprinted powder will remain unsintered and acted as a support to the build. New layer of raw powder is redeposited and this process was repeated until all layers have finished building. Blank layers may be included in the build to separate different parts.

The parts were left to cool with all heating parts switched off, before the cake was removed from the machine. Postprocessing involved powder removal through bead blasting process to obtain finished parts. Other properties enhancement technique such as infiltration of parts may follow if needed.

This research highlights the effects of three main build parameters on the mechanical properties of finished TPE parts. A study by Ellis et al. assessed the influence of print density on mechanical properties of HSS nylon parts [6]. Other research concerning the HSS process include the study of excess powder hardness using nylon with HSS [7] and the effect of IR power level on sintering behavior of Nylon-12 [8].

According to Kang [9], sinterability and the sintered microstructure of a powder compact are mainly determined by material variables and process variables. A set of key HSS build parameters were divided into the two groups and defined in Table 1.

### 3 Elastomer

TPE is elastomeric with the properties of thermoset rubber. It softens when heated to a flowable state but does not cure or set under heat as a thermoset does. Therefore, its chemical properties were unchanged during processing thus promoting recyclability [10]. This study focused on the manufacturing and testing of TPE210-S, a flexible elastomer sintering material supplied by ALM. The ASTM definition of elastomer is “a material which at room temperature can be stretched repeatedly to at least twice its original length, and, upon release of the stress, will return immediately to its approximate original length” [11]. The general mechanical properties for TPEs include low modulus and high yield strain, while Vasquez et al. characterized TPE210-S as having a narrow process window compared to polyamide [12]. Table 2 lists the main properties of TPE210-S as provided by the manufacturer, ALM when processed using LS.

**Table 2 TPE210-S material properties**

Properties	Value
Average particle size (D50)	85 $\mu\text{m}$
Melting point	178 °C
Tensile modulus	8 MPa
Elongation at break (uninfiltrated)	110%
Shore hardness (uninfiltrated)	40

TPE has existed for 40 years and comparable to conventional rubber for its ease of processability and flexibility. Injection molding is the principle process used in the fabrication of TPE parts, followed by extrusion processing. Injection molded TPEs have cost advantages at rapid production rates. TPEs have replaced thermoset rubbers in most of its former applications. TPE parts are widely used in automotive applications for both exterior (bumpers) and interior (dashboard) parts, including under-the-hood automotive applications, such as front-wheel drive components and air ducts [10].

## 4 Methodology

**4.1 Manufacture of Test Parts.** To investigate the influence of build parameters, test specimens were manufactured with variation in build bed overhead temperature, powder ratio and lamp speed. A design of the experiment was created as follows. Table 3 lists the complete build parameters used throughout the project. Tables 4–6 were build parameters with variations in lamp travel speed, build temperature, and powder composition (presence of flow agent), respectively. ASTM Type IV Tensile Test pieces (gage length 25 mm, width 6 mm) were manufactured and used throughout the experiments.

**4.2 Tensile Testing.** Tensile tests were carried out according to ASTM D638 standard test method for tensile properties of plastics [13] using a Tinius Olsen H5K-S Universal Testing Machine equipped with model 500LC Extensometer and HT36 grip under ambient conditions. The crosshead speeds of 5 mm/min and 10 mm/min were maintained during the tests. This method

**Table 3 HSS build parameters for manufacture of test specimens**

Parameter	Value
Build bed jacket temperature	35 °C
Build bed overhead temperature	90 °C 100 °C 110 °C
Feed bed jacket temperature	30 °C
Feed bed overhead temperature	35 °C
Layer thickness	0.1 mm
Maintenance layers	1
Orientation	XYZ
Powder temperature	Room temperature
Powder ratio	100% virgin 50% virgin 50% recycled Virgin + 0.2% Cab-O-Sil Virgin + 0.5% Cab-O-Sil
Sintering power	Lamp power Lamp speed
	100% (2000 W) 50 mm/s 60 mm/s 70 mm/s 80 mm/s 100 mm/s
Surface preheat	50% at 100 mm/s
Warm up time	30 min

**Table 4** Investigating the effect of lamp speed at two bed temperatures and constant powder composition parameter

Build no.	Powder ratio	Build bed overhead temperature (°C)	Lamp speed (mm/s)
1	50% Virgin 50% Recycled	90	60
			70
			80
2	50% Virgin 50% Recycled	100	50
			60
			70

**Table 5** Investigating the effect of bed temperature at two lamp speeds and constant powder composition parameter

Build no.	Powder ratio	Lamp speed (mm/s)	Build bed overhead temperature (°C)
1	50% Virgin 50% Recycled	70	90
			100
			110
2	50% Virgin 50% Recycled	60	90
			100
			100

**Table 6** Investigating the effect of flow agent addition at two lamp speeds and two bed temperatures parameter

Build no.	Build bed overhead temperature (°C)	Lamp speed (mm/s)	Flow agent level (% by weight to virgin TPE)
1	100	50	0
			0.2
			0.5
2	110	70	0
			0.2
			0.5

provided calculations of the EaB (%), Young's modulus (YM) (MPa), and ultimate tensile strength (UTS) (MPa).

**4.3 Thermal Analysis.** The thermal analysis of raw powder material was carried out as outlined by ASTM D3418 standard test method for transition temperatures and enthalpies of fusion and crystallization of polymers by differential scanning calorimetry (DSC) [13]. The tests were performed using a double furnace PerkinElmer DSC8500 instrument. The powder samples tested were 100% Virgin TPE210-S (0.0113 g) and Virgin TPE210-S mixed with 0.2% Cab-O-Sil (0.0167 g). The standard reference material was an empty pan.

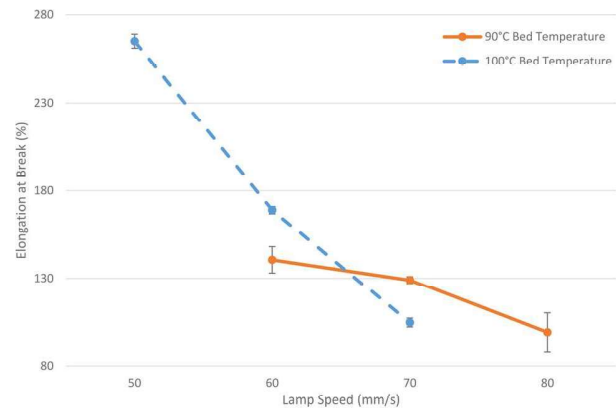
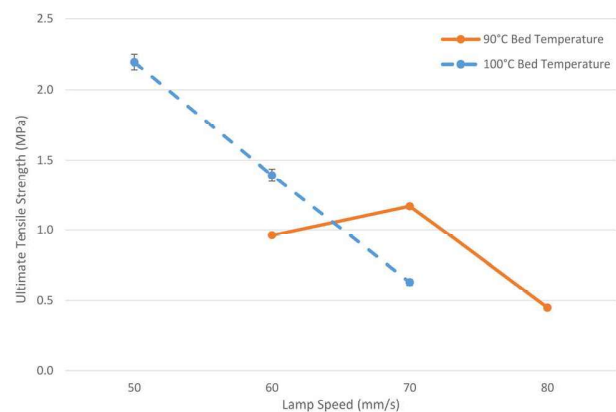
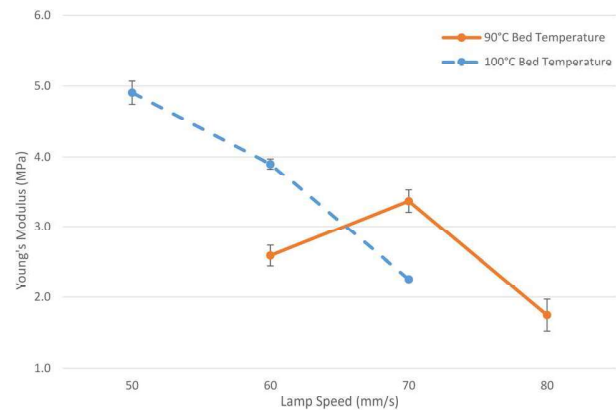
The samples were heated from 20 °C to 210 °C at the rate of 20 °C/min. The temperature was held isothermally at 210 °C for 1 min. Then it was cooled back to 20 °C at the rate of 20 °C/min. The temperature was held isothermally at 20 °C for 1 min. The cycle of heating, temperature hold, and cooling was repeated at the same rate. The DSC curves were plotted for all samples.

**4.4 Surface Roughness Testing.** Surface roughness testing was done using a Mitutoyo SurfTest contact profilometer rig to quantify the quality of high speed sintered TPE parts surface. Constant speed of 0.5 mm/s was maintained and evaluated along 20.0 mm length of the type IV ASTM test specimen during the test. The test was performed on both top and bottom surfaces of specimens. Values of roughness parameter, average roughness ( $R_a$ ) and average maximum height ( $R_z$ ), were obtained through this method.

## 5 Results and Discussion

### 5.1 Mechanical Properties

**5.1.1 The Effect of Lamp Speed at Two Different Bed Temperatures and Constant Powder Composition Parameter.** Figures 2–4 show the graphs of mechanical properties EaB, UTS, and YM plotted against increasing lamp speed at two different bed temperatures 90 °C and 100 °C, respectively. The maximum values of EaB, UTS, and YM are observed at the lowest lamp

**Fig. 2** Variation of EaB with lamp speed and bed temperature**Fig. 3** Variation of UTS with lamp speed and bed temperature**Fig. 4** Variation of YM with lamp speed and bed temperature



speed of 50mm/s, which are 265%, 2.20 MPa, and 4.91 MPa, respectively.

From these figures, it can be concluded that EaB increases with decreasing lamp speed. UTS increases with decreasing, and at a higher rate at low temperature compared to high temperature. The value of YM decreases with increasing lamp speed at both set of temperatures. The variation is not linear and remains low across all set of build parameter.

Though at different intensities, it can be observed that the mechanical properties of HSS printed TPE increase with decreasing speed within the range of parameters analyzed; highest properties achieved at lowest speed and conversely true. The influence of this parameter on mechanical properties can be related to energy density and sintering behavior. According to the Andrew Number, an established model formulated for LS energy density calculation, a decrease in laser power (comparable to HSS lamp power) results in an increase in energy density and directly mechanical properties.

*5.1.2 The Effect of Bed Temperature at Two Different Lamp Speeds and Constant Powder Composition Parameter.* Figures 5–7 show the graphs of mechanical properties EaB, UTS, and YM plotted against increasing build bed temperature at two different lamp speeds 70 mm/s and 60 mm/s, respectively. Within these parameters, the maximum values of EaB, UTS, and YM are observed at the highest build bed temperature of 110 °C, which are 267%, 1.69 MPa, and 4.24 MPa, respectively.

A slight fluctuation can be observed in values of EaB from 90 to 100 °C, which can be regarded as constant before a rapid increase at 110 °C. The same variation exist in tensile properties; an almost horizontal gradient that shows little effect of build bed temperature on UTS and YM until reaching 110 °C.

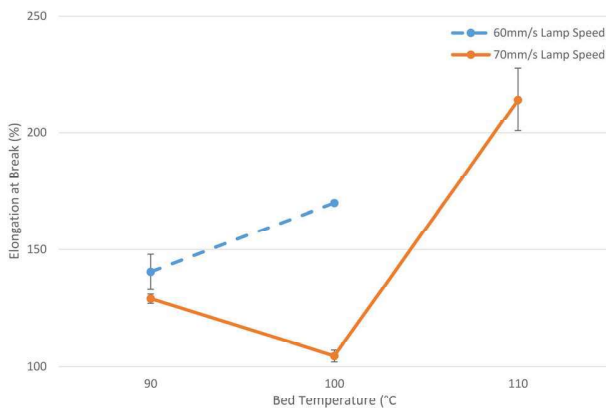


Fig. 5 Variation of EaB with bed temperature and lamp speed

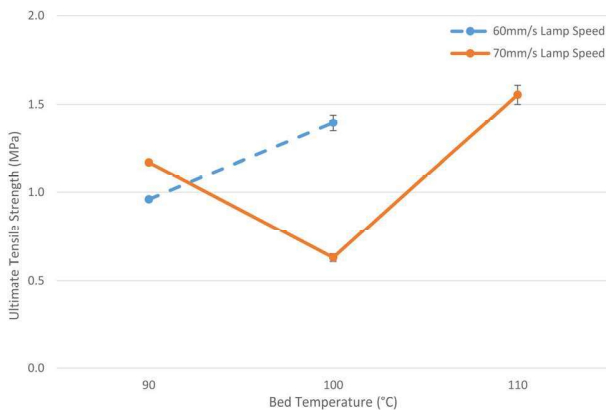


Fig. 6 Variation of UTS with bed temperature and lamp speed

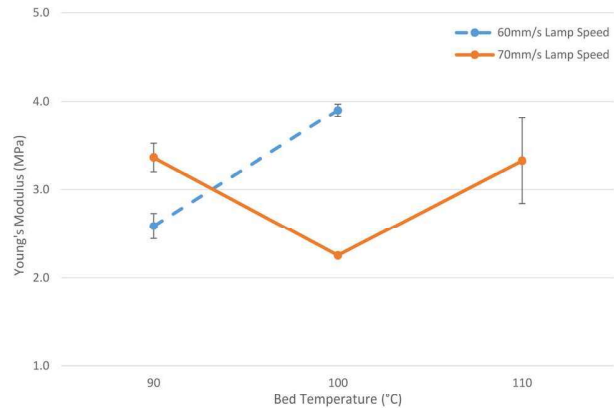


Fig. 7 Variation of YM with bed temperature and lamp speed

According to DSC analysis in Fig. 11, the temperature range of 100–110 °C is where the glass transition occurs for TPE210-S. During this critical temperature range, the material softens and flows at low viscosity before it melts completely, which provides the best characteristics for sintering. It is possible that high degree of sintering with full coalescence took place at this temperature, thus provided improved tensile properties of the sintered parts.

*5.1.3 The Effect of Flow Agent Addition at Two Different Lamp Speeds and Two Different Bed Temperatures Parameter.* A flow agent (fumed silica) was added to the following two best set of parameters to further enhance their finished parts properties: parameter 1 (100 °C bed temperature, 50 mm/s sintering speed) and parameter 2 (110 °C bed temperature, 70 mm/s sintering speed).

The influence of flow agent addition on EaB, UTS, and YM are plotted in Figs. 8–10, respectively, with comparison to 100% virgin-powder sintered parts. The maximum values of EaB, UTS, and YM within the parameters analyzed are observed at 0.2% flow agent by weight, which are 284%, 2.57 MPa, and 10.90 MPa, respectively.

All figures indicate a steady decrease in EaB, UTS, and YM when more flow agent is mixed with virgin powder pass 0.2% level. The influence of polymer additives on HSS part performance can be explained by Frenkel's Model of Sintering which relates particle viscosity to predicted sintering rate. Zero shear viscosity rate for TPE210-S is unknown; however, it is relatively high compared to Nylon-12. It can be speculated that fumed silica promotes fluidity and lowers viscosity of the TPE210-S mix. A decreased viscosity lowers sintering time, thus allowing less energy addition. As low thermal energy is absorbed and tensile

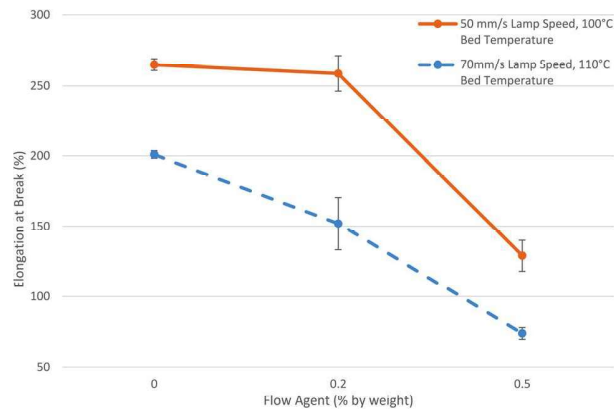
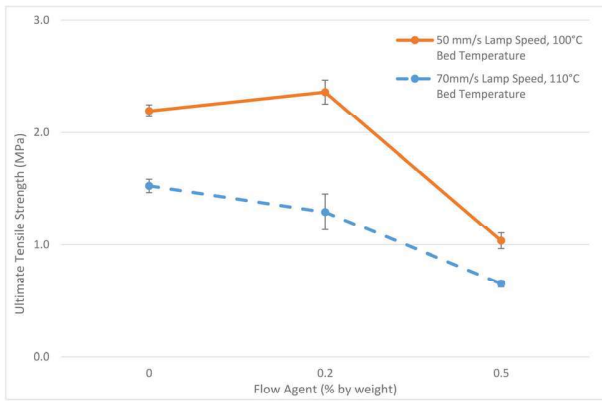
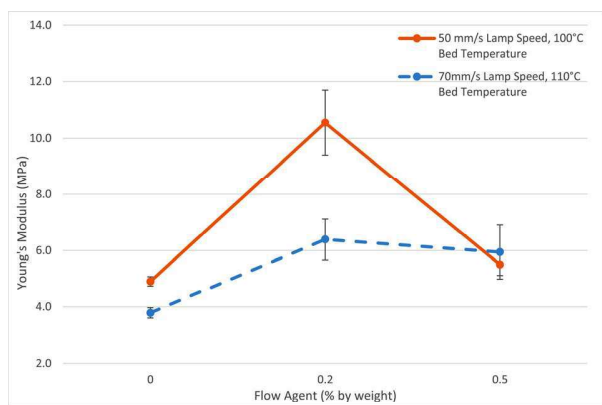


Fig. 8 Variation of EaB with flow agent level at different lamp speeds and bed temperatures



**Fig. 9** Variation of UTS with flow agent level at different lamp speeds and bed temperatures



**Fig. 10** Variation of YM with flow agent level at different lamp speeds and bed temperatures

properties depend largely on the amount of heat energy, this will subsequently result in parts of inferior properties.

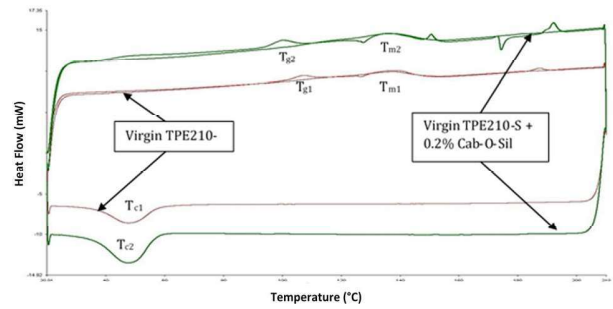
**5.1.4 Comparison Between Mechanical Properties of Parts Processed by HSS, LS, and Injection Molding.** Table 7 shows the mechanical properties of high speed sintered part in comparison with laser sintered and conventional injection molded parts.

**5.2 Thermal Properties.** Figure 11 shows the thermal scan of TPE210-S mixed with 0.2% by weight Cab-O-Sil compared to the thermal scan of virgin TPE210-S. The two curves are identical in shape, with physical transitions occurring at constant temperatures  $T_g$  (105 °C),  $T_m$  (140 °C), and  $T_c$  (50 °C). Minor distortions are observed which may be due to the effect of impurity during mixing or irregular sample composition in the pan.

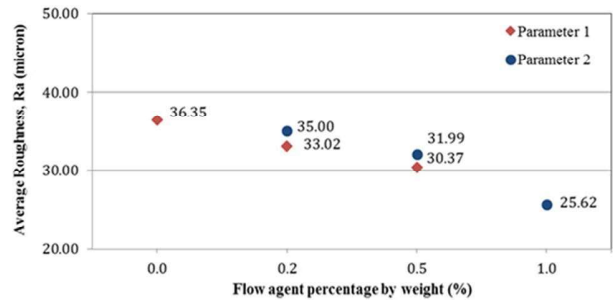
The mix powder curve (outer) has significantly shifted in the direction of heat flow at a value of around 5 mW from the virgin curve (inner). Both melt peak ( $T_{m2}$ ) and crystallization peak ( $T_{c2}$ )

**Table 7** Part performance: comparison among HSS, LS, and IM

Process	% by weight of fumed silica mix	EaB (%)	YM (MPa)	UTS (MPa)
HSS	0.2	259	10.55	2.36
HSS	0	265	4.91	2.20
LS (5)	0	110	8.00	N/A
Injection molding (9)	0	495	4.48	1.06



**Fig. 11** DSC scan of TPE210-S mixed with 0.2% Cab-O-Sil and virgin TPE210-S



**Fig. 12** Average roughness values against flow agent addition

appear sharper in the mix powder curve compared to  $T_{m1}$  and  $T_{c1}$ . This suggests the addition of flow agent has increased the amount of energy required to change the material from solid to liquid, i.e., heat of fusion,  $\Delta H_m$ , and the amount of energy released during crystallization,  $\Delta H_c$ . As both transitions take place at the constant temperatures of 140 °C and 50 °C, consequently higher thermal energy is involved in both phase changes. The presence of silica atoms in between the TPE atoms may have an effect on the molecules arrangement, making them closely packed together. This subsequently strengthens the intermolecular bonds, thus more energy is needed to break them. It is also observed that the range of  $T_g$  in both curves differed slightly, with  $\Delta T_{g2}$  higher than  $\Delta T_{g1}$ , by approximately 5 °C. The process window is widened, thus providing advantage to the sintering process at lower temperature range. In conclusion, the addition of flow agent in powder does not only alter the original physical properties of powder but also enhance its thermal properties.

**5.3 Surface Roughness.** The effect of adding flow agent into the powder mix can be observed through the following graph of average roughness variation in Fig. 12. The addition of flow agent generally reduces the surface roughness by promoting better flow between the particles during sintering. However, the values of  $R_a$  are still relatively high compared to parts produced by other manufacturing technologies and materials.

**6 Conclusions**

The experiments have shown that the HSS process produces superior parts compared to equivalent laser sintered parts. The addition of fumed silica decreases part surface roughness. However, further addition of fumed silica results in a decrease of EaB, evident increase of YM, and mixed results in UTS.

**References**

[1] Gibson, I., Rosen, D. W., and Stucker, B., 2010, *Additive Manufacturing Technologies: Rapid Prototyping to Direct Digital Manufacturing*, Springer, New York.



- [2] Hopkinson, N., Hague, R., and Dickens, P., 2006, *Rapid Manufacturing: An Industrial Revolution for the Digital Age*, Wiley, Chichester, UK.
- [3] Wohlers, T., 2007, *Wohlers Report 2007: State of the Industry: Annual Worldwide Progress Report*, Wohlers Associates Inc., Fort Collins, CO.
- [4] Starr, T., Gornet, T., and Usher, J., 2011, "The Effect of Process Conditions on Mechanical Properties of Laser-Sintered Nylon," *Rapid Prototyping J.*, **17**(6), pp. 418–423.
- [5] Advanced Laser Materials (ALM), "TPE210-S Technical Data Sheet," ALM official website, <http://www.alm.com>
- [6] Ellis, A., Noble, C. J., and Hopkinson, N., 2014, "High Speed Sintering: Assessing the Influence of Print Density on Microstructure and Mechanical Properties of Nylon Parts," *Addit. Manuf.* (in press).
- [7] Thomas, H. R., Hopkinson, N., and Erasenthiran, P., 2006, "High Speed Sintering—Continuing Research Into a New Rapid Manufacturing Process," Proceedings of 17th SFF Symposium, Austin, TX, pp. 682–691.
- [8] Majewski, C. E., Oduye, D., Thomas, H. R., and Hopkinson, N., 2008, "Effect of Infra-red Power Level on the Sintering Behaviour in the High Speed Sintering Process," *Rapid Prototyping J.*, **14**(3), pp. 155–160.
- [9] Kang, S., 2005, *Sintering Densification, Grain Growth, and Microstructure*, Elsevier Butterworth-Heinemann, Amsterdam, The Netherlands.
- [10] Harper, C. A., 1992, *Handbook of Plastics, Elastomers, and Composites*, McGraw-Hill, New York.
- [11] Walker, B. M., 1979, *Handbook of Thermoplastic Elastomers*, Van Nostrand Reinhold, New York.
- [12] Vasquez, M., Hopkinson, N., and Haworth, B., 2010, "Laser Sintering Processes: Practical Verification of Particle Coalescence for Polyamides and Thermoplastic Elastomers," ANTEC 2011 Conference, Society of Plastics Engineers Incorporated (SPE), Boston, MA, pp. 2458–2462.
- [13] ASTM, "ASTM International—Standards Worldwide," Available at: <http://www.astm.org>

ANOVA table for dimensional accuracy in x-direction

Source	Sum of squares	Degrees of freedom	Mean square	F value	P value
Model	0.421*	9	0.047	3.733	< .0001
Lamp	0.035	1	0.035	2.828	.095
Ink	0.248	4	0.062	4.946	.001
Lamp x Ink	0.152	4	0.038	3.024	.019
Error	2.043	163	0.013		
Total	4.206	173			
Corrected Total	2.464	172			

\*R<sup>2</sup> = .171, adjusted R<sup>2</sup> = .125

ANOVA table for dimensional accuracy in y-direction

Source	Sum of squares	Degrees of freedom	Mean square	F value	P value
Model	2.765*	9	0.307	57.463	< .0001
Lamp	1.543	1	1.543	288.670	< .0001
Ink	0.874	4	0.219	40.874	< .0001
Lamp x Ink	0.260	4	0.065	12.138	< .0001
Error	0.871	163	0.005		
Total	3.703	173			
Corrected Total	3.636	172			

\*R<sup>2</sup> = .760, adjusted R<sup>2</sup> = .747

ANOVA table for dimensional accuracy in z-direction

Source	Sum of squares	Degrees of freedom	Mean square	F value	P value
Model	1.535*	9	0.171	44.705	< .0001
Lamp	1.261	1	1.261	330.712	< .0001
Ink	0.141	4	0.035	9.212	< .0001
Lamp x Ink	0.100	4	0.025	6.525	< .0001
Error	0.622	163	0.004		
Total	3.900	173			
Corrected Total	2.156	172			

\*R<sup>2</sup> = .712, adjusted R<sup>2</sup> = .696